

**Proceedings of the
22nd Annual Imaging
Network Ontario Symposium**

**March 19 - 20, 2024
Hilton Meadowvale
Mississauga, Ontario**

Table of Contents

ImNO 2024 Co-Chairs.....	4
Organizing Committee	4
Scientific Committee	4
Planning Committee.....	4
Student Committee	4
Abstract Reviewers	5
Oral and Pitch/Poster Judges & Session Chairs.....	5
Welcome Letter	6
Imaging Network Ontario Code of Conduct	7
Supporting Consortia	8
Ontario Institute for Cancer Research Imaging Program.....	8
Machine Learning in Medical Imaging Consortium (MaLMIC).....	8
3D Ultrasound and Multi-Modality Imaging for Personalized Medicine.....	8
Toronto Metropolitan University	9
Corporate Sponsors	9
GE HealthCare	9
Siemens Healthineers	9
Scintica	10
NDI	10
Keynote Speakers.....	11
Anne Martel	11
Frédéric Leblond.....	12
Debate: The Role of AI in Medicine	13
Panel Session: Commercialization of AI-enabled Medical Imaging Technology.....	14
Program at a Glance.....	16
ImNO 2024 Program.....	17
Talk and Pitch Abstracts (in order of the talks).....	24
Session 1 Talks: Deep/Machine Learning 1	25
Session 2 Talks: MRI 1	30
Session 3 Pitches: Deep Learning.....	35
Session 4 Pitches: MRI.....	47
Session 5 Talks: Device, Hardware, Software Development.....	57
Session 6 Talks: Cancer	62

Session 7 Pitches: Device, Hardware, Software Development	67
Session 8 Pitches: Cancer.....	79
Session 9 Talks: Image-Guided Intervention.....	90
Session 10 Talks: Neuroimaging 1.....	95
Session 11 Talks: Cardiac and Lung.....	100
Session 12 Talks: Neuroimaging 2.....	105
Session 13 Pitches: Cardiac, Lung, Image Processing.....	110
Session 14 Pitches: Neuroimaging.....	119
Session 15 Talks: Deep/Machine Learning 2	130
Session 16 Talks: MRI 2	135
Session 17 Talks: Cellular and Molecular.....	140
Session 18 Talks: Ultrasound and Photoacoustic.....	145
Session 19 Pitches: Cellular and Molecular.....	150
Session 20 Pitches: Ultrasound and Optical	159
Author Index	169

ImNO 2024 Co-Chairs



[Michael Daly](#)
Princess Margaret Cancer Centre



[Elodie Lugez](#)
Toronto Metropolitan University

Organizing Committee

[Scientific Committee](#)

Sarah Aubert, Princess Margaret Cancer Centre
Viktoria Batarчук, Lakehead University
Elvis Chen, Robarts Research Institute
Amanda Hamilton, Western University
Justin Hicks, Lawson Health Research Institute
Amoon Jamazad, Queen's University

Angus Lau, Sunnybrook Research Institute
Jessica Rodgers, University of Manitoba
Ali Tavallaei, Toronto Metropolitan University
Eran Ukwatta, University of Guelph
Joseph Umoh, Robarts Research Institute

[Planning Committee](#)

Carol Richardson, OICR Imaging Program
Bobbi Hoffman, Gemstone Event Management

Shaina Scrimgeour, Gemstone Event Management
Kitty Wong, Robarts Research Institute

[Student Committee](#)

Joeana Cambranis, Robarts Research Institute
Samantha Flood, Western University
Lisa Garland, Robarts Research Institute
Kalysta Makimoto, Metropolitan University (Co-chair)
Stefanie Markevich, McMaster University (Co-Chair)

Teo Mesrkhani, University of Toronto
Ramtin Mojtahedi, Queen's University
Michael Singh, University of Toronto
HaPhan Tran, University of Toronto

Abstract Reviewers

Faranak Akbarifar
 Natasha Alves
 Corey Baron
 Viktoriia Bataarchuk
 Amanda Boyle
 Jeffrey Carson
 Elvis Chen
 Michael Daly
 Maria Drangova
 Razieh Enjilela
 Aaron Fenster
 Gabor Fichtinger
 Nancy Ford
 Stewart Gaede
 Donna Goldhawk
 Amanda Hamilton
 Wenchao Han
 Michael Hardisty

Justin Hicks
 Matthew Holden
 Eno Hysi
 Amoon Jamzad
 Miranda Kirby
 Ivan Kosik
 Manuela Kunz
 Andras Lasso
 Angus Lau
 Elodie Lugez
 Chris Macgowan
 Nooshin Maghsoodi
 James Mainprize
 Charles McKenzie
 Stewart McLachlin
 Emily Murrell
 Lucas Narciso
 Michael Noseworthy

Alexei Ouriadov
 Terry Peters
 Tamie Poepping
 Mihaela Pop
 Jessica Rodgers
 John Sled
 Dafna Sussman
 Sarah Svenningsen
 Jesse Tanguay
 Jonathan Thiessen
 Junchao Tong
 Joseph Umoh
 Tamas Ungi
 Justin Wan
 Jill Weyers
 Dan Xiao

Oral and Pitch/Poster Judges & Session Chairs

Natasha Alves-Kotzev
 Amal Aziz
 Jin-Young Bang
 Amy Boyle
 Joeana Cambranis
 Patrick Carnahan
 Pavel-Dumitru Cemelev
 Naz Chaudary
 Laura Connolly
 Michael Daly
 Ethan Danielli
 Paul Dubovan
 Aaron Fenster
 Shahin Ghaseminejad
 Donna Goldhawk

Amanda Hamilton
 Michael Hardisty
 Miriam Hewlett
 Justin Hicks
 Rebecca Hisey
 Shaelyn Horvath
 Eno Hysi
 Sina (Mohammadmahdi) Keshavarz
 Sule Karagulleoglu Kunduraci
 Andras Lasso
 Daniel Louie
 Elodie Lugez
 Kalysta Makimoto
 Ramtin Mojtahedi
 Gerald Moran
 Farah Mushtaha

Prashant Pandey
 Jessica Rodgers
 Nidhi Singh
 Qin (Daisy) Sun
 Ali Tavallaei
 Rachel Theriault
 Olivia Tong
 Tamas Ungi
 Michael Valic
 Gabriel Varela-Mattatall
 Wen Yao Xia
 Shuwei Xing
 Jing Yang
 Ju-Chi Yu
 Chao Zheng

Welcome Letter

Dear ImNO 2024 Attendees:

On behalf of the 2024 Organizing Committee, we are excited to welcome you to the 22nd annual Imaging Network Ontario (ImNO) Symposium. We are delighted to be in-person in Mississauga, Ontario this year and are looking forward to reconnecting with this exceptional community as we come together once again. The Annual two-day ImNO Symposium features world-class scientists and showcases multidisciplinary presentations from Ontario and across the country.

This rendez-vous of researchers promotes collaborations, broadcasts career opportunities, informs trainees on diverse imaging applications, and fosters a greater understanding of the commercialization process. The symposium features world-renowned keynote speakers and sessions that bring our trainees together with imaging scientists, clinicians, patient groups, and industry representatives.

Highlights for this year's program include two keynote speakers, Anne Martel and Frédéric Leblond, as well as a lunch-and-learn panel session on the commercialization of AI-enabled medical imaging technology. The Symposium will feature 124 accepted presentations split between 47 oral presentations and 77 pitch-and-poster presentations. There will also be plenty of opportunities for you to network with your imaging colleagues, including a reception and trainee social games.

We are pleased to thank the following groups for their support of the 2024 Symposium:

- Machine Learning in Medical Imaging Consortium (MaLMIC)
- Ontario Institute of Cancer Research (OICR) Imaging Program
- 3D Ultrasound and Multi-Modality Imaging for Personalized Medicine
- GE Healthcare
- Siemens Healthineers
- Scintica Instrumentation, Inc.
- Northern Digital Inc. (NDI)
- Toronto Metropolitan University

In closing, we would like to thank our reviewers who provided feedback on the proffered abstracts and acknowledge the significant contributions made by members of the Scientific, Student, and Planning Committees. These teams have worked very hard to bring us this year's Symposium.

We hope you enjoy this year's program of keynotes, discussion, oral talks, and pitch-and-poster presentations.

Sincerely,

Michael Daly and Elodie Lugez

ImNO Symposium 2024 Co-Chairs

Imaging Network Ontario Code of Conduct

All attendees, speakers, sponsors and volunteers at the ImNO Symposium are required to agree with the following code of conduct. Organisers will enforce this code throughout the event. We expect cooperation from all participants to help ensure a safe environment for everybody.

Need Help?

If you are being harassed, notice that someone else is being harassed, or have any other concerns, contact the Symposium Manager at imno@imno.ca or send an email to ombudsperson@ImNO.ca or chairs@ImNO.ca.

Overview

Imaging Network Ontario is committed to providing a harassment-free symposium experience for everyone, regardless of gender, gender identity and expression, age, sexual orientation, disability, physical appearance, body size, race, ethnicity, religion (or lack thereof), or technology choices. We do not tolerate harassment of symposium participants in any form. Use of sexualised language and imagery that does not convey a scientific message is not appropriate. We expect participants and sponsors to follow these rules for the duration of the symposium in any symposium venue or platform, including talks, social events, Twitter, and other online media. Symposium participants violating these rules may be sanctioned or expelled from the symposium without a refund at the discretion of the symposium organisers.

Details

All attendees, speakers, sponsors and volunteers at ImNO are subject to the anti-harassment policy.

Harassment includes offensive verbal comments related to gender, gender identity and expression, age, sexual orientation, disability, physical appearance, body size, race, ethnicity, religion, technology choices, sexual images in public spaces, deliberate intimidation, stalking, following, harassing photography or recording, sustained disruption of talks or other events, inappropriate contact, and unwelcome sexual attention. Use of images, activities, uniforms/costumes or other materials that create a sexualised environment will not be tolerated.

Anyone asked to stop any harassing behaviour is expected to comply immediately.

If anyone engages in harassing behaviour, the symposium organisers may take any action they deem appropriate, including warning the offender or expulsion from the symposium with no refund.

If you are being harassed, notice that someone else is being harassed, or have any other concerns, please contact a member of conference staff immediately. You can also send an email to the ImNO ombudsperson, Dr. Amanda Hamilton, at ombudsperson@ImNO.ca or the ImNO 2024 Chairs, Drs. Elodie Lugez or Michael Daly, at chairs@ImNO.ca.

We expect everyone to follow these rules for the duration of the Symposium within and outside Symposium venues and platforms, including but not limited to Symposium-related talks, workshops, and social events involving ImNO attendees, and in all Symposium-related communications, including social media.

Supporting Consortia

The Annual Meeting of Imaging Network Ontario (ImNO) is grateful for the support of our sponsors and their dedication to imaging research. The following consortia and programs supported the 2024 ImNO Symposium.

Ontario Institute for Cancer Research Imaging Program

Co-Director: Drs. Aaron Fenster and Martin Yaffe – [Ontario Institute for Cancer Research](#)



The OICR Imaging Program accelerates the translation of research into the development of new imaging innovations for earlier cancer detection, diagnosis and treatment through four major projects: probe development and commercialization, medical imaging instrumentation and software, pathology validation, and imaging for clinical trials. The Imaging Program facilitates improved screening and treatment options for cancer patients by streamlining advances in medical imaging through the complex pipeline from discovery to clinical translation and ultimately to clinical use.

Machine Learning in Medical Imaging Consortium (MaLMIC)

Working Group: Drs. Aaron Fenster, Anne Martel, Julia Publicover, Amber L. Simpson, Aaron Ward, Martin Yaffe – [Machine Learning for Medical Imaging](#)



The Consortium was launched to accelerate research and development of machine learning solutions for unmet needs in medical imaging through collaborations between academic and clinical researchers, and with Canadian industry.

3D Ultrasound and Multi-Modality Imaging for Personalized Medicine

Lead Researchers: Drs. Aaron Fenster and Alla Reznik

Sponsor: [Ontario Research Fund \(ORF\)](#)



Continued developments of medical imaging systems have vastly improved our ability to visualize body tissues and processes, enabling more accurate detection of medical conditions. However, recent trends for personalized or precision medicine, i.e., delivering “the right treatment to the right patient at the right time”, impose new requirements for imaging modalities in terms of diagnostic and predictive capabilities and change the emphasis from a nonspecific to an organ-specific imaging approach - a significant paradigm shift in medicine. Indeed, precision medicine often cannot be achieved with existing general purpose or whole-body imaging devices. Predictive and preventive precision medicine calls for new approaches where organ-specific imaging tools are customized for particular organs or diseases to obtain the highest efficacy and diagnostic capability.

Dual-modality imaging is an integral part of this approach as it provides complimentary visual and quantitative information that is based on aligned morphological and functional data. We have a long history of developing innovative imaging systems used to solve clinical unmet needs, some of which have been translated clinically and commercialized. Our efforts are driven by innovations resulting in improved diagnostic accuracy as well as increased patient comfort. The overarching goal of the ORF is to develop effective new imaging-based systems that will use ultrasound imaging with radionuclide imaging to overcome the limitations of independent systems and meet the challenges of unmet clinical needs.

Toronto Metropolitan University



Faculty of
Science

Toronto Metropolitan University is at the intersection of mind and action. What our students learn in the classroom is enhanced by real-world knowledge and experience. We champion diversity, entrepreneurship and innovation.

Corporate Sponsors



GE HealthCare

[GE HealthCare](#) is a leading global medical technology, pharmaceutical diagnostics, and digital solutions innovator, dedicated to providing integrated solutions, services and data analytics that clinicians more effective, therapies more precise, and patients healthier and happier. Serving patients and providers for more than 100 years, GE HealthCare is advancing connected and compassionate care, while simplifying the patient's journey across the care pathway. Together, we're creating a world where healthcare has no limits.



[Siemens Healthineers](#) pioneers breakthroughs in healthcare. For everyone. Everywhere. Sustainably. The company is a global provider of healthcare equipment, solutions and services, with activities in more than 180 countries and direct representation in more than 70. As a leading medical technology company, Siemens Healthineers is committed to improving access to healthcare for underserved communities worldwide and is striving to overcome the most threatening diseases. The company is principally active in the areas of imaging, diagnostics, cancer care and minimally invasive therapies, augmented by digital technology and artificial intelligence.

Scintica:

[Scintica](#) is a leading supplier of high-value instrumentation. We bridge the gap between innovative research needs and advanced scientific solutions, supporting scientists and the preclinical research community. Our cutting-edge preclinical imaging portfolio features systems such as PET, CT, SPECT, MRI, optical (FLI/BLI/NIR II), DXA, echoMRI, intravital microscopy, photoacoustic, and high-frequency ultrasound. These offerings are strengthened by comprehensive support and service. Our team of scientific experts, is ready to assist at every step of your research journey, ensuring optimal outcomes and unparalleled support. At Scintica, our mission extends beyond merely supplying tools and technologies; we are dedicated to empowering scientists with the precision instruments and comprehensive support necessary to advance scientific research. Visit us at scintica.com to explore a world where innovation meets excellence.



[NDI](#) is the world's leading innovator of optical and electromagnetic navigation technology. For 40+ years, we've helped medical device OEMs bring new surgical navigation applications—and clinical breakthroughs—to market.

Keynote Speakers

Tuesday, March 19, 2024, at 08:45

AI for Medical Image Analysis: Living with Limited Data

[Anne Martel](#), University of Toronto & Sunnybrook Research Institute

Anne Martel is a Professor in Medical Biophysics at the University of Toronto, a Senior Scientist and Tory Family Chair in Oncology at Sunnybrook Research Institute. She is also a Faculty Affiliate at the Vector Institute, Toronto.

Her research program is focused on medical image and digital pathology analysis, particularly on applications of machine learning for segmentation, diagnosis, and prediction/prognosis and she has over 160 publications with more than 6000 citations in this field.

Dr Martel is an active member of the medical image analysis community. She is a fellow of the MICCAI (Medical Image Computing and Computer Assisted Intervention) Society which represents engineers and computer scientists working in this field and served as board member from 2017-2021. She has

served as a general co-chair, scientific co-chair and educational chair for several MICCAI conferences and has also served as a program committee member for many SPIE and MICCAI conferences.

Dr Martel is currently on the editorial board of the journal Medical Image Analysis and previously served as an Associate Editor for IEEE Transactions in Medical Imaging. In 2006 she co-founded Pathcore (Toronto, ON), a software company developing complete workflow solutions for digital pathology.



Wednesday, March 20, 2024, at 16:15

Clinical Deployment of Raman Spectroscopy: Applications in Neurosurgery and Beyond

[Frédéric Leblond](#), Polytechnique Montréal

Frederic Leblond, PhD, is a professor in the Department of Engineering Physics at Polytechnique Montreal and Director of LumedLab. He is also a researcher at the CRCHUM medical research center and co-founder of the companies Reveal Surgical and Exclaro.

Professor Leblond holds a Bachelor's degree in Engineering Physics from Polytechnique Montreal, a Master's degree in Physics from Laval University and a PhD in Physics from McGill University.

After his Ph.D., he was a postdoctoral researcher at the University of Chicago. His doctoral and postdoctoral research focused on theoretical physics, particularly in relation to quantum mechanics and cosmology. He was then a senior researcher for three years and worked on the development of medical instruments at a Montreal medical imaging company.

Prior to joining Polytechnique, Professor Leblond was a professor of engineering at Dartmouth College, New Hampshire, for five years, where he was also affiliated with the Dartmouth-Hitchcock Medical Center.

Dr. Leblond's research is related to the development of light-based medical devices to characterize biological tissues and biofluids to improve the accuracy and safety of surgical procedures, as well as to develop techniques to improve the accuracy of medical diagnostics. He holds a dozen of patents and has published more than 110 peer-reviewed articles. He holds multiples research grants, including from the National Sciences and Engineering Council of Canada (NSERC) and the Canadian Institutes of Health Research (CIHR).



Debate: The Role of AI in Medicine

This debate will commence with an expert address, who will be discussing the current impact and potential role of AI for personalized patient care. Following the expert's presentation, two well-prepared student groups will engage in a series of short debates on pre-selected topics related to AI in medicine from two different standpoints. The organizing committee hopes you can join us in this engaging session of intellectual exchange from students through thought-provoking dialogues.

Opening talk: Ebrahim Bagheri, Toronto Metropolitan University

Ebrahim Bagheri is a Professor in the Department of Electrical, Computer and Biomedical Engineering at Toronto Metropolitan University, where he holds a Canada Research Chair in Social Information Retrieval and an NSERC Industrial Research Chair in Social Media Analytics. He is the Director of the NSERC CREATE program on the Responsible Development of AI (RAI)—a 6-year, multi-sector, multi-institutional, collaborative training program that draws co-applicants from TMU, Waterloo, Western, UQAM, and McGill.

Debate Moderator: Calvin Hillis

Debate Team 1: AI will narrow gaps in access to healthcare and Global Health Equity:

1. Ramtin Mojtahedi
2. Radin Hamidi Rad
3. Dumitru Cernelev

Debate Team 2: AI will exacerbate gaps in access to healthcare and Global Health Equity:

1. Mykelle Pacquing
2. Tyler Elliott
3. Laura Connolly

The students are from two NSERC CREATE teams, including **Medical Informatics** and **Responsible AI**.

Panel Session: Commercialization of AI-enabled Medical Imaging Technology

This panel session will include experts from industry and academia with direct experience in commercializing AI-enabled medical imaging technology. Moderator Anne Martel will lead a discussion on the opportunities and challenges of bringing novel devices to the marketplace for improved patient care. This will include questions on how the rapid development of AI technology is changing the commercialization process for image-guided and medical imaging technologies.

Moderator: Anne Martel, University of Toronto & Sunnybrook Research Institute

Panelists:

- Alexander Bilbily, University of Toronto
- Mathieu Burtnyk, Profound Medical
- Frédéric Leblond, Polytechnique Montréal
- Prashant Pandey, MOLLI Surgical
- Mike Wesolowski, Luxsonic

[Anne Martel](#), University of Toronto & Sunnybrook Research Institute

Anne Martel is a Professor in Medical Biophysics at the University of Toronto, a Senior Scientist and Tory Family Chair in Oncology at Sunnybrook Research Institute. She is also a Faculty Affiliate at the Vector Institute, Toronto. Her research program is focused on medical image and digital pathology analysis, particularly on applications of machine learning for segmentation, diagnosis, and prediction/prognosis and she has over 160 publications with more than 6000 citations in this field. Dr Martel is an active member of the medical image analysis community. She is a fellow of the MICCAI (Medical Image Computing and Computer Assisted Intervention) Society which represents engineers and computer scientists working in this field and served as board member from 2017-2021. She has served as a general co-chair, scientific co-chair and educational chair for several MICCAI conferences and has also served as a program committee member for many SPIE and MICCAI conferences. Dr Martel is currently on the editorial board of the journal Medical Image Analysis and previously served as an Associate Editor for IEEE Transactions in Medical Imaging. In 2006 she co-founded Pathcore (Toronto, ON), a software company developing complete workflow solutions for digital pathology.

[Alexander Bilbily](#), University of Toronto

Alexander Bilbily is a Toronto-based academic radiologist, nuclear medicine physician, and computer scientist. Dr. Bilbily is an Assistant Professor at the University of Toronto and Co-Founder & Co-CEO of 16 Bit Inc, an internationally award-winning AI medical imaging company with the vision of augmenting physician diagnostic ability using artificially intelligent tools. 16 Bit currently offers Health Canada approved SaMD for osteoporosis screening and pediatric bone age assessment.

Dr. Bilbily also serves as the director of the Augmented Precision Medicine (APM) lab at Sunnybrook Hospital and is a Scientific Advisory Committee member at Osteoporosis Canada. Dr. Bilbily believes that AI will be the foundation of next-generation tools that will improve the efficiency, quality, and reliability of care that physicians can offer to their patients.

Mathieu Burtnyk, Profound Medical

Mathieu Burtnyk is the Senior Vice President, Product Leader for the TULSA-PRO at Profound Medical, a medical device company which develops and markets customizable, incision-free therapies for the ablation of diseased tissue. After completing his PhD in Medical Biophysics at the University of Toronto in 2010, Mathieu made the transition to industry to focus on the commercialization of novel image guided therapies, design and implement go-to-market strategies, and ultimately bring these technologies to clinical practice.

Frédéric Leblond, Polytechnique Montréal

Frederic Leblond, PhD, is a professor in the Department of Engineering Physics at Polytechnique Montreal and Director of LumedLab. He is also a researcher at the CRCHUM medical research center and co-founder of the companies Reveal Surgical and Exclaro. Professor Leblond holds a Bachelor's degree in Engineering Physics from Polytechnique Montreal, a Master's degree in Physics from Laval University and a PhD in Physics from McGill University. After his Ph.D., he was a postdoctoral researcher at the University of Chicago. His doctoral and postdoctoral research focused on theoretical physics, particularly in relation to quantum mechanics and cosmology. He was then a senior researcher for three years and worked on the development of medical instruments at a Montreal medical imaging company. Prior to joining Polytechnique, Professor Leblond was a professor of engineering at Dartmouth College, New Hampshire, for five years, where he was also affiliated with the Dartmouth-Hitchcock Medical Center. Dr. Leblond's research is related to the development of light-based medical devices to characterize biological tissues and biofluids to improve the accuracy and safety of surgical procedures, as well as to develop techniques to improve the accuracy of medical diagnostics. He holds a dozen of patents and has published more than 110 peer-reviewed articles.

Prashant Pandey, MOLLI Surgical

Prashant Pandey is an Engineering Scientist at MOLLI Surgical and is responsible for developing machine learning technologies used in medical devices for breast tumor localization. He completed his doctoral research on ultrasound-guided orthopaedic surgery at the University of British Columbia, which enabled surgeons to perform radiation-free surgeries for pelvic fracture repairs. Prashant's expertise spans ultrasound imaging, surgical navigation, computer vision, and machine learning, and he is passionate about implementing technologies that improve the impact and global accessibility of surgical and medical care for patients. His achievements include the Vanier Scholarship, the Joule Innovation Grant, and the Oxford Canada Scholarship.

Mike Wesolowski, Luxsonic

Mike Wesolowski, PhD, is an entrepreneur, multidisciplinary researcher, and a passionate advocate of the concept of using "tech for good". Mike is the founder and CEO of Luxsonic, a Canadian medtech company whose mission is to transform the way that humans interact with medical images. In doing so, they aim to improve access to imaging for billions of people around the world. Luxsonic's groundbreaking Virtual Imaging Platform combines artificial intelligence with virtual reality to create unparalleled access to collaborative medical imaging workflow tools for academic, clinical, and diagnostic use cases.

In 2024, Forbes recognized Luxsonic as one of the top 100 Best Canadian Startup Employers. Mike also holds an Adjunct Professorship in Medical Imaging at the University of Saskatchewan and has co-authored over 35 academic publications in fields ranging from astrophysics to radiology. He firmly believes that technology can be a dramatic force of positive change in our society.

Program at a Glance

Tuesday, March 19, 2024	
Graydon Hall ABC	Greenwich Room
07:00 - 08:30 Breakfast (Graydon Hall Foyer)	
07:30 - 08:30 Siemens Breakfast Symposium (Greenwich Room)	
08:30 - 08:45 Opening Remarks (Graydon Hall ABC)	
08:45 - 09:30 Keynote I: AI for Medical Image Analysis: Living with Limited Data Anne Martel, University of Toronto (Graydon Hall ABC)	
09:30 - 09:45 Coffee Break (Graydon Hall Foyer)	
09:45 - 10:45 Session 1 Talks: Deep/Machine Learning 1	Session 2 Talks: MRI 1
10:45 - 11:20 Session 3 Pitches: Deep Learning	Session 4 Pitches: MRI
11:20 - 12:15 Poster Viewing (Pitch Sessions 3 & 4 presenting) (Graydon Hall D)	
12:15 - 12:45 Lunch Pickup (Graydon Hall Foyer)	
12:45 - 13:45 Debate: The Role of AI in Medicine (Graydon Hall ABC)	
13:45 - 14:45 Session 5 Talks: Device, Hardware, Software Development	Session 6 Talks Cancer
14:45 - 15:20 Session 7 Pitches: Device, Hardware, Software Development	Session 8 Pitches Cancer
15:20 - 16:15 Poster Viewing (Pitch Sessions 7 & 8 presenting) (Graydon Hall D)	
16:15 - 17:15 Session 9 Talks: Image Guided Intervention	Session 10 Talks Neuroimaging 1
17:15 - 19:15 Reception/Social Event (Graydon Hall D)	

Wednesday, March 20, 2024	
Graydon Hall ABC	Greenwich Room
07:00 - 08:30 Breakfast (Graydon Hall Foyer)	
08:30 - 08:45 Opening Remarks (Graydon Hall ABC)	
08:45 - 09:45 Session 11 Talks: Cardiac and Lung	Session 12 Talks: Neuroimaging 2
09:45 - 10:20 Session 13 Pitches: Cardiac, Lung, Image Processing	Session 14 Pitches: Neuroimaging
10:20 - 11:15 Poster Viewing (Pitch Sessions 13 & 14 presenting) Graydon Hall D	
11:15 - 12:15 Session 15 Talks: Deep/Machine Learning 2	Session 16 Talks: MRI 2
12:15 - 12:45 Lunch Pickup (Graydon Hall Foyer)	
12:45 - 13:45 Panel: Commercialization of AI enabled Medical Imaging Technology (Graydon Hall ABC)	
13:45 - 14:45 Session 17 Talks: Cellular and Molecular	Session 18 Talks: Ultrasound and Photoacoustic
14:45 - 15:20 Session 19 Pitches: Cellular and Molecular	Session 20 Pitches: Ultrasound and Optical
15:20 - 16:15 Poster Viewing (Pitch Sessions 19 & 20 presenting) (Graydon Hall D)	
16:15 - 17:00 Keynote II: Clinical Deployment of Raman Spectroscopy: Applications in Neurosurgery and Beyond Frédéric Leblond, Polytechnique Montréal (Graydon Hall ABC)	
17:00 - 17:30 Closing & Awards (Graydon Hall ABC)	

ImNO 2024 Program

Tuesday, March 19, 2024

07:00 - 08:30	Breakfast	Graydon Hall Foyer
07:30 - 08:30	Siemens Breakfast Symposium: Translating Image Reconstruction and Analysis Inline on the Scanner with OpenRecon Kelvin Chow	Greenwich Room
08:30 - 08:45	Opening Remarks Michael Daly and Elodie Lugez	Graydon Hall ABC
08:45 - 09:30	Keynote Session I Chairs: Jessica Rodgers and Olivia Tong AI for Medical Image Analysis: Living with Limited Data Anne Martel, University of Toronto	Graydon Hall ABC
09:30 - 09:45	Coffee Break	Graydon Hall Foyer
09:45 - 10:45	Session 01 Talks: Deep/Machine Learning 1	Session 02 Talks: MRI 1
	Graydon Hall ABC	Greenwich Room
	Chairs: Michael Hardisty and Laura Connolly	Chairs: Gabriel Varela-Mattatall and Rachel Theriault
	1-1: Video-Based Phase Recognition in Cataract Surgery Joshua Bierbrier, Queen's University	2-1: Agarose-Carrageenan Hydrogel MRI Phantom Shelf-Stability Sandra Alexander, Toronto Metropolitan University
	1-2: Innovative Solutions for Tissue Safety: Miniaturized Optical Sensors, Single-Pixel Imaging, and Machine Learning for Neurosurgical Retractors Lee Sikstrom, Western University	2-2: Effect of Stress and CD5L Levels on Mouse Brain Metabolites Using Magnetic Resonance Spectroscopy Colleen Bailey, Sunnybrook Research Institute
	1-3: Early Findings for Scribble-Based Weakly Supervised Segmentation of Neonatal Cerebral Ventricles from 3D Ultrasound Images Zachary Szentimrey, University of Guelph	2-3: An Entirely Noninvasive Restraint for Multi-Modal Functional Magnetic Resonance Imaging in Awake Mice Sam Laxer, Western University
	1-4: AI-Assisted Annotation of Surgical Tool Locations; Is It Worth It? Denesh Peramakumar, Queen's University	2-4: Data Compression for Compact Representation of Spatial Magnetic Field Variations Using Field Monitoring Paul Dubovan, Western University
10:45 - 11:20	Session 03 Pitches: Deep Learning	Session 04 Pitches: MRI
	Graydon Hall ABC	Greenwich Room
	Chairs: Daniel Louie and Ramtin Mojtahedi	Chairs: Ju-Chi Yu and Shaelyn Horvath
	3-1: Combining Diffuse Optical Tomography and Photoacoustic Imaging with Deep Learning Ben Motz, University Health Network	4-1: Towards the Suppression of Lipid Contamination in Whole Brain Slice Magnetic Resonance Spectroscopic Imaging Using Two-Dimensional Selective Excitation Jason Rock, Sunnybrook Research Institute
	3-2: Joint Medical Image Super-Resolution and Modality Translation via GAN Transformer-Based Model Melika Abdollahi, Ontario Tech University	4-2: A Single Breath Hold MT Pulse Sequence for Whole-Uterus Imaging Siddharth Sadanand, Toronto Metropolitan University

	<p>3-3: Radiomics Machine Learning and Deep Learning Ensemble for COPD Classification Using CT Images Kalysta Makimoto, Toronto Metropolitan University</p> <p>3-4: Vertebral Detection and Labelling Using Deep Learning for Spine MRI Registration Jonathan Chu, University of Waterloo</p> <p>3-5: Deep Learning for Automated Detection of Caenorhabditis Elegans in Hydrogel Teo Mesrkhani, Toronto Metropolitan University</p> <p>3-6: A Deep Learning Approach to Markerless Tumour Motion Forecasting Based on Optical Surface Imaging and Volumetric 4D-CT Timothy Yau, Western University</p> <p>3-7: 3D U-Net Segmentation of the Visceral Cavity of a MicroCT-Imaged Rat Joseph Umoh, Robarts Research Institute, Western University</p> <p>3-8: Using Deep Learning and a Feature Extraction Pipeline to Quickly Localize Catheter Tips in Prostate Brachytherapy Ultrasound Images Jessica de Kort, The University of Winnipeg and University of Manitoba</p> <p>3-9: Verifying the Classification Accuracy of a Machine Learning Core in an IMU Sensor Kyle Wilson, Western University</p> <p>3-10: Validation Dataset Construction for Laparoscopic Image De-Smoking Victoria Fan, Robarts Research Institute</p> <p>3-11: Moving Beyond Laparoscopy: Assessing the True Capabilities of Popular Surgical Phase Recognition Methods in Diverse Settings Rebecca Hisey, Queen's University</p>	<p>4-3: Robust Diffusional Kurtosis Computation Using Oscillating Gradient Encoding Jake Hamilton, Western University</p> <p>4-4: Echo-Time Dependence of Microscopic Fractional Anisotropy Using Single-Shot Spiral Encoding Farah Mushtaha, Robarts Research</p> <p>4-5: Minimization of Lipid Signal Contamination for Rapid MR Spectroscopic Imaging of the Brain Lubna Burki, University of Toronto</p> <p>4-6: Considering External Calibrant Signal Distributions When Quantifying ²³Na-MRI Maps Cameron Nowikow, McMaster University</p> <p>4-7: Pseudo-CT Image Generation from Magnetic Resonance Imaging (MRI) Using Generative Adversarial Networks (GANs) for Radiation Therapy Planning Nicola Billings, University of Guelph</p> <p>4-8: High-Resolution Magic-Angle Spinning (HR-MAS) NMR Spectroscopy in Cerebral Organoids Alejandra Castilla Bolanos, University of Toronto and Sunnybrook Research Institute</p> <p>4-9: Pulse Sequence Optimization for Highly Accelerated Low Field MRI: X-Centric and Sectoral Samuel Perron, Western University</p>
11:20 - 12:15	Poster Viewing (Pitch Sessions 3 & 4 presenting)	Graydon Hall D
12:15 - 12:45	Lunch Pickup	Graydon Hall Foyer
12:45 - 13:45	Debate: The Role of AI in Medicine	Graydon Hall ABC
13:45 - 14:45	Session 05 Talks: Device, Hardware, Software Development Graydon Hall ABC	Session 06 Talks: Cancer Greenwich Room
	Chairs: Natasha Alves-Kotzev and Amal Aziz	Chairs: Jessica Rodgers and Joeana Cambranis
	5-1: Development of a Photothermal Therapy Guidance Platform Using Photoacoustic Thermometry with Dynamic Diffuse Optical Tomography Temperature Calibration Ivan Kosik, University Health Network	6-1: Cisplatin Prodrug-Loaded Microbubbles for Targeted Cancer Therapy Sean McGrath, University of Toronto

	<p>5-2: MRI Motion Phantom of the Pregnant Human Abdomen Alexander Dunn, Toronto Metropolitan University</p> <p>5-3: Characterization of Picosecond Infrared Laser Ablation for Peripheral Artery Disease Revascularization Mahdi Tahmasebi, Toronto Metropolitan University</p>	<p>6-2: First Demonstration of Arterial Spin Labeling on a 1.5T MR-Linac for Glioblastoma Perfusion Dynamics Liam Lawrence, University of Toronto</p> <p>6-3: Comparison of the Localisation of Phototheranostic PORPHYSOME Nanoparticles in Rodent and Nonrodent Models of Prostate Cancer Michael Valic, Princess Margaret Cancer Centre and University Health Network</p>
	<p>5-4: Exploring Heart Rate Variability Metrics for Stress Assessment in Robot-Assisted Surgery Training Elizabeth Klosa, Queen's University</p>	<p>6-4: Analyzing the Effect of Neoadjuvant Stereotactic Ablative Radiotherapy (SABR) on Pancreatic Tumour Perfusion Using Computed Tomography Perfusion (CTP) Jin-Young Bang, London Regional Cancer Program</p>
14:45 - 15:20	<p>Session 07 Pitches: Device, Hardware, Software Development Graydon Hall ABC</p>	<p>Session 08 Pitches: Cancer Greenwich Room</p>
	<p>Chairs: Ali Tavallaei and Sule Karagulleoglu Kunduraci</p> <p>7-1: Deep Learning-Enabled 3D Fluorescence Imaging for Surgical Guidance: Identifying Tumor Margins Natalie Won, Princess Margaret Cancer Centre</p> <p>7-2: SlicerTrack: An Open-Source Extension to 3D Slicer for Target Displacement Visualization HaPhan Tran, Toronto Metropolitan University</p> <p>7-3: Development of An Internal Mammary Artery Phantom for Training in Harvesting Procedures Olivia Qi, Western University</p> <p>7-4: 3D Printing Prosthetics on the Thailand-Myanmar Border Olivia Radcliffe, Queen's University</p> <p>7-5: Machine Learning-Enhanced Mass Spectrometry Imaging for Perioperative Tissue Characterization Jade Warren, Queen's University</p> <p>7-6: Low-Cost X-Ray Exposure Meter for Low-Resource Settings Joseph Umoh, Western University</p> <p>7-7: Modifying Radix Lenses to Survive Low-Cost Sterilization: An Exploratory Study Emese Elkind, Queen's University</p> <p>7-8: Advancing Medical Imaging on the Web: Integrating High Throughput JPEG 2000 (HTJ2K) in Cornerstone3D for Streamlined Progressive Loading and Visualization Bill Wallace, Open Health Imaging Foundation</p>	<p>Chairs: Donna Goldhawk and Pavel-Dumitru Cernelev</p> <p>8-1: Polarization Speckle Allows for Snapshot in Vivo Skin Lesion Roughness Measurement Daniel Louie, University Health Network</p> <p>8-2: Micro-Ultrasound Photoacoustic Imaging of Prostate Cancer: Evaluation in a Pre-Clinical Model Nidhi Singh, University of Toronto</p> <p>8-3: Test Time Training for Prostate Cancer Detection: Addressing Distribution Shift with Self-Supervised Learning Mahdi Gilany, Queen's University</p> <p>8-4: An Automatically Tracked System for Cervical Brachytherapy 3D Ultrasound Imaging Tiana Trumpour, Western University</p> <p>8-5: Improving Model Adaptability: a Domain Knowledge-Integrated Deep Learning Approach for Ultrasound Image Segmentation and Classification Bining Long, Carleton University</p> <p>8-6: Quantification of the Tumor Microvascular Response to Stereotactic Body Radiation Therapy Using Optical Coherence Tomography Angiography and Dynamic Contrast Enhanced MRI Jeffrey Zabel, University of Toronto</p> <p>8-7: Automatic Segmentation of Metastatic Brain Tumours Using Magnetization Transfer Contrast Céline Dubroy-McArdle, Toronto Metropolitan University</p> <p>8-8: Dilated Convolutional Transformer-Based Segmentation for Primary and Secondary Liver Cancers Tumour: a Comparative Study Ramtin Mojtahedi, Queen's University</p>

	<p>7-9: Advancing Medical Imaging on the Web: Implementation of Hanging Protocols for Automated Image Display Configuration in OHIF V3 Alireza Sedghi, Open Health Imaging Foundation</p> <p>7-10: Advancing Medical Imaging on the Web: Optimizing the Dicomweb Server Architecture with Static Dicomweb Bill Wallace, Open Health Imaging Foundation</p> <p>7-11: Convolutional Neural Networks for Localization of Radioactive Sources with a Hand-Held Gamma Probe Sydney Wilson, Western University</p>	<p>8-9: Multi-Modal Imaging of Personalized Ovoids for Gynecological Brachytherapy Treatments Alissa van Gaalen, Western University</p> <p>8-10: Polarized Light Microscopy for Quantitative Assessment of Colorectal Cancer: Can We Predict Local Recurrence? Kseniia Tumanova, University of Toronto</p>
15:20 - 16:15	Poster Viewing (Pitch Sessions 7 & 8 presenting)	Graydon Hall D
16:15 - 17:15	Session 09 Talks: Image-Guided Intervention Graydon Hall ABC	Session 10 Talks: Neuroimaging 1 Greenwich Room
	Chairs: Tamas Ungi and Miriam Hewlett	Chairs: Ju-Chi Yu and Farah Mushtaha
	9-1: Percutaneous Nephrostomy Needle Guidance Using Real-Time 3D Anatomical Visualization with Live Ultrasound Segmentation Andrew Kim, Queen's University	10-1: Resting State Functional Brain Activity Differs by Sex in Pediatric Concussion Bhanu Sharma, McMaster University
	9-2: 3D-Printed Liver Tumour Flow Model for Simulating Embolization Procedures David Ng, Robarts Research Institute	10-2: An fMRI-Informed Transcranial Magnetic Stimulation Protocol Improved Memory Performance Hsin-Ju Lee, Sunnybrook Research Institute
	9-3: Feasibility Study of Using YOLOv8 for Cataract Surgical Tool Detection in Surgical Microscope Video Jianming Yang, Queen's University, the Perk Lab	10-3: Investigating Cortical GABA+ and Glx Levels in Individuals with Social Anxiety Disorder (SAD) Using Proton Magnetic Resonance Spectroscopy Sonja Elsaid, University of Toronto and Centre for Addiction and Mental Health
	9-4: Photoacoustic Detection of Residual Cancer in Breast-Conserving Surgery Laura Connolly, Queen's University	10-4: Microstructural MRI Evolution During Adult Mouse Brain Maturation Naila Rahman, Western University
17:15 - 19:15	Reception/Social Event	Graydon Hall D
Wednesday, March 20, 2024		
07:00 - 08:30	Breakfast	Graydon Hall Foyer
08:30 - 08:45	Opening Remarks Michael Daly and Elodie Lugez	Graydon Hall ABC
08:45 - 09:45	Session 11 Talks: Cardiac and Lung Graydon Hall ABC	Session 12 Talks: Neuroimaging 2 Greenwich Room
	Chairs: Gerald Moran and Amanda Hamilton	Chairs: Chao Zheng and Paul Dubovan
	11-1: Novel 4D Flow MRI Technique Without Contrast Agents for Pediatric Congenital Heart Disease Valérie Béland, University of Toronto	12-1: Investigating Brain Gaba and Glutamate+Glutamine Levels in Chronic Pain Patients with and Without Opioid Use Disorder: a Magnetic Resonance Spectroscopy Study Sheldon Bereznick, Centre for Addiction and Mental Health

	<p>11-2: Automated Diaphragm Dome Segmentation and Height Analysis for Chest CT Images in COPD Daniel Genkin, Toronto Metropolitan University</p> <p>11-3: Physical Replication and Validation of Mathematical Mitral Valve Models Patrick Carnahan, Robarts Research Institute</p> <p>11-4: Multi-Slice Hyperpolarized 129Xe Fractional Ventilation Mapping in Pediatric Cystic Fibrosis Faiyza Alam, Hospital for Sick Children</p>	<p>12-2: Towards Brain Blood Metabolite Measurement Using MRS with Pseudo-Continuous Arterial Spin Labeling Peter Truong, Sunnybrook Research Institute</p> <p>12-3: Regional Brain Abnormalities in Resting State Functional MRI Persist Past Symptom Resolution: Preliminary Findings Ethan Danielli, University Health Network</p> <p>12-4: Hippocampal Subfield-Specific Volume and Diffusion Changes in Treatment Resistant Depression Mahdiah Varvani Farahani, Western University</p>
09:45 - 10:20	<p>Session 13 Pitches: Cardiac, Lung, Image Processing Graydon Hall ABC</p> <p>Chairs: Michael Daly and Miriam Hewlett</p> <p>13-1: Comparing Visual Search Strategies: Pathologists' Adaptability to Non-Medical Contexts Alana Lopes, Western University</p> <p>13-2: CNR Degradation in Dual-Energy Thoracic Imaging with Photon-Counting Detectors Jeffrey Dhari, Toronto Metropolitan University</p> <p>13-3: System Specifications for Success of a Novel Synthetic Mask Energy Subtraction Technique Lisa Garland, Robarts Research Institute</p> <p>13-4: SegFormer for Precise Quantification of Lung Ventilation Defects in Hyperpolarized Gas Lung MRI Samuel Perron, Western University</p> <p>13-5: Fractional Ventilation Mapping Using Multiple Breath Washout MRI in the Rat Lung: Comparison of Hyperpolarized 129Xe and Perfluoropropane Gases Shaelyn Horvath, University of Toronto</p> <p>13-6: Automatic Fetal MRI Segmentation with Volume and Weight Estimations Dylan Young, Toronto Metropolitan University</p> <p>13-7: Survival Prediction of Lung Cancer Using Real and GAN Synthesized Low-Dose CT Images Jenita Manokaran, University of Guelph</p> <p>13-8: Characterizing the Tumor Microcirculatory System and Its Impact in Stereotactic Body Radiation Therapy Using Optical Coherence Tomography Hector Alejandro Contreras Sanchez, University of Toronto</p>	<p>Session 14 Pitches: Neuroimaging Greenwich Room</p> <p>Chairs: Amy Boyle and Kalysta Makimoto</p> <p>14-1: Assessing the Sensitivity of Cerebral Blood Flow and Oxygenation to High-Intracranial Pressure Using Combined Optical Spectroscopy Techniques Sule Karagulleoglu-Kunduraci, Western University</p> <p>14-2: Exploring the Effects of Phospholipase A2 Inhibition on Brain Metabolism and Pathology in a Rat Model of Alzheimer's Disease Emily Hiles, University of Toronto</p> <p>14-3: Cerebral Blood Flow During Selective Brain Cooling in Cerebral Ischemia Olivia Tong, Western University</p> <p>14-4: Longitudinal Changes in White Matter Diffusivity in First Episode Psychosis Patients Peter Van Dyken, Schulich School of Medicine and Dentistry</p> <p>14-5: Neural Biomarkers of Schizophrenia and Autism Spectrum Disorders During the Empathic Accuracy Task Ju-Chi Yu, Centre for Addiction and Mental Health</p> <p>14-6: Probing Microstructural Orientations of Hippocampal Gray Matter in Alzheimer's Disease Bradley Karat, Western University</p> <p>14-7: Neural Circuitry and Therapeutic Targeting of Depressive Symptoms in Schizophrenia Spectrum Disorders Julia Gallucci, University of Toronto</p> <p>14-8: Brain Perfusion in Social Anxiety Disorder and the Relationship with Symptom Severity: An Arterial Spin Labeling Investigation Christina Pereira, Centre for Addiction and Mental Health</p>

		<p>14-9: Heterogeneity in Functional Connectivity: Dimensional Predictors of Individual Variability During Rest and Task fMRI in Psychosis Maria T Secara, University of Toronto</p> <p>14-10: Higher General Intelligence Is Linked to Stable, Efficient, and Typical Brain Connectivity Patterns Justin Ng, University of Toronto</p>	
10:20 - 11:15	Poster Viewing (Pitch Sessions 13 & 14 presenting)		
11:15 - 12:15	Session 15 Talks: Deep/Machine Learning 2		Session 16 Talks: MRI
	Graydon Hall ABC		Greenwich Room
	Chairs: Prashant Pandey and Wenyao Xia		Chairs: Ethan Danielli and Shaelyn Horvath
	15-1: Deep Learning-Enabled Quantitative Fluorescence Imaging for Surgery: Application to Post-Resection Residual Cancer Jerry Wan, Princess Margaret Cancer Centre		16-1: Single Frequency Birdcage Coils for Improved 19F Molecular MRI in Mice Sean McRae, Western University
	15-2: Evaluating the Utility of Deep Learning for Automatic Tumor Contouring in Breast Cancer Surgery Chris Yeung, Queen's University		16-2: Correction of Motion and Resulting Field Offsets for Quantitative MRI Using Navigators Miriam Hewlett, Western University
	15-3: Development and Evaluation of SlicerGPT: GPT Tailored for Enhancing Interaction with 3D Slicer Software Pavel-Dumitru Cernelev, Queen's University		16-3: Laterally Oscillating Trajectory for Undersampling Slices (LOTUS) Mayuri Sothynathan, Robarts Research Institute
	15-4: Exploring Osteosarcopenia Progression in Prostate Cancer Patients Using AI-Enabled Musculoskeletal Imaging Biomarkers Saleh Tabatabaei, Sunnybrook Research Institute		16-4: Real-Time Radiation Beam Imaging on a 1.5T MR Linear Accelerator Using Quantitative T1 Mapping Brandon Tran, University of Toronto
12:15 - 12:45	Lunch Pickup		Graydon Hall Foyer
12:45 - 13:45	Panel: Commercialization of AI-enabled Medical Imaging Technology		Graydon Hall ABC
13:45 - 14:45	Session 17 Talks: Cellular and Molecular		Session 18 Talks: Ultrasound and Photoacoustic
	Graydon Hall ABC		Greenwich Room
	Chairs: Justin Hicks and Rachel Theriault		Chairs: Eno Hysi and Nidhi Singh
	17-1: Comparing the Cellular Detection Limits of Magnetic Particle Imaging and Bioluminescence Imaging Sophia Trozzo, Western University		18-1: Three-Dimensional Ultrasound for Investigating Synovial Blood Flow Changes with Exercise in Thumb Osteoarthritis Megan Hutter, Western University
	17-2: Spatial-Frequency Fluorescence Imaging for Surgical Guidance: Pre-Clinical Oral Cancer Experiments Using Porphysome Nanoparticles Christina Negus, Princess Margaret Cancer Research Centre		18-2: Quantitative Analysis of Photoacoustic and Ultrasound Imaging of Red Blood Cell Aggregation in the Human Radial Artery Taehoon Bok, St. Michael's Hospital
	17-3: Synaptic Density in Mental Health Treatment-Seeking Youth with a Substance Use Disorder: Positron Emission Tomography Studies of [18F]SynVesT-1 in the Toronto Adolescent & Youth (TAY) Cohort Study Maia Zilberman, Centre for Addiction and Mental Health		18-3: Ultrasound Transducers for Microvascular Imaging with Superharmonic Contrast Imaging: Resolution and Field of View Comparison Elvira Catalina Vazquez Avila, University of Toronto

	<p>17-4: Preliminary Preclinical Pet Neuroimaging of [18F]ROCK202 for Rho-Associated Protein Kinase 2 Mark Bortolus, University of Toronto and Centre for Addiction and Mental Health</p>	<p>18-4: Assessments of Vascular Damage During Kidney Transplantation Using Photoacoustic Imaging Sarah Dykstra, University of Toronto</p>
14:45 - 15:20	<p>Session 19 Pitches: Cellular and Molecular Graydon Hall ABC</p>	<p>Session 20 Pitches: Ultrasound and Optical Greenwich Room</p>
	<p>Chairs: Amanda Hamilton and Olivia Tong</p>	<p>Chairs: Daniel Louie and Patrick Carnahan</p>
	<p>19-1: Developing Magnetic Resonance Reporter Gene Imaging: Co-localization of Magnetotactic Bacteria Proteins Qin (Daisy) Sun, Lawson Health Research Institute</p>	<p>20-1: Multi-Objective Multiple Instance Learning for Improving Prostate Cancer Detection in Ultrasounds Mohamed Harmanani, Queen's University</p>
	<p>19-2: Visualizing Real-Time Mechanosensory Response of Endothelial Cells to Multi-Directional Wall Shear Stress Kevin Moore, Western University</p>	<p>20-2: A Four-Dimensional Ultrasound System for Assessing Ligament Laxity in Basal Thumb Osteoarthritis Randa Mudathir, Western University</p>
	<p>19-3: Bridging Micro-to-Clinical Dosimetry for Alpha Particle Targeted Radionuclide Therapy Shahin Ghaseminejad, Western University</p>	<p>20-3: Realization of Automated Whole Breast 3D Doppler Ultrasound for Characterization of Breast Lesions Amal Aziz, Western University</p>
	<p>19-4: Magnetic Particle Imaging Serves As a Biomarker for Measuring Tumour Associated Macrophage Density In Vivo Nitara Fernando, Western University</p>	<p>20-4: Plane Wave Approaches with Dual-Frequency Arrays for Superharmonic Contrast Imaging Jing Yang, University of Toronto</p>
	<p>19-5: Monte Carlo Dosimetry Calculations of Cellular S-Values for 177Lu and 225Ac Thanh-Tai Duong, Western University</p>	<p>20-5: Color Doppler Ultrasound for the Diagnosis of Placenta Accreta Spectrum Using Fused Texture Features from Multiple Domains Dylan Young, Toronto Metropolitan University</p>
	<p>19-6: MRI of Bacteria: in Vitro Characterization of Lactobacillus Crispatus ATCC33820 at 3T Gabriel Varela-Mattatall, Lawson Health Research Institute</p>	<p>20-6: Multimodal Scattering Agent for the Development of Training Phantoms: Finding a Substitution for Talc Joeana Cambranis Romero, Western University</p>
	<p>19-7: Pet Imaging Neuroinflammation with COX-1 Targeted [11C]PS13 in Mouse Models of Multiple Sclerosis Amy Boyle, Centre for Addiction and Mental Health</p>	<p>20-7: Qualitative Validation of a Cost-Effective Contrast Agent for Use in Doppler Flow Test Phantom Emma Zhang, Western University</p>
	<p>19-8: Novel Hyperpolarized 129Xe R3-Noria-Methanesulfonate Supramolecular Cage at 3.0 T MRI Vira Grynko, Lakehead University</p>	<p>20-8: Polarimetric Image Guidance on Resected Breast Tumors to Optimize Mass Spectrometry Analysis Michael Singh, University of Toronto</p>
		<p>20-09: Polarization Speckle Pattern Analysis for the Investigation of Optical Properties in Biological Tissue Carla Kulcsar, University of Toronto</p>
15:20 - 16:15	<p>Poster Viewing (Pitch Sessions 19 & 20 presenting)</p>	Graydon Hall D
16:15 - 17:00	<p>Keynote Session II Chairs: Michael Daly and Sule Karagulleoglu Kunduraci</p>	Graydon Hall ABC
	<p>Clinical Deployment of Raman Spectroscopy: Applications in Neurosurgery and Beyond Frédéric Leblond, École Polytechnique de Montréal</p>	
17:00 - 17:30	<p>Closing and Awards Michael Daly and Elodie Lugez</p>	Graydon Hall ABC

Talk and Pitch Abstracts (in order of the talks)

Session 1 Talks: Deep/Machine Learning 1

Abstracts

Video-Based Phase Recognition in Cataract Surgery

Joshua Bierbrier¹, Rebecca Hisey¹, Jianming Yang¹, Adrienne Duimering¹, Christine Law¹, Gabor Fichtinger¹, Matthew Holden²

¹Queen’s University, Kingston, Ontario, Canada, ²Carleton University, Ottawa, Ontario, Canada

Introduction. Cataract surgery is increasingly common¹ and requires skilled surgeons to ensure optimal patient outcomes. Training ophthalmology residents is a meticulous task that requires significant time investment from staff ophthalmologist. As a result, recent efforts have set out to automate the task of skill assessment. Hisey et al. demonstrated that an object detection approach based only on the surgical video was more robust at cataract surgical skill assessment than an optical tool tracking approach². Whereas Hisey et al. provide an overall score for the surgical procedure, recognizing the phase of the procedure can enable step-by-step feedback. Furthermore, surgical phase recognition could open the possibility of creating a computer-based cataract surgery training module, identifying surgical inefficiencies, and aiding in related tasks like surgical tool tracking. Therefore, our goal is to classify the phase of cataract surgery from surgical videos using a deep learning approach. To this end, we train a hierarchical long short-term memory (LSTM) network on phase-labelled cataract surgery data that predicts the phase of surgery from the surgical video.

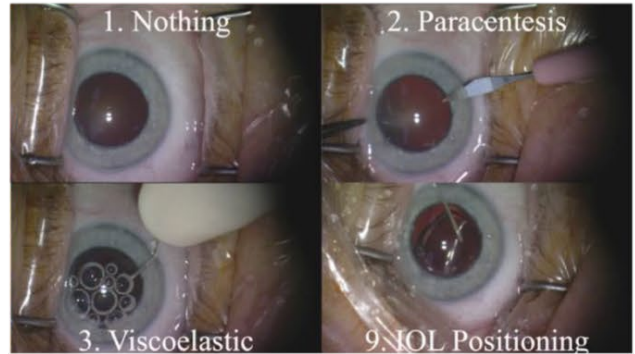


Figure 1. Select phases of cataract surgery. (IOL: Intraocular Lens).

Methods. Six cataract surgery videos, collected from operating theatres from Kingston Health Sciences Centres, were used: 3 from ophthalmology residents (“residents”) and 3 from staff ophthalmologists (“staff”). The surgical phases were manually annotated for each video (Figure 1). There are 11 surgical phases and one additional phase (“Nothing”) that is assigned to frames where no task is occurring. The videos range from 641.33 to 1117.86 seconds and were captured at 30 frames per second. We trained a hierarchical LSTM model that uses a convolutional feature extractor. The feature extractor, ResNet50, was retrained to estimate the phase of the surgery. To add contextual information, the output from the convolutional network was used as input for a hierarchical LSTM, which estimates the phase. The dataset was arbitrarily split into 4 training videos, 1 validation video, and 1 test video. The CNN and LSTM were trained with a learning rate of 10^{-6} and early stopping. The LSTM sequence length was 100. Training samples varied by phase (from 466 for Paracentesis to 52966 for Phaco). Class balancing with replacement was therefore performed. The primary outcome of interest was the model’s accuracy.

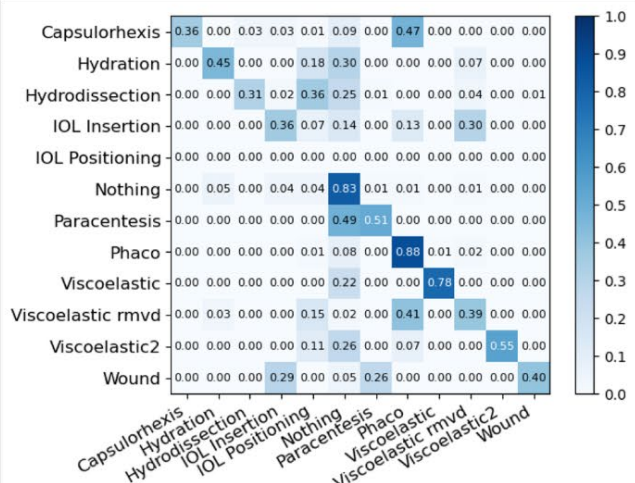


Figure 2. The model's normalized confusion matrix.

Results. The model achieved an accuracy of 68.59% on the test set. The confusion matrix is presented in Figure 2. The model performs best on the “Phaco” phase and worst on the “Hydrodissection” phase.

Conclusion. The model performs satisfactorily but leaves room for improvement. Phase classification in the surgical environment presents several challenges, including patient and ocular movements. The spectrum of surgeon proficiency (residents and staff) adds a further challenge for the model. Residents and staff may differ in technique and phase length. Notably, two of the staff did not perform the “IOL Positioning” step. These added complexities may partially account for the model’s performance, given that it was trained primarily on resident data and validated and tested on staff data. Indeed, they may help explain why the model performs well on the “Nothing” phase, where there is comparably less information to distinguish residents and staff. The hierarchical LSTM model represents a first step towards an automated approach to cataract surgery phase classification in surgical settings. Eventually, the model could provide surgical feedback, aid in training, or identify inefficiencies.

References. 1 Hatch, W. V. et al. *Archives of Ophthalmology* 130, 1479–1481 (2012) 2 Hisey, R. et al. *TBME. (In Revision)*. (2023)

Innovative Solutions for Tissue Safety: Miniaturized Optical Sensors, Single-Pixel Imaging, and Machine Learning for Neurosurgical Retractors

Lee D. Sikstrom¹, David W. Holdsworth^{1,2,3}

¹Dept. of Medical Biophysics and Medical Imaging, ²School of Biomedical Engineering, ³Dept. of Surgery, University of Western Ontario

Introduction: In neurosurgery, the use of retractors poses a risk to healthy brain tissue due to a lack of real-time monitoring for applied force, heart rate, and blood oxygenation. Our research aims to address this gap by developing a retractor with miniaturized optical sensors to alert surgeons to conditions that could lead to tissue damage. The optical sensor directly monitors tissue perfusion, a key factor in preventing harm. Due to the complexity of the optical signals, machine learning is used to correlate the optical signal with applied force. A specific challenge for this application of machine learning is developing an algorithm that can operate stand-alone, at low power, on a small device (surgical retractor), and meeting the size and space requirements of the surgical procedure; this restricts the use of conventional deep-learning algorithms. The objective of this study is to determine: (1) if machine-learning can be used to predict vascularized tissue contact force to within ± 0.5 N from single pixel imaging, using the optical signals generated by a photoplethysmography (PPG) sensor, and (2) which machine-learning model performs the best within given the constraints of the application.

Methods: We have implemented the MAXM86161 PPG miniaturized optical data-acquisition system; it contains three LEDs, 530 nm, 660 nm, and 880 nm, as well as a photodiode. During testing, the applied force was measured simultaneously using a beam load-cell. The applied force ranged from 0 to 10 N. PPG optical signals and force data was collected from the pad of the left and right-hand index finger ($n=1$) at a rate of 50 Hz for 240,000 data points split between 7 files.

Table 1 Results for evaluated models in N except R^2 .

Model	R^2	MAE	95%CI	RMS
Decision Tree	0.81 \pm 0.08	0.5 \pm 0.2	0.03 \pm 0.01	1.1 \pm 0.4
Random Forest	0.87 \pm 0.07	0.4 \pm 0.2	0.03 \pm 0.01	0.9 \pm 0.3
Extra Random	0.87 \pm 0.07	0.4 \pm 0.2	0.03 \pm 0.01	0.9 \pm 0.3
KNN	0.86 \pm 0.07	0.4 \pm 0.2	0.03 \pm 0.01	1.0 \pm 0.3
RANSAC	0.51 \pm 0.09	1.2 \pm 0.2	0.05 \pm 0.02	1.8 \pm 0.3
Theil Sen	0.43 \pm 0.11	1.3 \pm 0.2	0.05 \pm 0.02	1.9 \pm 0.2
Linear	0.51 \pm 0.08	1.2 \pm 0.2	0.05 \pm 0.02	1.8 \pm 0.3
AdaBoost	0.88 \pm 0.07	0.3 \pm 0.2	0.02 \pm 0.01	0.8 \pm 0.3
Bagging	0.79 \pm 0.09	0.4 \pm 0.2	0.03 \pm 0.01	1.0 \pm 0.3
SGD	0.51 \pm 0.08	1.2 \pm 0.2	0.05 \pm 0.02	1.8 \pm 0.3
SVM	0.57 \pm 0.14	1.0 \pm 0.2	0.05 \pm 0.01	1.7 \pm 0.3
XG Boost	0.84 \pm 0.08	0.5 \pm 0.2	0.03 \pm 0.01	1.0 \pm 0.3

The machine-learning model takes in three singular datapoints, one for each frequency of light, to estimate the applied force value (N). To determine the best machine learning architecture to use, each file was split into an 80/20 training and test set. The training set of each file was used to find the best hyperparameters for each potential model using a random search. The model was then trained using the best hyperparameters for each model. The performance metrics of each model was determined using the 20% test set and averaged over 7 files.

Results: The AdaBoost model performed the best. The AdaBoost model found that the best model to base the AdaBoost algorithm on was the Extra Random Forest model, so the AdaBoosting improves the R^2 score, Mean Absolute Error (MAE), 95% confidence interval (CI), and Root Mean Squared (RMS) error of the machine learning model. See Table 1 for a summary of the models tested and the results for each with the best scoring model in each metric highlighted in green.

Conclusions: In our preliminary investigations, the best model was an AdaBoosted Extra Random Forest model, which predicted the know force value to within ± 0.3 N. These results show that it is possible to predict the force applied to vascularized tissue by using a PPG sensor as a single-pixel imager, using machine learning. This is better than our target value of 0.5 N. Future work will involve collecting data from a porcine model to train an algorithm that will produce force predictions for exposed brain tissue. The long-term goal of this project is to develop a miniaturized, real-time monitoring system that can be incorporated into a conventional brain retractor, to reduce tissue trauma during brain surgery.

Early Findings for Scribble-based Weakly Supervised Segmentation of Neonatal Cerebral Ventricles from 3D Ultrasound Images

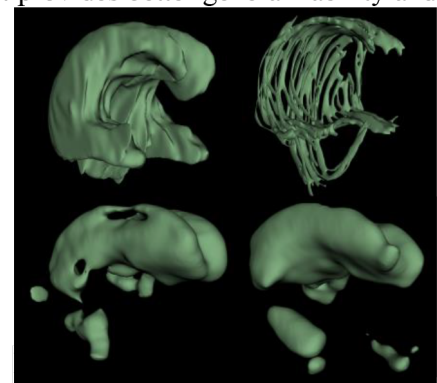
Zachary Szentimrey¹, Sandrine de Ribaupierre^{2,3}, Aaron Fenster², Eranga Ukwatta¹

¹School of Engineering, University of Guelph, Guelph, Ontario, Canada; ²Robarts Imaging, University of Western Ontario, London, Ontario, Canada; ³Department of Clinical Neurological Sciences, University of Western Ontario, London Health Sciences Centre, London, Ontario, Canada

Introduction: Intraventricular hemorrhaging (IVH) affects 20-30% of very low birth weight infants (<1500g). IVH can lead to post-hemorrhagic ventricle dilation (PHVD) (the abnormal enlargement of the ventricles) and developmental delays. Monitoring the changes of the ventricles obtained through fully automated segmentation is critical because it can provide clinicians with more information for choosing the best treatment to prevent further neurological degradation. However, given the difficulty and time-consuming process of manually segmenting the irregular ventricle shapes in the three-dimensional (3D) ultrasound (US) images, labelled data is scarce and may not capture variability in ventricle shapes. To this end, we are developing a scribble-based weakly supervised segmentation method for 3D US images made from inexperienced users that provides better generalizability and accuracy when compared to non-scribble-based methods. Scribbles are long or short marks that indicate an area of the image contains useful information.

Methods: The dataset consists of 45 labelled 3D US images (both masks and scribbles), including images of both lateral ventricles and images with varying degrees of PHVD. The dataset was split between train/test where 25 images were used for training, 5 for validation and 15 for testing. Test images and patients were not used during model training. The images were collected by a motorized 3D US system developed specifically for cranial imaging of neonates. Images were segmented on sagittal view at 1mm intervals using multi-planar reformatting software. The scribbles were created manually by a graduate student researching in medical imaging with no previous clinical experience. One scribble was drawn per sagittal slice such that it was drawn to extend from the most superior and anterior position to the inferior position in one or more continuous segments. The baseline supervised learning (SL) method used a 3D U-Net architecture and is the backbone for the scribble-based method. We tested the 3D U-Net using both masks and scribbles as the ground truth training data. In addition, we used the WSL4MIS scribble-based method with the scribble training data to compare a baseline 3D U-Net to a state-of-the-art (SOTA) scribble-based method. The WSL4MIS method uses an auxiliary decoder with additional dropout layers and formulates a novel loss between the main and auxiliary decoder branches. The Dice similarity coefficient (DSC) and Wilcoxon signed-rank test (WSRT) were used for statistical analysis. WSRT was used to compare the WSL4MIS method and all other methods.

Results: The mean and standard deviation of the DSC values were calculated and are shown in Table 1. The SOTA method had a higher mean DSC and lower standard deviation than that of the baseline 3D U-Net when both used scribble data for training. The WSRT does not show a significance between both scribble-based methods. The 3D U-Net trained using expert segmented masks had the highest DSC as expected since it trained on segmentations. One 3D US image requires approximately 2-5 minutes to scribble by a non-expert versus 45 minutes to segment by an expert. Example segmentations from the 3D U-Net with scribbles and WSL4MIS models are in Figure 1, including ground truth expert made masks and non-expert made scribbles.



Top left: ground truth. Top right: non-expert created scribbles. Bottom left: 3D U-Net with scribbles. Bottom right: WSL4MIS.

Table 1: DSC and results for each model tested.

Type of Data	Method	DSC \pm SD (%)	Wilcoxon Signed-Rank Test
Mask	3D U-Net	51.1 \pm 6.8	<0.001
Scribble	3D U-Net	40.4 \pm 9.4	<0.5
Scribble	WSL4MIS	42.8 \pm 7.9	-

Conclusions: We implemented deep learning models to automatically segment 3D US images of neonatal cerebral ventricles using scribble-based techniques. Further experiments are being conducted with larger amounts of scribble data and a novel 3D US specific scribble-based method is under development for this application. The goal is to use only non-expert made scribbles and achieve similar or better performance than a model trained on expert made segmentation masks. The current amount of data and results are not yet sufficient for clinical use.

AI-assisted annotation of surgical tool locations; Is it worth it?Denesh Peramakumar¹, Rebecca Hisey¹, Gabor Fichtinger¹¹Queen's University, Kingston, Ontario, Canada

Introduction: Using computer vision models to detect surgical instruments during procedures offers exciting potential applications such as workflow recognition and skill assessment. These object detection models are generally developed by training the model on images that are annotated by human labelers, a critical yet laborious and time-consuming process. AI-assisted annotation is a promising method to expedite data labeling, however, there is currently limited research on the utility of AI-assisted annotation. Moreover, most pretrained models are focused on identifying common objects such as cars, animals, and people rather than objects from specialized domains like surgical tools. The purpose of this research is to determine how much labeled data is required to develop an effective model for annotation assistance in surgical procedures and quantify the potential time and effort that can be saved.

Methods: All images used for this study were acquired during simulation of a central line procedure. These images had been manually labeled using bounding boxes for 8 classes: ultrasound, anesthetic, scalpel, syringe, catheter, guidewire, and guidewire casing. The model used for training was YoloV5. A 'good' model and a 'poor' model were trained using a different number of images. The poor model was trained on about 10 images per class while the good model was trained on over 4000 images per class. Images from two participants of the simulation were excluded from the training set to be used for the test set and experimental procedures. For the experimental procedure, we invited 10 students with varying levels of annotation experience to label images containing surgical instruments using a custom-built annotation software. The participants were first acclimated to the software and the labeling process through a set of practice images. Following this, they were asked to label 3 sets of 10 images. Each set of images was accompanied by label predictions from a model offering a different level of AI-assistance (no assistance, poor assistance, and good assistance). Each participant encountered the sets in a random order to mitigate the impact of the learning effect. The comparative performance of participants on each set of images was analyzed using paired t-tests.

Results: On average, annotation with the good model took the least amount of time at $581s \pm 168s$, while annotation with the poor model took the most amount of time at $786s \pm 245s$. Similarly, the good model needed the lowest number of edits on average at 60 ± 19 , while the poor model required the largest number of edits at 104 ± 24 . There was a significant difference in both time and number of edits when using a good model versus using a poor model ($p < 0.05$), but no significant difference between using a good model and no model at all.

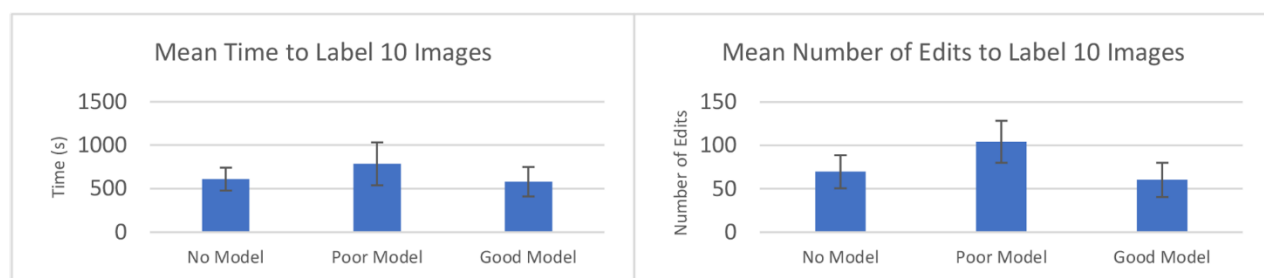


Figure 1, left. Mean time taken for participants to label 10 images using various levels of AI-assistance. **Figure 1, right.** Mean number of edits participants performed while labeling 10 images using various levels of AI-assistance.

Conclusions: Overall, the results of this study suggest that AI-assistance may not provide substantial benefit in manual labeling. However, the number of images labeled in this experiment was small due to time constraints and the true benefit may not be evident unless participants label a greater number of images. Moreover, using a poor model will slow down annotation over using no model at all.

Session 2 Talks: MRI 1

Abstracts

AGAROSE-CARRAGEENAN HYDROGEL MRI PHANTOM SHELF-STABILITY

Sandra Alexander^{1,2}, Renée Berahzer¹, Sid Sadanand^{1,2}, Dafna Sussman^{1,2,3}

¹Department of Electrical, Computer and Biomedical Engineering, Toronto Metropolitan University, Toronto, Canada ²Institute for Biomedical Engineering, Science and Technology (iBEST), Toronto Metropolitan University and St. Michael's Hospital, Toronto, Canada ³Department of Obstetrics and Gynecology, University of Toronto, Toronto, Canada

INTRODUCTION: An imaging phantom is an object that is designed to resemble human tissue under imaging and can be evaluated, analyzed or manipulated to study the performance of the target imaging device. Anthropomorphic MRI phantoms are used to mimic a combination of tissue specific relaxation values and dielectric properties, along with anatomical morphology [1]. Gelatin-based and similar organic material phantoms are advantageous in their lower cost, high solubility in water, as well as ability to be formed in a variety of shapes [2]. These phantoms have an observed longevity lasting from one day to two weeks before becoming affected by organic degradation and loss of their MRI characteristics. Such a short shelf-life necessitates remaking these phantoms which is time consuming and suboptimal for use in longitudinal studies. A shelf-stable gelatin-based phantom material is highly desirable to facilitate long-term sequence development projects.

Aim: We aim to evaluate the longevity of an agarose-carrageenan based hydrogel phantom material, as previously developed [3], to determine its T1 and T2 stability over the course of 1 year. We also aim to evaluate storage temperature.

METHODS: 6 brain phantom samples were prepared as outlined in [3], where $GdCl_3$ was used as a T1 modifier and agarose served as a T2 modifier. They were preserved with NaN_3 , kept in air-tight containers, and were split between room temperature (23°C) and refrigerated (4°C) storage conditions. These 6 phantoms were prepared weekly over six weeks and scanned every six weeks over 52 weeks to represent weekly change in relaxation at a lower scanning cost. A 3.0 T scanner was used with a multi-echo spin-echo sequence to acquire T2 images and an inversion recovery sequence to acquire T1 images.

RESULTS: The change in T1 and T2 over time between room temperature and refrigerated conditions for gray matter (T1, $p < .01$; T2, $p < .01$) and white matter phantoms (T1, $p < .01$; T2, $p < .01$) was found to be statistically different using an ANOVA test between the data linear regression models. Fridge storage conditions were found to provide better stability, with T1 relaxation values varying from 3.14% to 5.54% and T2 relaxation values varying from 23.66% to 28.01% between white and gray matter phantoms, respectively, over 52 weeks. No visible organic degradation was observed, but liquid separation of the phantom was observed after three months in one triplicate of refrigerated phantoms.

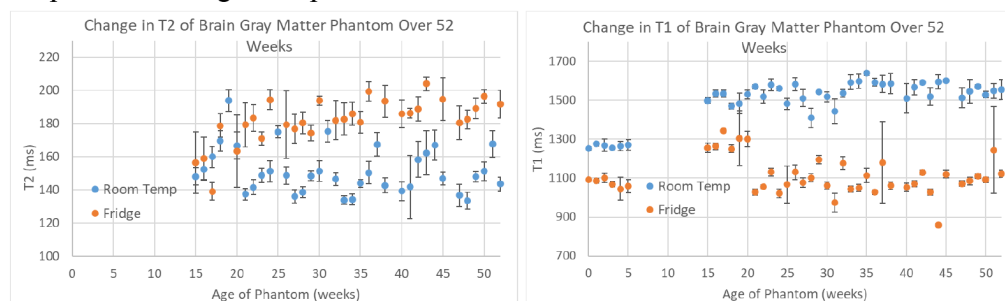


Figure 1: Change in Relaxation of Gray Matter Phantom Samples Over a Year.

CONCLUSIONS: While T1 drift over a year is within acceptable population variability, T2 drift needs to be improved. Further investigation will be needed to determine sustainable T2 modification techniques as well as to test phantom weight, structure, and composition longevity in unsealed or handling environments.

REFERENCES: [1] M. Shulman *et al.*, *Magn. Reson. Mater. Phys. Biol. Med.*, vol. 33, no. 2, pp. 257–272, Apr. 2020, doi: 10.1007/s10334-019-00775-x. [2] H. Jonasson *et al.*, *J. Biomed. Opt.*, vol. 27, no. 7, p. 074712, Jul. 2022, doi: 10.1117/1.JBO.27.7.074712. [3] N. R. Crasto, “Carrageenan brain phantom for use in MRI”, Toronto Metropolitan University, 2021.

Effect of stress and CD5L levels on mouse brain metabolites using magnetic resonance spectroscopyColleen Bailey¹, Deeva Uthayakumar², Jamie Near^{1,2}, Chao Wang^{1,2}¹Sunnybrook Research Institute, Toronto, ON; ²University of Toronto, Toronto, ON**INTRODUCTION:**

The CD5L protein regulates T helper 17 (Th17) immune cells, and is believed to be involved in the body's natural response to stress¹. Magnetic resonance spectroscopy (MRS) detects markers of inflammation and breakdown, including myo-inositol and choline². In this study, we examine changes in brain metabolites using MRS in wild type and transgenic mice with varying CD5L levels following 2 and 6 weeks of a stress protocol. We hypothesize that markers of inflammation increase following stress, with larger effects in knockout mice.

METHODS:

Wild type (WT), heterozygous (CD5L^{+/-}, HET) and knockout (CD5L^{-/-}, KO) male C57BL/6 mice underwent baseline MRI, then were subjected daily to mild, randomized stressors. MRI was repeated at 2 and 6 weeks of stress. MRI was conducted under 1-2% isoflurane on a 7 T Bruker Avance (Bruker BioSpec, Billerica, MA) with a 20 mm receive surface coil. For MRS, voxels were placed in the left dorsal hippocampus and the hypothalamus for Point RESolved Spectroscopy (PRESS) sequences with water suppression (TE=8.77 ms, TR=2500 ms, 2048 data points, spectral width 4000 Hz, 250 averages). Spectra were fitted with an 18-metabolite, 9-macromolecule basis set in LCModel (Stephen Provencher Inc., Oakville, ON). Significant differences were tested with a mixed ANOVA on each metabolite, followed by post hoc multiple comparisons (paired t-test) with correction.

RESULTS:

The mean SNR of the NAA peak was 10.5 ± 2.0 in the hippocampus and 8.4 ± 2.1 in the hypothalamus. Significant metabolite changes are shown in Figure 1.

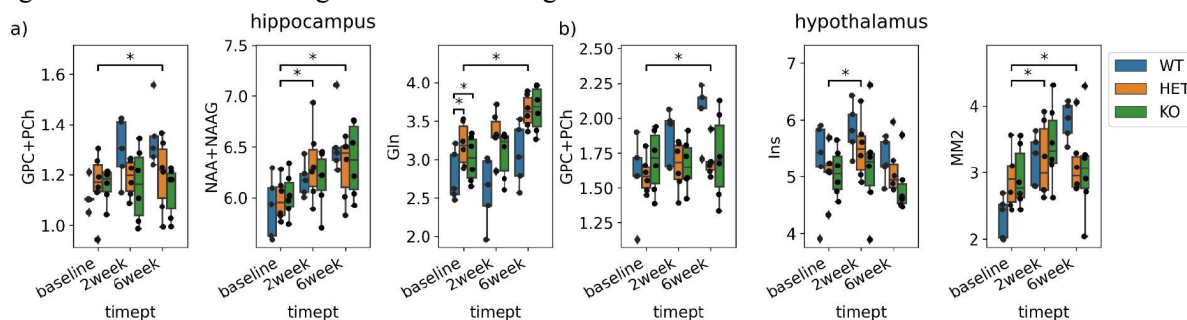


Figure 1 Significant metabolite differences in the (a) hippocampus and (b) hypothalamus. In the hippocampus, there was an increase in total choline at 6 weeks, an increase in NAA+NAAG from baseline to 2 and 6 weeks, and an increase in glutamine from baseline to 6 weeks. There was a difference in glutamine between wild type and heterozygous mice, as well as between wild type and knockout mice. In the hypothalamus, there was an increase in choline from baseline to 6 weeks, an increase in myo-inositol (Ins) at 2 weeks but not at 6 weeks, and an increase in macromolecular component at 1.3 ppm from baseline to 2 and 6 weeks. (* indicates $p < 0.05$)

CONCLUSIONS:

Increases in choline and myo-inositol support the hypothesis that markers of stress and neuroinflammation are detectable with MRS following stress^{2,3}, but changes were not significant when broken out by genotype, despite the known role of CD5L in stress¹. Increased glutamine in HET and KO mice at baseline suggests a link between CD5L and the pathway of the neurotransmitter glutamate, but the mechanism needs further study. The significant increase in the macromolecular peak at 1.3 ppm is associated with more mobile lipids, but is also linked to protein degradation in multiple sclerosis⁴. In addition, CD5L affects amino acid and fatty acid metabolism *in vitro* in Th17 cells¹. Future work will increase animal numbers and examine effects in female mice, which produce lower levels of CD5L than males and are more susceptible to stress-induced depression. This would support the use of MRS for monitoring markers of stress in the brain.

REFERENCES:

¹Wang C, et al. Cell. 2015;163(6):1413. ²McKiernan E, et al. NMR Biomed. 2023;36(7):e4896. ³Chang L, et al. J Neuroimmune Pharmacol. 2013;8(3):576. ⁴Mader I et al. Brain. 2001; 124(5): 953.

An Entirely Noninvasive Restraint for Multi-Modal Functional Magnetic Resonance Imaging in Awake Mice

Sam Laxer^{1,2}, Amr Eed^{1,2}, Kyle Gilbert^{1,2}, Peter Zeman¹, Miranda Bellyou¹, and Ravi Menon^{1,2}

¹Centre for Functional and Metabolic Mapping, Western University, London, Ontario, Canada

²Department of Medical Biophysics, Western University, London, Ontario, Canada

Introduction: Functional Magnetic Resonance Imaging (fMRI) is a widely used technique in neuroscience research, providing a surrogate measure of brain activity over time. Despite its wide usage, the physiological mechanisms leading to signal variations remain unclear [1]. Using mice, we can perform multi-modal recording, specifically combining fMRI with optical techniques, to better understand these physiological mechanisms. Unfortunately, the two current techniques used to prevent motion while scanning mice are not compatible with this approach. The first technique, imaging subjects under anesthesia, has recently been shown to have significant alterations in brain hemodynamics and function compared to awake subjects [2]. The second technique, head fixation, avoids the issues related to anesthesia but requires a headpost surgically implanted to the skull. This headpost obstructs access to the skull required for the optical techniques. Consequently, the objective of this work was 2-fold: 1) to develop an entirely noninvasive restraint compatible with the optical technique, and 2) to evaluate the performance of the restraint in terms of animal welfare and data quality.

Methods: 15 wild type (C57BL/6) mice were used in this study. They were split into two cohorts: a noninvasive group (n = 8: 4 males, 4 females) and a headpost group (n = 7: 4 males, 3 females) for comparison. The noninvasive restraint was designed and 3D printed from polycarbonate (Figure 1). Custom single-loop coils were built for each restraint. Both groups were acclimated to their respective restraint device and the MRI environment through a 9-day acclimation protocol. All mice were then scanned at the Centre for Functional and Metabolic Mapping at Western University (9.4 T Varian magnet with a Bruker AV3HD console). Functional (T2*-weighted) images were acquired to measure brain activity and high resolution anatomical (T2-weighted RARE) images were acquired for registration. Data quality was evaluated by analyzing motion and brain networks that could be extracted from the data. Motion was measured using the framewise displacement between consecutive images. Brain networks were analyzed by running group independent component analysis (ICA) on all subjects to extract temporally correlated brain regions (networks). Additionally, animal stress for subjects in the noninvasive group was evaluated by monitoring weight changes.



Figure 1. Novel noninvasive restraint (left) and conventional headpost-style restraint (right).

Results: Motion was higher in the noninvasive group with 4.9% of frames exceeding the voxel size (300um x 300um x 500um). 0% of frames in the headpost group exceeded this threshold. Brain networks generated through ICA were identifiable in both groups. Networks in the noninvasive group were more significantly activated, likely due to falsely activated voxels due to the increased motion (refer to [3]). Mice lost 4% +/- 3% of their body weight throughout the acclimation session.

Conclusions: The designed noninvasive restraint is capable of effectively restraining mice without posing additional stress compared to traditional headpost restraints [2]. Motion was considerably elevated in the noninvasive group which is expected since there is no direct contact with the skull. However, distinct and well-established brain networks were still identifiable in both groups. This work demonstrates the feasibility of the developed noninvasive restraint for awake mouse fMRI and its potential for future multi-modal experiments.

References

[1] Hall, et al., *Philosophical Transactions Royal Soc B Biological Sci*, 2016. [2] Gutierrez-Barragan, et al., *Curr Biol*, 2022. [3] Caballero-Gaudes, et al., *NeuroImage*, 2017.

Data compression for compact representation of spatial magnetic field variations using field monitoring

Paul I. Dubovan^{1,2}, Gabriel Varela-Mattatall^{1,3}, Ravi S. Menon^{1,2}, Adam B. Kerr^{4,5}, Corey A. Baron^{1,2}

¹Department of Medical Biophysics, Western University, London, Canada, ²Centre for Functional and Metabolic Mapping, Western University, London, Canada, ³Lawson Health research Institute, London, Canada, ⁴Center for Cognitive and Neurobiological Imaging, Stanford University, Stanford, California, USA, ⁵Department of Electrical Engineering, Stanford University, Stanford, California, USA

Introduction: During MRI scans, magnetic field deviations arising from eddy currents,¹ heating,² mechanical vibrations³, and motion can introduce significant artefacts. Field monitoring (FM), a technique that uses NMR probes positioned in the imaging volume is known to effectively reduce image distortions by measuring and accounting for described field perturbations in image reconstructions. A traditional system consisting of 16 field probes can characterize spatial field variations up to 3rd order using spherical harmonic basis functions. However, for high-performance head gradient systems, 16 probes may not sufficiently capture the complex spatial field variations, especially when probes are not optimally arranged or are outside the imaging volume, leading to erroneous field characterization and corrupted images.⁴ In this work, we propose a method that performs a system calibration scan using more probe positions to accurately characterize field dynamics up to higher orders, which is then used to create a compression matrix⁵ that compresses FM data acquired with the original 16 probe arrangement to fewer basis functions, with the goal of improving diffusion-weighted image (DWI) quality.

Methods: Scans were performed on a Siemens 7T head-only MRI. A spherical phantom and healthy volunteer's brain were scanned using a diffusion-weighted acquisition with a spiral trajectory and the following imaging parameters: FOV = 192 x 192 mm², in-plane resolution = 1.5 x 1.5 mm², slice thickness = 3 mm, slices = 10, TE/TR = 33/2500 ms, acceleration = 2, 1 b = 0 s/mm² acquisition, 6 diffusion directions, b-value = 1000 s/mm². FM was performed simultaneously using a Skope field camera with 16 probes integrated into an RF head coil.⁶ For the calibration, FM measurements from different probe locations were performed on an identical sequence by advancing the scanner bed across 14 positions in 1 cm increments. This data was used to generate a synthetic probe array consisting of 41 probes, where only probes located in the imaging region were included. A 4th-order fit was then performed with this data (Eq. 1; \mathbf{k} = basis function coefficients; \mathbf{P} = basis functions; $\boldsymbol{\varphi}$ = phase of probes),⁷ after which a compression matrix (\mathbf{C}) was devised from the singular value decomposition (SVD) of the coefficients (over all slices, time points and diffusion directions), as per Equations 2 and 3. Compression was performed on 2nd to 4th order coefficients (21 terms) down to 5 "custom" basis functions described by $\hat{\mathbf{P}}$ (Eq. 4). Fitting of 1st order and compressed basis functions was then performed simultaneously using 16 probes (Eq. 5).

$\mathbf{k}_{calib}(t) = \mathbf{P}_{calib}^+ \boldsymbol{\varphi}_{P,calib}(t)$ (1), $\mathbf{k}_{orig}(t) = \mathbf{U}\boldsymbol{\Sigma}\mathbf{V}^T$ (2), $\mathbf{C} \equiv \mathbf{U}^T$ (3), $\hat{\mathbf{P}}_{orig} = \mathbf{C}\mathbf{P}_{orig}$ (4), $\hat{\mathbf{k}}_{orig}(t) = \hat{\mathbf{P}}_{orig}^+ \boldsymbol{\varphi}_{P,orig}(t)$ (5)

Images were reconstructed in MATLAB using an in-house reconstruction toolbox^{8,9} with the compressed and conventionally fit FM data. In-vivo DWI and fractional anisotropy (FA) maps were compared qualitatively, while phantom images were compared quantitatively by evaluating the normalized-root-mean-squared-error (NRMSE) of DWI across all directions and slices relative to b_0 images due to presenting negligible eddy current effects.

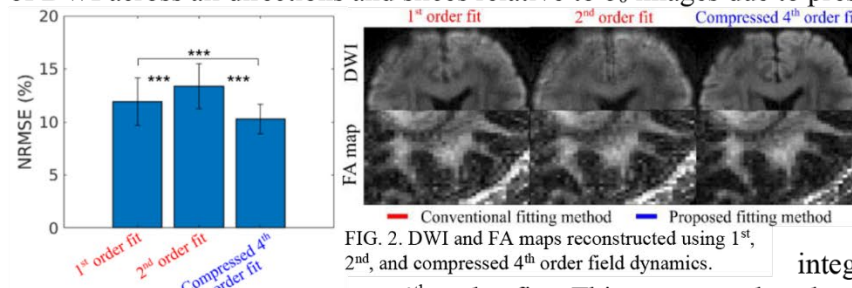


FIG. 1. NRMSE comparison of phantom DWI relative to b_0 images when using 1st, 2nd, and compressed 4th order field dynamics. Error bars represent standard error across diffusion directions. $p < 0.001$

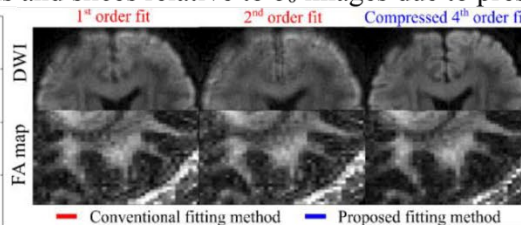


FIG. 2. DWI and FA maps reconstructed using 1st, 2nd, and compressed 4th order field dynamics.

Results: The lowest NRMSE and standard error was exhibited when images were informed with compressed coefficients (Fig. 1). Similarly, in-vivo single-direction DWI (Fig. 2) and FA maps (Fig. 3) exhibited significantly reduced blurring and improved FA

integrity, respectively, when using compressed

4th order fits. This suggests that the proposed method enables accurate higher spatial order fits and verifies its ability to fit beyond conventional 3rd order, while still routinely using 16 probes. Conventional 3rd order results (not shown) presented further image quality degradation. The accuracy improves because truncating the singular values reduces the number of basis functions that the

original 16 probes fit, which improves conditioning when solving Eq. 5. The number of singular values used was heuristically determined. Future work will investigate automatic singular value thresholds. Also, including more diffusion directions and sequences in the calibration scan may be needed to improve calibration generalizability.

Conclusions: A method for calculating field dynamics was presented, resulting in improved quality of DWI and diffusion metrics. This promotes accurate field monitoring on high-performance MRI that may exhibit complex field variations, while only requiring one calibration scan to characterize a scanner's dominant spatial modes.

References: ¹Boesch et al. *MRM* (1991), ²Ebel et al. *MRM* (2005), ³Wu et al. *MRM* (2000), ⁴Dubovan et al. *MRM* (2023), ⁵Wilm et al. *MRM* (2020), ⁶Gilbert et al. *MRM* (2021), ⁷Barnet et al. *MRM* (2008), ⁸Varela-Mattatall et al. *MRM* (2023), ⁹Wilm et al. *MRM* (2017).

Session 3 Pitches: Deep Learning

Abstracts

Combining Diffuse Optical Tomography and Photoacoustic Imaging with Deep Learning

Ben Motz (McMaster University, Princess Margaret Cancer Center), **Ivan Kosik** (University Health Network), **Brian C. Wilson** (Medical Biophysics, University of Toronto), **Robert A. Weersink** (Institute of Biomaterials and Biomedical Engineering, Radiation Oncology, University of Toronto)

Introduction:

Diffuse Optical Tomography (DOT) and Photoacoustic Imaging (PAI) are optics-based imaging modalities that both struggle with clinical scale quantitative deep tissue imaging due to the ill posed nature of the image reconstruction inverse problem. DOT struggles resolving structural information but is able to converge on accurate optical property maps using structural and/or spectral constraints. In contrast, PAI excels in providing spatial information but faces challenges in recovering quantitative optical properties when using only detected signal amplitudes because the PAI signal also depends on the excitation fluence distribution. Recognizing their complementary strengths and limitations, we propose that an integrated deep-learning (DL) based reconstruction approach can accurately reconstruct both structural and optical property information.

Methods:

Deep learning datasets were generated using the open-source MATLAB software packages NIRFAST for light propagation and K-Wave for simulating acoustic wave propagation. PAI simulations were excited at 808 nm. The PA signals were detected using 120 ultrasonic transducers with a bandwidth of 160% which were distributed 360° around the region of interest. Additionally, the DOT data involved the use of 8 transducers and 8 sources placed in the same configuration as the ultrasonic transducers at wavelengths of 670 nm, 750 nm, and 808 nm. A total of 10000 samples were used to train, validate and test the model, resulting in a split of 8000/1000/1000 and a training time of approximately 4 hours. A modified U-Net [1] was developed to estimate absorption and reduced scattering maps given PAI and DOT amplitude signals. This model included 2 encoders for the DOT and PAI inputs, which are then concatenated before the decoder sequence. The simulated 8cm diameter 2D imaging space contained interconnected blobs with radii ranging from 3-10mm, featuring uniform optical properties throughout each of the inclusion and background regions. Simulated optical properties for both the inclusion and background were varied by 0.2mm^{-1} and 2.6mm^{-1} for absorption and scattering respectively.

Results:

Figure 1 shows an example result, comparing DL-reconstructed images of absorption and scattering to ground truth images. In early models, the DL algorithm efficiently reconstructs simulated absorption and scattering profiles with a mean absolute percent error $<10\%$ and Dice coefficient >0.90 in less than a second. DL-based combined reconstructions were substantially more accurate and were significantly faster than conventional approaches which could require up to 120 seconds.

Conclusion:

We demonstrated rapid, accurate deep tissue image reconstruction of DOT and PAI signal. This would enable real-time monitoring of procedures such as photothermal or HIFU therapy where the optical characteristics of tissues undergo dynamic changes. We are currently assessing the image reconstructions on phantom measurements.

References:

[1] J. Feng et al., "Deep-learning based image reconstruction for MRI-guided nearinfrared spectral tomography," *Optica*, vol. 9, no. 3, pp. 264–264, Feb. 2022, doi: <https://doi.org/10.1364/optica.446576>.

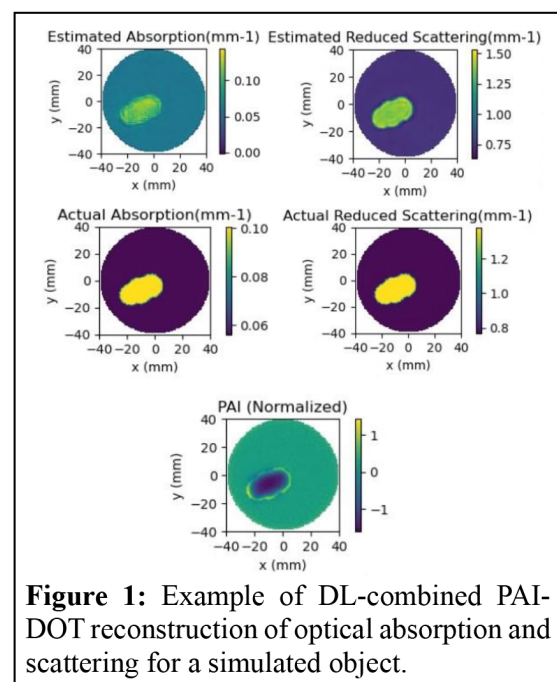


Figure 1: Example of DL-combined PAI-DOT reconstruction of optical absorption and scattering for a simulated object.

Joint Medical Image Super-Resolution and Modality Translation via GAN Transformer-based Model

Melika Abdollahi, Heidar Davoudi, and Mehran Ebrahimi

Faculty of Science, Ontario Tech University, Oshawa, ON, Canada

Introduction: In medical image analysis and computer-aided diagnosis, precise capture of intricate anatomical and pathological details is essential, especially across diverse imaging modalities. We present a novel GAN (Generative Adversarial Network) transformer-based model specifically designed for combined super-resolution and modality translation of magnetic resonance images (MRI). The primary goal of this model is to simultaneously enhance input image resolution and enable seamless translation between different imaging modalities, such as T1 and T2 MRI data. This innovative approach aims to provide more detailed visualizations, potentially aiding in diagnosis and treatment planning. The model's efficacy will be validated using the BraTS (Multimodal Brain Tumor Segmentation Challenge) dataset [1], with an anticipated 4x increase in resolution and successful modality translation between T1 and T2 MRI pairs. This addresses situations where higher resolution or specific modalities are either unavailable or cost-prohibitive.

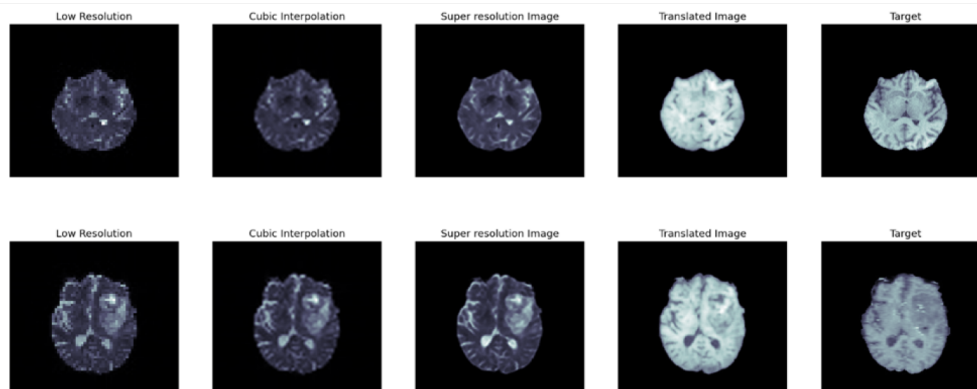
Methods: Our approach combines transformer architectures with GAN for medical image super-resolution and modality translation. Using Vision Transformer (ViT) in a conditional GAN framework, it employs self-attention and position encodings for improved long-range dependencies and spatial relationships. The generator, with a patch-merging ViT, integrates image patches for thorough context. Meanwhile, the discriminator uses a ViT backbone to distinguish real and synthetic images. The model operates in two stages: GAN-based super-resolution (Intermediate stage) followed by modal translation (Post stage). Slices from 3D MRI volumes of 285 subjects yield 33,576 training and 5,786 test slices. To prevent mixing, each volume's slices are exclusively assigned to either training or test sets. Each T1 input slice is down-sampled by a factor of 4 in both x and y directions and compared to its high-resolution ground-truth T2 slice after passing through the network. Training includes binary cross-entropy, L1 losses, multi-head self-attention, feedforward networks, layer normalization, skip connections, and Adam optimizer (learning rate: 0.0002, batch size: 16) over 40 epochs.

Results: The GAN transformer-based model exhibits promise in improving medical image resolution and translating modalities on the BraTS dataset [1]. Improved metrics in Table I indicate its effectiveness. To our knowledge, there are no established state-of-the-art methods available for a joint model comparison.

Conclusion: The model shows promise in creating detailed high-resolution (HR) T2 images from low-resolution (LR) T1 inputs, suggesting potential improvements with further refinement and more training on larger datasets.

	Pre	Intermediate	Post
RMSE (↓)	0.084 ± 0.0024	0.078 ± 0.0023	0.049 ± 0.001
MAE (↓)	0.031 ± 0.0006	0.028 ± 0.0005	0.018 ± 0.0003
MSE (↓)	0.009 ± 0.0001	0.008 ± 0.0001	0.004 ± 0.00004
PSNR (↑)	36.72 ± 17.19	37.13 ± 20.55	37.47 ± 19.97
SSIM (↑)	0.829 ± 0.007	0.862 ± 0.006	0.932 ± 0.001
NCC (↑)	0.880 ± 0.005	0.882 ± 0.005	0.966 ± 0.003
FID (↓)	185	145	63

TABLE I
PERFORMANCE OF THE PROPOSED GAN TRANSFORMER MODEL ON THE
BRATS VALIDATION SET FOR THE PRE-PROCESSING, INTERMEDIATE
SUPER-RESOLUTION, AND FINAL TRANSLATION STAGES.



Qualitative evaluation of the two stages model; from left to right; (a) Input (LR T1 image), (b) Cubic interpolation image (c) The generated T1 (after super-resolution), (d) Output (generated HR T2), and (e) Real T2 image (T2 ground truth).

References:

- [1] B. H. Menze, A. Jakab, S. Bauer, J. Kalpathy-Cramer, K. Farahani, J. Kirby, et al. "The Multimodal Brain Tumor Image Segmentation Benchmark (BRATS)", IEEE Transactions on Medical Imaging 34(10), 1993-2024 (2015)
DOI: 10.1109/TMI.2014.2377694

Radiomics Machine Learning and Deep Learning Ensemble for COPD Classification using CT Images

Authors and Institutions: Kalysta Makimoto BSc¹, Sara Rezvanjou MSc¹, James C. Hogg MD, PhD², Jean Bourbeau MD^{3,4}, Wan C. Tan MD² and Miranda Kirby PhD¹

¹Toronto Metropolitan University, ON; ²Center for Heart, Lung Innovation, University of British Columbia, BC;

³Montreal Chest Institute of the Royal Victoria Hospital, McGill University Health Centre, QC; ⁴Respiratory Epidemiology and Clinical Research Unit, Research Institute of McGill University Health Centre, QC.

Introduction: Chronic obstructive pulmonary disease (COPD) is a progressive smoking-related lung disease and the 3rd leading cause of death globally, but it remains largely undiagnosed in the population.¹ Lung cancer screening using chest computed tomography (CT) imaging is increasingly used in those with smoking histories¹, and COPD structural changes are detected on CT,² presenting the opportunity for earlier COPD detection. To utilize CT images to classify COPD, machine learning (ML) with radiomics analysis³ and deep learning (DL) models⁴ have been investigated. However, COPD classification is more challenging in mild COPD due to subtle disease changes in the lung.⁵ Although ML and DL models have shown to be able to classify COPD in CT images, it is unknown how ML and DL models compare for classification in a mild cohort, and if an ensemble of ML and DL result in improved performance. The objective of this study was to compare ML and DL models and develop an ensemble model that combines ML and DL models that utilize CT images for binary COPD status classification.

Methods: Participants from Canadian Cohort Obstructive Lung Disease (CanCOLD), a population-based multicenter study of mainly mild COPD, underwent CT imaging at baseline. The dataset was split into a testing dataset (n=378, with 54% COPD), using one site as the test set, and a training dataset (n=924, with 47% COPD), using the remaining (n=8) sites, to classify binary COPD status. Binary COPD status was defined using lung function measurements. For the ML model, a total of 107 CT radiomic features were extracted using PyRadiomics.⁶ Combinations of 6 feature selection and 5 ML classification methods were evaluated and the combination with the highest area under the receiver operating characteristic curve (AUC) in the test set was reported. For the DL model, CT images were down sampled so that only 15 slices along the z-axis were selected, resulting in an input of (256, 256, 15) into a 3D VGG-like model consisting of five 3D convolution layers, 5 max-pooling layers, 5 batch normalizations, 1 dense layer, 1 GlobalAveragePooling3D, and 1 dropout layer. Adam optimizer was used with an exponential decay learning rate of 0.5, an initial learning rate of 1e-5 and 1e4 decay steps. A 5-fold Keras validation method was used with a batch size of 5 and 17 epochs, determined using trial-and-error. To combine the ML and DL models, we proposed a radiomics ML and DL ensemble method, Rad-Ens, that applies the accuracy of the models as weights to the ML and DL probabilities and averages them to obtain the new probabilities for the Rad-Ens model. Models were compared using the AUC, F1-score, accuracy, precision, and recall from the test dataset. DeLong's test was used to test for significant differences between AUC values.

Results: A total of 1302 participants were evaluated. Between the training and testing group, there were no significant differences between age (training=66.8±10.4yrs; testing=66.5±9.6yrs; p=.63) or sex (n=388 (42%) females in training; n=157 (42%) females in testing; p=.88). The Rad-Ens model obtained the same AUC (AUC=0.76) as the ML model (AUC=0.76; p=.30), and a higher AUC compared to the DL model (AUC=0.69; p<.001) (Table 1). The ML model (AUC=0.76) obtained a higher AUC than the DL model (AUC=0.69; p=.02).

Table 1: Performance metrics for the various models for classifying binary COPD status.

	AUC	F1-Score	Accuracy	Precision	Recall
<i>Machine Learning (ML) Model</i>	0.76	0.66	0.66	0.69	0.66
<i>Deep Learning (DL) Model</i>	0.69*	0.64	0.64	0.64	0.64
<i>ML-DL Ensemble (Rad-Ens)</i>	0.76 [†]	0.69	0.69	0.71	0.69

*Statistically different from ML Model (p<.05). [†]Significantly different from DL Model (p<.05).

Conclusion: By combining a ML model that utilizes lung CT radiomics and a DL model, Rad-Ens, we were able to classify binary COPD status with higher performance compared to a DL model alone. However, there was no difference between the Rad-Ens and ML model, indicating that the Rad-Ens is not providing additional information for classifying COPD status. Future work will look at investigating other ML-DL ensemble methods to improve model performance. For example, using the whole 3D CT image instead of 15 slices as the input. These models could be used in settings with undiagnosed COPD where CT imaging is available, such as lung cancer screening trials. Earlier COPD detection could lead to earlier treatment initiation, and improved patient outcomes.

References: ¹Zhang et al. 2017. *Sci.Rep.* ²Muller, et al. 1988. *Chest.* ³Westcott et al. 2019. *Radiol.* ⁴Gonzalez et al. 2017. *Am J Respir Crit Care Med.* ⁵Chen et al. 2020. *Radiographics.* ⁶Griethuysen et al. 2017. *Cancer Res.*

Vertebral Detection and Labelling using Deep Learning for Spine MRI Registration

Jonathan Chu¹, Michael Hardisty^{2,3}, Alexander Wong¹, Stewart McLachlin¹
¹University of Waterloo, ²Sunnybrook Research Institute, ³University of Toronto

INTRODUCTION: Magnetic resonance imaging (MRI) is vital in many clinical workflows. Specifically, spine MRI is commonly used to detect various pathologies such as infections, metastases, nerve root disorders, and disc abnormalities [1]. Due to this, image segmentation and deformable registration are commonly used to spatially align areas of interest for better pathological understanding [2], specifically between multi-modal images. However, registration of spine MRI is difficult due to different fields of views (FoVs), resulting in the need of time-consuming manual landmarking. To assist in the process of determining the different FoVs in spine MRI, the objective of this study was to automate identification and labelling of vertebrae using a Mask R-CNN model. This component will allow for the automated detection of individual vertebrae within multi-modal images, which can then be used to seed initial alignment or crop to appropriate FoV for subsequent registration.

METHODS: A dataset of T1w 2D, mid-sagittal cervical spine images was extracted from the Spine Generic Dataset [3]. The dataset consists of 267 healthy subjects imaged from 42+ centers around the world. Ground truth segmentations, bounding boxes, and labels were created using Spinal Cord Toolbox (SCT) [4] and 3D Slicer [5]. SCT was used to generate spinal cord segmentations, vertebral level labels along the cord, and vertebrae semantic segmentations (from the PAM50 template [6]). Next, 3D Slicer was used to generate individual vertebrae instance segmentations by breaking up the SCT semantic segmentations into individual islands, and labelling based on the proximity to the SCT vertebral level labels. Quality checks were performed to inspect for segmentation and/or labelling errors, with 149/267 images passing. The passing set of 149 images were then cropped to the cervical spine (C1-C7). Minor manual segmentations were also performed to clean up the selected 149 segmentations to ensure robust ground truth segmentation masks and bounding boxes.

The Pytorch torchvision Mask R-CNN with a ResNet50-FPN (pre-trained on the COCO 2017 dataset) was then trained to localize and label eight classes (C1-C7 and background). The dataset was randomly split by subject for training, validation, and testing 70%:20%:10% (106:29:14 subjects). The main challenge metric was mAP@75, a score that considers precision, recall, and intersection over union with the ground truth bounding. Other metrics include MAE of bounding box centroids, dice loss of generated segmentations, and identification rate (IDR), which is a measure of vertebrae correctly detected and labelled compared to the total amount of vertebrae in the image.

RESULTS: The model was successful trained, and evaluated on 14 unseen test subjects, resulting in a mAP@75 of 0.676, bounding box centroid MAE of 1.573 voxels, dice loss of 0.111, and IDR of 1.0. The mAP@75 score demonstrates the model's robustness in localizing and labelling vertebrae. The IDR of 1.0 shows the model was able to detect all vertebrae in all test images with some false positives generated (Figure 1).

CONCLUSIONS: Use of a Mask R-CNN model demonstrated the ability to localize and label vertebrae for FoV cropping towards improving initial affine and deformable registration of spine MRI.

REFERENCES: [1] Jarvik *et al.* 2002, *Annals of Internal Medicine*. [2] El-Gama *et al.* 2016, *Egyptian Informatics Journal*. [3] Cohen-Adad *et al.* 2021, *Nature Protocols*. [4] De Leener *et al.* 2017, *NeuroImage*. [5] Fedorov *et al.* 2012, *Magnetic Resonance Imaging*. [6] De Leener *et al.* 2018, *NeuroImage*.

ACKNOWLEDGEMENTS: NVIDIA Academic Hardware Grant Program, NSERC CREATE Program

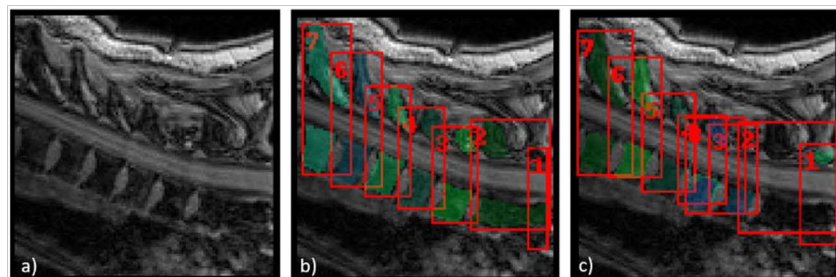


Figure 1: Example of inference on test set. a) Input MRI. b) Ground truth. c) Output prediction

Deep Learning for Automated Detection of *Caenorhabditis elegans* in Hydrogel

Teo Mesrkhani^{1,2}, Sinthuran Jegatheeswaran^{1,2,3}, Wei Liu¹, Mohammad Kashif¹, Dae Kun Hwang^{1,2,3},
Elodie Lugez^{1,2}

¹Toronto Metropolitan University, ²Institute for Biomedical Engineering, Science and Technology (iBEST),
³Keenan Research Centre for Biomedical Science, St. Michael's Hospital, Toronto, Canada, Toronto
Metropolitan University

Introduction: The nematode *Caenorhabditis elegans* (*C. elegans*) is considered to be a valuable model organism for studying human genes and diseases due to its genetic similarity with humans [1]. Monitoring protein aggregation in the body tissue of these worms presents an opportunity to understand human disease progression. *C. elegans* immobilization is necessary to ensure their clear visualization. Traditional immobilization methods involve anesthetics or physical constraints which contain limitations [2]. We developed a novel microfluidic device to immobilize these worms after being detected by our worm-recognition model. This study investigates the use of YOLOv5 [3] for the detection of *C. elegans* worms used in our novel immobilization device.

Methods: An automated worm encapsulation method using a deep-learning-assisted worm-recognition model was developed. Real-time processing of camera footage from the inverting microscope is carried out using a Python script with the OpenCV library, while the You Only Look Once (YOLO) algorithm is used for real-time object detection. The dataset used to train the model used for worm-recognition contained 25,079 images containing five classes: larva worm, adult worm, bubbles, wall, and debris. A stratified five-fold cross-validation was used to train and evaluate the model, as the data set contained a significant number of worm instances. By triggering UV-induced polymerization using this model, we achieve the automated encapsulation of both larval *C. elegans* and adult *C. elegans* in the hydrogel while remaining viable, as shown in Figure 1 by an encapsulated adult *C. elegans*.

Results: The detection of a larva worm using YOLOv5 is shown in Figure 2. Our finalized model achieved a precision score of 0.95 for larva worms and 0.95 for adult worms, with a mAP50 value of 0.98 for larva worms and 0.96 for adult worms. Precision of the worm classes was greatly improved by performing data augmentation to the worm images, and with the introduction of the bubble, wall, and debris classes.

Conclusions: With the use of a deep-learning model for worm-recognition, worms can be encapsulated without the need for manual intervention. It provides new opportunities to explore the genetic interactions and disease progression in *C. elegans*, which in turn can further our understanding of human diseases with homologous genes.

References: [1] O' Reilly, et al. (2013). *C. Elegans* in high-throughput drug discovery, *Advanced Drug Delivery Reviews*, 0 247-253.

[2] Jang, S. et al. Glycolytic enzymes localize to synapses under energy stress to support synaptic function. *Neuron* 90, 278–291 (2016).

[3] Glenn Jocher, et al. Ultralytics/yolov5: V7.0 - Yolov5 SOTA Realtime Instance Segmentation. v7.0, Zenodo, 22 Nov. 2022, doi:10.5281/zenodo.7347926.

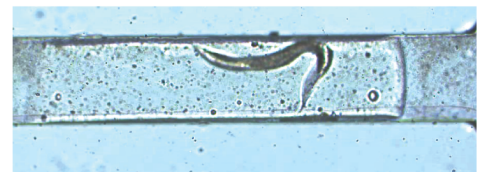


Figure 1: Adult worm encapsulated in hydrogel



Figure 2: Larva worm Detected with YOLOv5 model

A deep learning approach to markerless tumour motion forecasting based on optical surface imaging and volumetric 4D-CT

Yau T^{1,3}, Lee TY^{1,2}, S Gaede^{1,3}

¹Department of Medical Biophysics, Western University, ²Robarts Research Institute, ³London Regional Cancer Program

Introduction: External beam radiation therapy is a common modality used in the treatment of lung cancers. However, the presence of patient respiration can introduce significant motion in the tumour that must be accounted for during treatment to avoid irradiating healthy tissue. An ideal method for motion management is real-time tumour tracking where the radiation beam follows the tumour in real-time to ensure correct target coverage and normal tissue sparing. However, inherent machine latency necessitates that tracking algorithms predict future tumour motion to avoid lagging behind the true tumour position. Typically, surgically implanted fiducial markers are imaged during treatment for real-time tumour localization, but can carry various risks such as pneumothorax and marker migration¹. Instead, a prediction model using deep learning based on optical surface imaging could provide a markerless alternative for tumour motion forecasting. Volumetric 4D-CT (v4D-CT) is already capable of artifact-free imaging of simultaneous chest and tumour motion over time that could be used to train such a model². Our aim was to investigate the feasibility of a deep learning workflow based on v4D-CT for generating patient-specific prediction models for tumour tracking driven through surface guidance.

Methods: V4D-CT images were acquired for four lung cancer patients with a 16cm axial field-of-view and 280ms temporal resolution for 35-45 seconds at a single table position. Each voxel along the patient's 3D surface was tracked along the anterior-posterior axis to generate a 3D surface mesh that could be monitored for respiratory motion and used as model input. The respiratory trace was divided into a 70% -30% train-test split and each model was trained using a combination of recurrent neural network (RNN) layers and full connected (FC) layers to predict the centroid of the tumour 280, 570, 840, and 1120ms ahead of the current time point. The number and size of RNN and FC layers were optimized per patient using the Hyperband algorithm. An ensemble of 20 model instances were trained per patient and the averaged response taken for evaluation using root mean squared error (RMSE).

Results: RMSE values for forecasted tumour centroids 280ms ahead were 0.30-0.57mm, 0.59-0.88mm, and 0.19-0.64mm in the left-right, anterior-posterior, and superior-inferior directions respectively. Additionally, RMSE values remained under 1.0mm when increasing the forecasting gap up to 1120ms. Utilizing model ensembles reduced RMSE values by 0.05-0.77mm in each direction over individual model instances.

Conclusions: v4D-CT combined with deep learning algorithms is capable of generating accurate, patient-specific tumour motion prediction models for markerless tumour tracking using the patient's 3D surface contour. Tracking accuracy is comparable to other deep learning forecasting models, although most models still rely on implanted fiducials as the input signal³. Future work will include increasing the patient population as well as investigating the optimal subset of the 3D surface required to maximize tumour forecasting accuracy while minimizing computational burden.

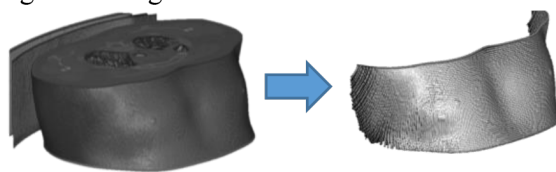


Figure 1: Visualization of the 3D surface mesh generated from the patient CT image

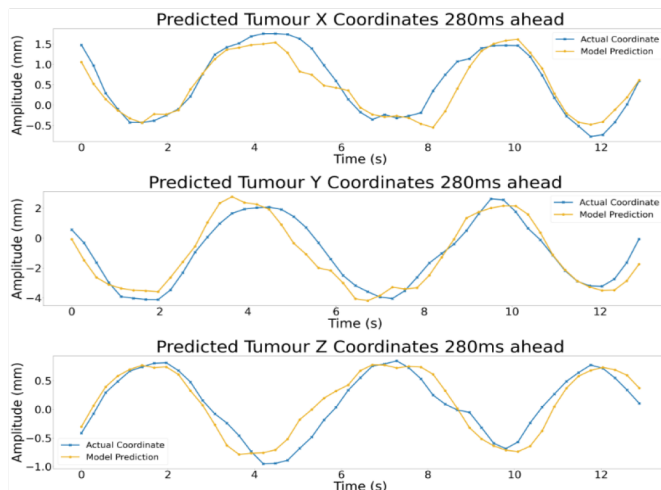


Figure 2: Comparison of model predictions (shown in yellow) against the true tumour centroid (shown in blue) for a sample patient with a 280 ms forecasting distance

References:

- [1] Bhagat N, et al. *Cardiovasc Intervent Radiol*. 2010;33(6):1186-1191.
- [2] Young H, et al. *J Appl Clin Med Phys*. 2021;22(8):295-302.
- [3] Chang P, et al. *J Med Internet Res*. 2021;23(8):e27235

3D U-Net Segmentation of the Visceral Cavity of a MicroCT-Imaged Rat

Joseph U. Umoh,¹ Jaques Milner,¹ David W. Holdsworth^{1,2}

¹Preclinical Imaging Research Centre, Robarts Research Institute, Western University, London, ON, Canada, ²Depts. of Medical Biophysics and Surgery, Western University, London, ON, Canada.

Introduction: The visceral cavity stores adipose tissue and organs in the body. In rats and other small animals, the adipose tissue has especially been applied in animal study of obesity. To compute the mass¹ of the visceral adipose tissue, the visceral cavity (Fig. 1) needs to be segmented. This segmentation has been manually done and is time-consuming. This study uses U-Net network to segment the volume of the visceral cavity in rats. The rats were imaged using micro-computed tomography (microCT) technique. Our objective is to provide a three-dimensional (3D) segmentation solution that can be used to automatically segment a rat image volume. This will save time in segmentation.

Methods: Data was preprocessed, first by down-sampling the 16-bit rat image volume to 8-bit to reduce the file size. In order to load the data into the data-processing program, the .vff files which contained the rat images were converted to .nii file format using the *Convert3D* medical image processing tool. The image data was normalized by dividing the image value by 255. Then, image mask was created for each volume, by manually segmenting the visceral cavity. The mask was converted into a binary image by replacing the image values inside the cavity with 1 and those outside the cavity with 0. The U-Net segmentation approach in this study was segmenting the mask in 2D slices and then combining them to form the volume.² In our preliminary run, 480 slices from four rats were used for the training and 160 for testing. Batch size during training and testing was 32 and number of epochs was 80.

U-Net architecture consists of an input layer; two convolutions layer followed by max-pooling; bottle neck layer; two transposed convolution layers followed by unpooling; and one output layer. In this study, the activation function in the convolution and transposed convolution layers was *relu* and the one in the output layer was *sigmoid*. The model optimizer was *Adam* (Adaptive Moment Estimation), loss function was *binary_crossentropy*, and metrics was *accuracy*.

The U-Net model was trained and run using *TensorFlow* and *Keras* library.

Results: Fig. 2 shows the preliminary results of the segmentation of the test dataset. The slice shows an excellent agreement between the true and predicted mask in the sagittal plane with a *loss* of less than 5% and *accuracy* of more than 95%.

Conclusions: These preliminary results successfully demonstrate the use of deep learning with 3D U-Net architecture to segment the volume of rat visceral cavity. Further work is in progress to validate the model and use it to segment other rat datasets.

References:

1. D. Wong, J.U. Umoh, D.W. Holdsworth *et al.* Supplementation on body composition in the APP/PS1 mouse model of Alzheimer's Disease following chronic vitamin D deficiency. *J Alzheimers Dis.* 2021.
2. D. Madsen. 3D image segmentation (CT/MRI) with a 2D UNET (online). <https://www.youtube.com/watch?v=CogGIdkDA8g>, June 2023.

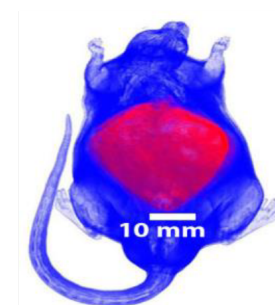


Fig.1: MicroCT image-rendering of a whole-body (face-up) rat, showing the visceral cavity (red).

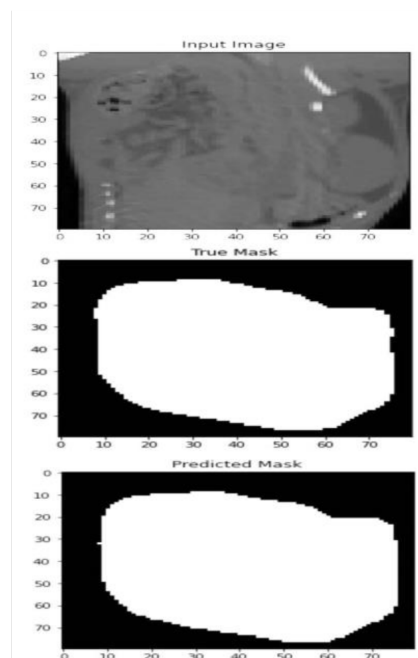


Fig. 2: 2D slice image of a rat visceral cavity showing the input, true mask and the predicted mask obtained from the model test run.

Using deep learning and a feature extraction pipeline to quickly localize catheter tips in prostate brachytherapy ultrasound images

Jessica de Kort^{1,2*}, Nicole Kitner³, Dr. Tamas Ungi³, Dr. Martin Korzeniowski⁴, Dr. Timothy Olding⁴, Dr. Parvin Mousavi³, Dr. Gabor Fichtinger^{4,5}, and Dr. Jessica R. Rodgers¹

¹ Department of Physics and Astronomy, University of Manitoba, Winnipeg, Manitoba

² Department of Physics, University of Winnipeg, Winnipeg, Manitoba

³ School of Computing, Queen's University, Kingston, Ontario

⁴ Department of Oncology, Queen's University, Kingston, Ontario

⁵ Kingston Health Sciences Centre, Kingston, Ontario

Introduction: A diagnosis of prostate cancer is the leading male cancer in Canada with one in nine people who were assigned male at birth receiving a diagnosis in their lifetime. One way to treat prostate cancer is through high dose rate brachytherapy, which inserts multiple catheters (typically 16–18) into the prostate and surrounding tissues. A radioactive source is passed through the catheters to destroy cancerous cells. Transrectal ultrasound (TRUS) images are often used to guide catheters into their places but due to shadowing artifacts and how small the catheters are, locating catheters can be difficult and time-consuming, especially as they may bend during insertion. To further reduce risks that are associated with prolonged anesthesia, integrating intraoperative tools that decrease procedure time are necessary. The objective of this work was to integrate automated tools for tip identification of curved catheters in three-dimensional (3D) TRUS images using a deep-learning and feature extraction pipeline.

Methods: There were 67 patients in the training dataset and the testing dataset included 15 patients. The pipeline passed TRUS images through a 3D U-Net architecture to produce point-cloud predictions, which provided predicted segmentations for each point in the images. The point-cloud outputs were refined using the 3D Hough transform to discern curved catheter shafts, with curve-fitting applied to form continuous catheter predictions. Catheter end-length data are recorded intraoperatively and, if desired, can be used to adjust catheter lengths through the interface. Predicted catheters were compared to ground truths, manually identified by medical physicists.

Results: Following refinement with curve-fitting, the average Dice coefficient was 0.42 ± 0.01 ($n = 343$), indicating a moderate pixel-wise overlap between the ground truth and predicted catheters, requiring further refinement. The average difference found in catheter shaft positions was 1.9 ± 0.1 mm and the average tip difference was 3.0 ± 0.4 mm (Fig. 1). The maximum tip difference of the curved catheters after the Hough transform was 3.2 ± 1.5 mm.

Conclusions: Future studies will focus on reducing the tip identification error. Automatic localization of curved catheter tips in TRUS images using a deep-learning and feature extraction pipeline can decrease associated risks from prolonged anesthesia and reduce human uncertainties in the clinical workflow.

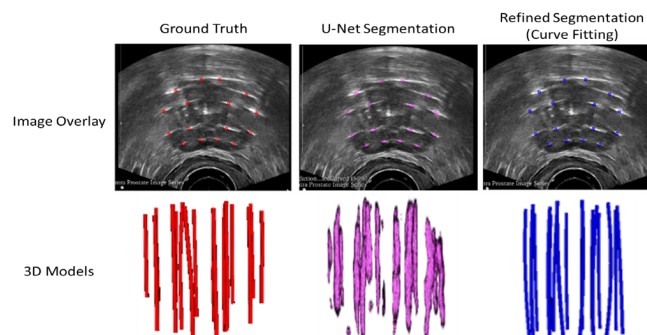


Figure 1: Example of ground truths and segmentations after the TRUS images have passed through each step of the pipeline shown at the mid-level of the prostate for one patient in the testing dataset. The top row shows the segmentations overlaid on the corresponding slice of the TRUS image and the second row shows 3D renderings of the segmented catheters.

Verifying the Classification Accuracy of a Machine Learning Core in an IMU Sensor

Kyle Wilson^{1,2}, Steven Pollmann², David W. Holdsworth^{2,3,4}

¹Faculty of Engineering, ²Robarts Research Institute, ³Dept. of Medical Biophysics, Schulich School of Medicine and Dentistry, ⁴Dept. of Surgery, Schulich School of Medicine and Dentistry, Western University

Introduction: Arthritis is one of the most common chronic illnesses in North America [1]. Clinical treatments can improve quality of life by reducing joint pain and increasing range of motion, however, clinicians typically rely on self-reporting outcomes to assess the efficacy of treatment methods, leaving reported data subject to bias. Therefore, there is need for devices that can objectively measure and record patients' daily physical activity. Inertial measurement units (IMUs) are sensors that combine an accelerometer and gyroscope to quantitatively measure physical motion. Machine learning (ML) algorithms are ideally suited to convert the raw IMU data into a format that is both readable and relevant to the users. Some newer IMU models contain embedded Machine Learning Cores (MLCs), enabling the sensors to perform Edge AI. The current objective is to verify whether the MLC in the LSM6DSOX IMU can classify motion in real-time, at a sufficient level of accuracy.

Methods: To acquire training data to configure the MLC for activity recognition, 5 participants were recruited and asked to wear an IMU while performing designated activities in a specific order. The IMU was attached at the base of the participants spine to acquire information about the user's gait. The 5 participants each performed 2 separate trials. The collected data was manually segmented and labelled based on the type of motion occurring at each time point. Prior to training, the data was down sampled to a lower frequency to match the sampling rate of the IMU. The MLC was then trained and tested using an application provided by STMicroelectronics called Unico. Prior to training, Unico assigns trials to a training and testing set, ensuring that all classes are represented in each set. Training required manually optimizing the features extracted from the data to be used as inputs to the decision tree algorithm. After training, the application checks the accuracy on the test set. Once the desired level of accuracy is achieved, the model can be exported for use with an Arduino Nano microcontroller to program the IMU and MLC. Programming the Arduino to print the MLC output to the serial monitor is a simple check that it functions as intended. In previous work, a post-processing ML model was custom designed in Python using the exact same training data. The model was a hybrid convolutional neural network and long short-term memory network.

Results: All data points were successfully labeled and input to the machine learning model to train the binary decision tree in the MLC. The trained model from the Unico app was seamlessly exported to the MLC. Making predictions on the test set resulted in the confusion matrix in Figure 1, with a test accuracy of 96% and an average precision of 95%. However, this performance was only achieved after consolidating jogging and sprinting as one output category called running.

Comparatively, the hybrid neural network achieved a similar accuracy of 92% but required no consolidation of the output categories, demonstrating better accuracy at differentiating between similar activities than the MLC.

Conclusion: Both the hybrid network and the MLC confirmed it is possible to use ML models to classify physical activities based on data measured by a single IMU located at the base of the spine. However, the post-processing approach is very computationally expensive, requiring cloud computing. Also, it would require constant IMU data storage during implementation, increasing storage demands and power consumption. Utilizing edge AI, such as the MLC in this case, allows for low power operation, minimizes storage demands, and maximizes privacy making it ideal for long-term remote applications. At the cost of some unnecessary classification granularity, the MLC was proven capable of performing on par with the post-processing neural network. This work could lead to a new type of low-cost motion data acquisition system that provides objective activity data acquired outside of a clinic that could significantly improve the assessment of therapies for musculoskeletal conditions, like arthritis.

References: 1. Arthritis Society Canada, "The Truth About Arthritis," 2022. [Online].

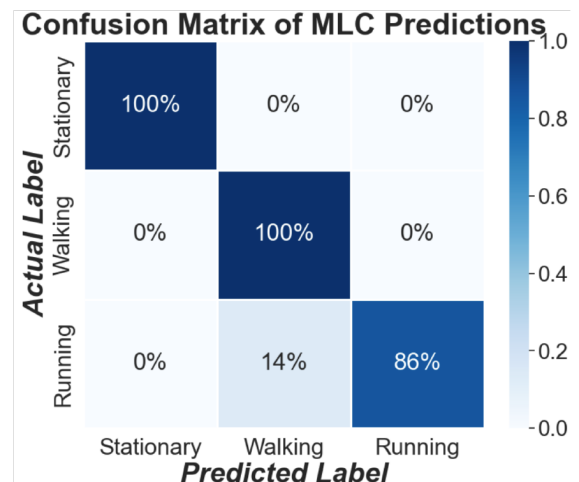


Figure 1: Confusion matrix of classification results performed on test set.

Validation Dataset Construction for Laparoscopic Image De-smoking

Victoria Fan¹, Wenyao Xia¹, Terry M. Peters^{1,2}, Elvis Chen^{1,2,3}

¹ Robarts Research Institute, Western University, London, ON, Canada

² School of Biomedical Engineering, Western University, London, ON, Canada

³ Department of Electrical and Computer Engineering, Western University, London, ON, Canada

Introduction: Laparoscopic surgeries are susceptible to the obscuring effects of surgical smoke, which can impact the visibility of critical anatomical structures. Addressing this issue requires developing effective de-smoking algorithms, which ultimately require reliable datasets consisting of real laparoscopic smoky images and their smoke-free counterparts. Nevertheless, constructing such a dataset in realistic laparoscopic settings poses significant challenges. To the best of our knowledge, all existing laparoscopy de-smoking datasets are synthetic, and may not authentically capture the complexity of real surgical scenes. We hypothesize that it is possible to identify sequential smoky images with minimal tissue and tool movements, which can serve as a reliable basis for constructing a validation dataset. This de-smoking dataset made from existing laparoscopic videos, is a cost-effective approach to represent realistic surgical scenes for the purpose of validation and possible AI training in the future.

Methods: We used data-mining techniques by manually searching through laparoscopic video recordings, locally obtained from a local hospital, to identify suitable sequences from existing robotically assisted laparoscopic surgery videos. The motions during smoky sequences can be mainly contributed by the breathing pattern of patients and tool movements from surgeons. Depending on the surgeon's habits, it is possible to identify cauterization sequences with minimal amount of tool motions, which provides good candidates of still frames where smoke emerges. To compensate for small deformations between frames caused by breathing, a pixel-based video tracking algorithm is applied. Strict visual inspection is then applied to reject frames with large motions to facilitate tracking algorithms through the smoke. From the motion corrected sequence, the initial smoke-free image is used as the ground-truth for subsequent smoky images.

Results: We found 14 possible video sequences from 25 laparoscopic prostatectomy procedure recordings, 37 minutes on average per video, roughly 0.04% of entire video frames. This resulted in the construction of a total number of 516 pairs of smoky images and their corresponding smoke-free ground-truths. An example of a motion corrected image pair is shown in Figure 1. Quantitative assessment involved placing anatomical landmarks on smoky images and their corresponding ground-truth images. The locations between each landmark pair were measured. The average distance between landmarks was found to be less than 1.5 pixels, indicating close alignment. Although cauterization may cause small visible changes in local tissue, they are usually hidden behind the tool and would not significantly impact validation.

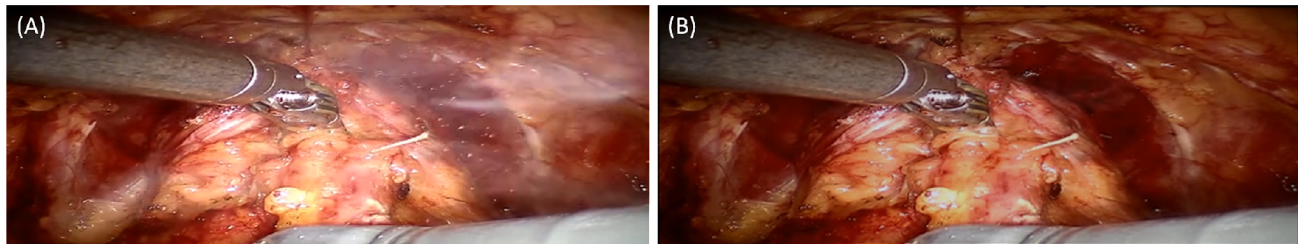


Figure 1. (A) Foggy image taken from a laparoscopic procedure recording after motion correction; (B) The smoke-free ground-truth used. Since lighting differences are caused by the lack of reflected light and smoke, the main difference between the pair of images is the presence of smoke.

Conclusion: In this study, we were the first to create a laparoscopic de-smoking dataset under realistic surgical settings. This dataset can be used to accurately validate existing de-smoking algorithms and create a new benchmark for de-smoking algorithm comparison. With future expansion of the dataset, it can be used to train deep learning models for laparoscopic de-smoking.

Moving beyond laparoscopy: Assessing the true capabilities of popular surgical phase recognition methods in diverse settings

R. Hisey¹, D. LaFleur², J. Erb², T. Ungi¹, G. Fichtinger¹

¹School of Computing, Queen's University, Kingston, Canada

²Department of Anesthesiology, Queen's University, Kingston, Canada

Introduction: Surgical workflow recognition is the field of research that aims to automatically segment recordings of procedures into their individual surgical phases. For many years this field has focussed almost exclusively on minimally invasive procedures. The field has largely ignored the application of this technology to open or percutaneous procedures where the setting is considerably more complex. As a result, the efficacy of so-called “state-of-the-art” models and training techniques have only been evaluated in a very limited clinical context and it is not clear how effective these methods truly are on more complex procedures. One example of this is the current belief that the inclusion of weak tool presence labels during the training process of phase recognition models leads to improved phase prediction accuracy [1]. In the minimally invasive approach, this technique makes sense as the tools which are visible to the camera are those that are actively being used. This is not always the case in open or percutaneous procedures. In this work, we investigate the efficacy of using weak tool presence labels against the use of strong tool bounding box labels and compare these approaches against the simpler approach of only using the phase labels to train a phase recognition model.

Methods: Five medical students and five senior anesthesiologists recorded five trials of central venous catheterization on a venous access phantom. Each frame of the videos was annotated both with the surgical phase that was occurring at the time the frame was captured as well as the bounding box location of all surgical instruments. The weaker tool presence labels were obtained from the bounding box annotations by determining which boxes were present in each frame.

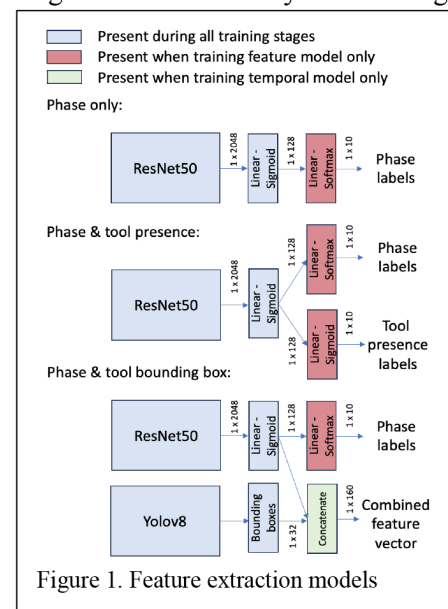
The basic architecture of our workflow recognition network consists of a feature extractor and a temporal model. In all cases our temporal model was a recurrent network that used a hierarchical long short-term memory (LSTM) structure. For this work, we trained 3 different versions of the feature extractor. In the simplest version the feature extractor was a ResNet50 model that was trained using the phase labels. The second was a multi-headed Resnet50 model that was trained simultaneously on both the phase label and multi-class tool presence labels. The final feature extractor consisted of a ResNet50 model trained on the phase labels, combined with the bounding box output of a YOLOv8 network that was trained on the strong bounding box tool labels. In all cases the final classification layer of ResNet50 was removed prior to training the temporal model.

Each of the three architectures was trained using a leave-two-user-out cross-validation scheme, whereby all videos from one expert participant and one medical student were reserved as the test set with each fold. The folding process repeated until all participants had been in the test set once. The models generated the phase prediction for each frame of the video. The predicted results were compared against the ground truth phase labels using the average class weighted Jaccard similarity index across all folds.

Results: The architecture that included the predicted bounding boxes along with the ResNet50 features as inputs to the temporal model had the highest average Jaccard similarity index at 0.63 ± 0.06 . The model that used the feature extractor trained on the phase labels only had the next highest score at 0.61 ± 0.08 , while the model that used the feature extractor trained on both phase and weak tool presence labels had the lowest score at 0.58 ± 0.10 . Further testing is required to establish statistical significance.

Conclusions: The model that used the tool bounding box locations had the highest performance, while the model that included information only about which tools were present had the lowest performance, lower even than using no tool labels at all. This result highlights the need to examine the current “state-of-the-art” approaches for surgical phase recognition in a broader context on more varied clinical procedures. In this way, we can ensure that our state-of-the-art methods are truly generalizable and not limited to small, specific scopes of application.

References: [1] Twinanda AP, et al. EndoNet: A Deep Architecture for Recognition Tasks on Laparoscopic Videos. IEEE T.M.I. 2017.



Session 4 Pitches: MRI

Abstracts

Towards the suppression of lipid contamination in whole brain slice magnetic resonance spectroscopic imaging using two-dimensional selective excitation

Jason Rock^{1,2}, Simon Graham^{1,2}, Jamie Near^{1,2}

1 Medical Biophysics, University of Toronto; 2 Sunnybrook Research Institute

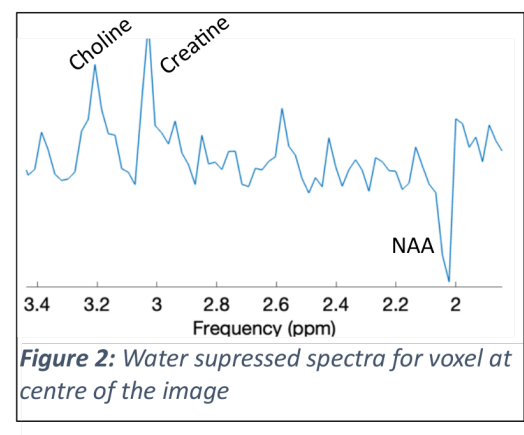
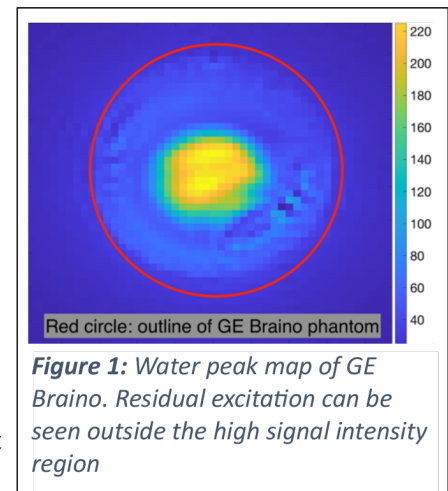
Introduction: Magnetic Resonance Spectroscopic Imaging (MRSI) is a versatile tool for investigating brain tumors and neurodegenerative diseases, including Alzheimer's and Multiple Sclerosis (1,2). However, a significant challenge of performing MRSI on whole-brain slices is the issue of lipid contamination. Extracranial lipids, found in the skin and adipose tissue of the scalp, produce MRSI signals with substantially greater amplitudes compared to the brain's primary metabolites, due to their orders-of-magnitude higher concentrations. These extracranial lipid spectral signals tend to 'leak' into MRSI voxels within the brain, owing to the inherently low spatial resolution (typically on the order of centimetres) of MRSI. Consequently, the dominant lipid spectral signal obscures the weaker spectral signals originating from common brain metabolites, such as *N*-Acetylaspartate (NAA), choline, creatine, and myo-inositol, making accurate quantification challenging. By using two-dimensional (2D) radiofrequency (RF) pulses, an arbitrary excitation region can be formed. By creating a brain shaped excitation region, we aim to effectively eliminate lipid contamination in MRSI by exclusively exciting the brain and excluding extracranial lipids.

Methods: A rapid slice-selective spin-echo MRSI sequence with a rosette k-space trajectory was modified by replacing the conventional slice selective excitation pulse with a 2D RF pulse and the associated trajectory gradients. The 2D RF pulse used a spiral-in k-space trajectory, and for this initial proof of concept, the prescribed excitation region was rectangular in the x-y plane. A GE Braino phantom was used with lard pasted on the exterior to mimic extracranial lipids. The MRSI acquisition parameters follow: FOV 240mm x 240mm, 48x48 matrix size, 25mm slice thickness, TE 15ms, TR 1500ms, 3 number of averages.

Results: The MRSI data were processed using FID-A (3). Figure 1) shows a map of the absolute water peak integral using this new sequence. The excitation region appears circular, rather than the expected rectangular region, possibly due to experimental imperfections including B1 inhomogeneity, sub-optimal RF power calibration, imperfect slice refocusing, and timing imperfections between the 2D RF and trajectory gradients. Finally, the water suppressed spectra showed first order phase artifacts and relatively low signal-to-noise ratio (SNR) (see Figure 2), likely due to the same reasons mentioned above. The first order phase artifact results in an inverted NAA peak.

Conclusion: Using a 2D selective excitation pulse for MRSI is feasible for exciting arbitrary regions of interest such as brain regions with no lipid contamination. Further work will involve 1) adjusting the timing of the sequence to remove the first order phase artifact; 2) refining the 2D RF pulse for customized excitation regions; and 3) improving the RF power calibration to achieve improved SNR. Ultimately, this method is expected to help improve the clinical usage of MRSI by improved brain coverage with removed lipid contamination.

References: [1] Posse et al. J Magn Reson Imaging. [2] Graff-Radford et al. Neuropsychiatric Dis Treat 2013 [3] Simpson et al. Magn Reson Med. 2017



A SINGLE BREATH HOLD MT PULSE SEQUENCE FOR WHOLE-UTERUS IMAGING

Sid Sadanand^{1,2}, Rob Stobbe³, Greg Stanisz^{4,5}, Dafna Sussman^{1,2,6}

¹Departments of Biomedical Physics & Engineering, Toronto Metropolitan University, ²Institute for Biomedical Engineering, Science and Technology (iBEST), Toronto Metropolitan University & St. Michael's Hospital,

³University of Alberta, ⁴Sunnybrook Research Institute, ⁵Department of Medical Biophysics, University of Toronto, ⁶Department of Obstetrics & Gynecology, University of Toronto

INTRODUCTION: Magnetization transfer (MT) in MRI measure signal from macromolecules like myelin^[1], predominantly used preclinically in brain and tumour imaging. MT signal is derived by measuring the water pool of protons' magnetization before and after RF saturation of broad macromolecular resonances^[1]. The resultant difference in water signal corresponds to the amount of saturation transfer (ST), proportional to the concentration of the MT pool^[1]. MT MRI pulse sequences consist saturation, ST, and water signal measurement^[2]. This process is iterated across an array of chemical shifts to build a so-called Z-spectrum^[2]. Gaussian and Lorentzian lineshapes are fitted to the Z-spectrum to extract MT signal from other ST confounds; direct saturation (DS) of water, nuclear Overhauser effect (NOE), and chemical exchange saturation transfer (CEST)^[3]. Lengthy MT sequence acquisition hinders its application to gestational imaging, where spontaneous fetal and maternal respiratory and peristaltic motion cause image subtraction artefacts^[4]. Where complications in neuronal migration and myelination during fetal development are difficult to detect on clinical imaging until structural changes become apparent – after function-sparing interventions are no longer effective^[5] – MT imaging could be sensitive earlier in gestation to some neurodevelopmental complications. In this work, we demonstrate a novel 3D MT-weighted (MTw) MRI pulse sequence (YB MT) optimized for gestational imaging. YB MT acquires a field of view (FoV) covering the entire gravid uterus within a 15s breath hold. As proof of principle, we include initial MT + ST confound phantom data. YB MT is presently being evaluated in late gestation pregnancies.

METHODS: Sequence development and imaging was conducted on a 3T Siemens Prisma Fit clinical system. YB MT was developed from the Siemens stock 2D GRE sequence. The following modifications were made to the sequence to enable 3D MTw imaging: 1) the facility to read in arbitrary readout gradients from text file 2) the facility to read in arbitrary saturation RF pulse shapes from CSV file was added, 3) steady state (SS)-driving acquisitions were added, alongside pre-saturation and spoiling blocks, and a reference acquisition. In order to suppress asymmetric MT confounds of NOE and CEST, amplitude- and phase-modulated multiband saturation pulses were used. A 3-point magnetization transfer ratio asymmetry (MTR_{asym}) was used to derive an MT signal. To accelerate imaging, an interleaved yarnball (YB) trajectory^[6] was used to acquire the volume. Aqueous and agar-containing MT phantoms with CEST confounds were prepared spanning 0-4% w/w agar. Imaging parameters were $TR=3.3ms$, $TE=0.12ms$, $n_{interleaves}=512$, $n_{sat\ pulses}=30$, $FA_{sat\ per\ pulse}=4500^\circ$, $FA=4.05^\circ$, $FoV=350mm$, 5mm isotropic resolution, $TA=28s$.

RESULTS: Fig. 1 Phantom arrangement. Fig. 2 MTw image

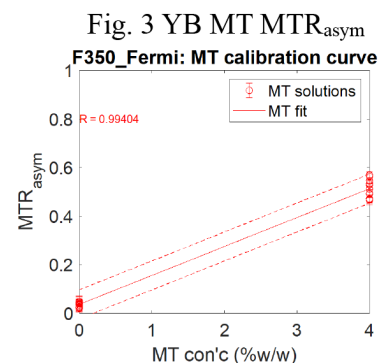
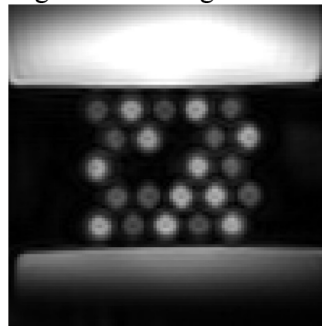
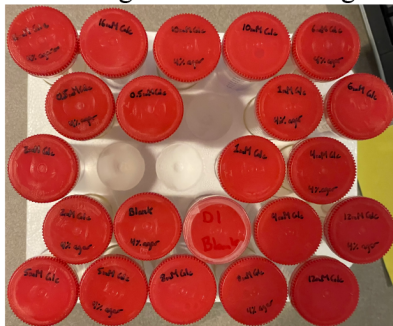


Figure 2 shows MT sensitivity at physiological MT pool size, as per phantom arrangement in Figure 1. Figure 3 depicts small inter-voxel variance amongst samples of the same MT pool size, with $LOD = 0.3\%$ w/w agar, and $LOQ = 1.1\%$ w/w, independent of CEST confound pool size.

CONCLUSIONS: This work demonstrates a viable gestational MTw MRI sequence, with sensitivity on the order of physiological MT, an FoV covering the uterine volume, and the ability to resolve features on the scale of early 3rd trimester major fetal organs, including the brain. The results of ongoing gestational imaging will follow in future work.

REFERENCES: [1] Henkelman, R.M. et al., NMR in Biomed (2001) 14:57-64. [2] Wolff, S.D. et al., Radiology (1994) 192:593-599. [3] Henkelman, R.M., et al., Magn Reson Med (1993) 29(6):759-766. [4] Saleem, S.N., J Adv. Research (2014) 5:507-523. [5] Jarvis, D.J. et al., JMRI (2019) 49:632-646. [6] Meadus W.Q., Univ. Alta. (2020).

Robust Diffusional Kurtosis Computation Using Oscillating Gradient Encoding

Jake Hamilton^{1,2}, Kathy Xu^{3,4}, Nicole Geremia^{3,4}, Vania F. Prado^{3,4}, Marco A.M. Prado^{3,5}, Arthur Brown^{3,4}, Corey A. Baron^{1,2}

¹Centre for Functional and Metabolic Mapping (CFMM), Robarts Research Institute, ²Department of Medical Biophysics, ³Translational Neuroscience Group, Robarts Research Institute, ⁴Department of Anatomy & Cell Biology, ⁵Department of Physiology and Pharmacology, Western University, London, Ontario, Canada

Introduction: Diffusion MRI (dMRI) is a method that sensitizes the MR signal to the diffusion of water molecules, probing tissue on a microstructural level not attainable with traditional MRI techniques. While conventional dMRI has shown use in various research avenues, more sensitive and specific techniques are necessary to further characterize changes in tissue microstructure at various spatial scales. Encoding diffusion using oscillating gradients increases sensitivity to smaller spatial scales¹, and diffusional kurtosis imaging (DKI)² provides a more comprehensive representation of the dMRI signal, increasing sensitivity to microstructural changes. While combining these techniques may allow for increased sensitivity and specificity to various microstructural changes, the generation of the large b-values (diffusion weighting) required for DKI is challenging when using oscillating gradients, and DKI maps are often confounded by noise. Accordingly, the objective of this work is to present a method that combines an efficient encoding scheme and a fitting algorithm that utilizes spatial regularization that address these challenges and provides robust estimates of diffusional kurtosis.

Methods: dMRI data was acquired in n=8 mice on a 9.4 Tesla scanner with gradient oscillation frequencies of 0, 60, and 120 Hz with b-values shells of 1,000 and 2,500 s/mm² (each with a 10-direction scheme which has twice the efficiency of traditional schemes in generating b-value) and parameters: 200 x 200 x 500 μm^3 resolution, 30 slices, TE/TR = 35.5/15000 ms, 4 averages, total scan time of 66 minutes. To compare with a traditional protocol, in one mouse we acquired a second protocol with 40 directions, no averaging, TE/TR = 52/15000 ms, same total scan time. To reduce noise levels in kurtosis maps, we implemented spatial regularization during DKI fitting using isotropic total variation³ (code available at <https://gitlab.com/cfmm/matlab/matmri>), where regularization weighting was heuristically chosen. Contrast-to-standard-deviation ratio (CSR)⁴ was measured to assess contrast and noise levels, averaged across all subjects. Finally, we provide quantitative comparison between spatial regularization and Gaussian smoothing in their ability to control noise levels, where regularization and smoothing weighting were chosen to provide accurate comparison between methods.

Results: The efficient 10-direction scheme resulted in much higher signal-to-noise ratio (SNR) of b=0 volumes (30.6 vs 11.4) and improved kurtosis map quality compared with the conventional 40-direction scheme as evident by a reduction in erroneous kurtosis estimation in low SNR regions towards the bottom of the brain (Figure 1). Implementing spatial regularization during fitting reduced noise while preserving contrast shown both qualitatively and quantitatively (Figure 2) and showed better contrast preservation in radial kurtosis maps measured by greater increases in CSR with increasing regularization (0.2625 to 0.6281) compared to Gaussian smoothing (0.2625 to 0.4567).

Conclusion: The presented acquisition and analysis pipeline allows for DKI fitting when using oscillating gradient encoding by addressing key challenges when combining their use, and we showed the advantages of each component over conventionally used methods. This pipeline may facilitate enhanced detection of microstructural changes that occur over the course of healthy aging and due to various pathological alterations.

References: ¹Schachter et al. *JMR* (2000). ²Jensen et al. *MRM* (2005). ³Rudin et al. *Physica* (1992). ⁴Kingsley et al. *MRM* (2005).

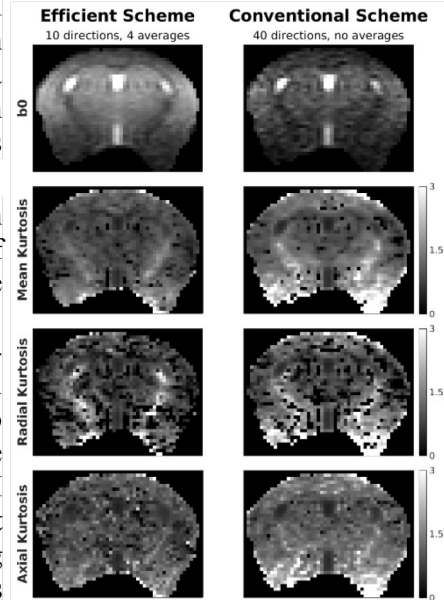


Figure 1. Comparison of b=0 volumes and diffusional kurtosis parameter maps computed with the efficient 10-direction scheme (left) and a conventional 40-direction scheme (right), with no regularization. Data shown is from the 0 Hz acquisition.

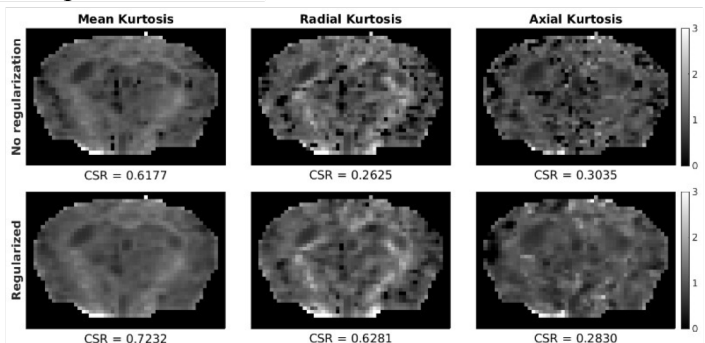


Figure 2. Comparison of kurtosis maps with and without implementation of our regularization algorithm. CSR was calculated for each subject, and the mean across subjects is reported. Data shown is from the 0 Hz acquisition.

Echo-time dependence of microscopic fractional anisotropy using single-shot spiral encoding.

Farah N. Mushtah, Paul Dubovan, Ali R. Khan, Corey A. Baron
Robarts Research Institute, Western University, London, Canada

Introduction: Diffusion magnetic resonance imaging (dMRI) sensitizes MRI contrast to the diffusion of water molecules. Water diffusion is inhibited by cellular microstructure making dMRI a promising method to characterize axon density. Fractional anisotropy (FA) is a dMRI parameter that describes the directionality of water movement; however, it's also sensitive to fibre orientation. Microscopic fractional anisotropy (μ FA) is a dMRI parameter that overcomes the confounding of fibre orientation sensitivity while still being sensitive to axon density^{1,2}, potentially making it more specific to axon integrity. Notably, TE-dependence of standard diffusion parameters can be exploited in microstructural modelling³. However, the TE-dependence for more advanced parameters such as μ FA is unknown and challenging to explore. Accordingly, we combined μ FA with a single-shot spiral MRI acquisition, which allows for large reductions in TE without compromising resolution.

Methods: dMRI was implemented at 3T (Siemens Prisma) with a single-shot spiral sequence with linear tensor encoding (LTE; standard diffusion encoding) and spherical tensor encoding (STE; b-tensor encoding required for μ FA) at variable b-values. Five healthy subjects were scanned with 1.5 mm isotropic resolution at TE = 76ms, 86ms, 96ms, and 106ms, with diffusion times of 30.7ms, 34ms, 34.3ms, and 40.7ms using rate 2 simultaneous multislice (SMS) excitation, with 11 minutes of scan time per scan. T1 weighted images were acquired for registration and brain segmentation. Field monitoring (Skope Clip-On Camera) was performed on an identical acquisition to correct for field perturbations from sources such as eddy currents. MatMRI toolbox was used for image reconstruction. Brain images were registered using FSL, and segmented using Freesurfer into global white matter (WM), cortical grey matter (GM), and deep GM. Linear regression was calculated for μ FA versus TE in the three regions of interest (ROI).

Results: μ FA was the highest in WM, followed by deep GM, and cortical GM. From a TE of 76ms to 106ms, mean μ FA averaged 0.815 for both TEs in WM, decreased from 0.615 to 0.592 in cortical GM, and decreased from 0.710 to 0.695 in deep GM (Figure 1). Linear regression fitting showed a downward trend in μ FA in cortical GM, and deep GM as TE increased.

Conclusion: In this work, we observed a change in μ FA at different TEs in GM but not in WM. This TE-dependence can potentially be explained by different T_2 between white and grey matter, and be exploited for microstructural modelling. Future work will look at assessing more subjects to confirm trends and capitalize on the relatively high resolution of 1.5 mm by investigating regional variability to better understand the μ FA dependence on TE.

References: [1] Arezza et al. *Magn. Reson. Imaging* (2021) [2] Lasič et al. *Frontiers in Physics* (2014) [3] Barakovic et al. *NeuroImage* (2021).

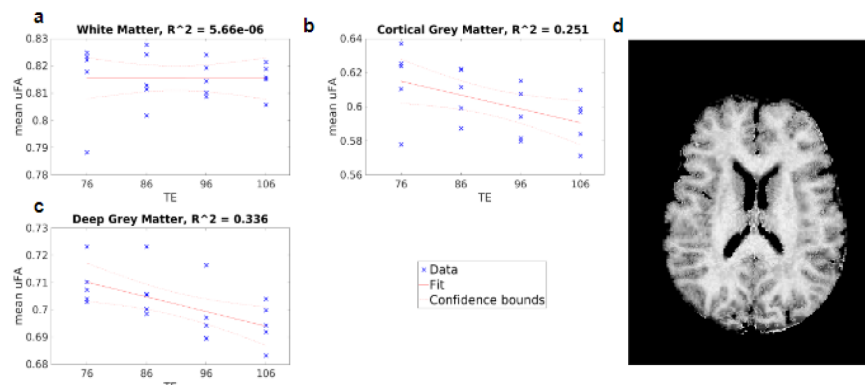


Figure 1. Mean μ FA from 5 healthy subjects at varying TEs with 95% confidence intervals for the following brain regions: a) white matter b) cortical grey matter, and c) deep grey matter. d) μ FA image of the brain.

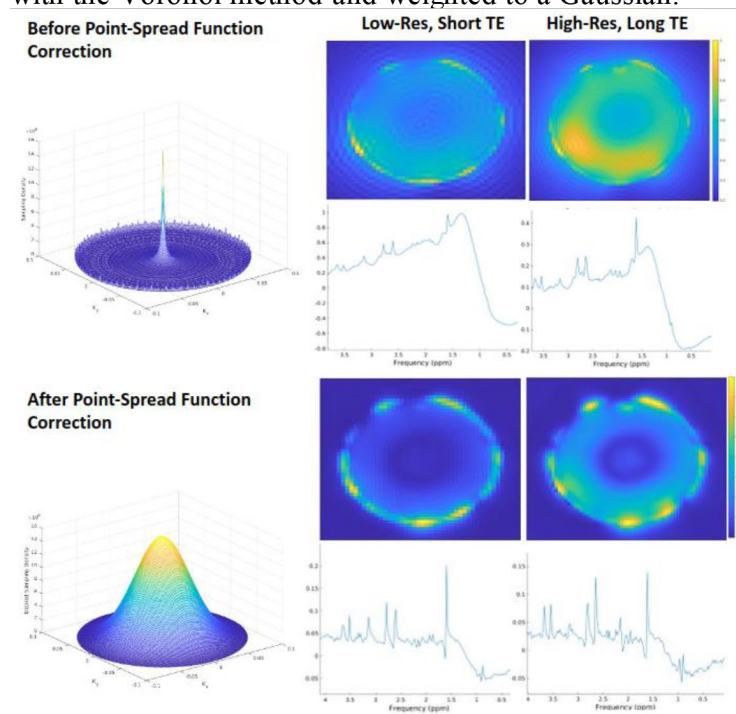
Minimization of Lipid Signal Contamination for Rapid MR Spectroscopic Imaging of the Brain

Lubna Burki (1,2), Sneha Senthil (3), Jamie Near (1,2)

(1) Sunnybrook Research Institute, (2) Medical Biophysics, University of Toronto, (3) Integrated Program in Neuroscience, McGill University

Introduction: A major challenge in whole-brain magnetic resonance spectroscopic imaging (MRSI) is that extracranial adipose tissue can give rise to lipid signals which, due to imperfect localization, appear in the MR spectra of voxels within the brain, ultimately making it difficult to reliably quantify relevant metabolites. Conventional methods of lipid peak removal have been established, as well as their limitations. For example, volume pre-selection as in PRESS and STEAM pulse sequences requires the neglect of tissue in cortical regions close to the skull. Other methods such as L2 regularization¹ involve removal of the lipid peak during post-processing of MRSI data, thus compromising signals of relevant metabolites whose resonance frequencies lie in the lipid range, notably lactate. The specific objective of this project is to develop and evaluate three techniques of rapid MRSI pulse sequences and processing tools for removal of the extracranial lipid signals without the limitations related to volume removal or suppression of relevant metabolites.

Methods and Rationale: *Technique 1)* T2 relaxation time of lipids is shorter than most metabolites of interest, indicating increased signal loss at longer echo times for lipids. To test this hypothesis, we developed a slice-localized spin echo MRSI pulse sequence in the Siemens (Erlangen, Germany) IDEA environment and tested the effects of various echo times (5, 15, and 30ms) on the degree of lipid contamination. This pulse sequence uses a rapid Rosette k-space trajectory², which takes advantage of the self-rewinding nature to decrease scan time. A scan was performed on a Siemens 3T PRISMA MRI scanner using a brain mimicking phantom surrounded by a layer of lard to simulated extracranial lipids. MRSI data processing was performed using the FID-A toolkit. *Technique 2)* A major cause of lipid contamination in MRSI is the broad point spread functions (PSF) resulting from poor spatial resolution. Using a field of view of 24x24 cm, we scanned with matrix sizes of 48x48 and 64x64. *Technique 3)* PSF can be described as a representation of the signal contribution to a given nominal voxel from surrounding areas. The lipid signal arises due to the ringing behaviour in the PSF, which can be manipulated via the Fourier relation of PSF to k-space sampling density. Sampling density maps were produced with the Voronoi method and weighted to a Gaussian.



Results: Performance of techniques were analysed with lipid maps (Figure 1) generated by taking an integral of the MRSI spectra in the frequency range at which extracranial lipids resonate (0.9-1.4ppm). Higher echo times and implementation of PSF correction improved spectral quality and spatial localization of lipid concentration.

Discussion and Conclusion: In addition to the analysis of lipid maps and MR spectra indicating higher echo times and implementation of Gaussian PSF correction, improvements in spectra at higher resolutions is also observed. This motivates future work in the direction of increasing resolution. To circumvent hardware restraints, temporal interleaves will be implemented.

Figure 1. Normalized lipid maps and corresponding central voxel MR spectra at low resolution and short echo time are contrasted with high resolution and long echo times before and after PSF correction. High values in lipid maps indicate lipid localization.

¹ Bilgic B et al. Fast image reconstruction with L2-regularization. J Magn Reson Imaging. 2014 Jul;40(1):181-91. doi: 10.1002/jmri.24365.

² Noll DC. Multishot rosette trajectories for spectrally selective MR imaging. IEEE Trans Med Imaging. 1997 Aug;16(4):372-7. doi: 10.1109/42.611345. PMID: 9262995.

Considering External Calibrant Signal Distributions when Quantifying ^{23}Na -MRI Maps

Cameron Nowikow^{1,2} and Michael D. Noseworthy^{1,2,3,4}

¹School of Biomedical Engineering, McMaster University, Hamilton; ²Imaging Research Centre, St. Joseph's Healthcare, Hamilton; ³Electrical and Computer Engineering, McMaster University, Hamilton; ⁴Radiology, McMaster University, Hamilton

Introduction: To quantify a ^{23}Na -MRI map, a set of reference standards need to be used to map the signal intensities of the image voxels to their corresponding concentration. The most common method involves including tubes of agar with known sodium concentrations within the coil field-of-view (FOV) during image acquisition. After image reconstruction, a region-of-interest (ROI) can be placed within each external calibrant and the mean signal intensity of that calibrant can be extracted. As the calibrants' concentrations are known, a signal intensity vs. concentration curve can be calculated and used to map the voxel intensities in the image to their concentration. However, the use of a mean assumes the signal distributions in calibrants are normal. But due to the low signal-to-noise ratio (SNR)¹, low resolution introducing partial voluming², and non-Cartesian sampling schemes that require re-gridding and often zero-padding,³ a normal distribution is likely not accurate when it comes to ^{23}Na MRI. Thus, we sought to explore whether there are more appropriate ways to extract "true" external calibrant signal intensities that can then be used to produce more accurate sodium concentration maps.

Methods: Three independent sets of density adapted 3D radial (DA-3DPR) images were acquired (TR/TE=9.2/0.2ms, 10 NEX, $\theta = 50^\circ$) of a spherical phantom of 3% agar and 15mM sodium. Embedded in the agar were tubes of 3% agar with sodium concentrations ranging 30-110mM. This phantom was to serve as the "subject" and surrounding the subject was placed additional tubes of agar with sodium concentrations 30, 45, and 70mM in three different sizes to act as the external calibrants (**Fig.1**). Signal distributions were taken from spherical ROIs placed within each calibrant (the average distributions are shown in **Fig.1**) and a mean, median, and mode (i.e. the signal apex after smoothing to remove noise/outliers) was extracted from each distribution to calculate signal intensity vs. concentration curves. The curves were created by linear regression (**Fig.2**) and compared to the values of the mean signal extracted from the tubes of known concentrations within the subject phantom. The mean was used as the signal distribution within the subject phantom was normal.

Results: The average signal distributions of each external calibrant (**Fig.1**) shows that distributions are not normal, and taking a mean or even a median, inappropriately "shifts" the signal lower than it should be. This was confirmed by the signal intensity vs. concentration curves shown in **Fig.2**, where using the mode of the distributions as the input into the regression creates a curve that more accurately represents the concentrations found within the subject phantom. **Figs.1&2** show data from the medium sized external calibrants, but the same holds true for the larger and smaller calibrants. The signal intensity with

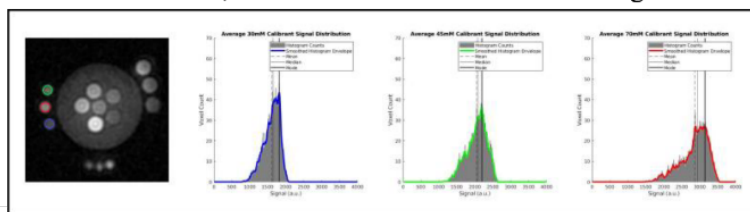


Figure 1: A sample ^{23}Na -MRI image of the phantom and calibrants, and the average signal distributions across the 3 acquisitions for the corresponding external calibrants.

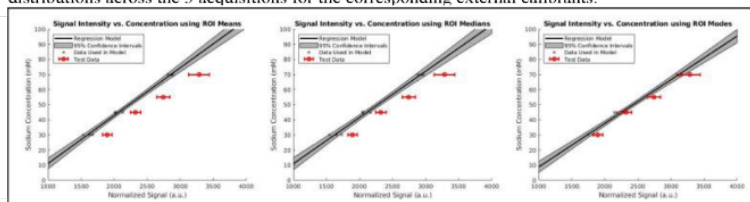


Figure 2: Signal intensity vs. concentration curves when using the means, medians, and modes of the signal distributions inside the external calibrants. The red data points are the target values extracted from the subject phantom.

the larger external calibrants is non-uniform due to B_0 inhomogeneities that remain even after field corrections.

Conclusions: While a deeper investigation into other sampling schemes is necessary to paint a more comprehensive picture about how signal distributions behave across the most common ^{23}Na -MRI acquisitions, this work shows that using the mean when extracting signal intensity from an external calibrant will introduce a source of error that can be accounted for by using other statistical metrics such as mode, or distribution apex.

References: [1] Thulborn KR (2018) *NeuroImage* 168:250–268. [2] Stobbe RW and Beaulieu C (2018) *Magn. Reson. Med* 79(6):2968–2977. [3] Stobbe RW and Beaulieu C (2011) *IEEE Trans. Med. Imaging*, 30(7): 1381–1390.

Pseudo-CT Image Generation from Magnetic Resonance Imaging (MRI) Using Generative Adversarial Networks (GANs) for Radiation Therapy Planning

Nicola Billings^{*a}, Ryan Appleby^b, Amin Komeili^c, Eranga Ukwatta^a

a. Department of Engineering, University of Guelph, 50 Stone Rd E, Guelph

b. Department of Clinical Studies, University of Guelph, 50 Stone Rd E, Guelph

c. Department of Biomedical Engineering, University of Calgary, 2500 University Dr, Calgary

Introduction: Radiation therapy plans require CT imaging to generate electron density maps for dose prescription and MRI imaging to aid in tumor delineation. This dual imaging approach significantly increases the cost, time investment, and congestion within veterinary imaging departments. The objective of this study is to observe if GANs can develop accurate pseudo-CT images from MRI images for radiation therapy planning.

Methods: This study used radiation therapy head standard CT images and T2 TRAN + C 3D FSPGR head MRI images for 45 non-brachycephalic canines with brain tumors who received radiation therapy at the Ontario Veterinary College. Image preprocessing for this study involved resizing the CT images, rigid registration of the MRI and CT images, and normalization of the pixel data between 0 and 1. A conditional GAN (CGAN) with a U-Net encoder and PatchGAN classifier for the discriminator was used to generate the pseudo-CT images. Quantitative performance metrics for this study include mean absolute error (MAE), peak signal to noise ratio (PSNR), normalized mutual information (NMI), and dice similarity coefficients for the entire cranial cavity and bone. Qualitative assessment for the pseudo-CT images involved having veterinary radiologist rank the quality of the pseudo-CT images in comparison to the actual CT images on a scale of 1 (poor quality) to 5 (exceptional quality). The metrics were calculated between the actual CT images and the pseudo-CT images.

Results: The average MAE was 142.92 ± 6.29 HU, the PSNR was 43.03 ± 6.29 dB, and the NMI was 0.64. The dice similarity coefficient for the entire cranial cavity (fat, white matter, grey matter, water, and bone) and the bone were 0.718 and 0.361, respectively (Figures 1 and 2). For qualitative results the average score given by the veterinary radiologists was a 2 (low quality).

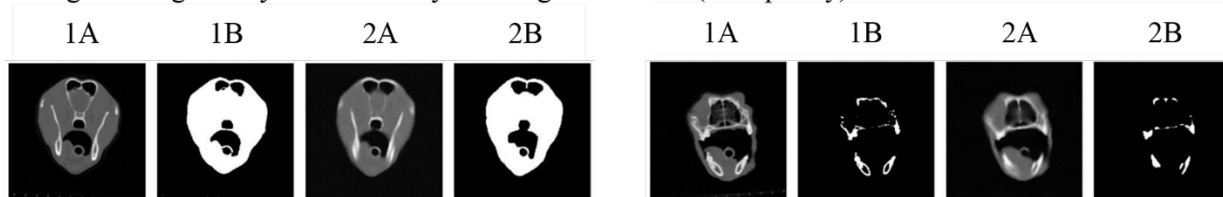


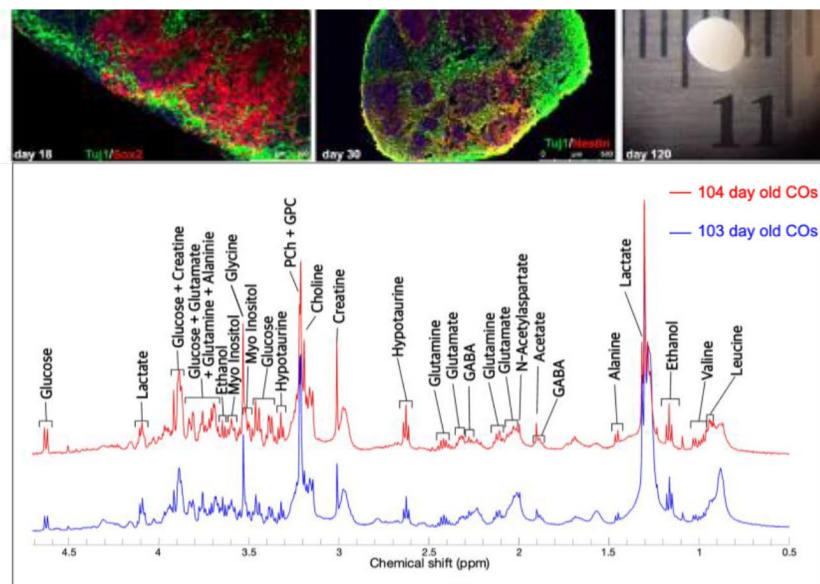
Figure 1: The actual CT (1A) and its respective binarized mask (1B) compared to the pseudo-CT (2A) and its binarized mask (2B).

Figure 2: The actual CT (1A) and its respective bone binarized mask (1B) compared to the pseudo-CT (2A) and its bone binarized mask (2B).

Conclusion: This CGAN model can produce relatively accurate pseudo-CT images; however, different generator architectures such as ResNet, U-Net ++, and DCNN should be explored. These generator architectures have the potential to increase performance by leveraging their ability to capture hierarchical features and prevent the loss of spatial information by implementing more skip connections. Other GAN extensions like CycleGAN, Wasserstein GAN, and Least Square GAN should be implemented to attempt to produce more accurate pseudo images. This model demonstrates that MRI-based radiation therapy planning may be possible in veterinary medicine with further exploration.

High-resolution magic-angle spinning (HR-MAS) NMR spectroscopy in cerebral organoids

^{1,2}Alejandra Castilla B, ¹Vorapin Chinchalongporn, ³Rajshree Ghosh Biswas, ³Andre Simpson, ^{1,4}Carol Schuurmans, ^{1,2}Jamie Near:
¹Sunnybrook Research Institute, ²Department of: Medical Biophysics, ³Chemistry, ⁴Biochemistry, University of Toronto, CA



Introduction: cerebral organoids (COs) are self-organizing three-dimensional clusters of brain tissue, derived from human pluripotent stem cells[1]. COs take on genetic and phenotypic features of the donor, suggesting a potential role for personalized medicine[2]. **In this study, we used high-resolution magic angle spinning (HR-MAS) NMR to evaluate the neurochemistry of 100-day old COs.** **Methods:** Human embryonic stem cells (hESCs) were used to derive COs. Briefly, hESCs were plated in embryoid body (EB) seeding medium. On day 9, EBs were embedded in Matrigel and maintained in StemCell Tech expansion medium. On day

13, EBs were transferred to a Spin Omega bioreactor for CO formation and maintained at 37°C. High-resolution comprehensive multiphase (CMP) NMR[3] was performed on a Bruker 500 MHz 1H spectrometer (Bruker, Switzerland AG, Fällanden, Switzerland) fitted with a magic angle gradient. ~100 days of maturity COs were scanned individually. Each CO was weighed and placed in a 4 mm reduced volume (50 µl) Teflon rotor (HZ07213, Bruker) with D₂O for locking. For the duration of each experiment, samples were maintained at 278 K and spun at the magic angle with a spin rate of 2500 Hz to prevent the rupture of biological tissue[4]. Spectra were processed in Matlab (Natick, MA, USA) using the FID-A toolkit[5]. Metabolite concentrations were estimated with an external reference of alanine with a concentration of 10 mM and a volume of 50 µL in Topspin 4.3.0 (Bruker).

Results: neuronal (TUJ1) and astrocyte (GFAP) biomarkers were found in COs. ¹H spectra were obtained from ~100 day hESC-derived COs. High-quality spectra were obtained with excellent spectral resolution and narrow metabolite linewidths of <2.5 Hz. More than 17 metabolites were detected, including glucose, lactate, creatine, glutamine, glutamate, alanine, ethanol, glycine, hypotaurine, phosphocholine (PCh), glycerophosphocholine (GPC), GABA, N-acetylaspartate, acetate, valine, and leucine. We are currently working on improving the model fitting and metabolite quantification. **Conclusion:** NMR allows assessment of neurochemistry in human-derived COs. At ~100 days of age, COs display a rich neurochemical profile. Future work will aim to assess neurochemical development as the COs mature, and in disease. **Key words:** *Cells (cerebral organoids); Modality: Nuclear Imaging, Cellular and molecular imaging, Application: Neuro (HR magic angle spinning NMR spectroscopy)*

Acknowledgements: This work is supported by the Canadian Institutes for Health Research (PJT-183715).

Table 1. Concentration of Metabolites in human-derived COs.(mmol/L)

	Lactate	GABA	Glutamine	NAA	hTau	Creatine	Choline	Glycine	Myo-inositol
Average	0.33	0.31	0.28	0.02	0.15	0.05	0.06	0.07	0.25

References:

1. Chiaradia, I. and M.A. Lancaster, Nat Neurosci, 2020. **23**(12): p. 1496-1508.
2. Slanzi, A., et al., Front Cell Dev Biol, 2020. **8**: p. 328.
3. Fortier-McGill, B.E., et al., Agric Food Chem, 2017. **65**(32): p. 6779-6788.
4. Taylor, J.L., et al., Magn Reson Med, 2003. **50**(3): p. 627-32.
5. Simpson, R., et al., , 2017. **77**(1): p. 23-33.

Pulse Sequence Optimization for Highly Accelerated Low Field MRI: X-Centric and Sectoral

Samuel Perron¹, Matthew S. Fox^{1,2}, and Alexei Ouriadov^{1,2,3}

¹Department of Physics and Astronomy, University of Western Ontario, London, Canada; ²Lawson Health Research Institute, London, Canada; ³School of Biomedical Engineering, University of Western Ontario, London Canada

Introduction: The optimal field strength range for pulmonary imaging using hyperpolarized (HP) ^{129}Xe has been shown to be around 0.1T to 0.6T²: however, the low field regime poses some issues with clinical imaging, such as low sensitivity and low hardware adoption. We have recently demonstrated³⁻⁵ a Compressed-Sensing (CS) acceleration method able to reduce scan times while improving SNR of low field images: this technique assumes a set of accelerated images has a predictable signal trend^{6,7} across it which can be fitted to the Stretched-Exponential Model.⁸⁻¹⁰ This signal trend is assumed to represent the decreasing density of resonant isotope in lungs after each wash-out breath, and can be “enforced” by averaging for every unique combination of images in the set without overlap. We have found that the X-Centric and Sectoral pulse sequences exhibited fewer reconstruction artefacts than traditional sequences such as gradient echo (GRE): in this work, we develop and investigate different sampling patterns for the X-Centric¹¹ and Sectoral^{12,13} sequences to minimize reconstruction artefacts and improve image quality of highly accelerated images.

Methods: The X-Centric sequence consists of separating each echo into two half-echoes, acquired from the centre-out in the readout direction; an alternating pattern (unique phase-encode order for each half) and a non-alternating pattern (same for both halves) are presented here (Fig. 1). The Sectoral sequence splits k -space into “pizza”-shaped sectors (here, 64), acquiring in a centric-out semi-radial fashion but gridded onto a Cartesian grid: this ensures the k -space centre is prioritized and oversampled compared to the undersampled edges. The simplest acceleration method to implement consists of prematurely stopping the acquisition of a sector before moving on to the next.

¹H MR was performed on a resolution phantom at 73.5mT. Seven sets of 9 images each were acquired using the X-Centric sequence: three sets per X-Centric sampling scheme for each acceleration factor (AF=7, 10, 14, where only 1/AF of k -space is acquired), and one fully-sampled set to be retrospectively undersampled using the Sectoral sampling pattern (Fig. 1, left). In all cases, the averaging pattern described previously was applied before reconstruction, and FOV = 8x8cm², 128x128px².

Results: Representative 7-fold accelerated images are shown in Fig. 2, generated from standard Fourier transform (top row) and the CS reconstruction (bottom row) for the three sampling schemes. Structural similarity index (SSI) was used to compare images, shown in the corners of each resulting image. The Sectoral FT image yielded the highest SSI score, but X-Centric performed better in the CS reconstructions.

Conclusion: Although an improvement over GRE⁴, the X-Centric sequence still showed significant artefacting for both sampling patterns, with the non-alternating scheme faring better. The Sectoral images showed very minimal artefacting even before applying the CS-based reconstruction: although blurry, structure and image contrast appear unaffected by the aggressive undersampling, even at 14-fold acceleration (not shown).

The CS reconstruction improved edge resolution but introduced unwanted artefacts, possibly from over-fitting reconstruction parameters. As the Frequency-Encoding Sectoral sequence has been shown to be well optimized for HP ^{129}Xe lung MRI even at low field¹³, these results suggest that this pulse sequence is an optimal choice for accelerating this type of imaging.

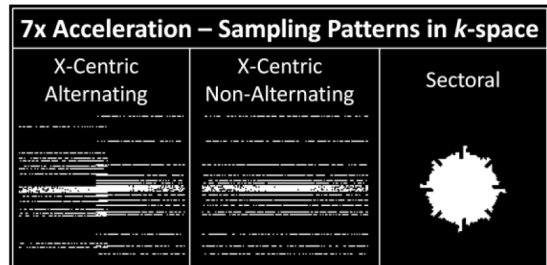


Figure 1. Representative sampling patterns in k -space for 7-fold acceleration. White pixels are sampled k -space points. Matrix size = 128x128

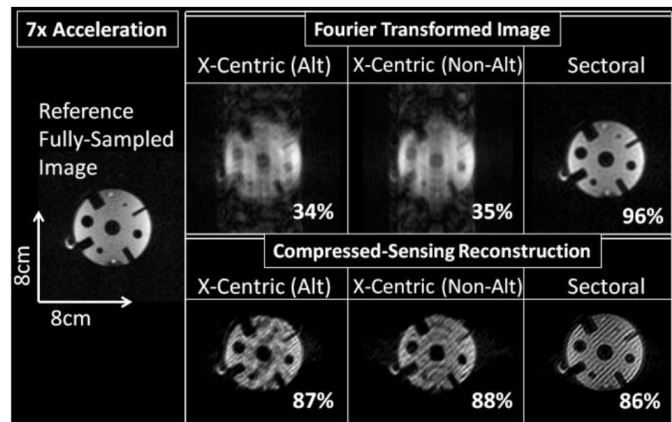


Figure 2. Representative 7x accelerated images obtained from Fourier transform and CS reconstruction, with SSI scores.

We acknowledge the support of NSERC, R5942A04.

References: 1. Stewart, N.J. et al. MRM. (2015); 2. Parra-Robles, J. et al. Med Phys. (2005); 3. Perron, S. et al. ISMRM (2021); 4. Perron, S. et al. ISMRM (2022); 5. Perron, S. et al. ISMRM (2023); 6. Santyr, G.E. et al. MRM. (2008); 7. Ouriadov, A.V. et al. MRM. (2015); 8. Westcott, A. et al. JMRI. (2019); 9. Abascal, J. et al. IEEE Trans Med Imaging. (2018); 10. Parra-Robles, J. et al. ISMRM (2013); 11. Ouriadov, A.V. et al. MRM. (2017); 12. Khrapitchev, A. A., et al. JMR (2006); 13. Perron, S. et al. JMR (2022).

Session 5 Talks: Device, Hardware, Software Development

Abstracts

Development of a photothermal therapy guidance platform using photoacoustic thermometry with dynamic diffuse optical tomography temperature calibration

Ivan Kosik (University Health Network), **Ben Motz** (McMaster University, Princess Margaret Cancer Center), **Robert Weersink** (Institute of Biomaterials and Biomedical Engineering, Radiation Oncology, U of Toronto), **Brian Wilson** (Medical Biophysics, U of Toronto)

Introduction: Photothermal therapy (PTT) for cancer uses thin optical fibers to deliver near infrared laser light to tumors causing a local rise in temperature beyond cell survival ($> 55^{\circ}\text{C}$). As a result, PTT represents a minimally invasive treatment alternative that avoids surgery, radiation, and chemotherapy along with the personal and financial costs. Our center hosts a phase II clinical trial of MRI-guided PTT for prostate cancer with no reported cases of erectile dysfunction, incontinence or perioperative complications following image guided PTT of localized PCa, with 75% of patients released same day¹. This compares favorably with the reported 79% erectile dysfunction, 15% incontinence and average 2-day hospitalization of prostatectomy². However, MR thermometry guidance presents significant complexity due to slow indirect imaging guidance resulting in $\sim 30\%$ undertreatment rate¹. We previously reported on the development of a unique optical-acoustic hand-held guidance platform prototype based on photoacoustic (PA) and diffuse optical tomography (DOT), for the first time capable of deep tissue wide-field (5 cm x 5 cm) thermometry as well as treatment response monitoring without the cost and complexity of MRI³. However, our DOT prototype's clinical measurements in prostate cancer patients also revealed that the local tissue optical properties (absorption, scattering) are dynamically altered during PTT due to heat shock, edema, and coagulation, promising a corrupted temperature calibration of the system. Here we show further complementarity between PA and DOT data by using the photon simulation platform NIRFAST, to dynamically inform the calibration of PA thermometry.

Methods: Our proof-of-concept hand-held PA thermometry probe prototype was combined with a DOT array of 8 sources and 8 detectors, as shown in Fig.1(a), providing 64 DOT data points for NIRFAST simulation. Furthermore, a dynamic phantom designed to simulate thermally coagulating tissue was constructed and imaged. It consisted of a 5 mm diameter central tube (the imaging target) with flowing variable temperature contrast solution, and a surrounding balloon, Fig 1 (b). The balloon was progressively filled with 3% Intralipid solution from 6 mm–20 mm diameter and immersed in a background of 1% Intralipid. This mimicked the conditions of coagulating tissue during PTT where the optical scattering coefficient undergoes a multifold increase in value.

Results: Figure 1(c) shows the PA signal amplitude as a function of temperature for 5 balloon diameters indicating a significant and increasing underestimate for progressively larger diameters (e.g. 50°C w/ 1 cm balloon $\sim 30^{\circ}\text{C}$ w/no balloon, i.e. 20°C or 67% error). However, using DOT reconstructed fluence corrections, Fig 1(d), the revised signal-temperature accuracy is substantially improved (e.g. 45°C w/ 1 cm balloon $\sim 50^{\circ}\text{C}$ w/no balloon, i.e. 5°C or 10% error).

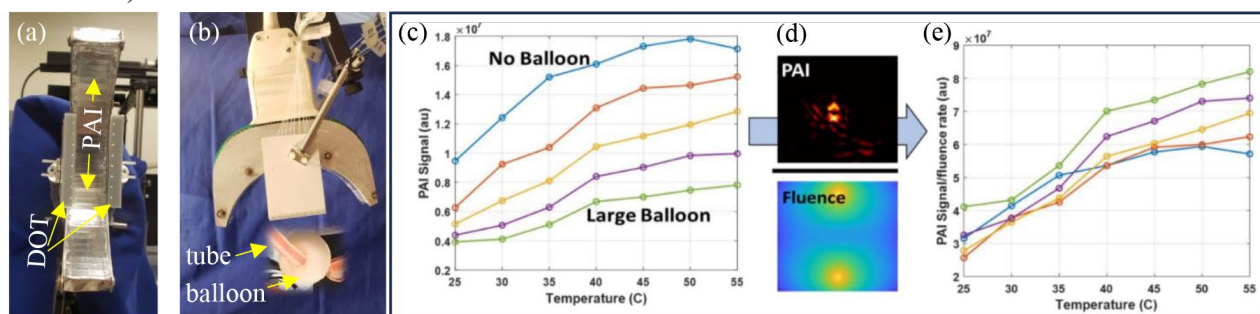


Figure 1(a) Handheld probe showing DOT and PA sensor geometry. (b) Probe and balloon phantom. (c) PA signal vs temperature with no fluence correction. (d) Fluence map (e) PA signal with correction.

Conclusions: We have shown that combining the complimentary information provided by PA and DOT data is effective at reducing thermometry errors during dynamic changes of tissue optical properties associated with PTT treatments. Future and ongoing work aims to improve the speed and accuracy of DOT corrected PA thermometry reconstruction using advanced deep learning methods.

References: 1. Lindner U, et al. J Urol. 2009;182(4):1371-7. 2. Arnold L. et al. JNCI. 2004;(96)18: 1358–1367. 3. Kosik I, et al. Proc. SPIE PC123791Z, Photons Plus Ultrasound: Imaging and Sensing 2023; doi: 10.1117/12.2650785

MRI MOTION PHANTOM OF THE PREGNANT HUMAN ABDOMEN

Alexander Dunn^{1,2}, Mitchell Lee^{1,2}, Eunyoung Cho^{1,2}, Daniel Sare^{1,2}, Sid Sadanand^{1,2}, M. Ali Tavallaei^{1,3} Dafna Sussman^{1,2,4}

¹*Departments of Biomedical Physics and of Biomedical Engineering, Toronto Metropolitan University,* ²*Institute for Biomedical Engineering, Science and Technology (iBEST) at Toronto Metropolitan University and St. Michael's Hospital,* ³*Sunnybrook Health Sciences Centre, Toronto, Canada* ⁴*Department of Obstetrics and Gynecology, University of Toronto*

INTRODUCTION: The development of magnetic resonance imaging (MRI) pulse sequences is logistically challenging and costly [1]. This is in large part due to facility fees, the recruitment of trial subjects, and the requirement of research ethics approval [1], [2]. This challenge is particularly pronounced in fetal MRI studies, which require specific gestational age windows and have a limited participant pool [3]. To combat these issues and facilitate MRI research, phantoms are used to mimic the MR signal, anatomical shape, and/or motion of a real subject. Phantoms form a testing reference for sequence development since they allow for repeatable testing under reproducible conditions. Currently, there are no commercial MRI gestational phantoms that replicate MR signal, anatomical structures, and fetal body motion [1]. We propose a method for constructing and evaluating a motion phantom that accurately mimics fetal morphology, relaxometry and movement patterns.

METHODS: To create this fetal MRI motion phantom, tissue-mimicking materials were used to create a fetal body and placenta. Each component replicated the T1 and T2 relaxation properties and morphology of a late third-trimester fetus and placenta. Tin-catalysed crosslinked polydimethylsiloxane (PDMS) was used for the gross fetal body and musculature, and MnCl₂ doped carrageenan was used for the placenta. 3D printed molds were produced from segmented fetal MRI scans. To generate gross fetal body motion, a parallel robot with 6 degrees of freedom was constructed using MRI compatible materials. The robot's movement was controlled by stepper motors, outside of the MRI bore with long driving shafts, to reduce electromagnetic interference.

RESULTS: Fig. 1 Silicone Fetal Body



Fig. 2 Hydrogel Placenta



Fig. 3 Parallel Manipulator



The robotic actuator was tested to have a positioning and orientation accuracy of ± 2.1 mm (SD 0.87 mm) and $\pm 1.7^\circ$ (SD 2.9°) respectively. SNR degradation, measured by proton density-weighted single shot fast spin echo imaging (PDw ssFSE), remained below 2% during robot operation, along with a maximum B₀ variation of 1 ppm. The molding of the fetal body with PDMS (shown in Fig. 1) proved successful, with minimal entrapped air bubbles which did not cause visible artefacts upon imaging, and good mechanical strength for attaching to the robot end effector. Similarly, the placenta (shown in Fig. 2) was molded without encountering any issues. Both phantom materials closely replicated the relaxation properties of in-vivo imaging with the silicone body having T1 & T2 values of 987 & 50 ms respectively and the placenta having T1 & T2 values of 1500 & 280 ms respectively. The fetal body was affixed to the robot's end effector through a custom-designed attachment point, cast into the silicone structure of the fetal body (shown in Fig. 3). This allowed for the execution of preprogrammed motion paths, mimicking the gross body movements of a fetus.

CONCLUSIONS: This project addresses the logistical challenges of in-vivo fetal MRI pulse sequence development and testing by developing a comprehensive phantom that replicates fetal anatomy and allows for repeatable motion-imaging testing. This novel solution for fetal MRI sequence development can help accelerate gestational MRI research. Future work will incorporate a fetal brain into the silicone body and image the complete assembly under static and moving conditions.

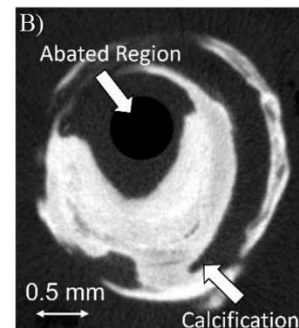
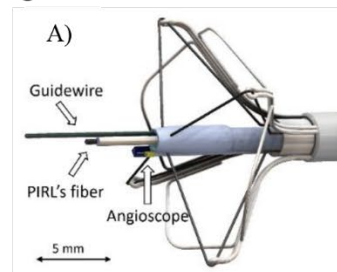
REFERENCES: [1] M. Shulman et al., *Magn. Reson. Mater. Phys., Biol. Med.* (2020) 33(2), 257–272. [2] N. E. Swales et al., *J. Magn. Reson. Imaging* (2011) 34(2), 941–946. [3] D. Bulas and A. Egloff, *Semin. Perinatol.* (2013) 37(5), 301–304.

Characterization of Picosecond Infrared Laser Ablation for Peripheral Artery Disease Revascularization

Mohammadmahdi Tahmasebi^{1,2}, Rob Reyes Perez⁴, Andrew Marques⁴, Yohannes Soenjaya^{2,3}, Mohammad Khoobani^{1,2}, Mohammadmahdi Keshavarz^{1,2}, Ahmed Kayssi², Andrew Dueck², Darren Kraemer⁴, Christine Demore^{2,3}, R. J. Dwayne Miller⁵, Graham Wright^{2,3}, M. Ali Tavallaei^{1,2}

¹Faculty of Engineering and Architectural Science, Toronto Metropolitan University ²Sunnybrook Health Sciences Centre ³Department of medical biophysics, University of Toronto ⁴Light Matter Interaction Inc ⁵Department of Chemistry and Physics, University of Toronto. Toronto, Canada.

Introduction: Peripheral Artery Disease (PAD) and Critical Limb Ischemia (CLI) significantly increase the risks of amputation and mortality. For endovascular revascularization of such arteries, the first step is crossing of the occlusion with a wire, which is then followed by balloon angioplasty. However, these procedures often fail (15-20% failure) due to the inability of crossing the occlusion with the wire. This study assesses the use of a Picosecond mid-Infrared Laser (PIRL) fiber to facilitate crossing. The integration of PIRL with the CathCam system is proposed to potentially enhance treatment efficacy. **Methods:** 12 Popliteal artery lesion samples were acquired from a donated amputated limb of a patient suffering from CLI. A customized system was developed that allowed advancing the PIRL fiber with controlled speeds towards the occlusion. The setup permitted precise targeting of various morphological segments of the lesion while permitting measurement of forces exerted on the lesion with ± 0.1 gr accuracy. The fiber was advanced at various speeds of 0.019, 0.025, 0.1, 0.25, 0.5 mm/s, with its power either OFF or ON with 500 mW or 1000 mW and at a wavelength of $2.96 \mu\text{m}$ with 1kHz repetition rate. The lesions were scanned using μ -CT before and after the test and were analyzed with histology after the procedure. Experiments were repeated for various tissue types within a specified chronic total occlusion (CTO), encompassing lipid, collagen, and calcified tissues. A 40gr of force threshold was applied in the experiments to protect the fiber tip from breaking. Additionally, the feasibility of using PIRL for laser atherectomy with the CathCam in crossing challenging harvested CTOs was assessed under X-ray fluoroscopy guidance. **Results:** When comparing the laser ON (with a speed of 0.025 mm/s) vs. it OFF, we observed a significant improvement in crossing success rate (95.6% vs 73.9, $p < 0.05$). Moreover, the mean maximum force exhibited a significant reduction with the laser ON compared to the laser OFF condition (5.5 ± 9.8 gr vs. 17.2 ± 12.3 gr; $p < 0.05$). Subsequent tests examining various fiber advancement speeds yielded distinct success rates: 100% at 0.019 mm/s, 86.6% at 0.025 mm/s, 85.7% at 0.1 mm/s, 20% at 0.25 mm/s, and 30% at 0.5 mm/s. Correspondingly, the mean maximum measured force was recorded as 8.9 ± 9.3 gr, 7.9 ± 14.7 gr, 13.5 ± 13.5 gr, 31.2 ± 15.4 gr, and 34.3 ± 13.14 gr for 0.019, 0.025, 0.1, 0.25, and 0.5 mm/s, respectively. These findings suggest that the speeds within the range of 0.019-0.1mm/s were deemed optimal for PIRL ablation. When comparing power outputs, no significant difference in success rates was observed between half-power and full-power laser outputs at both 0.1 mm/s and 0.5 mm/s fiber advancement speeds. The feasibility test for crossing PAD CTOs using CathCam under X-ray fluoroscopy was successful, indicating the and feasibility of utilizing PIRL for PAD atherectomy. **Conclusion:** Histological images, distal force measurements, 3D μ CT, together with fluoro X-ray experiments illustrate the overall concept feasibility of the use of PIRL fiber for crossing CTO samples. Integrated with the CathCam the system can potentially improve procedure success rates in challenging CTO cases.



A) Schematic of the CathCam with PIRL integrated. B) μ CT image of the lesion post-ablation using PIRL.

Exploring heart rate variability metrics for stress assessment in robot-assisted surgery trainingElizabeth Klosa^a, Renáta Levendovics^b, Kristóf Takács^b, Gabor Fichtinger^a, Tamás Haidegger^b^aLaboratory for Percutaneous Surgery, School of Computing, Queen's University, Kingston, Canada^bAntal Bejczy Center for Intelligent Robotics, EKIK, Óbuda University, Budapest, Hungary

INTRODUCTION: Accurately measuring stress is challenging due to individual differences in how stress is perceived and managed. Current methods, such as questionnaires, can provide valuable insight into an individual's perception of stress, but are susceptible to subjective biases and lack measurements of physical changes associated with stress. Ongoing research explores more objective methods, such as measuring the presence of indicators like cortisol and catecholamines, among others. However, these measurements can be easily influenced by variables not directly related to a stress response. Other studies explore the use of heart rate variability (HRV), to measure the physiological responses that occur under stress [1]. HRV has been noted to change in response to stress, decreasing as mental stress increases [2]. The first goal of this study is to investigate if the HRV metrics differ significantly between participant groups, suggesting that the stress levels between the groups also differ. The second goal is to explore the efficacy of using HRV for measuring stress levels as a substitute for traditional questionnaire-based stress measurement. **METHODS:** An electrocardiogram (ECG) was used to collect heart rate data from novices, residents and surgeons, as they performed a sea spike test on the da Vinci xi surgical system. RR intervals, representing the time between successive R waves from the QRS signal on an ECG, were extracted from the raw data and preprocessed to correct for artifacts and noise. Time domain metrics such as standard deviation of the N-N interval (SDNN) and root mean square of successive differences (RMSSD) between normal

Table 1: p-value for each HRV metric for the 3 distinct groups

	SDNN	RMSSD	LF	HF	LF/HF
Novice	69.63	43.80	1041.95	536.26	2.43
Resident	55.74	23.22	491.67	312.23	3.43
Surgeon	57.17	27.51	668.36	319.25	2.74
p-value	0.084	0.0025	0.0086	0.078	0.98

heartbeats were calculated. Additionally, frequency domain metrics such as the low frequency (LF) and high frequency (HF) band, and the LF/HF ratio were calculated. Analysis then involved determining the p-value for each HRV metric across the three participant groups to assess for significant differences. Each participant completed a

questionnaire, ranking how mentally and physically demanding they found the task, how complex they found the task and how restless they felt during it. Using these questionnaire metrics and the HRV metrics, p-values were calculated to investigate correlations between them. **RESULTS:** The RMSSD and LF metrics effectively differentiated between the participant groups, with a p-value below the significance threshold of 0.05, as seen in Table 1. SDNN and HF are just above this threshold of 0.05, suggesting differences between groups without statistical significance. Novices exhibited notably higher values for the first four metrics in Table 1 compared to residents and surgeons, whose values are more closely aligned, indicating that, during this study, novices coped better with stress and were more relaxed. Table 2 highlights that physical exhaustion most significantly correlates

Table 2: p-value for relationship between each HRV metric and questionnaire metric

	Mental exhaustion	Physical exhaustion	Complexity	Restlessness
SDNN	0.20	0.056	0.020	0.33
RMSSD	0.35	0.036	0.89	0.71
LF	0.98	0.22	0.34	0.16
HF	0.90	0.050	0.50	0.90
LF/HF	0.60	0.028	0.51	0.27

with HRV metrics, as majority of the p-values are below or near 0.05. While complexity and SDNN show significant correlation, other HRV metrics do not correlate significantly. Mental exhaustion and restlessness are not significantly correlated with the HRV metrics.

CONCLUSION: Significant differences in the RMSSD and LF HRV metrics indicate their potential

for differentiating stress levels among varying skill levels of surgeons. Novice HRV metrics differ notably from the residents and surgeons. From the questionnaire metrics, physical exhaustion shows the most promising correlation to the HRV metrics. With continued research and additional data collection, HRV metrics will hopefully be useful as an alternative to traditional questionnaire-based measurements of stress.

ACKNOWLEDGEMENTS: The authors acknowledge the collaboration and input from the colleagues at the Department of Surgery, Transplantation and Gastroenterology at Semmelweis University, Faculty of Medicine, Budapest, Hungary.

REFERENCES:

- [1] A. Bellido, P. Ruisoto, et al., "State of the art on the use of portable digital devices to assess stress in humans," *Journal of Medical Systems*, vol. 42, no. 100, p. 0, 2018.
- [2] A. The, I. Reijmerink, et al., "Heart rate variability as a measure of mental stress in surgery: a systematic review," *International Archives of Occupational and Environmental Health*, vol. 93, no. 0, pp. 805–821, 2020.

Session 6 Talks: Cancer

Abstracts

Cisplatin prodrug-loaded microbubbles for targeted cancer therapy

Sean McGrath¹, Emma Durocher², Suresh Gadde² and Naomi Matsuura^{1,3,4}

¹Institute of Biomaterials and Biomedical Engineering, University of Toronto, ²Division of Cellular and Molecular Medicine, University of Ottawa, ³Department of Material Science and Engineering, University of Toronto, ⁴Department of Medical Imaging, University of Toronto

Introduction: Cisplatin is a common chemotherapeutic agent used for cancer treatment [1]. Despite its prevalence, systemic cisplatin injections are dose limited by its systemic toxicity [2]. Cisplatin prodrugs, consisting of the cisplatin molecule axially bound to hydrocarbon ligands, are an attractive alternative to standard cisplatin because of their lower systemic toxicity [3]. Cisplatin prodrugs have been shown to improve cisplatin uptake by increasing the lipophilicity of the drug, increasing the drugs' ability to traverse the cell membrane [3]. However, even with these improvements, systemic injections of prodrugs may still have associated dose-limiting effects. By loading cisplatin prodrugs into drug carriers for their release inside of the tumor, we can further help reduce the systemic toxicity and increase local drug uptake [4]. This project aims to create cisplatin prodrug-loaded microbubbles (MBs). Upon exposure to high pressure ultrasound, loaded MBs cavitate and can release the prodrug, resulting in targeted drug delivery. Using two different prodrugs (CisPt(octyl)₂ and CisPt(octadecyl)₂) we will synthesize loaded MBs, and confirm their echogenicity, quantify their stability and prodrug loading, and measure the prodrug cytotoxicity.

Methods: Two cisplatin prodrugs were synthesized [3], with either an 8-carbon chain (CisPt(octyl)₂) or an 18-carbon chain (CisPt(octadecyl)₂). Prodrug-loaded and unloaded MBs were synthesized with a DSPC, DPPA, and DPPE-mPEG5k shell and a perfluorobutane core. MB echogenicity was assessed at 37 °C under flow with contrast-enhanced ultrasound (Aplio SSA-790A with PLT-604AT, 6 MHz, MI = 0.05). MB size distribution and stability was tested on a Coulter Counter (20 µm aperture diluted to approximately 3x10⁶ MBs/mL, Multisizer 4e, Beckman Coulter). Prodrug loading was assessed by centrifuging at 80 RCF for 3 minutes in order to concentrate the MBs, followed by ICP-MS to evaluate Pt content. Cytotoxicity of both cisplatin prodrugs were evaluated using AE17-OVA mouse mesothelioma cells, plated 5000/well in 96-well plates and treated in an MTT assay (using regular cisplatin treatment as a baseline). Statistical comparisons between MTT assay treatment groups were performed using a one-way ANOVA at each concentration. Statistical significance of data was determined at a probability of p<0.05.

Results: MBs containing cisplatin prodrug had similar echogenicity to control MBs. CisPt(octyl)₂-loaded and CisPt(octadecyl)₂-loaded MBs had a reduction in volume concentration after 1 hour at 37°C to 49% and 57% of their original volume, respectively, as compared to 32% for unloaded MBs. CisPt(octyl)₂ MBs contained 37% ± 2% of total Pt, as compared to CisPt(octadecyl)₂ MBs containing just 12 ± 2% of total Pt. This indicates that CisPt(octadecyl)₂ may not incorporate as well into the microbubble shell as CisPt(octyl)₂. Both cisplatin prodrugs showed no significant difference from cisplatin at lower concentrations (Figure 1), however at higher concentrations CisPt(octyl)₂-loaded had significantly higher cytotoxicity (p<0.05). This increased cytotoxicity may be due to the cisplatin prodrugs having increased cellular uptake due to their lipophilicity [3].

Conclusion: MBs were successfully synthesized using CisPt(octyl)₂ and CisPt(octadecyl)₂, and showed echogenicity and stability at 37 °C. This may allow for targeted cisplatin prodrug release, allowing for a reduction in administered dose. Next steps include conducting preclinical testing, and evaluation of subcellular distribution.

References: [1] Q Yao et al., *Theranostics*. 2022;12(5):2115-32. [2] R.Y. Tsang et al., *Drug Saf.* 2009;32(12):1109-22. [3] Y. Zheng et al., *J Am Chem Soc.* 2014;136:8790-98. [4] HK Chen et al., *Cancers*. 2018;10(9):311.

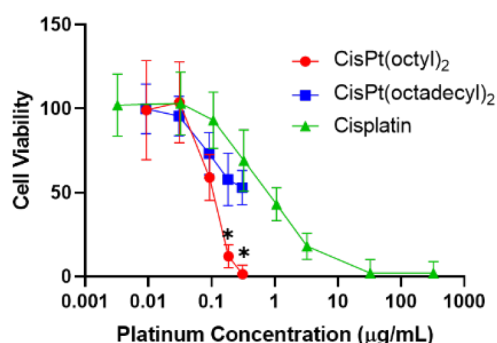


Figure 1: Cell viability with cisplatin and cisplatin prodrug treatment, measured using MTT assay (* p < 0.05).

First demonstration of arterial spin labeling on a 1.5T MR-Linac for glioblastoma perfusion dynamics

Liam S. P. Lawrence,^a Brige Chugh,^b James Stewart,^b Mark Ruschin,^b Aimee Theriault,^b Jay Detsky,^b Sten Myrehaug,^b Pejman J. Maralani,^b Chia-Lin Tseng,^b Hany Soliman,^b Mary Jane Lim-Fat,^b Sunit Das,^c Arjun Sahgal,^b Angus Z. Lau^{a,b}

a. U of T, Toronto, ON. b. Sunnybrook Hospital, Toronto, ON. c. St. Michael's Hospital, Toronto, ON.

Introduction: MRI linear accelerators (MR-Linacs) are combined MRI-radiotherapy devices that allow adaptive radiotherapy based on daily imaging. Perfusion MRI could be useful for guiding radiotherapy adaptation in glioblastoma, highly vascularized brain tumours. Knowledge of perfusion dynamics during treatment is limited,¹ but is needed for determining adaptation strategies. Hence, we developed an arterial spin labeling (ASL) protocol on a 1.5T MR-Linac for the brain. To our knowledge, this is the first report of MR-Linac ASL. The objective of this study was to characterize imaging performance and tumour perfusion dynamics.

Methods: Twenty-two glioblastoma patients received radiotherapy (dose schedule ranges: 40-60 Gy, 15-30 fractions) on a 1.5T MR-Linac (Unity, Elekta) and concurrent temozolomide (NCT04726397, NCT05565521, NCT05720078). Two healthy volunteers were also imaged. MRI scans included daily T₁-weighted (T₁w) imaging (3D MPRAGE), with weekly contrast enhancement (T₁w + C), and single-post-label-delay ASL with a calibration image 1-2 times per week (3D GRASE, TR/TE=4100/16 ms, 4×4×8 mm³ voxels, matrix size=64×64×16, 8 control-label pairs, label duration=1.8 s, post-label delay=2.0 s) (**Fig. 1A**). Thirteen patients had repeated ASL. CBF maps were calculated using Oxford_asl. Regions of interest included gross tumour volume (GTV: enhancing tumor plus surgical cavity), clinical target volume (CTV: 5 mm expansion on the GTV plus involved T₂-FLAIR hyperintensities), and automatically segmented white/grey matter (WM/GM) masks. The median and 95% quantile of CBF were calculated over each ROI. The grey matter within-subject standard deviation (wSD) for the median CBF was used as a repeatability measure. The repeatability coefficient ($RC = 2.77 \times wSD$) was used as the threshold for significant change in tumour.

Results: Median grey matter CBF across patients was lower than expected from literature (23 vs. 36.5 ml/100g/min) but its wSD was comparable (4.4 vs. 5.3 ml/100g/min).^{2,3} CBF values in tumour tended to decrease, often without structural changes (**Fig. 1B**). The 95% quantile of CBF over the CTV changed by more than $\pm RC$ for 11/13 patients with repeated ASL, indicating statistically significant changes during therapy (**Fig. 1C**).

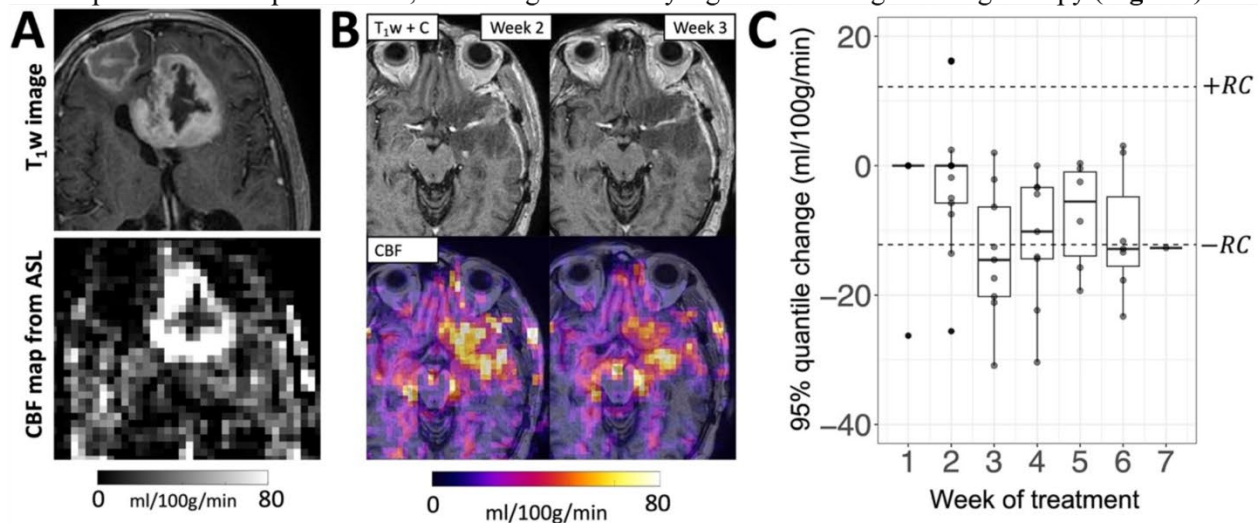


Figure 1: (A): Representative structural and ASL-CBF images. (B): Weekly ASL imaging revealed decreases in CBF during treatment without structural changes. (C): Change in 95% quantile of CBF over CTV.

Conclusions: We found regions of hyperperfusion in glioblastoma tend to decrease in CBF during treatment. The lower CBF in grey matter compared to literature should be investigated, so that MR-Linac CBF measurements can be used in longitudinal, multi-scanner studies. Comparison with ASL from a conventional MRI scanner is warranted because of MR-Linac hardware differences. MR-Linac ASL allows frequent perfusion imaging in glioblastoma, which could be used to guide adaptive, biologically targeted radiotherapy in the future.

References:

1. Zhou et al., *Tomography*, 2020. 2. Leidhin et al., *NeuroImage*, 2021. 3. Mutsaerts et al., *PLoS ONE*, 2014.

Comparison of the Localisation of Phototheranostic PORPHYSOME Nanoparticles in Rodent and Nonrodent Models of Prostate Cancer

Carl Fisher[†], Michael S. Valic[†], Mark Zheng, Celina Li, Alyssa Goldstein, Nicholas Bernards, Alexander Gregor, Abdullah El-Sayes, Jenny Ma, Lili Ding, Michael Halim, Pamela Schimmer, Juan Chen, Robert Weersink, Gang Zheng^{*}, Brian C. Wilson^{*}

Princess Margaret Cancer Centre, University Health Network, Toronto, ON, Canada

[†]Authors contributed equally to work.

^{*}Corresponding authors: Gang.Zheng@uhn.ca; Brian.Wilson@uhn.ca

Introduction

Prostate cancer (PCa) is the most prevalent cancer in men. For early-stage PCa localised to the prostate, there is growing interest in minimally invasive light-based therapies such as photothermal therapy (PTT) that can precisely target the intraprostatic lesion while sparing healthy surrounding organs from damage. Our group has previously demonstrated focal PTT ablation of PCa xenografts using phototheranostic PORPHYSOME (PS) nanoparticles with selective tumour uptake and enhanced photothermal energy conversion (Jin et al.). In the present study, we evaluate if the localisation of PS in larger, more anatomically relevant rat and canine models of orthotopic PCa exhibit similar uptake and tumour-to-prostate selectivity as observed in mice.

Methods

PS nanoparticles were physicochemically characterised for size and morphology. Models of orthotopic prostatic adenocarcinoma were established in three animal species: (1) PC-3 human xenografts in nude mice (0.025 kg), (2) syngeneic MAT-Ly-Lu rat allografts in ACI rats (0.300 kg), and (3) syngeneic ACE-1 canine allografts in immunosuppressed mongrel canines (~30 kg). For in vivo studies PS were radiolabelled with positron-emitting Copper-64 (specific activity > 3.1 MBq/mg) and injected intravenously at scaled PS doses (mg/kg). Plasma was collected for pharmacokinetic and chelation stability analyses. 24 hours post-injection the uptake in the tumour, healthy prostate, and surrounding organs was evaluated using PET/MRI, ex vivo fluorescence imaging and γ counting. Fluorescence microscopy of frozen tissue sections was also performed.

Results

The plasma pharmacokinetics of PS in all three models were similar. Mice had the highest weight adjusted volume of distribution (184 mL/kg) and clearance (8.9 mL/h·kg) whereas canines had the lowest values (62.9 mL/kg, 3.0 mL/h·kg). The circulatory half-life of PS was 14~19 hours in all three animal species. PS uptake in the prostate tumour 24 hours post-injection was *highest* in the ACE-1 canine model (2.46 SUV), followed by the MAT-Ly-Lu rat model (2.27 SUV) and PC-3 mouse model (1.23 SUV). However, when compared to PS concentration in the healthy prostate, the tumour-to-prostate selectivity of PS was *lowest* in the canine model (1.35 ratio) and highest in the rat (3.75 ratio) and mouse (5.71 ratio) models. Fluorescence microscopy of PS localisation in MAT-Ly-Lu rat tumours confirmed selective uptake of PS in tumour cells along the lesion margin, whereas fluorescence imaging of cross-sections of ACE-1 canine tumours revealed unexpectedly high uptake by the healthy prostate gland not observed in the prostates of rats or mice.

Conclusion

PS demonstrated unexpected variability in tumour uptake and tumour-to-prostate selectivity depending on the type of PCa model used: mouse and rat models exhibited the most favourable tumour selectivity whereas the canine model did not. Which of these three preclinical models of orthotopic PCa will be most predictive of PS localisation (and responses to PS-PTT treatments) to human disease remains to be seen.

Reference

Jin, Cheng S., et al. "Nanoparticle-Enabled Selective Destruction of Prostate Tumor Using MRI-Guided Focal Photothermal Therapy: Porphysome Enabled MRI-Guided Focal Photothermal Therapy." *The Prostate*, vol. 76, no. 13, Sept. 2016, pp. 1169–81. <https://doi.org/10.1002/pros.23203>.

Analyzing the effect of neoadjuvant stereotactic ablative radiotherapy (SABR) on pancreatic tumour perfusion using computed tomography perfusion (CTP)

Bang JY^{1,2}, Gaede S^{1,2}, Lee TY^{1,3}

¹Department of Medical Biophysics, Western University

²London Regional Cancer Program

³Robarts Research Institute

Introduction: Currently, surgical resection is the sole curative option for pancreatic cancer. Unfortunately, surgery is only feasible if a patient is deemed resectable, which means that the cancer is nonmetastatic, well-localized, and has minimal involvement of the critical blood vessels around the primary tumour. Eligible patients with poor surgical prognosis due to the involvement of the surrounding vasculature, also known as the borderline resectable patients, often undergo presurgical or neoadjuvant therapy (NAT), such as neoadjuvant chemotherapy, to help reduce the tumour volume and downstage the tumour conditions for better surgical outcome. However, the highly limited blood perfusion to the pancreatic tumour still poses a significant challenge as it restricts the delivery of systemic cancer drugs to the tumour site. Recently, clinical studies in liver and rectal cancer have demonstrated the feasibility of administering hypofractionated radiotherapy to increase tumour perfusion shortly after treatment. An emerging form of radiotherapy known as stereotactic ablative radiotherapy (SABR) is one such technique, which can precisely deliver high doses of radiation in only 3~5 fractions with the guidance of an integrated imaging system. However, there remains a lack of studies investigating the effect of such high-dose radiotherapy specifically on pancreatic tumour perfusion. Therefore, the objective of this preliminary study was to analyze the effect of neoadjuvant SABR on pancreatic tumour perfusion using computed tomography perfusion (CTP).

Methods: Adults aged 18 or older with histologically confirmed primary pancreatic cancer were prospectively recruited on the basis of informed consent and medical fitness for surgical resection. The recruited patients were divided into 2 study arms based on the degree of involvement of the critical vessels around the tumour volume: resectable (n = 1) and borderline resectable patients (n = 6). All patients underwent neoadjuvant SABR with a prescription dose to the planning target volume (PTV) ranging between 27~30 Gy in 3 fractions. A dose boost of up to 45 Gy was also given to the metabolically active areas of the tumour site indicated by positron emission tomography (PET). For perfusion analysis, computed tomography perfusion (CTP) images of the abdominal region were acquired using the GE HealthCare Revolution CT scanner (GE HealthCare, Chicago, USA) with a z-axis coverage of 16 cm. Images were acquired from patients in both arms at multiple instances over the course of their treatment: a) at baseline; b) 6 hours after administering the first fraction of neoadjuvant SABR; and c) 4 weeks after completing SABR, prior to surgical resection. For the borderline resectable patients, images were also taken after neoadjuvant chemotherapy (FOLFIRINOX). From the CTP images acquired at each study instance, an in-house, deconvolution-based CTP software was used to generate perfusion maps of hemodynamic parameters including blood flow (F), blood volume (V), and the permeability surface area product (PS). For quantitative analysis, circular regions-of-interest (ROIs) were drawn over the delineated pancreatic tumour volume, and the area-weighted mean value was calculated for each parameter.

Results: Preliminary CTP analysis of the first borderline resectable patient showed that, relative to baseline values (F = 27.00 mL/100g/min; V = 3.14 mL/100g; PS = 8.83 mL/100g/min), there was a marked increase in tumour perfusion after neoadjuvant chemotherapy (F = 62.00 mL/100g/min; V = 11.75 mL/100g; PS = 20.87 mL/100g/min) and 6 hours after delivering the first fraction of neoadjuvant SABR (F = 58.57 mL/100g/min; V = 11.83 mL/100g; PS = 22.13 mL/100g/min). Tumour perfusion was also well maintained at 4 weeks after the completion of neoadjuvant SABR (F = 65.57 mL/100g/min; V = 10.14 mL/100g; PS = 26.27 mL/100g/min). In the resectable arm, an increase in tumour BF and BV could be observed at 6 hours after the delivery of the first SABR fraction relative to baseline (F = 109.99 vs 83.50 mL/100g/min; V = 19.13 vs 17.06 mL/100g), which was also maintained at 4 weeks post-SABR. However, no significant change in the PS could be observed.

Conclusion: While these observations have yet to be verified with additional CTP data from the recruited patients still undergoing treatment, preliminary evidence from the patients enrolled to date demonstrates that neoadjuvant SABR may be a feasible option to induce a transient increase in pancreatic tumour perfusion; thus, opening a window of opportunity to overcome tumour chemoresistance by enhancing the delivery of further systemic NAT to the tumour site.

Session 7 Pitches: Device, Hardware, Software Development

Abstracts

Deep Learning-Enabled 3D Fluorescence Imaging for Surgical Guidance: Identifying Tumor Margins

Natalie Won,¹ Mandolin Bartling,² Jerry Wan,¹ Christina Negus,¹ Stephanie Markevich,¹
Alon Pener-Tessler,² Esmat Najjar,² Brian C. Wilson,¹ Jonathan C. Irish^{1,2} and Michael J. Daly¹

¹Princess Margaret Cancer Centre, University Health Network, Toronto ON

²Department of Otolaryngology – Head & Neck Surgery, University of Toronto

Introduction: Accurate identification of 3D tumor margins remains a challenge during surgical interventions.¹ Current 2D fluorescence-guided surgery systems provide precise lateral margin delineation at the tissue surface (“width”), yet there remains a need for quantification of the sub-surface superior and inferior margins of tumors (“depth”). To address this, our group is developing a custom deep learning (DL)-enabled 3D fluorescence system to provide depth and fluorescence concentration maps. Here, we assess performance in two classes of simulated tumors: i) (Fig. a) the bottom surface of mucosal “iceberg” tumors (e.g., oral, colon); and ii) (Fig. b) the top surface of submerged “submarine” tumors (e.g., breast, brain).

Methods: The optical device uses spatial frequency domain imaging (SFDI) that projects structured light to capture depth information and tissue optical properties. Spatial-frequency fluorescence images (FL) and optical properties (OP) are inputs to an adapted convolutional neural network architecture (Fig. c).² The network performs a series of convolutions (Activation Function: ReLU) for each arm of the network (OP: $3 \times 2DConv$; FL: $1 \times 3DConv$ and $2 \times 2DConv$), the data is concatenated and subsequently downsampled ($3 \times 2DConv$) to produce depth and concentration maps. The architecture (920,642 parameters) is trained with two separate datasets of 10,000 synthetic tumors to create two DL models. Synthetic tumors are generated with composite spherical harmonics: 4 spherical harmonics of randomly generated order, degree, and radius are merged and undergo multiple transformations to create a diverse dataset (widths=10–40mm, depths=1–10mm). The first dataset includes “iceberg” tumors and the second adds a random shift factor to create “submarine” tumors. Both datasets are passed to a numerical diffusion-theory-based light propagation model to produce synthetic FL and OP for DL training (8.6 hours, AWS SageMaker, ADAM optimizer). DL models are tested (<1s) with two sets of 9 patient-derived tumors (depths=1–10mm): tumors shifted to be “iceberg” (n=9) and “submarine” (n=9×10 (translate: 1-10mm)).

Results: (Fig. d) The DL model assessing the deep margin of “iceberg” tumors had a depth and concentration error of 0.82 ± 1.12 mm and 0.39 ± 0.63 $\mu\text{g/mL}$. (Fig. e) The DL model assessing the superior margin of “submarine” tumors had a depth and concentration error of 1.01 ± 2.09 mm and 1.36 ± 1.55 $\mu\text{g/mL}$.

Conclusions: The custom DL model architecture is multipurpose and can be implemented to detect both the inferior and superior margins of “iceberg” and “submarine” inclusions. These initial results indicate that synthetic tumors capture the complex geometries of both “iceberg” and “submarine” patient tumors. Future studies will employ optical phantoms to assess imaging system performance with experimentally collected data.

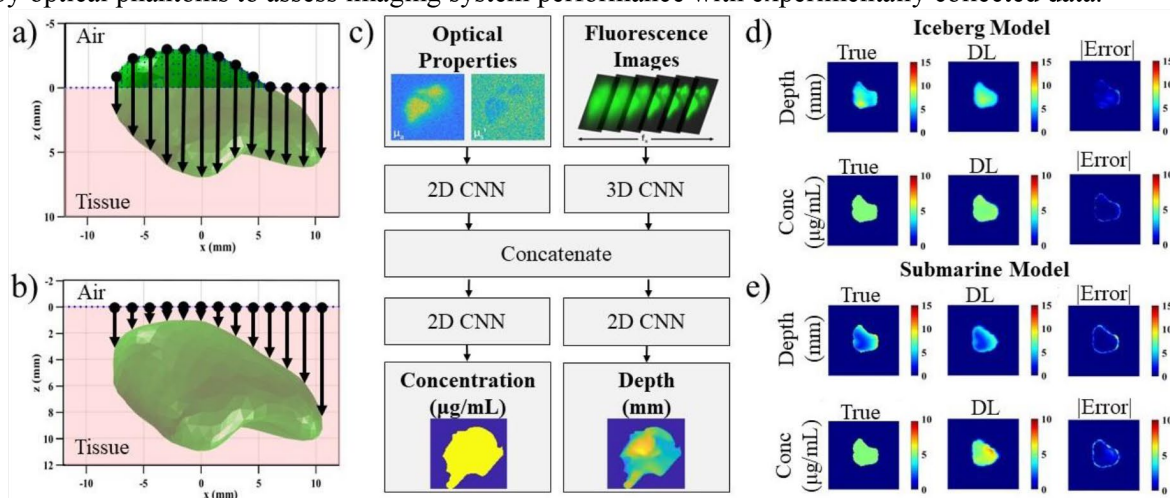


Figure. Testing DL models with surface and submerged *in silico* patient-derived tumors. (a) “Iceberg” tumor. (b) “Submarine” tumor. (c) DL architecture. (d) “Iceberg” DL results. (e) “Submarine” DL results.

References: 1. Orosoco et. al., Sci Reports 2018. Positive Surgical Margins in the 10 Most Common Solid Cancers.
2. Smith JT et. al., Opt Lett. 2020 45(15):4232-4235.

SlicerTrack: an open-source extension to 3D Slicer for target displacement visualization

HaPhan Tran, Teo Mesrkhani, Jacqueline Banh, Nicholas Caro Lopez, Venkat Guru Prasad, Elodie Lugez
Toronto Metropolitan University

Introduction: Dynamic sequential medical resonance (MR) images (cine images) are extremely valuable for tracking clinical targets, such as in image-guided therapy. 3D Slicer is widely employed by the medical image computing community because it offers a wide range of functionalities through its base installation and modules, and it allows researchers to contribute their extensions. However, 3D Slicer does not have built-in functionalities capable of visually verifying target tracking results, causing users to manually inspect and verify each frame. To further the functionalities of 3D Slicer, the SlicerTrack extension facilitates visual validation of the computed displacements of a region of interest (ROI) via the corresponding cine images and its 3D segmentation.

Methods: 3D Slicer's Python application programming interface (API) was utilized for the extension's development. The graphical user interface (GUI) was developed using Qt in combination with the API. The extension was developed to replay cine images, and overlaying the outline of the ROI at its respective position. The target displacement results were computed using the method proposed by Keiper et al. [1]. SlicerTrack's performance was assessed by timing cine image batch uploads to 3D Slicer. The tests were conducted three times and averaged for reliability using a macOS Sonoma 14.2.1 Operating System with an Apple M2 CPU (3.00 GHz, 8-core) and 16 GB RAM.

Results: SlicerTrack accepts three unique inputs from the user: a set of cine images, a 3D segmentation of the ROI, and transformation data. To track the ROI, the extension goes through the series of cine images and overlays the 3D segmentation on the current image at a position determined on the transform file (Figure 1). SlicerTrack accepts various file formats. Furthermore, users can adjust the playback speed, jump to desired frames, and adapt the overlay opacity. The average load times for 100 images (43KB each) is 1.47s, 12.86s for 1,000 images, and 136.98s for 10,000 images. The extension is publicly available on GitHub [2].

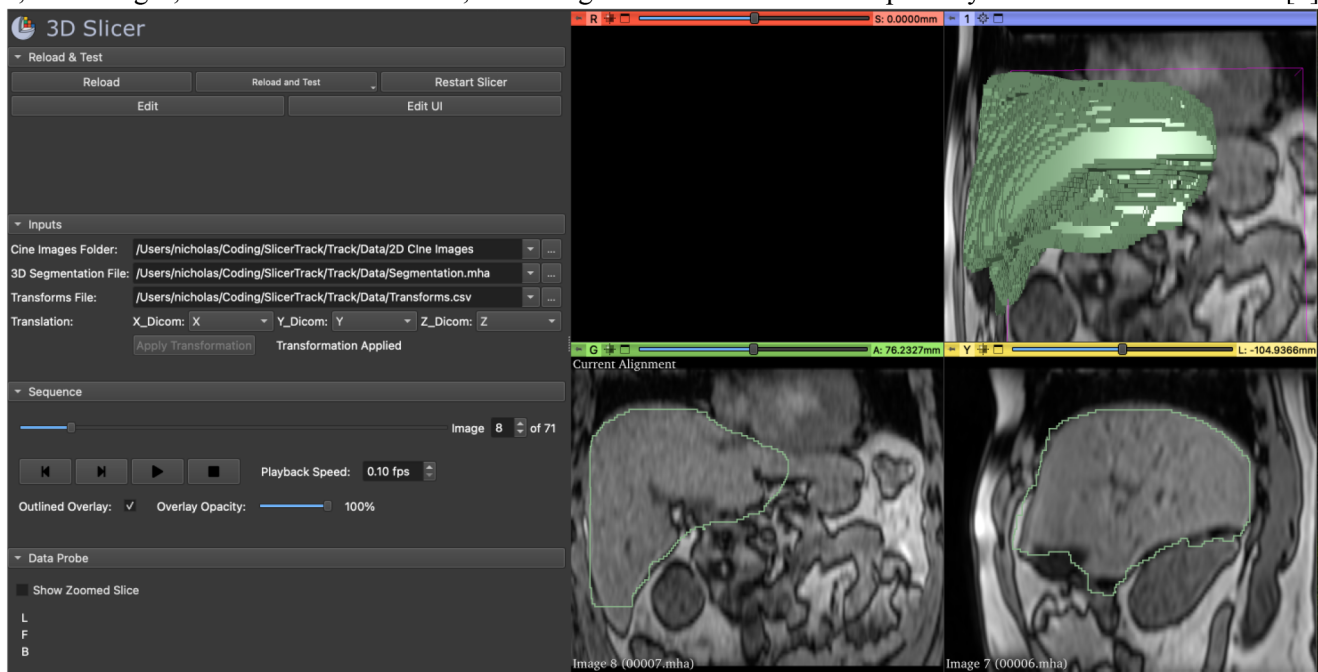


Figure 1: SlicerTrack playback – the ROI outline, shown in green, is overlaid on cine images

Conclusion: SlicerTrack is an open-source extension to 3D Slicer that offers the medical field a convenient tool for visualizing the ROI displacement. SlicerTrack simplifies the process of validating algorithms for ROI tracking on cine images and simplifies tasks that were previously time-consuming and labor-intensive. Future studies will focus on user evaluation for the extension.

Acknowledgments: The authors would like to acknowledge the direct and indirect aid of the following people – James McCafferty, Fabyan Mikhael, Mubariz Afzal – in the development of SlicerTrack

References:

[1]: Keiper et al. Motion tracking with cine MRI (2020) [2]: <https://github.com/laboratory-for-translational-medicine/SlicerTrack> (2023)

Development of an Internal Mammary Artery Phantom for Training in Harvesting Procedures

Olivia Qi^{1,5}, John Moore⁵, Shuwei Xing^{4,5}, Joeana Cambranis Romero^{4,5}, Gianluigi Bisleri⁷, Terry Peters^{2,3,4,5}, Elvis C.S. Chen^{1,2,3,4,5}

Department of Medical Science¹, Department of Electrical and Computer Engineering², Department of Medical Imaging³, School of Biomedical Engineering⁴, Robarts Research Institute⁵, Department of Medical Biophysics⁶, St. Michael's Hospital⁷, Western University, London, Ontario, Canada

Introduction: The scarcity of cadaver resources for Coronary Artery Bypass Graft surgery training has prompted the development of a low-fidelity Internal Mammary Artery (IMA) simulator.¹ A PolyVinyl Alcohol cryogel (PVA-c)-based phantom is a good candidate to aid IMA harvesting practice for medical professionals, as it replicates various tissue properties. Therefore, our objective is to create a PVA-c phantom with realistic IMA tissue properties, that is, to achieve different tissue stiffness by conducting different FTC using PVA-c. Our phantom mimics IMA, fat, and fascia layers, validated through shear wave elastography (SWE) to measure stiffness in kilopascals (kPa).^{2,3}

Methods: Firstly, a mold was designed and 3D- printed using polylactic acid (PLA). PVA-c gel (10% by weight) was cooked from the crystal form. Secondly, Fascia and IMA, undergoing the same

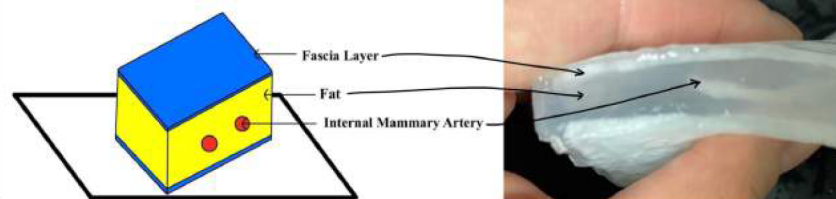


Fig.1. Cross section of the IMA phantom, components are labeled as above.

freeze thaw cycles (FTC), were prepared before assembling fat proportions. Fascia mold was poured with 1-2 mm of gel, while the IMA mold was filled using a syringe, they underwent FTC cycles. Thirdly, after creating two fascia and one IMA with this FTC, a final mold is assembled in the sequence of fascia, PVA-c gel, IMA, PVA-c gel, and fascia; the PVA-c gel served as the fat in the end product, shown in Fig. 1. Finally, phantom validation was conducted in three trials using ultrasound (Canon Aplio i700, Tokyo Japan) shear wave elastography. Human tissue served as a control, and the evaluation was on PVA-c IMA/Fascia and PVA-c fat tissue samples. The i8CX1 probe (center frequency = 4 MHz) was used at a rate of 20 fps, measuring elasticity and propagation using the map type. The Twin-view function, which enables both B-mode and color Doppler to be side by side, was employed for accuracy, guiding a stable heatmap and capturing data in regions with parallel shear waves.³

Results: The mean values of tissue stiffness, measured in kPa, for three trials are presented in Fig. 2. Specifically: Human IMA/Fascia sample(A): 15.03 ± 1.83 kPa, PVA-c IMA/Fascia sample (B): 15.8 ± 3.9 kPa, c) Human fat sample (C): 8.43 ± 3.33 kPa, and PVA-c fat sample (D): 8.67 ± 2.3 kPa.

Conclusion: SWE results preliminarily demonstrate our IMA phantom's tissue properties, particularly the stiffness, closely match human tissue, showing the potential of our simulator to enhance IMA harvesting practice. In addition, this underscores cost-effectiveness and enhances accessibility for effective training.

References: [1] Mohammadi H. et al., "Simulation of Anastomosis in Coronary Artery Bypass Surgery". Cardiovasc Eng Technol, Dec 2016. [2] Culjat M. O. et al., "A Review of Tissue Substitutes for Ultrasound Imaging", Ultrasound in Medicine & Biology, 2010. [3] Taljanovic M. S. et al., "Shear-Wave Elastography: Basic Physics and Musculoskeletal Applications". Radiographics, May 2017.

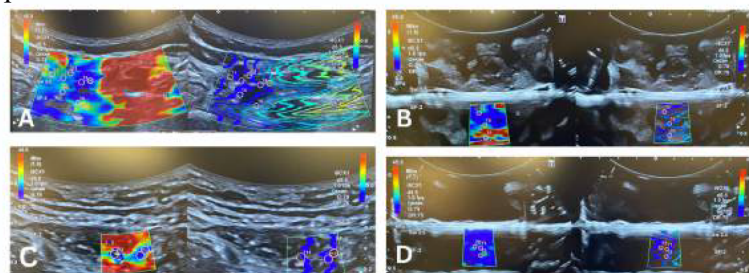


Fig.2. SWE on tissue samples. A is the Human IMA sample, B is the PVA-c IMA sample, C is the Human Fat sample, and D is the PVA-c Fat sample. A and B were compared to each other. C and D were compared to each other.

3D printing prosthetics on the Thailand-Myanmar border

Olivia Radcliffe¹, A. Tun², N. Chan², L. Connolly¹, T. Ungi¹, K. Thornton², C. Davison¹, E. Purkey¹, P. Mousavi¹, G. Fichtinger¹

¹Queen's University, Kingston, Canada, ²Burma Children Medical Fund, Mae Sot, Thailand

INTRODUCTION: 3D printing has revolutionized the field of prosthetics, making it possible to create customizable and affordable prosthetic limbs for patients with limited financial and healthcare resources. With the help of computer-aided design (CAD) software, 3D printers can produce prosthetic limbs tailored to the specific needs and measurements of the individual. The ongoing civil war in Myanmar (Burma) has caused millions of people to flee, with an estimated 1.9 million registered migrant workers in Thailand [1]. Burma Children Medical Fund (BCMF, www.burmachildren.com), a non-governmental organization in Mae Sot, Thailand, created a team to provide 3D-printed prosthetics and address the lack of access to medical resources and traditional prostheses for Burma citizens, as well as migrants and refugees living in Thailand. They focus on printing upper limbs for individuals affected by congenital birth defects, and those who lost limbs due to disease, injury, or weapon-wounding. Despite the progress 3D printing has made for those without previous knowledge of prostheses, the outcome relies heavily on open-source designs or experience with CAD software. BCMF faces challenges involving access to CAD training for staff, accurate fitting, and gaps in the availability of open-source prosthetics. One gap is in prosthetics for individuals with short below-elbow residual limbs. Existing open-source models are insufficient and slip off when bending their arms. In this paper, we address this gap in open-source prosthetics, our partnership with BCMF, and some of our ongoing efforts to address the challenges with 3D printing prosthetics for underserved people on the Thai-Myanmar border.

METHODS: BCMF's current prostheses workflow entails downloading a 3D prosthetic model from open-source software (Thingiverse, www.thingiverse.com), then measuring the patient, adjusting or scaling the model, printing, assembling, fitting, and offering rehabilitation. BCMF provided many patients with 3D-printed prosthetic arms across Thailand and Myanmar before our partnership, but some limitations had to be addressed. Specifically, we created a process for generating a prosthetic for short below-elbow residual limbs without disrupting the existing workflow, techniques, and materials used at BCMF. We solved this problem by directly editing BCMF's most-used prosthetic limb model. Training and workshops were coordinated with the staff to familiarize them with CAD software. The overarching technical challenge, securing the prosthetic on a short below-elbow residual limb, was then addressed by editing the model to utilize the elbow epicondyle bones, a technique from traditional prostheses. Furthermore, with a POP 3D scanner (www.revopoint3d.com), we generated a 3D model of a patient's limb (Fig. 1) and visually overlaid the prosthetic and residual limb. We use OpenSCAD to create a user-friendly customization process (Fig. 2) for the open-source community and BCMF since patient measurements can be easily inputted for sizing and different features can be selected.

RESULTS: The resulting prosthetic model was suitable for recipients with short below-elbow residual limbs and modifiable for varying patient sizes and requirements. We found the POP 3D scanner, accompanied by manual measurements, contributed to a more accurate fit and reduced the number of reprints. To date, 4 patients use this prosthetic with satisfaction (Fig. 3). The BCMF team has solidified the workflow and fabrication process for continued use.

CONCLUSIONS: We continue to optimize our short below-elbow design, streamline the customization process, and send volunteers. This work highlights the importance and impact of partnership and knowledge mobilization to address pressing clinical needs amidst an ongoing humanitarian crisis.

REFERENCES: [1] The Myanmar Development Observatory (MDO). (2023, November 30). *Seeking opportunities elsewhere: Exploring the lives and challenges of Myanmar migrant workers in Thailand*. UNDP. <https://www.undp.org/myanmar/publications/seeking-opportunities-elsewhere-exploring-lives-and-challenges-myanmar-migrant-workers-thailand>

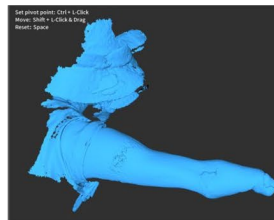


Fig 1: 3D scan of patient's short below-elbow residual limb.

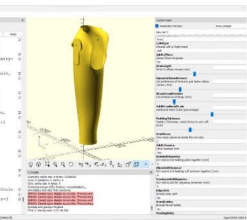


Fig 2: 3D prosthetic model in OpenSCAD.



Fig 3: Left: Printed short below-elbow prosthetic. Right: Recipient testing their fitted prosthetic.

Machine Learning-Enhanced Mass Spectrometry Imaging for Perioperative Tissue Characterization

Jade Warren, A. Jamzad, T. Jamaspishvili, R. Iseman, A. Syeda, M. Kaufmann,
J. Rudan, G. Fichtinger, D.M. Berman, P. Mousavi
Queen's University, Kingston, ON, Canada

INTRODUCTION: Surgical excision is an integral part of cancer treatment, demanding precise removal of cancer while conserving as much healthy tissue as possible. However, identification of cancer at the time of surgery can be challenging, and cancer remaining postoperatively results in an increased risk of recurrence and secondary treatment [1]. One possible way to differentiate cancer and benign tissue is by analyzing the distribution of lipids and metabolites, as changes in metabolism are indicative of cancer [1]. Desorption electrospray ionization mass spectrometry imaging (DESI-MSI) is a molecular imaging technique that facilitates rapid and sensitive metabolomic profiling of tissue samples [2]. Compared to histopathology assessment of surgical margins, utilizing machine learning (ML) models for tissue classification based on ion signals in metabolomic profiles is unbiased and has a much quicker processing time. To demonstrate how ML optimizes DESI-MSI metabolic profiling for perioperative tissue characterization, this study analyzes prostate biopsies obtained from prostates removed by prostatectomy.

METHODS: Fourteen prostate biopsy cores from fourteen patients were analyzed. Mass spectral data was visualized using Principal Component Analysis (PCA) imaging, highlighting metabolomic differences through ion signals. Histopathology images (Fig. 1., top and middle), were registered with PCA visualizations using fiducial markers for similarity registration.

This registration provided visual guidance from pathology for precise annotation of tissue classes, enabling spatially selective labelling of pixels by tissue type. Ion signals from selected segments formed a mass spectral dataset, which was compiled and aligned across all samples, and then normalized on the total ion current. Upon balancing and refining the dataset to include only cancer, benign and stroma-labelled pixels, it yielded 13,205 spectra, allowing for binary classification of cancer vs benign/stroma. It was then divided into a training set of ten samples and a test set of four. A PCA and linear discriminant analysis model trained on this dataset was assessed for its precision in distinguishing cancer from non-cancer tissue on the unseen test set.

RESULTS: The test set results indicate a balanced accuracy of 0.92 in binary classification (cancer vs. benign/stroma), with 0.96 accuracy in correctly classifying cancer observed across four samples (Table 1). When deployed on mass spectra data of a single sample in the test set, the model generated a qualitative visual representation of its class predictions. The colour map (Fig. 1, bottom) illustrates the model's class predictions for cancer, stroma and benign tissue regions, aligning closely with histopathology (Fig 1, middle).

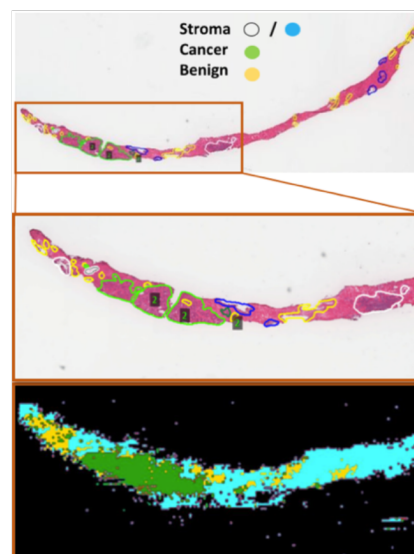


Fig. 1. Top: histopathology of prostate biopsy core. Middle: magnification of the cancerous region (green contour line.) Bottom: ion colour map showing stroma, cancer and benign tissue regions generated from the model's prediction on a test sample.

		Predicted	
		Cancer	Benign/Stroma
Actual	Cancer	0.96	0.04
	Benign/Stroma	0.10	0.90

CONCLUSIONS: ML's precise cancer characterization provides clinical benefits, enhancing perioperative surgical margin assessment and overall resection outcomes. Beyond this prostate dataset, optimizing metabolomic profiles will further improve the surgical treatment of cancer. Future studies can address sample size constraints by training on larger datasets with increased variation. Additionally, studying cancer grading is an avenue for further investigation.

REFERENCES: [1] Hanahan D. "Hallmarks of Cancer: New Dimensions." *Cancer Discov.* Jan. 2022. [2] Hu H, Laskin J. "Emerging Computational Methods in Mass Spectrometry Imaging." *Advanced Science*, 2203339. Oct. 2022.

Low-cost x-ray exposure meter for low-resource settings

Peter Fleming,¹ Lee D. Sikstrom,^{2,3} Joseph Umoh,² Ian A. Cunningham,³ William Wasswa,⁵ David W. Holdsworth^{1,2,3,4}

¹Dept. of Engineering, ²Robarts Research Institute, ³Dept. of Medical Biophysics, Schulich School of Medicine and Dentistry, ⁴Dept. of Surgery, Schulich School of Medicine and Dentistry, Western University and Dept. of Biomedical Sciences and Engineering, ⁵Mbarara University of Science and Technology, Mbarara Uganda

Introduction: Digital radiographic imaging systems are becoming more widely deployed in low-resource settings, potentially reducing the inequitable access to medical imaging that persists today. Even when resources are made available to install digital x-ray equipment, challenges remain with respect to ongoing maintenance and recommended quality assurance programs. Recent studies have indicated that a significant fraction of radiographic installations in Africa are not assessed at recommended intervals due to the lack of high-cost x-ray exposure meters. As a result, errors in x-ray exposure parameters (*e.g.* current, exposure time, or kilovoltage) can lead to suboptimal image quality, repeated exams, and unnecessary radiation exposure to patients and staff. Our hypothesis is that contemporary low-cost electronics can be used to fabricate and calibrate an x-ray exposure meter for routine quality assurance programs in low-resource settings.

Methods: We have developed a low-cost solution for routine x-ray quality assurance measurements, which takes advantage of commercial-off-the-shelf (COTS) components integrated with a low-power microprocessor controller. The design is adapted from earlier work for mammography quality assurance (1,2). The device employs four sensitive phototransistors (TEMT6000) connected to a multiplexed 16-bit analog-to-digital converter (ADS1115) with software-selectable gain, resolution and acquisition rate. Light input to the optical sensors is provided by a rare-earth phosphor screen (Lanex regular), which emits green light primarily near 550 nm under exposure to x-rays. The fastest acquisition rate (860 Hz) is used to interrogate the sensor channels and facilitate estimation of x-ray spectral properties (such as half-value layer). Estimation of spectral properties is enhanced by the use of filters on three of the four photosensors: two with different thicknesses of aluminum, and one with 0.025mm equivalent thickness of tungsten. Acquisition is controlled by an open-source microprocessor (Arduino Nano 33 BLE) with capabilities for wireless data transmission. The total cost of all components is less than \$100 USD.

Results: The sensor and phosphor were sealed in a light-tight housing to keep out all ambient light, after initial tests showed a substantial amount of light was able to penetrate the outer case. X-ray exposures tests were implemented with a clinical diagnostic radiography unit (Carestream DRX Evolution) over tube potentials from 60 to 140 kVp. At a constant kVp there is a consistent linear relationship between exposure levels and analog-to-digital unit (ADU) values produced by the TEMT sensor. Comparisons against a calibrated commercial exposure meter (ThinX Rad, RaySafe) indicate that the optical-based measurements of x-ray exposure are linear and accurate to within $\pm 3\%$, over the range from 60 to 140 kVp.

Conclusions: This project demonstrates the feasibility of providing accurate, robust solid-state x-ray exposure meters in low-resource settings. In the future, novel machine learning algorithms (such as random forest) will be developed to estimate x-ray spectral properties from the multi-channel optical data.

References:

1. M. Gambaccini, M. Marziani, and O. Rimondi, "A fast non-invasive beam check for mammography X-ray units," *Physics in Medicine and Biology*, vol. 39, no. 9, pp. 1423–1435, 1994.
2. M. Gambaccini, M. Marziani, and O. Rimondi, "Radiation probe for indirect evaluation of the high-voltage waveform of a Mo anode mammography unit," *Medical Physics*, Vol. 16, no. 1, pp 94–97, 1989.

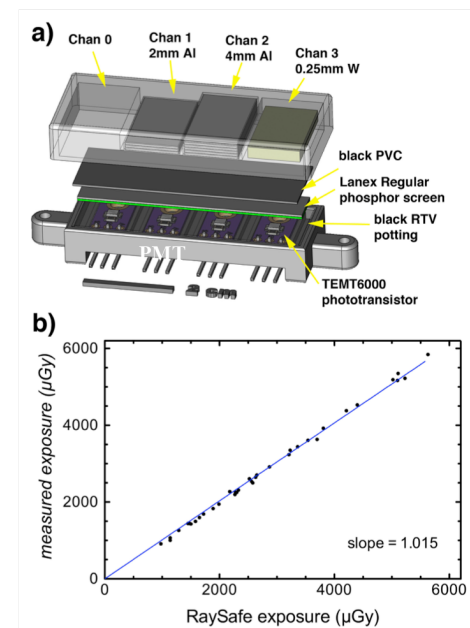


Figure 1: (a) schematic design of the x-ray exposure sensor components, (b) measured exposure vs known exposure (μGy) over a range of exposure rates.

Modifying Radix Lenses to Survive Low-Cost Sterilization: An Exploratory Study

Emese Elkind¹, K. Barr¹, C. Barr¹, K. Moga², T. Garamvolgy², T. Haidegger², T. Ungi¹, G. Fichtinger¹

1. Queen's University, Kingston, Canada 2. Obuda University, Budapest, Hungary

INTRODUCTION: A major challenge with deploying infrared camera-tracked surgical navigation solutions, such as NousNav [1], in low-resource settings is the high cost and limited availability of disposable retroreflective infrared markers. Developing an accessible method to reuse and sterilize retroreflective markers could lead to significant increase in the uptake of tracked surgical navigation. Since none of the known infrared markers can endure standard autoclaving and many healthcare settings do not have access to gas sterilization, attention is focused on cold liquid sterilisation methods. These are commonly used for laparoscopy instruments and other optical tools that cannot be sterilized in a conventional autoclave.

METHODS: Radix lenses are uniquely promising candidates for liquid sterilization given their smooth, spherical surface making them easier to sterilize perioperatively compared to other retroreflective infrared marker designs. Initial experiments show that liquid sterilization agents degrade the marker's retroreflective gold coating (Fig. 1). Hence the objective of this project is to develop a method to protect the Radix Lenses with a layer of coating material that does not allow the sanitizing agent to degrade the reflective gold coating. The goal is to enable the lens to survive multiple sanitation cycles while retaining sufficient tracking accuracy. We tested two cold liquid sterilisation agents, household bleach which is a common ingredient of most liquid sterilisation solutions and

Sekusept™ Aktiv (Ecolab, Saint Paul, MN, USA), well-known for sterilizing laparoscopy instruments. Store-bought nail polish (Essie, L'Oreal Group) and Zink-Alu Spray were used as low-cost, proof-of-concept materials to coat the lenses. Data were obtained by recording five tests each with five rounds of sterilization, each tested with six trials, for a total of 150 recordings. The five tests with Radix lenses were as follows: 1) coated with nail polish and bleached, 2) uncoated and bleached, 3) coated with nail polish and Sekusepted, 4) uncoated and Sekusepted, and 5) coated with Zink-Alu Spray and Sekusepted. To assess the impact of the sterilization on the lens's fiducial localization error, two metal marker frames equipped with four Radix lenses each were used. The reference marker frame was secured to a flat table while the other marker frame moving a fixed path on the table. Marker clusters position and orientation were streamed into 3D Slicer using the Public Library for Ultrasound Toolkit (PLUS). A plane was then fitted to the recorded marker poses in 3D Slicer using Iterative Closest Point and the marker registration error (RMSE) was computed. Distance from the camera, angle of view, and distance from the edges of the field of view were constant throughout the experiments.

RESULTS: With each round of sterilization, the error of coated lenses was lower than the unprotected lenses, showing a slightly increasing trend (Fig. 2). For the intended application of this sterilization paradigm submillimeter error is deemed sufficient. With each additional round of sterilization, the lenses appeared fainter in the tracking software while all lenses remained trackable and visible despite the degradation of reflective coating.

When the reflective coating was fully rubbed off the lenses, the tracking software could still localize the markers; however, the lenses did appear significantly fainter in the tracking software. We observed that the reflective coating rubs off the lens in routine handling, and recoating with Zink-Alu spray can partially restore marker visibility. Using protective nail polish coating prevented the reflective coating from rubbing off altogether.

CONCLUSIONS: This exploratory study represents a uniquely promising step toward achieving low-cost sterilization of retroreflective infrared markers. We propose to modify the NDI Radix™ Lens [1], single-use retroreflective spherical marker manufactured by Northern Digital, Waterloo, Canada. Further studies with the NousNav system are needed to assess the extent of degradation in tracking accuracy is tolerable as a side effect of marker sterilization. A wider evaluation of existing biocompatible options for optical coatings will also be completed to determine the most effective material that can be used safely.

REFERENCES: [1] NousNav: A low-cost neuronavigation system for deployment in lower-resource settings, International Journal of Computer Assisted Radiology and Surgery, 2022 Sep;17(9):1745-1750. [2] NDI Radix™ Lens (<https://www.ndigital.com/optical-measurement-technology/radix-lens/>)

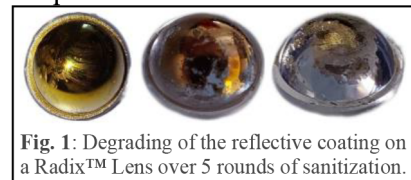


Fig. 1: Degrading of the reflective coating on a Radix™ Lens over 5 rounds of sanitization.

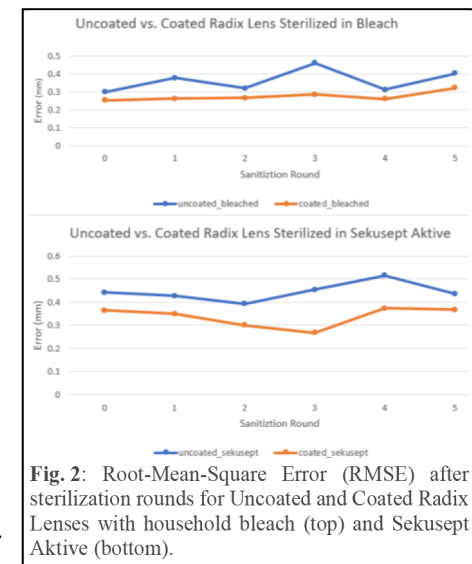


Fig. 2: Root-Mean-Square Error (RMSE) after sterilization rounds for Uncoated and Coated Radix Lenses with household bleach (top) and Sekusept Aktiv (bottom).

Advancing Medical Imaging on the Web: Integrating High Throughput JPEG 2000 (HTJ2K) in Cornerstone3D for Streamlined Progressive Loading and Visualization

Bill Wallace^{1,2}; Alireza Sedghi^{1,2}; Joe Boccanfuso^{1,2}; Leonardo Campos^{1,2}; Erik Ziegler^{1,3}; James Hanks^{1,3,4}; Daniel Rukas^{1,4}; Trinity Urban¹; Rob Lewis^{1,2}; Chris Hafey^{1,5}; Gordon J. Harris^{1,3,4}

1) Open Health Imaging Foundation, 2) Radical Imaging LLC, 3) Yunu Inc. 4) Massachusetts General Hospital
5) Amazon Web Services

Introduction: Digital Imaging and Communications in Medicine (DICOM) is the global standard for medical imaging, preferred over simpler formats like NIFTI and NRRD due to its compatibility with clinical practices and PACS systems. It supports multiple compression techniques, notably JPEG 2000, known for high compression and progressive transmission but limited by its computational demands, especially in streaming and decoding high-resolution images. Addressing these challenges, the DICOM Standards Committee introduced High Throughput JPEG 2000 (HTJ2K) in December 2023, significantly boosting processing speed while retaining the essential features of JPEG 2000. **Methods:** Cornerstone3D (CS3D <https://www.cornerstonejs.org/>) is a comprehensive and lightweight JavaScript library designed for visualizing and manipulating medical images on the web. The image rendering in CS3D traditionally fetched every image completely using an HTTP request, then decoded the entire image. For multi planar reconstructions (MPR), this was done across a 3D volume for every slice, displaying each slice as it arrived. CS3D was modified to use the HTJ2K feature allowing decoding of a prefix of the entire image data. Additionally, for MPR views, CS3D was modified to allow a selected set of images to be fetched and interpolated to produce a lossy progressive MPR view. The first render is thus the first time the image or volume can be seen, while the final render is the time for the complete, lossless/all images to be fetched. **Results:** The adoption of HTJ2K in Cornerstone3D has led to significantly more responsive loading and interaction with both large 3D medical imaging volumes and DX/MG images. A quarter resolution image (1/16 of the size) takes about 1/10th of the time to decode to first render, with MPR views being similar. Final render and non-progressive times using JPEG-LS are similar and are not shown separately. You can try an online demo here <https://www.cornerstonejs.org/live-examples/htj2kvolumebasic>

Method	Size	Network	First Render	Final Render
HTJ2K Streaming (1 stage)	11 MB	4G	175 ms	3745 ms
HTJ2K Byte Range (2 stages)	31.4 MB	4G	888 ms	8017 ms

Table 1: Comparison of HTJ2K streaming methods

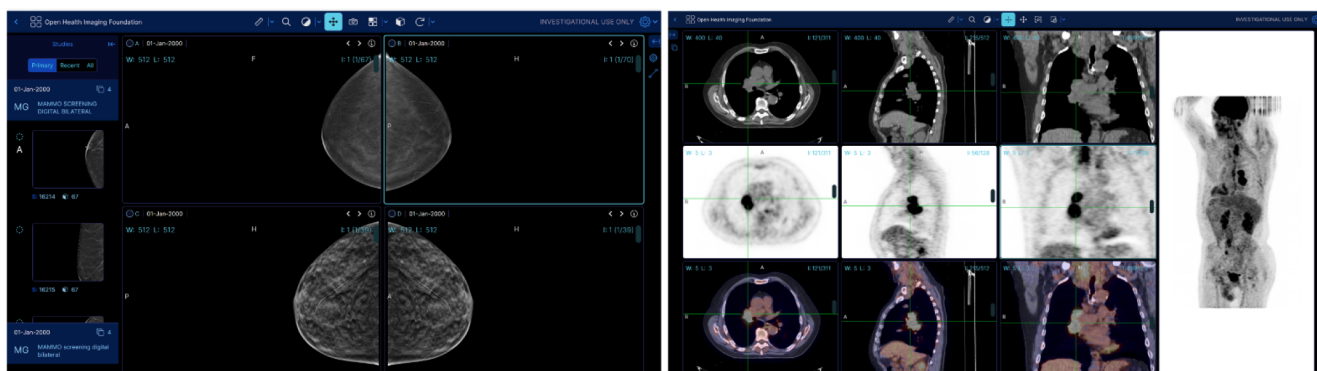
Conclusions: Progressive rendering using HTJ2K surpasses not only single frame display, but also non-progressive JPEG LS MPR rendering in time to first render and maintains lossless final image display of high bit depth images, enhancing medical imaging in web applications like Cornerstone3D. Its broader adoption promises to improve medical imaging workflows and expand possibilities in the field. This work is funded in part by the National Cancer Institute grant number U24CA258511.

Advancing Medical Imaging on the Web: Implementation of Hanging Protocols for Automated Image Display Configuration in OHIF Viewer v3

Alireza Sedghi^{1,2}; Bill Wallace^{1,2}; Joe Boccanfuso^{1,2}; Leonardo Campos^{1,2}; Erik Ziegler^{1,3}; James Hanks^{1,3,4}; Daniel Rukas^{1,4}; Trinity Urban¹; Rob Lewis^{1,2}; Chris Hafey^{1,5}; Salim Kanoun⁶; Gordon J. Harris^{1,3,4}

1) Open Health Imaging Foundation, 2) Radical Imaging LLC, 3) Yunu Inc., 4) Massachusetts General Hospital
5) Amazon Web Services 6) Pixilib

Introduction: The implementation of a Hanging Protocol (HP) system is a critical component in modern medical imaging workflows, particularly in radiology. This implementation aims to simplify and expose site and user arrangement of images within a radiological display, without overwhelming users with complexity. The HP system ensures that the most relevant images are presented in an optimal layout, tailored to the specifics of each case. **Method:** The standard DICOM Hanging Protocol format is a binary format designed for image display customization, yet its complexity often poses challenges. Transitioning to a simpler, JSON-based format, the OHIF Viewer streamlines image selection through "Display Sets," an already grouped and sorted sets of images. Further, system integrators (or experts) can expose attributes composed from the base DICOM metadata by registering javascript functions with the viewer. This reduces the burden on users by allowing them to focus on higher level information than that in the straight DICOM metadata. This approach lightens the users' workload, shifting their focus to more abstracted information rather than dealing directly with the intricate DICOM metadata. For instance, in arranging mammography images, users typically prefer to categorize image sets using straightforward terms like "Right Cardio-Cranial" or "Left Medio-lateral Oblique," rather than navigating through complex criteria involving a mix of patient orientation, view direction, patient laterality, study descriptions, view codes, or other detailed parameters. Key features of the Protocol Engine include: 1) Dynamic Protocol Matching: The engine uses a scoring system to determine the winning protocol for running a study, based on the evaluation of the study metadata. This process involves considering various attributes and constraints to select the most suitable protocol for each study. 2) Layout Customization: Users can extensively customize the viewer's layout, including adjusting the number of rows and columns and creating complex, multi-row and column configurations all within a JSON file 3) Series Matching Rules: It specifies attributes like modality or seriesNumber or description to ensure accurate display of specific image types. 4) Per-Viewport Customization: The engine provides users with precise control over display settings for each viewport. This includes adjusting orientations, selecting initial images, synchronizing parameters like camera or window levels, along with aligning images to the edges, initial color maps, and loading strategy (e.g., top-to-bottom, interleave).



Results: The HP system underwent testing with 5 PT/CT and 3 MG studies. For the MG studies, the system made the layout definition simpler by only needing two rules per viewport instead of many more. It also successfully managed a complex 10-view setup in the multi-series studies for the PT/CT studies. Furthermore, we conducted a questionnaire with a collaborative radiologist who has 10 years of experience to gather their thoughts on the ease of use, accuracy, and overall satisfaction of the HP system. The radiologist gave it a score of 4 out of 5 in each category. **Conclusion:** The Hanging Protocol Engine in OHIF Viewer offers an automated, efficient, and customizable approach to image arrangement, enhancing radiological workflows. This work is funded by the National Cancer Institute grant number U24CA258511.

Advancing Medical Imaging on the Web: Optimizing the DICOMweb Server Architecture with Static DICOMweb

Bill Wallace^{1,2}; Alireza Sedghi^{1,2}; Joe Boccanfuso^{1,2}; Leonardo Campos^{1,2}; Erik Ziegler^{1,3}; James Hanks^{1,3,4}; Daniel Rukas^{1,4}; Trinity Urban¹; Rob Lewis^{1,2}; Chris Hafey^{1,5}; Gordon J. Harris^{1,3,4}

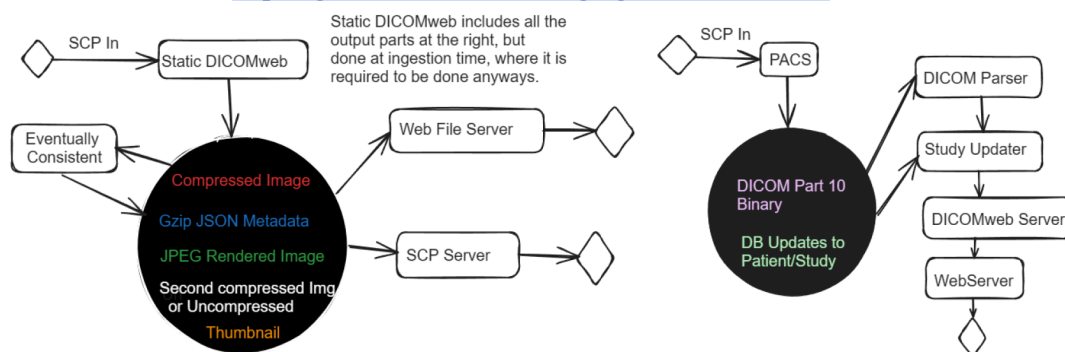
1) Open Health Imaging Foundation, 2) Radical Imaging LLC, 3) Yunu Inc. 4) Massachusetts General Hospital 5) Amazon Web Services

Introduction: DICOMweb is the global standard for web access to medical imaging data due to its compatibility with both web clients and Picture Archiving and Communication Systems (PACS) systems containing DICOM data. However, many implementations suffer from performance issues both during ingestion of data as well as during serving of data. Furthermore, most DICOMweb servers cannot handle distributed loss of connectivity as they use centralized locking to ensure data consistency and integrity. **Methods:** Static DICOMweb is a DICOMweb accelerator that enhances DICOMWeb’s efficiency by converting standard binary DICOM files into compressed format for DICOMweb responses, which are then stored on a file system. The ingestion mechanism generates hash codes on the data to allow fast detection of changes between systems, as well as to allow co-operative updates to the data, ensuring that the eventual final study data structure is consistent regardless of how many systems it is received on. This eventual consistency allows a significant reduction in locking required across systems and reduces ingestion load at high concurrency levels. The conversion of data into the DICOMweb response format allows for just streaming requests for imaging data directly from the file system, with the compression having been done ahead of time. The file system can be a cloud based server or a local system or any combination of the two, allowing for very high performance local caches, with a large cloud storage of lower priority data. **Results:** The implementation of Static DICOMweb improves response times for DICOMweb clients, approaching the speed of retrieving data from the file system and network transmission. The efficiency of PACS systems varies depending on the optimization strategies used. A comparative evaluation (see Table 1) shows that transferring compressed cached metadata is about three times faster than transferring uncompressed metadata. Generating series metadata took around 1400 ms on the referenced system. While metadata generation during data ingestion may seem time-consuming, a significant portion of this time is spent on binary DICOM parsing. This parsing is necessary during the ingestion phase and the additional time for writing cached metadata is negligible. In the case of compressed images, accessing imaging data from a binary DICOM file requires parsing, which took approximately 150 ms in the examined server. Compared to streaming raw data, this process takes about four times longer.

Conclusions: Using a freely available preprocessor to store DICOM data in DICOMweb native format provides low server/cloud compute cost access to DICOM data for typical client type use, reducing ingest, storage, transmission and cloud/server costs, while simultaneously significantly improving client response times. with a scalable/distributed ingestion design.

Client use of DICOMweb: <https://www.cornerstonejs.org/live-examples/htj2kvolumebasic>

Static DICOMweb GitHub: <https://github.com/radicalimaging/static-dicomweb>



	Size/gzipped	PACS	Static DICOMWeb
Single Series Metadata	4,420/170 KB	1,780 ms (309 ms after cache)	119 ms
All Series Query	5.6/0.9 KB	21 ms	14 ms
Compressed Image	173 KB	210 ms	54 ms

Convolutional Neural Networks for Localization of Radioactive Sources with a Hand-Held Gamma Probe

Sydney Wilson^{1,2}, David W. Holdsworth^{1,2,3}

¹School of Biomedical Engineering, ²Robarts Research Institute, ³Dept. of Medical Biophysics, Schulich School of Medicine and Dentistry, Western University

Introduction: Radioguided surgery is a technique that uses a hand-held gamma probe to localize radiolabeled lesions during cancer surgery. While gamma probes excel at detecting lower energy radioisotopes, increased septal penetration and scattering in the probe's collimator at higher energies rapidly degrades the resolution and limits the use of gamma probes for detection of high-energy radioisotopes. Presently, however, most receptor targeted radiopharmaceuticals that have a high affinity for cancerous cells, and are thus ideal surgical markers, contain high-energy (511 keV) radionuclides. In this work, we aim to use machine learning to improve the resolution of a previously developed focused gamma probe with a 4-segmented collimator and detector [1] for localization of positron emitting sources. Specifically, the objective is to determine the accuracy of a neural network in predicting the location of a 511 keV radioactive source using the 4-channel energy spectrum from our gamma probe.

Methods: The data used in this study was obtained by performing Monte Carlo simulations in a well validated software called GATE (Geant4 Application for Tomographic Emission). A 511 keV radioactive point source was embedded in simulated phantom breast tissue, 35 mm below the collimator of the gamma probe. The source was placed at x, y locations within a 40 mm grid and an energy spectrum corresponding to each quadrant of the scintillation crystal was recorded. The simulations were repeated 300 times and then the data was split 80/20 for training and testing. The model hyperparameters were tuned using 3-fold cross-validation on the training set.

A convolutional neural network (CNN) was optimized to predict the x, y source location from the 4-channel energy spectra. The CNN architecture, as shown in Figure 1, is an adaptation of the network presented by Wang *et al* [2]; while this algorithm was proposed for a different application, it successfully demonstrated that blocks of 1D convolutional operations could identify patterns in energy spectra. Our CNN was trained using a mean squared error loss function and Adam optimizer. The accuracy of the final model was evaluated by analyzing the relationship between the true and predicted x- and y-coordinates, as well as the error in radial distance.

Results: The predicted location of the radioactive source was linearly correlated with the true location over the entire space with an R^2 of 0.92; the line of best fit between the true and predicted x and y coordinates had a slope of 0.935 and 0.929, with an offset of 0.004 and 0.395, respectively. The measured error between the true and predicted coordinates were normally distributed, with a mean radial error of 2.9 mm (± 1.8 mm standard deviation).

Conclusions: As desired, there was a strong linear relationship between the true and predicted coordinates. The CNN was able to predict the radioactive source location to within 6.5 mm 95% of the time, which is a significant improvement compared to existing gamma probes where the resolution can be several tens of millimeters. It should be noted that while the reported resolution is intrinsic, the positron range of ^{18}F , the most common positron emitter, is less than 1 mm in soft tissue and should have minimal effect on the system resolution. To the best of our knowledge, this is the first report to use machine learning to improve the localization capabilities of a hand-held gamma probe. Overall, this work presents a new technique that extends the usability of gamma probes for detection of high-energy, 511 keV radiolabels, and thus has the potential to enhance surgical accuracy.

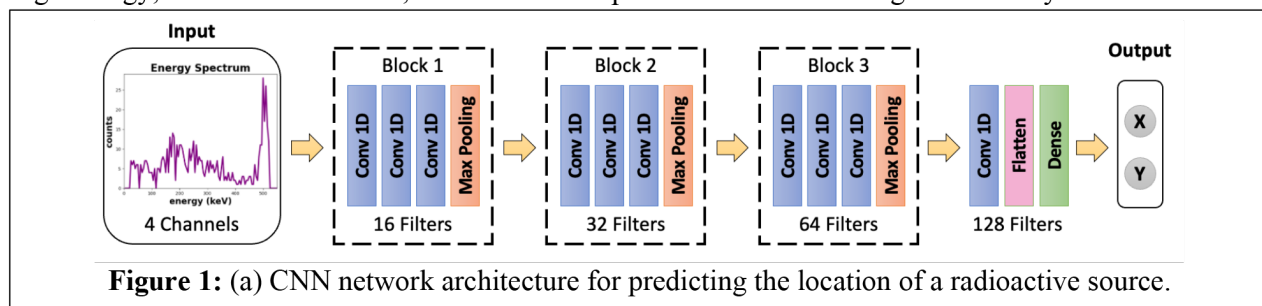


Figure 1: (a) CNN network architecture for predicting the location of a radioactive source.

References: 1. Holdsworth *et al.*, "Gamma Probe and Multimodal Intraoperative Imaging System," United States Patent US 11,402,515 B2, 2022. 2. Y. Wang *et al.*, "Explainable radionuclide identification algorithm based on the convolutional neural network and class activation mapping," *Nuclear Engineering and Technology*, 2022.

Session 8 Pitches: Cancer

Abstracts

Polarization speckle allows for snapshot *in vivo* skin lesion roughness measurement

Daniel C. Louie^{1,2,3}, Lioudmila Tchvialeva^{1,3}, Jamie Phillips^{1,3}, Haishan Zeng^{1,4}, Harvey Lui^{1,4}, Tim K. Lee^{1,2,3}

¹Department of Dermatology and Skin Science, University of British Columbia;

²School of Biomedical Engineering, University of British Columbia;

³Cancer Control Research, BC Cancer; ⁴Integrative Oncology, BC Cancer

Introduction: The skin is the most visible and accessible organ of the body, which inspires much research into developing non-invasive sensing methods for skin properties. Skin surface morphology is an important feature in the diagnosis and monitoring of many skin diseases. However, there exist few practical methods of quantifying skin roughness values in a clinical setting. Polarization speckle is an optical method designed to obtain snapshot roughness measurements with a portable form-factor. This study tests a novel polarization speckle technique by quantitatively measuring the average roughness of skin lesion types *in vivo*.

Methods: Polarization speckle is a stochastic interference pattern formed when laser light scatters from the skin. As shown in Fig 1, roughness measurement is achieved by imaging the speckle pattern and matching the contrast C to roughness by a calibration curve (methodology established in [1]). The device was tested in a clinical study on patients with malignant and benign skin lesions that resemble cancer (malignant diagnoses were histopathologically confirmed). Cancer included 11 malignant melanomas (MM), 43 basal cell carcinomas (BCC), 27 squamous cell carcinomas (SCC). Benign included 108 seborrheic keratoses (SK), 81 nevi, 11 actinic keratoses (AK). Normal skin roughness was obtained for the same patients (307 body sites proximal to the lesion).

Results and Conclusions: The average root mean squared (rms) roughness \pm standard error of the mean for MM and nevus was equal to $19 \pm 5 \mu\text{m}$ and $21 \pm 3 \mu\text{m}$ respectively. Normal skin was found to have mean rms roughness $31 \pm 3 \mu\text{m}$, other lesions have roughness $35 \pm 10 \mu\text{m}$ (AK), $35 \pm 7 \mu\text{m}$ (SCC), $31 \pm 4 \mu\text{m}$ (SK), and $30 \pm 5 \mu\text{m}$ (BCC). An independent-samples Kruskal-Wallis Test indicates that MM and nevus can be separated from each of the tested types of lesions ($p < 0.05$), except each other. These results quantify clinical knowledge of lesion roughness towards rapid and noninvasive cancer detection.

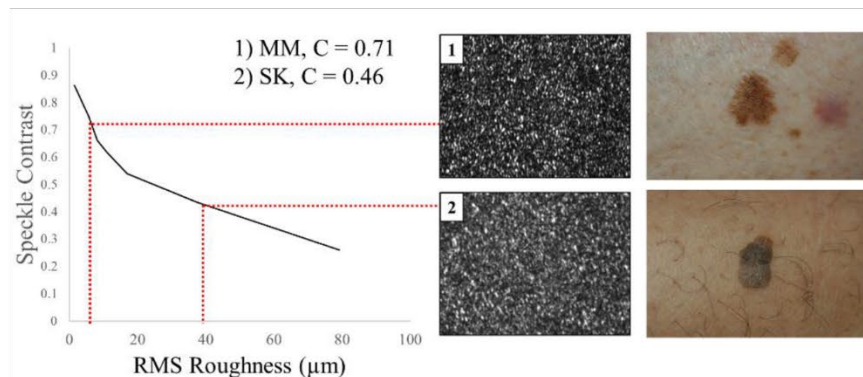


Figure 1. Example of calibration curve matching speckle contrast to RMS skin roughness (left). Speckle patterns belonging to melanoma and seborrheic keratosis can be separated despite similar clinical presentation (right)

[1] L. Tchvialeva, W. Shenkenfelder, A. Doronin, I. Meglinski, I. Markhvida, and T. K. Lee, "In vivo laser speckle measurements of skin roughness: clinical study," in *Optics in the Life Sciences*, OSA Technical Digest (online) (Optica Publishing Group, 2015), paper JT3A.28.

Micro-Ultrasound Photoacoustic Imaging of Prostate Cancer: Evaluation in a Pre-Clinical Model

Nidhi Singh^{1,2}, Emmanuel Chérin², Carlos-Felipe Roa^{1,2}, Yohannes Soenjaya², Gang Zheng^{1,3}, Brian C. Wilson^{1,3}, F. Stuart Foster^{1,2}, Christine E. M. Démoré^{1,2}

¹ University of Toronto, Toronto, Canada, ² Sunnybrook Research Institute, Toronto, Canada, ³Princess Margaret Cancer Centre, Toronto, Canada.

Background, Motivation and Objective

Focal therapies like photothermal therapy (PTT) can be used to treat solid tumors locally without damaging the sensitive structures and healthy tissue near the tumor. This can provide an alternate treatment option for prostate cancer (PCa), which is a multifocal cancer, in which the risk of progression is determined by the index lesion or largest lesion. To deliver the treatment effectively, it is required to accurately delineate the index lesion to enable pre-treatment planning and real-time guidance. We previously demonstrated a combined micro-ultrasound (micro-US) and photoacoustic (PA) system by adapting a clinical transrectal micro-US system [1]. In this study, we performed multispectral PA imaging using the combined system to image subcutaneous prostate cancer xenografts in a mouse model. We also use biodegradable, porphyrin-lipid based PA-active nanoparticles (Porphysomes) to enhance the signal from the tumor and monitor the nanoparticle accumulation over a 48h period.

Methods

The pre-clinical imaging was done using a micro-US ExactVu system (Exact Imaging, Markham, ON, Canada) adapted to perform PA imaging. A subcutaneous prostate tumor model was developed by inoculating the hind limb of a 5-weeks old, SCID SHO female mouse with DU145 human prostate cancer cells. An Nd:YAG tunable laser (Fujifilm VisualSonics Inc., Toronto, ON, Canada) was used as the light source, coupled into a side-fire optical fiber to deliver the light to the tumor. The fiber was designed to be suitable for transurethral (TU) illumination of the prostate. Tumor growth was monitored through visual inspection and imaging was carried out at 3 weeks after inoculation. Both B-mode and multispectral PA-mode imaging were performed using the combined system. The mouse was also injected *i.v.* with 10 mg/kg Porphysomes (PS), and multispectral PAI and B-mode images were acquired 3, 6, 24 and 48 h later. Spectral unmixing was used to separate the PA signals from oxygenated (HbO₂), deoxygenated hemoglobin (Hb) and PS. Mean signal in the region of interest in the tumor was used to compare the PA signal measured at all timepoints. The animal experiments were performed in compliance with the Sunnybrook Research Institute approval.

Results/Discussion

Fig. 1a shows the experiment set up with the optical fiber positioned to fire towards the side of the tumor and US transducer at the top. Spectral unmixing of the PA data revealed the signal spatial maps from HbO₂, Hb (not shown) and PS before and after injection. Fig. 1b and 1c show representative US and PA image at 6-hour post injection. The PA signal from PS increased as the nanoparticles circulate and are taken up by the tumor. The peak PA signal was at 6 h. Continuing investigations entail: 1) comparing the imaging results with histology, and 2) using multiple animals with the same imaging protocol to assess the repeatability of this temporal trend.

Acknowledgements. This work was supported by the Terry Fox Research Institute.

[1] N. Singh *et al.*, “A new photoacoustic imaging platform for potential applications in prostate cancer,” Proc. *IEEE IUS 2020*, Sep. 2020.

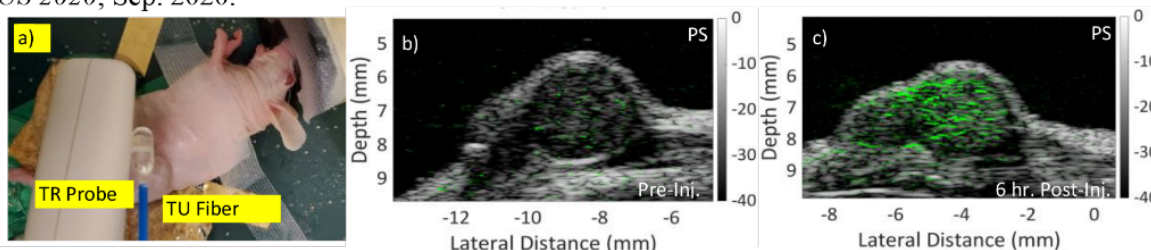


Figure. 1a) Experiment setup showing the position of the transrectal (TR) US transducer and transurethral (TU) optical fiber with respect to the tumor being imaged. Pseudo-color PA-mode image of spectrally unmixed Porphysomes overlaid on grayscale B-mode image of the tumor, b) before and c) 6h after PS injection.

Test-Time Training for Prostate Cancer Detection: Addressing Distribution Shift with Self-Supervised Learning

Mahdi Gilany¹, Paul Wilson¹, Amoon Jamzad¹, Mohammed Harmanani¹, M. N. Nhat To², Brian Wodlinger³, Purang Abolmaesumi², Parvin Mousavi¹

¹Queen’s University, Kingston, Ontario, Canada, ² University of British Columbia, Vancouver, British Columbia, Canada,

³Exact Imaging, Markham, Ontario, Canada

INTRODUCTION: Histopathological examination of prostate tissue samples, typically obtained through transrectal ultrasound (TRUS)-guided biopsies, remains the prevalent method for diagnosing and grading prostate cancer (PCa). However, TRUS approach is often hindered by a high false-negative rate and substantial risks of negative biopsy-related effects. To enhance the PCa detection via ultrasound, a range of deep learning techniques have been introduced. These methods utilize ultrasound Bmode or radio-frequency images to determine the characteristics of the underlying tissues, thereby pinpointing areas that may require closer examination. Nonetheless, a significant challenge with these deep learning techniques is the data distribution shift across different hospitals, patients, or even within multiple images from the same patient, which is a crucial factor for the real-world deployment of these models. To overcome this obstacle, we suggest a strategy of adapting the deep model to the distribution of the test data during the inference phase through the use of self-supervised learning.

METHODS: Our study utilizes a proprietary dataset obtained using advanced micro-ultrasound technology (29 MHz center frequency) from 693 patients across five centers. These patients were part of a clinical trial (NCT02079025) and had undergone systematic TRUS-guided biopsies. Our approach tailors test-time training [1] to adapt the model to the test distribution. As depicted in Figure 1, we employ ResNet10 as the feature extractor to derive feature vectors from each region of interest (ROI) in both the prostate area (unlabeled data) and the needle region (labeled data). The classification head and self-supervised learning (SSL) heads are employed to transform the feature vectors derived from labeled and unlabeled regions of interest (ROIs) into classes and SSL features, respectively. We utilize cross-entropy for the classification head, while the SSL head is trained using “Bootstrap Your Own Latent (BYOL)” method [2]

loss. During the training phase, the feature extractor and both heads are concurrently trained. In the inference phase, the feature extractor and SSL head are fine-tuned using unlabeled test data, adjusting to test distribution.

RESULT & CONCLUSION: Our proposed method, in Table 1, has significantly improved performance compared to the baseline approach, as evidenced by the 4% improvement in ROI-wise AUROC and 5% in core-wise AUROC. Test-time training, applied to test data prior to making predictions, enables the model to adapt to the test distribution, thus significantly enhancing its real-world robustness and performance.

REFERENCES: [1] Grill et al., Neurips 2020 [2] Sun et al., ICML2020 [3] Gilany et al., MICCAI 2022

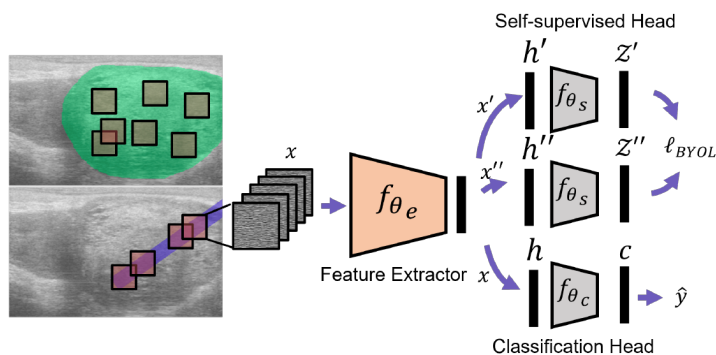


Figure 1: Summary of the proposed method: unlabeled ROI patches are extracted from prostate region to train feature extractor and SSL head. Labeled ROI patches are extracted from needle region where pathology annotation exist, and they train feature extractor and classification head. During inference, unlabeled test data is used to fine-tune the feature extractor before prediction is made.

Table 1: Comparison of the proposed method to baseline methods. Metrics are threshold independent area under the ROC curve (AUROC) for both ROIs and cores (all ROIs in the needle).

Method	Core AUROC	ROI AUROC
ResNet10 [3]	71.1	62.1
TTT-ResNet10 (ours)	76.6	66.6

An automatically tracked system for cervical brachytherapy 3D ultrasound imaging

Tiana Trumpour^{1,2}, Jamiel Nasser³, Jeffrey Bax², Lori Gardi², Lucas Mendez⁴, Kathleen Surry^{1,4,5}, Aaron Fenster^{1,2,5}

¹ Department of Medical Biophysics, Western University, Canada ² Robarts Research Institute, Western University, Canada ³ Department of Physics and Astronomy, University of Waterloo, Canada ⁴ London Regional Cancer Program, Canada ⁵ Department of Oncology, Western University, Canada

Introduction: High dose-rate brachytherapy is considered a necessary part of the cervical cancer treatment paradigm [1]. During treatment, specialized applicators are placed inside the patient's pelvic cavity. Typically, advanced medical imaging such as computed tomography (CT) or magnetic resonance (MR) methods are used to localize the applicator and ensure accurate planning of radiation dose. Previously, our group developed a more accessible imaging option that leverages the fusion of three-dimensional (3D) trans-abdominal ultrasound (TAUS) and 3D trans-rectal ultrasound (TRUS) images using a custom nonlinear weighted voxel combination technique [2]. However, the manual nature of our previous method indicated the need for improved 3D TAUS-3D TRUS registration. In response, we have designed and developed an automated, inherently registered 3D US system for intra-procedural cervical brachytherapy imaging.

Methods: We constructed a multi-jointed mechatronic arm from aluminum and stainless steel to accommodate our 3D TAUS mover (Fig. 1A). The arm contains encoders in each joint for spatial tracking and is complementary to our previously developed 3D TRUS system. The 3D TAUS system sweeps a curvilinear US transducer through a hybrid tilt and translation motion while the 3D TRUS system rotates an end-fire endocavity probe within the patient's rectum. The workflow is as follows: (1) The physician places the systems in an initial scan position, (2) a brief mechanical calibration between all joints is completed, (3) images are acquired from both a TAUS and TRUS view, and (4) the resultant images are fused in the manner described by our previous work, creating a combined 3D US image. The initial calibration of the two systems was examined using a physical external coordinate system (Fig. 1B). The tracked encoder values were compared to the known physical positions of the divots in the calibration jig and reported as Euclidean distance errors. The tracking capability of our 3D TAUS arm was investigated by analyzing data from an external optical tracker (Fig. 1C). The encoder values (N=180) were used to train and test a linear regression and Euclidean distance errors were reported. Once the errors were quantified, a calibration was performed to transform the encoder values into the correctly calibrated coordinate system.

Results: The coordinate system calibration resulted in a root-mean-square error of 0.5 mm in the mediolateral axis, 0.6 mm in the craniocaudal axis, and 0.4 mm in the anteroposterior axis, with respect to the position of the arm on the patient bed. The optical tracking validation experiments resulted in a mean absolute difference between the encoders and external system of 0.5 ± 0.3 mm. The error between the encoder values and optical tracker, relative to a fixed reference point was found to be 0.4 ± 0.1 mm.

Conclusions: This novel device for automated tracking and registration of 3D US images during cervical brachytherapy procedures may enhance visualization of the female pelvic region and improve dosimetric outcomes. We will evaluate image registration and fusion in future phantom experiments, with the expectation that system imaging errors will propagate into the final registration. This underscores the importance of our sub-millimeter calibration transformation accuracy resultant from this preliminary work. The ability to use fused 3D US guidance with this technique creates a more accessible imaging modality for healthcare centers that may lack advanced modalities.

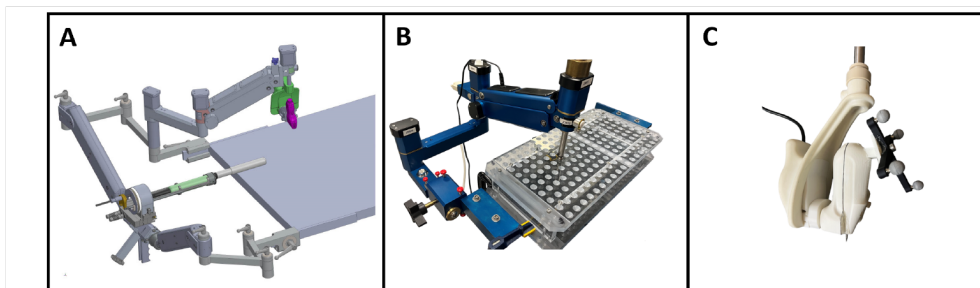


Figure 1: A) Computer-aided design of the 3D TAUS- 3D TRUS system attached to the patient bed, B) 3D TAUS arm with external coordinate system jig, C) Optical tracking device within the 3D TAUS scanner

References:[1] Tanderup K. et al. *Int J Radiat Oncol Biol Phys.* 2014. 88(3); [2] Trumpour et al. *SPIE Med. Imaging* 2022. 12038

Improving Model Adaptability: A Domain Knowledge-Integrated Deep Learning Approach for Ultrasound Image Segmentation and Classification

Bining Long, Yanran Guan and Matthew Holden
School of Computer Science, Carleton University, Canada

Introduction: Ultrasound imaging is a non-invasive, widely-used imaging modality for breast cancer detection. We develop a model for breast ultrasound image segmentation and classification, focusing on its economical deployment across diverse clinical settings. We investigate the performance of our existing two-stage neural network model [1] when applied to breast ultrasound images collected from various hospitals, distinct from its initial training dataset. Moreover, we explore transfer learning using our pre-trained model, incorporating domain insights from the original ultrasound dataset, and demonstrate the adaptability of our model to new datasets.

Methods: We employ a two-stage model from our prior work [1], integrating image segmentation and classification. The first stage is built on a U-Net architecture, to generate segmented tumor masks, as shown in Figure 1, followed by the second stage of a convolutional neural network (CNN) for classifying tumor type. To enhance the model's efficiency, we introduce a new feature fusion method for the CNN input, fusing the predicted mask, the original ultrasound image, and their product representing the region of interest.

Our evaluation extends beyond the breast ultrasound images dataset (BUSI) [2], where our model was first trained, to include two additional datasets, the UDIAT Diagnostic Centre dataset (UDIAT) [3] and the Mendeley ultrasound dataset (BUSC) [4]. We initially apply the model trained on the original dataset directly to new datasets, establishing a baseline performance of the model when confronted with datasets sourced from different hospitals, with potential differences in the equipment and operator skill. Next, we analyze the impact of transfer learning, by comparing models with weights pre-trained on the original dataset and fine-tuned on additional datasets against models trained from scratch. We quantitatively evaluate the model's performance based on the segmentation intersection over union (IoU) and the classification accuracy (ACC).

Results: We first train our model on the BUSI dataset covering 2 tumor classes (benign and malignant), achieving a test IoU of 0.6071 and an ACC of 0.9385. Subsequently, we directly apply this trained model to the entire UDIAT and BUSC datasets, treating them as test sets. The results show an IoU of 0.5492 for UDIAT and 0.6852 for BUSC, along with an ACC of 0.7669 for UDIAT and 0.6080 for BUSC.

To better adapt our model to new datasets, we employ transfer learning. We split UDIAT and BUSC into 80 : 20 training and test sets, then train new models. In Table 1, we present a comparison between two groups of models on their test sets: models trained from scratch and models fine-tuned with pre-trained weights from BUSI. We observe that, transfer learning leads to an increase in segmentation IoU by 0.1627 for UDIAT and 0.0946 for BUSC. Concurrently, it increases the classification ACC by 0.0606 for UDIAT and 0.0800 for BUSC.

Conclusions: In this work, we enhanced the feature fusion phase in the classification stage and demonstrated the added value of transfer learning utilizing a medical dataset from the same imaging modality, verified across two datasets. This approach effectively integrates domain knowledge to improve the model's adaptability. To promote practical utility and generalizability of diagnostic decision-support models, we suggest future work to further tackle the inherent heterogeneity of data.

References

- [1] B. Long, Y. Guan, and M. Holden, "A two-stage neural network model for breast ultrasound image classification," in *Proceedings of the IEEE International Conference on Bioinformatics and Bioengineering*, pp. 129–133, 2023.
- [2] W. Al-Dhabyani, M. Gomaa, H. Khaled, and A. Fahmy, "Dataset of breast ultrasound images," *Data in Brief*, vol. 28, p. 104863, 2020.
- [3] M. H. Yap, G. Pons, J. Martí, S. Ganau, M. Sentís, R. Zwigelaar, A. K. Davison, and R. Martí, "Automated breast ultrasound lesions detection using convolutional neural networks," *IEEE Journal of Biomedical and Health Informatics*, vol. 22, no. 4, pp. 1218–1226, 2018.
- [4] A. Iqbal and M. Sharif, "PDF-UNet: A semi-supervised method for segmentation of breast tumor images using a U-shaped pyramid-dilated network," *Expert Systems with Applications*, vol. 221, p. 119718, 2023.

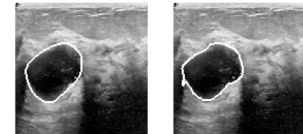


Figure 1: Ultrasound images with tumor mask boundaries (in white): ground truth mask (left) and predicted mask (right).

Table 1: Models' test performance without and with transfer learning (TL).

	Without TL		With TL	
	UDIAT	BUSC	UDIAT	BUSC
IoU	0.4986	0.7260	0.6613	0.8206
ACC	0.8182	0.9067	0.8788	0.9867

Quantification of the Tumor Microvascular Response to Stereotactic Body Radiation Therapy Using Optical Coherence Tomography Angiography and Dynamic Contrast Enhanced MRI

W. Jeffrey Zabel¹, Hector Alejandro Contreras Sanchez¹, Nader Allam¹, Warren D. Foltz^{2,3}, Costel Flueraru⁴, Edward Taylor^{2,3}, I. Alex Vitkin^{1,2,3}.

¹Department of Medical Biophysics, University of Toronto, Toronto, Canada.

²Radiation Medicine Program, Princess Margaret Cancer Centre, Toronto, Canada.

³Department of Radiation Oncology, University of Toronto, Toronto, Ontario.

⁴National Research Council Canada, Information Communication Technology, Ottawa, Canada.

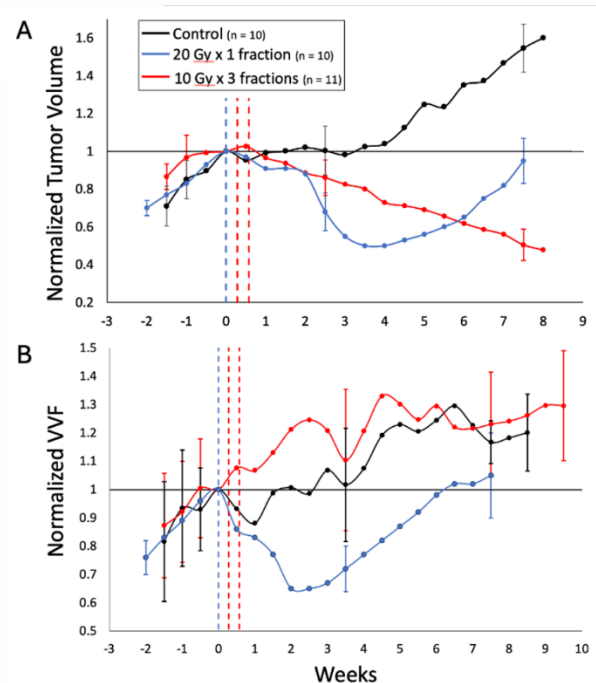
Introduction: Stereotactic Body Radiation Therapy (SBRT) is a cancer treatment that involves the delivery of much higher doses of radiation in fewer fractions than conventional radiation therapy. Preliminary evidence has suggested that the high doses associated with SBRT lead to vascular ablation and thus the tumor vascular response to SBRT may be an important determinant of treatment outcome.

Speckle Variance Optical Coherence Tomography (svOCT) allows for high resolution ($\sim 10 \mu\text{m}$) 3D imaging of the vascular network in a tumor xenograph window chamber mouse model enabling longitudinal vascular quantification. Dynamic Contrast Enhanced Magnetic Resonance Imaging (DCE MRI) is a more clinically applicable imaging modality however its limited spatial resolution (mm scale) may not be able to image the tumor microvasculature (μm scale). To overcome this ‘resolution gap’, we directly correlated high resolution svOCT images of the microvasculature to the comparably lower resolution DCE-MRI in the same animals. Successful discovery of correlates between svOCT derived microvascular information and DCE-MRI macrovascular metrics will support the use of DCE-MRI in the clinic for SBRT microvascular response monitoring potentially enabling personalized SBRT treatment adaptations.

Methods: $n = 42$ mice were subcutaneously injected with human pancreatic cancer cells (BxPC3 cell line) and plastic window chambers were installed. Mice were exposed to several fractionation schedules: 20 Gy in 1 fraction ($n = 10$ mice), 30 Gy in 3 fractions ($n = 10$ mice), and 45 Gy in 3 fractions ($n = 10$ mice). All multi fraction schedules were delivered in one week (Monday, Wednesday, Friday). $n = 12$ mice were kept as unirradiated controls. svOCT and DCE-MRI was performed at regular intervals before, during, and up to 2.5 months after SBRT. Tumor volume (TV) and the vascular volume fraction (VVF) were extracted from the OCT structural and microvascular images respectively and were longitudinally monitored.

Results: Normalized changes in the TV and VVF are shown in figure 1A and B respectively. Data analysis for 45 Gy in 3 fractions are ongoing. The strongest correlation was found between svOCT’s mean intervascular distance and DCE-MRI’s time to peak contrast enhancement metric (Spearman correlation coefficient, $r = -0.81$, $P < 0.0001$). svOCT microvascular correlations with the Toft’s model was also performed. Data analysis for timepoints during and after SBRT is ongoing.

Conclusions: The microvascular insights afforded by svOCT are important for understanding what role the microvasculature plays in determining treatment response during SBRT. Furthermore, linking svOCT micro-vascular metrics to DCE-MRI macro-vascular metrics provides a ‘bridge’ to the clinic so that microvascular information may be used to personalize/optimize a patients treatment plan.



Automatic Segmentation of Metastatic Brain Tumours using Magnetization Transfer contrast

Céline Dubroy-McArdle^{1,2}, Dafna Sussman^{1,2,3}, Greg Stanis^{4,5}, Wilfred Lam^{4,5}, Daniel Nussey^{1,2}

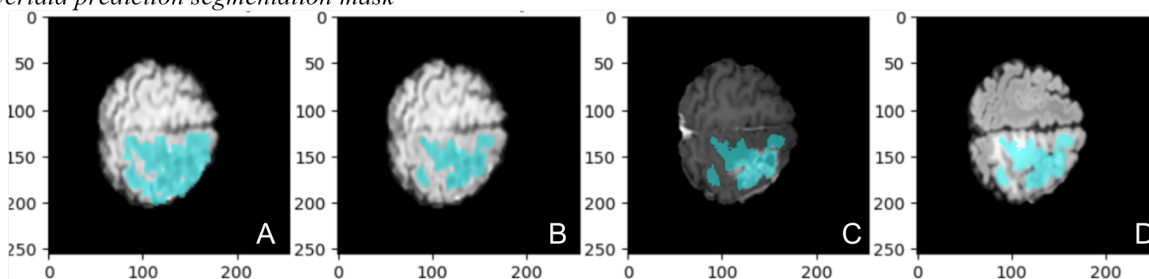
1 Departments of Biomedical Physics & Engineering, Toronto Metropolitan University, 2 Institute for Biomedical Engineering, Science and Technology (iBEST), Toronto Metropolitan University & St. Michael's Hospital, 3 Department of Obstetrics & Gynecology, University of Toronto 4 Sunnybrook Research Institute, 5 Department of Medical Biophysics, University of Toronto

Introduction: Metastatic brain tumours are cancer cells that originated in one part of the body and migrated to the brain. Brain metastases are 10 times more common than primary brain tumours, and affect about 20% of all cancer patients ^[1]. Brain tumour segmentation is useful in determining the unique anatomy and metabolism of the lesion in order to guide diagnosis and treatment planning, as well as monitor tumour progression. ^[2] The current standard for segmenting brain tumours includes manually delineating enhanced, necrotic and edema regions on T1w post-Gd and T2w FLAIR images. ^[2] Unlike traditional T1w and FLAIR imaging, magnetization transfer (MT) presents a unique magnetic resonance imaging (MRI) contrast that can be useful in identifying metabolic changes, such as a diminished capacity of macromolecules to exchange magnetization in tissues. These changes could extend beyond the visible lesions on traditional T1W images. The aim of this research is to create an automatic segmentation algorithm for accurate delineation of MT contrast regions, specifically in metastatic brain tumours.

Methods: 3D T1W post-Gd, FLAIR and MT MR images were obtained from 62 patients at Sunnybrook Health Science Centre with various lesions, numbers, size and primary tumour causes. The 3D MT volumes were manually segmented using ITK-SNAP to create the ground truth for the MT region of interest. The 3D volumes were registered, sliced into 2D images in the third dimension keeping only images that contained a region of interest, reshaped while minimizing distortion, then overlaid on top of each other. The MT images were thresholded with a max percentile value of 99. The final dataset contained 2098 2D images. The 2D dataset was split into a training, validation and test set, at a ratio of 68:16:16, respectively. A U-shaped Neural Network was used with a 6-fold cross validation.

Results: Preliminary model resulted in a DICE similarity score of 0.59 and 0.59 for the training and validation with an associated standard deviation score of 0.014 and 0.017 for the cross validation. The test set resulted in DICE similarity score of 0.51 for the MT enhanced region. Other performance metrics such as recall, precision and the Jaccard index were also found and recorded to be 0.60, 0.77, and 0.51 respectively.

Figure 1: A) MT image with mask ground truth, B) and prediction segmentation mask. C) T1w-post Gd and D) T2w FLAIR with overlaid prediction segmentation mask



Conclusions: The work demonstrates a proof of concept and yields promising results for a radiological tool for identification and delineation of MT regions in metastatic brain tumour. This tool could serve as an aid in treatment planning or monitoring of tumour metabolic changes over time. Further work is focused on improving the model as well as adding other tissue types such as enhanced, necrotic and edema regions in order to gather more comprehensive information about the anatomy of the tumour and its surroundings.

References: [1] P. Sacks and M. Rahman, "Epidemiology of brain metastases," *Neurosurgery Clinics of North America*, vol. 31, no. 4, pp. 481–488, 2020. [2] N. Gordillo, E. Montseny, and P. Sobrevilla, "State of the art survey on MRI Brain Tumor Segmentation," *Magnetic Resonance Imaging*, vol. 31, no. 8, pp. 1426–1438, 2013. [3] R. M. Henkelman, G. J. Stanis, and S. J. Graham, "Magnetization transfer in MRI: A Review," *NMR in Biomedicine*, vol. 14, no. 2, pp. 57–64, 2001.

Dilated Convolutional Transformer-Based Segmentation for Primary and Secondary Liver Cancers Tumour: A Comparative Study

Ramtin Mojtahedi¹, Mohammad Hamghalam^{1,2}, William R. Jarnagin³,
Richard K. G. Do⁴, Amber L. Simpson^{1,5}

¹*School of Computing, Queen's University, Kingston, ON, Canada*

²*Department of Electrical Engineering, Qazvin Branch, Islamic Azad University, Qazvin, Iran*

³*Hepatopancreatobiliary Service, Department of Surgery, Memorial Sloan Kettering Cancer Center, New York, NY, USA*

⁴*Department of Radiology, Memorial Sloan Kettering Cancer Center, New York, NY, USA*

⁵*Department of Biomedical and Molecular Sciences, Queen's University, Kingston, ON, Canada*

INTRODUCTION: Primary liver cancer ranks as the sixth most common cancer and is the fourth leading cause of cancer-related deaths worldwide, causing around 830,000 deaths each year. Liver cancers such as hepatocellular carcinoma (HCC), intrahepatic cholangiocarcinoma (ICC), and colorectal liver metastasis (CRLM) often spread to the liver. Accurate tumour delineation is critical for treating these cancers. Recently, transformer-based models have proven effective in tumour segmentation, and enhancing these models is crucial for improving cancer treatment approaches.

METHODS: In this study, we utilized computed tomography (CT) images from a dataset provided by the Memorial Sloan Kettering Cancer Center. The dataset comprised 107 cases of ICC, 155 cases of HCC, and 197 cases of CRLM. Our aim was to train two advanced transformer-based segmentation networks: Swin UNETR and UNETR [2, 3]. These networks were evaluated in their standard forms, which employ conventional convolutional kernels, as well as in their configurations that incorporated dilated convolutional blocks. We compared the performance of dilated convolutional blocks versus standard convolutional blocks within both the encoder and decoder components of the networks. We assessed their performance based on metrics such as the Dice coefficient, Intersection over Union (IoU), and Hausdorff Distance (HD95), for both tumours and the liver organ. Figure 1 provides an overview of the proposed methodology.

RESULTS: This study found that Swin-UNETR and UNETR models with dilated convolutions significantly enhanced the segmentation of HCC, ICC, and CRLM cancers. Swin-UNETR showed a 7.94% increase in liver Dice, 13.62% in liver IoU, and a 22.01 mm decrease in liver HD95, indicating more accurate tumor edge detection. UNETR also improved, with a 5.98% rise in liver Dice, 10.99% in liver IoU, and an 8.40 mm drop in liver HD95. Figure 2 confirms these improvements in segmentation across all metrics compared to the baseline.

CONCLUSION: The study indicated that applying dilated convolutions to transformer-based structures like UNETR and Swin UNETR enhances segmentation performance, potentially leading to improved cancer treatment and patient outcomes.

REFERENCES: [1] P. Dasgupta et al., *Front Oncol*, 2020. [2] A. Hatamizadeh et al., *WACV 2022*. [3] A. Hatamizadeh, V. Nath, Y. Tang et al., *LNCS*, 2022.

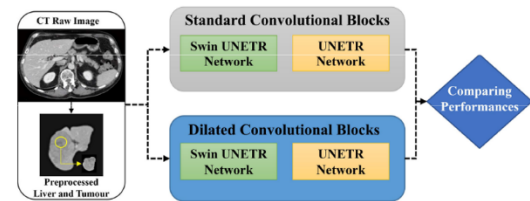


Figure 1: Overview of the methodology.

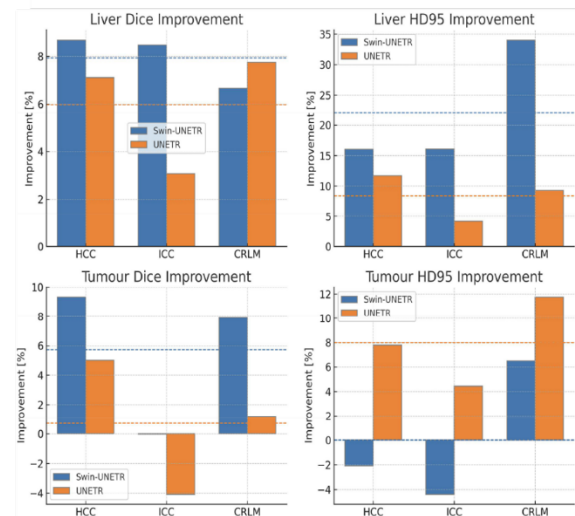


Figure 2: Segmentation improvement results shown for each metric in Swin UNETR and UNETR.

Multi-modal imaging of personalized ovoids for gynecologic brachytherapy treatments

Alissa van Gaalen^{1,2}, Tiana Trumpour^{2,3}, Kevin Barker², Douglas Hoover^{3,4,5}, Kathleen Surry^{3,4,5}, Aaron Fenster^{2,3,5}

¹Department of Physics and Astronomy, University of Waterloo, Waterloo, Canada ²Robarts Research Institute, Western University, London, Canada ³Department of Medical Biophysics, Western University, London, Canada ⁴London Regional Cancer Program, London, Canada ⁵Department of Oncology, Western University, London, Canada

Introduction: High-dose rate brachytherapy is a part of the typical treatment process for gynecologic cancer. Through accurate and timed placement of radioactive sources locally to the malignancy, the required dose can be delivered while avoiding surrounding healthy tissue. This is accomplished through the intracavitary insertion of a specialized applicator and/or interstitial needles. Previous work has evaluated the use of a Fletcher/tandem-and-ovoids applicator with the addition of preset holes in both ovoids to accommodate interstitial needles [1]. However, extremely dorsally- or laterally-presenting malignancies may be less accessible without the ability to dynamically control the interstitial needle trajectories [1, 2]. We propose a suite of low-cost, rapidly prototyped ovoids that contain holes angled up to 30 degrees with rotation about their central axes to accommodate various patient geometries and tumor positions. Moreover, the ability to successfully and safely image the device with computed tomography (CT), magnetic resonance (MR), and three-dimensional transabdominal ultrasound (3D TAUS) will be demonstrated.

Methods: A custom tri-modal tissue mimicking female pelvic phantom with internal structures was created. A commercial Fletcher applicator base was used, with the tandem embedded in the phantom pelvic cavity, and the ovoids replaced with our prototyped set before insertion (Fig.1 A). Both plastic and titanium brachytherapy needles were investigated, and images were acquired with all three modalities. Qualitative analysis of needle insertion through various ovoid holes and angles into a dorsally-presenting tumor was assessed with the agar phantom by examining the ovoid and needle visibility in all imaging modalities. A second iteration of the prototype that includes steerable ovoid rotation will be analyzed to account for more lateral/laterodorsal tumors. Quantitative results will be obtained by assessing the precision and trajectory of needle placement into fiducial markers within the representative tumor.

Results: The first iteration of phantom images using 3D-printed ovoids with 10- and 15-degree hole angles is depicted in Fig. 1 B-D. Needle insertion through the custom ovoids was successfully identified on multi-modal imaging for a laterodorsal tumor. We also demonstrate the ability to view all relevant anatomy and applicator information with the use of 3D TAUS in comparison to advanced modalities. We anticipate the potential to target embedded fiducials with the introduction of dynamic ovoid rotation. Ease of use of the rotational device will be qualitatively assessed with a Likert scale from three trained users to evaluate operator dependence. We also aim to investigate the potential of transferring the permutations of ovoid rotation and hole angle into a treatment planning system through optical scanning and 3D rendering procedures.

Conclusions: Using rapidly-prototype ovoids with angled holes and rotational compatibility, a larger range of gynecologic tumors will be accessible when combining the Fletcher applicator with interstitial needles. Moreover, the 3D-printed nature of the proposed device is visible using 3D TAUS imaging, indicating a more accessible brachytherapy treatment and imaging option. This work has future capacity to improve dosimetric outcomes for patients in a more personalized manner.

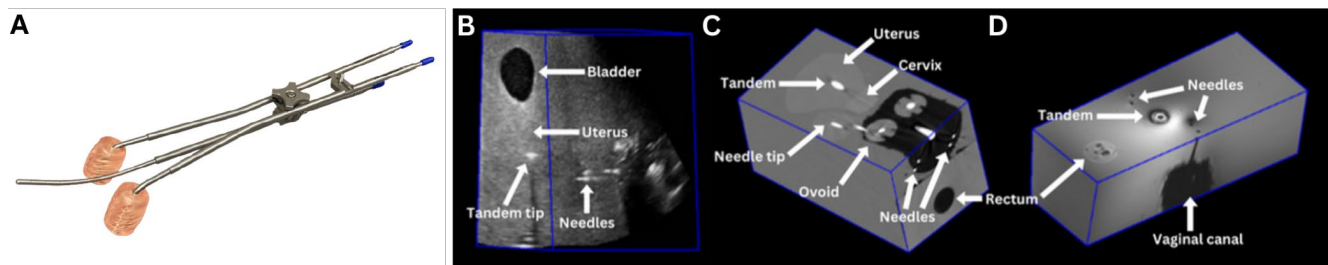


Figure 1: (A) The applicator with preset holes in both ovoids; (B) 3D TAUS, (C) CT, and (D) MR image

References: [1] Nomden et al. *IJROBP* 2012. 82(4); [2] Tambas et al. *Pract Radiat Oncol* 2021. 11(4)

Polarized light microscopy for quantitative assessment of colorectal cancer: can we predict local recurrence?

Kseniia Tumanova, Department of Medical Biophysics, University of Toronto, Toronto, Canada
k.tumanova@mail.utoronto.ca

Stefano Serra, Department of Laboratory Medicine and Pathobiology, University of Toronto, Toronto, Canada

Anamitra Majumdar, Department of Medical Biophysics, University of Toronto, Toronto, Canada

Jigar Lad, Department of Medical Biophysics, University of Toronto, Toronto, Canada

Fayez Quereshy, Department of Surgery, University of Toronto, Toronto, Canada

Mohammadali Khorasani, Department of Surgery, University of British Columbia, Victoria, Canada

Alex Vitkin, Departments of Medical Biophysics and Radiation Oncology, University of Toronto, Toronto, Canada

Introduction

Colorectal cancer (CRC) is a widespread oncologic disease, with local recurrence (LR) occurring in up to 50% of patients following primary curative surgery. Detecting LR promptly is vital, as aggressive treatment of LR can significantly improve survival rates. The architecture of peri-tumoural stroma, which is predominantly composed of collagen, has been shown to play a critical role in the response to therapy and patient outcomes in CRC. Utilizing the anisotropic properties of collagen, which strongly interacts with polarized light, Mueller matrix (MM) polarimetry presents a quantitative method for analyzing the microenvironment of cancerous tissues. This technique could serve as a valuable tool for prognostication in CRC.

Methods

We conduct our analysis on 38 stage III CRC patient samples, utilizing MM polarized light microscopy on unstained histology slides. By employing MM transformation and polar decomposition parameters, we assess their correlation with 5-year LR outcomes in patients.

Results

The analysis identified statistically significant differences (p -value < 0.05) in anisotropy- and retardance-related polarimetric parameters when comparing patients with and without LR (Fig. 1). Higher values in recurrent CRC patients suggest structural collagen reorganization, indicating a higher risk of LR. These results were obtained using the Mann-Whitney U test, highlighting the potential prognostic relevance of MM polarimetry parameters.

Conclusions

MM parameters may be prognostically valuable towards improving clinical management/treatment stratification in CRC patients. However, further advancements and refinements are necessary to translate these promising results into potential clinical applications.

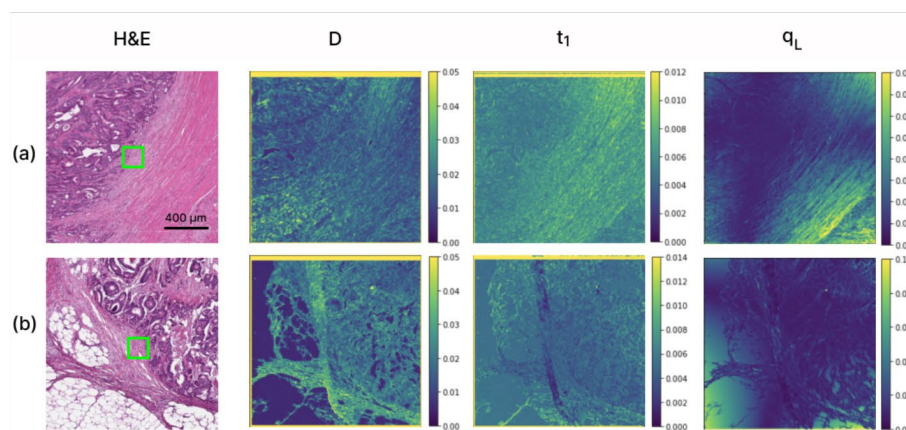


Fig. 1 – Mueller matrix polarimetry of human stage III left-sided colorectal cancer. H&E, diattenuation (D), anisotropy degree (t_1) and linear-to-circular polarization conversion (q_L) images around a particular ROI (green boxes on the H&E) are shown in: (a) a LR-free patient; (b) a patient with 5-year LR.

Session 9 Talks: Image-Guided Intervention

Abstracts

Percutaneous nephrostomy needle guidance using real-time 3D anatomical visualization with live ultrasound segmentation

Andrew Kim¹, Chris Yeung¹, Robert Szabo², Kyle Sunderland¹, Rebecca Hisey¹, David Morton¹, Parvin Mousavi¹, Tamas Haidegger², Tamas Ungi¹, Gabor Fichtinger¹

¹Queen's University, Kingston, ON, Canada; ²Óbuda University, Budapest, Hungary

INTRODUCTION: Obstructive uropathy accounts for approximately 10% of all cases of renal failure[1]. Across several studies, urinary obstruction was the most common indication for percutaneous nephrostomy (PCN)[2]. PCN is a commonly performed procedure to drain urine to provide relief in patients with hydronephrosis. Conventional PCN needle guidance methods can be difficult, expensive, or not portable. In sub-Saharan African countries such as Senegal, patients requiring PCN are not seen until the hydronephrosis becomes more severe because of the low prevalence of trained urologists. In these areas, a low-cost, portable solution would greatly improve the likelihood of patients receiving PCN to relieve their symptoms. With this in mind, we propose an open-source real-time 3D anatomical visualization aid system for needle guidance with live ultrasound segmentation and 3D volume reconstruction using free, open-source software. **METHODS:** Basic hydronephrotic kidney phantoms were created, and recordings of the phantom models were manually segmented on 3D Slicer: a free, open-source platform for medical image visualization and analysis [3]. We trained a u-net with the nnU-Net[5] method on our data and deployed it as a real-time service (<https://github.com/SlicerIGT/aigt>). Electromagnetic tracking was utilized on the ultrasound probe and needle for spatial tracking. We wrote a program to process ultrasound input frame-by-frame, make predictions on each frame using the prediction model, and project both ultrasound input and segmentation predictions to 3D Slicer in real-time for every frame. We utilized modules within the SlicerIGT extension [4] to reconstruct a 3D volume using these live segmentation predictions[6]. Novice participants received a presentation on the two needle guidance methods and their goal being to draw water from the needle at their final placements and had 15 minutes to practice each method. They performed 5 needle insertions with the visualization aid and 5 insertions with ultrasound needle guidance on a kidney phantom in randomized order, and these were recorded. Recordings of the trials were analyzed for needle tip distance to the center of the target calyx, needle insertion time, and success rate. Participants also completed a survey on their experience.

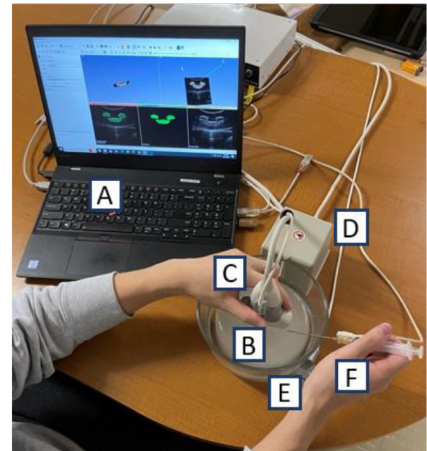


Fig 1. Experimental setup: Navigation computer (A), kidney phantom (B), ultrasound probe (C), field generator (D), reference sensor (E), needle with hub sensor and syringe (F).

RESULTS: Using our visualization aid showed significantly higher accuracy of needle placement, while needle insertion time and success rate were not statistically significant at our sample size (Table 1). Participants responded positively to the visualization aid and 80% found it easier to use than ultrasound needle guidance (Table 2).

Table 1. Participant performance metrics for 3D and ultrasound needle guidance methods (N = 25, *, $p < 0.01$).

Parameter	Visualization Aid	US Needle Guidance
Needle insertion time (s)	16.7 ± 7.8	21.3 ± 12.3
Needle tip to target distance (mm)	*5.3 ± 2.5	13.4 ± 6.0
Success rate (%)	64	52

Table 2. Survey results of participant experience (N = 5, *, $p < 0.01$).

Parameter	Visualization Aid	US Needle Guidance
Mean ease of use score (out of 10)	7.8 ± 2.99	7.2 ± 0.75
Median ease of use score (out of 10)	9	7
Participant preference (%)	80	20

CONCLUSIONS: We found that our visualization aid produced increased accuracy of the needle placement compared to US needle guidance and an overall positive experience. We demonstrated that our system is functional and believe that the workflow with this system can be applied to other procedures. This visualization aid system is effective on phantoms and is ready for translation in concept with clinical data.

REFERENCES: [1] Siddiqui et al., Medical Clinics of North America 2011. [2] Dagli et al., Seminars in Interventional Radiology 2011. [3] Fedorov et al., Magn. Reason. Imaging 2012. [4] Ungi et al., Medical Image Analysis 2016. [5] Isensee et al., Nature Methods 2021. [6] Hu et al., IJCARS 2022.

3D-printed liver tumour flow model for simulating embolization procedures

David Ng^{1,2}, Hristo N. Nikolov¹, Elizabeth Tai³, Leandro C. Leite³, Daniel Gelman¹, David W. Holdsworth^{1,2}, and Maria Drangova^{1,2}

¹Robarts Research Institute, ²Department of Medical Biophysics, ³Department of Medical Imaging, Schulich School of Medicine and Dentistry, Western University

Introduction: Transarterial chemoembolization (TACE) is commonly used to treat liver cancer. TACE involves the injection of small particles into tumour-feeding arteries to restrict blood flow and slowly administer chemotherapy. Clinicians rely primarily on visual cues from real-time x-ray imaging to monitor and determine when to stop the procedure [1]. Partial stoppage of blood flow to the tumour can be chosen to minimize liver toxicity and allow for multiple TACE sessions [2]. Complete stoppage can be chosen to increase necrosis and prevent drug washout. Therefore, clinicians need to be able to distinguish between different degrees of vessel obstruction, especially towards the end of the procedure where excess injections can lead to a backflow of particles that can block flow to healthy tissue [3]. The objective of this study was to develop a flow model for simulating embolization procedures that mimics anatomical, hemodynamic, and radiographic properties of a liver with a tumour, with applications in training interventional radiologists as well as in research programs to improve embolization therapy.

Methods: A liver model with an exchangeable, single-use tumour model was designed and fabricated using 3D-printing in polylactic acid plastic. To overcome the difficulty of 3D printing small individual vessels, gyroid patterns with small winding and branching pathways were used to simulate tumour microvasculature. A proof-of-principle tumour vessel model was designed to have a 1.5 cm sphere made of gyroid patterns with gradually decreasing pore sizes which provided restrictive passages that trap embolic material. Blood flow properties were replicated using a pulsatile flow pump containing a glycerol-water mixture. Hepatic artery flow resistance was mimicked by adding calculated lengths of small-bore tubing to each outlet vessel. Tissue-mimicking material was introduced around the liver model to produce uniform x-ray images and appropriate x-ray scatter. A state-of-the-art clinical fluoroscopy system was used to provide real-time x-ray imaging while simulating embolization procedures with the liver model. Three tumour models were embolized with 500–700 μm beads, with each procedure culminating in reflux being observed in the feeding artery.

Results: Uniform x-ray images were produced by surrounding the liver model with a baking soda and cornmeal mixture (44%:56%). Contrast agent injections revealed a tumour blush (Fig. 1a) created by the gyroid patterns. Embolization of the liver model proceeded gradually with contrast agent accumulating in the tumour over time where reflux developed (Fig. 1b) after injecting 5.4 ± 2.4 mL of a bead/contrast mixture. The pulsatility of the blood mimicking fluid was clearly seen when contrast agent was injected, which allowed the counting of pulses before the contrast agent left the vessel.

Conclusions: The liver flow model was able to replicate key visual characteristics of embolization procedures. Multiple bead injections were required to block the tumor model, allowing visual differentiation of various perfusion levels, including backflow, which provides feedback on over-injection. The 3D printed modular flow model design facilitates the reusability of the liver model following embolization and can easily be adapted to support larger tumor sizes, allowing for a more efficient and versatile tool for embolization training and research applications.

References: [1] Lu et al. *Hepatobiliary Surg Nutr.* 2021;**10**:661-671. [2] Liapi and Geschwind *Cardiovasc Intervent Radiol.* 2011;**34**:37-49. [3] Malagari et al. *Intervent Radiol.* 2011;**34**:774-785

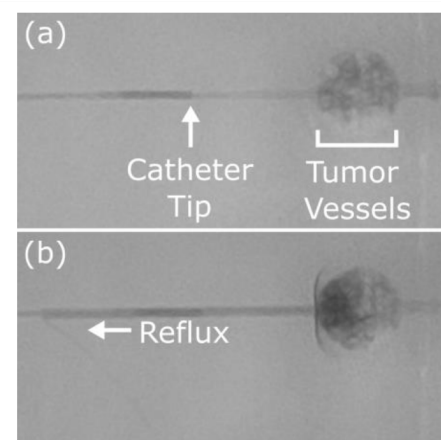


Fig. 1 X-ray image of contrast agent flowing through the tumor model with (a) unobstructed flow, (b) backflow into a neighbouring vessel

Feasibility study of using YOLOv8 for cataract surgical tool detection in surgical microscope videoJianming Yang¹, Rebecca Hisey¹, Joshua Bierbrier¹, Christine Law¹, Gabor Fichtinger¹, Matthew Holden²¹Queen's University, Kingston, Ontario, Canada, ²Carleton University, Ottawa, Ontario, Canada

Introduction: Surgical skill assessment sets proficiency benchmarks and offers feedback, facilitating surgeons' continuous improvement while aiming for successful surgery outcomes. There is a growing need for a computer-assisted assessment system that would reduce the time and effort required from expert reviewers evaluating surgical performance and providing objective feedback. Recently, Hisey et al. developed a method for automatic skill assessment in cataract surgery based on tracking instruments using object detection and validated this approach in a simulated training environment [1]. This approach involved first detecting the surgical instruments in microscope videos and tracing their movements to compute objective metrics that could be used for skill assessment. While validating this approach to automatic skill assessment in a simulated setting was valuable, the trained model was inherently underfitted to clinical data's complexity and variability. As it was also important that these methods can translate to the clinical setting and provide objective feedback, we aimed in this work to establish whether the object detection model, YOLOv8 is capable of recognizing surgical tools in videos recorded during cataract surgery. (See more technical details in <https://github.com/ultralitics/ultralitics>.)

Methods: The Kingston Health Sciences Centers operation room dataset was composed of 12 cataract surgery videos recorded using a binocular surgical microscope with monocular recording. The videos ranged in length from 570s to 1118s at 30 FPS and include the first four phases of the procedure, terminating after capsulorhexis.

Of the 12 recorded procedures, 6 procedures were performed by ophthalmology residents and 6 were completed by expert ophthalmologists. Videos were divided into individual frames and a subset of every 10th frame was manually annotated with bounding box locations for 8 object classes, including: iris (position reference for tools), eye speculum, forceps, diamond keratome straight, viscoelastic cannula, cystotome needle, diamond keratome iso, and capsulorhexis forceps (Figure 1). We trained a YOLOv8 model on the images with annotation and evaluated this network using a leave-two-video-out cross-validation method. This resulted in 6 folds: with each fold consisting of 8 videos for training, 2 videos for validation, and 2 videos for testing, ensuring each video was included in the test set once. The predictions were evaluated by the standard benchmark metrics for object detection: mean average precision (mAP) at a 50% intersection over union (IOU) threshold (mAP50) and the average mAP at IOU thresholds between 50-95% (mAP50-95).

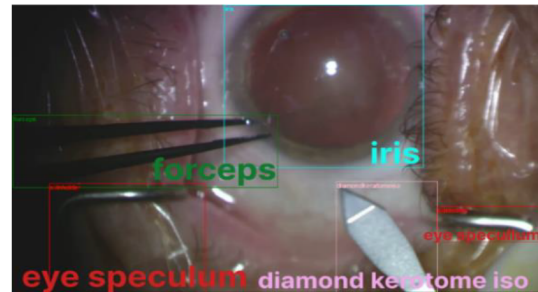


Fig 1. Labelled objects in differently coloured bounding boxes.

Results: The average number of instances of each class is presented in Table 1 along with the mAP results for each class. The model achieved an average mAP50 of 95%, while the average of mAP50-95 was 79.8%. All classes achieved a mAP50 of greater than 90%. The eye speculum and the forceps had the comparatively lowest performance when subject to the stricter IoU thresholds. In contrast, the iris class had the highest mAP in both benchmark metrics.

Conclusions: The average of both benchmark metrics of YOLOv8 showed comparable results to the previous research [1] which already demonstrated feasibility for skill assessment using a detection model. The challenges in recognizing classes like eye speculum and forceps were likely due to occlusions, reduced image quality and motion artifacts. By incorporating more surgical video data, we expected to mitigate these quality issues, thereby improving surgical instrument recognition. Overall, the results suggested that YOLOv8 was a promising model for surgical tool detection in clinical data, and it had the potential to deliver valuable inputs for the automatic skill assessment approach.

References: [1]. Hisey et.al. (2023) Objective skill assessment for cataract surgery from surgical microscope video. *TBME*. (In Revision).

Table 1. Object Instance and Prediction Performance

	Instance	mAP50 (%)	mAP 50-95 (%)
iris	6442	99.4	94.1
eye speculum	12706	92.6	65.3
forceps	1341	93.9	68.5
diamond keratome straight	417	95.0	79.4
viscoelastic cannula	630	91.8	80.8
cystotome needle	889	95.2	82.3
diamond keratome iso	548	94.1	82.6
capsulorhexis forceps	1950	97.9	85.8
Average	---	95.0	79.8

Photoacoustic detection of residual cancer in breast-conserving surgery

Laura Connolly^{1,2}, H. Song², K. Xu², A. Deguet², S. Leonard², G. Fichtinger¹,
P. Mousavi¹, R. H. Taylor², E. Boctor²

1. Queen's University, Kingston, Canada, 2. Johns Hopkins University, Baltimore, USA

INTRODUCTION: Residual cancer tissue often remains on the surface of the tumor bed after breast-conserving surgery (BCS). Histological analysis of the excised tumor specimen can be used to identify cancerous tissue but precludes intraoperative correction and necessitates revision surgery. Furthermore, this approach may lead to false positives when a thick layer of tissue is cauterized during resection, because cancerous tissue that is presumed to be left behind had been actually incinerated at the specimen border. This problem is exacerbated when surgical navigation and advanced imaging techniques are used to achieve narrow resection margins. Photoacoustic imaging is an emerging modality that shows promise for identifying residual cancer in BCS procedures. This technique relies on the photoacoustic effect, which occurs when pulses of laser light induce localized, optical absorption-based thermal expansion [1]. This expansion of tissue generates an acoustic wave that an acoustic receiver, like a conventional ultrasound probe, can detect. Targeted contrast agents can further enhance this effect to help differentiate distinct pathologies [2]. In this paper, we present a proof of concept for photoacoustic tumor bed inspection and preliminary results from benchtop testing.

METHODS: Our proposed methodology is that a targeted photoacoustic contrast agent is injected preoperatively, and BCS proceeds as usual. After the tumor has been removed, a tracked laser light source is used to systematically illuminate the surface of the tumor bed while an ultrasound probe is fixed to the outside of the breast to detect the absence or presence of the induced photoacoustic signal (Fig. 1) [3]. We used an Ultrasonix L14-5 ultrasound probe (BK Medical, USA), with a frequency range of 5-14 megahertz and a field of view of approximately 38 millimeters. If the tissue at a given illumination spot induces a photoacoustic signal, we presume that the piece of tissue has taken up the contrast agent and is considered as residual cancer.

We performed benchtop testing to demonstrate this approach using a robot to guide the laser for precise positioning and a fixed ultrasound probe on the outside of the breast. We created 3 tissue-mimicking phantoms in the shape of a resection cavity, with a tattoo ink (a photoacoustic agent) dispersed in place of residual cancer and common plastisol in place of healthy tissue (Fig. 1, bottom left). The cavity was propped open with a 3D-printed retractor to reveal the surface of the tumor bed. The phantom was imaged with the proposed technique, and the raw ultrasound data was monitored at every given illumination point. The position of the laser spot was marked with a red dot if a photoacoustic signal was detected at that scan point, overlaid on a volume reconstructed from a CT of the phantom (Fig. 1, bottom right).

RESULTS: In a series of 3 experiments, 1 scan per phantom, our method demonstrated an average specificity of 95.5% and sensitivity of 11.6%. The false negatives, which contribute to the low sensitivity, presumably occurred when the acoustic wave was outside of the field of view of the receiver.

CONCLUSIONS: We have shown the viability of this method using simulated tumor bed conditions. One of the limitations of this work is that the results were obtained using a single ultrasound probe orientation, and detection of the photoacoustic signal is highly sensitive to probe directivity. In the future, this could be addressed by using a 3D ultrasound transducer, a probe with a broader field of view, or a wobbler probe. For future clinical translation, the deployment of the laser should follow the existing standards in place for laser ablation.

REFERENCES: [1] Attia, A.B.E., et. al. A review of clinical photoacoustic imaging: Current and future trends. *Photoacoustics* 16, 100144 (2019). [2] Wu, Y et. al. System-level optimization in spectroscopic photoacoustic imaging of prostate cancer. *Photoacoustics* 27, 100378 (2022). [3] Connolly, L. et. al. Photoacoustic tumor bed inspection: a testbed and proof of concept. *International Conference on Information Processing in Computer-Assisted Interventions (IPCAI) 2024* (In review).

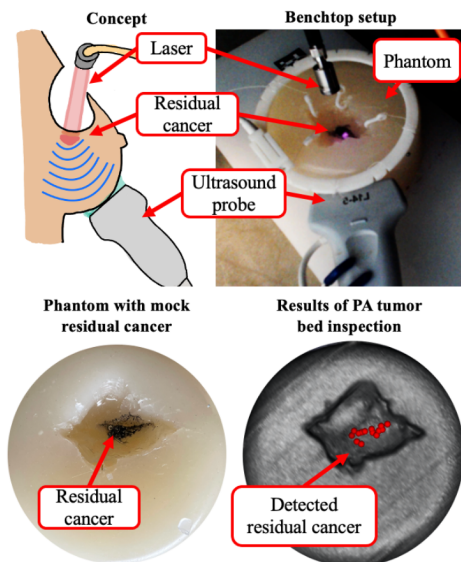


Fig 1: Top left: Concept overview. Top right: Benchtop testing setup. Bottom left: RGB image of one of the tumor bed phantoms. Bottom right: Detected residual cancer on sample phantom with new technique.

Session 10 Talks: Neuroimaging 1

Abstracts

Resting state functional brain activity differs by sex in pediatric concussion.

Bhanu Sharma^{1,4,5,*}, Cameron Nowikow^{4,6}, Carol DeMatteo^{2,3}, Michael D. Noseworthy^{4,5,6,7}, Brian W. Timmons^{1,3}

Affiliations: ¹Child Health and Exercise Medicine Program, Department of Pediatrics, McMaster University, 1280 Main Street West, Hamilton, ON L8S4L8, Canada. ²School of Rehabilitation Science, McMaster University, Hamilton, Canada. ³CanChild Centre for Childhood Disability Research, McMaster University, Hamilton, Canada. ⁴Imaging Research Centre, St. Joseph's Healthcare, Hamilton, ON, Canada. ⁵Department of Electrical & Computer Engineering, McMaster University, Hamilton, Canada. ⁶McMaster School of Biomedical Engineering, McMaster University, Hamilton, Canada. ⁷Department of Radiology, McMaster University, Hamilton, Canada. *Presenting author.

Introduction: Concussion, one of the most common pediatric injuries, can result in persistent symptoms in up to 30% of cases. Sex-differences have been reported with respect to subjective measures of symptom burden in both pediatric and adult concussion, wherein females report more symptoms and symptoms with greater severity than males. However, less is understood as to whether objective functional measures of concussion differ by sex. Data from adults suggests that in a pattern similar to symptom burden, females with persistent concussion symptoms also demonstrate greater resting state fMRI (rs-fMRI) functional connectivity impairments. Our goal was to perform the first analysis of sex-specific differences in resting state functional connectivity in pediatric concussion.

Methods: We performed a secondary data analysis of prospectively collected rs-fMRI data on 29 children with concussion (aged 12-18 years, 13 females), recruited from McMaster Children's Hospital. We compiled a large healthy control database (at a 12:1 ratio, matching for age and sex) from open-source neuroimaging data available through the ABIDE-II database, originally created for research on autism. We performed seed-based and ROI-analyses to determine group- and sex-effects, using threshold-free cluster enhancement (TFCE) and family-wise error (FWE) corrections during analysis.

Results: In comparing females with concussion to healthy females, groupwise differences were observed irrespective of seed selected. We observed (in order of largest effect) hypo-connectivity between the anterior cingulate cortex of the salience network and the thalamus and precuneus (TFCE = 1473.5, p-FWE < 0.001) and the cingulate gyrus (TFCE = 769.3, p-FWE = 0.009), and the seed (posterior cingulate cortex (PCC)) of the default mode network and the paracingulate gyrus (TFCE = 1275.7, p-FWE < 0.001). Hyper-connectivity was observed between the salience network seed and the cerebellum (TFCE = 1719.3, p-FWE < 0.001) and the PCC and the thalamus (TFCE = 1198.3, p-FWE < 0.001), cuneal cortex (1070.9, p-FWE = 0.001), and lateral occipital cortex left (TFCE = 832.8, p-FWE = 0.006). In comparison, only one cluster was found to differ between healthy males and males with concussion. ROI-to-ROI differences were observed between females with concussion vs. healthy females (**Figure 1**), with absence of such change in males.

Conclusions: These data show that similar to adults, in pediatric concussion there are greater rs-fMRI disturbances in females vs. males. These findings offer a potential explanation for the sex-specific symptom profiles in pediatric concussion.

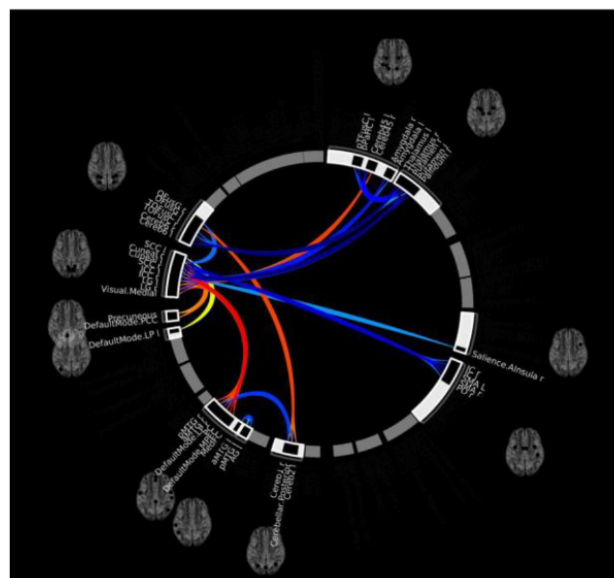


Figure 1: Inter-region hypo- (cool colour) and hyper-connectivity (warm colour) in females with concussion vs. healthy females.

An fMRI-informed transcranial magnetic stimulation protocol improved memory performance

Hsin-Ju Lee^{1,2}, Fa-Hsuan Lin^{1,2}

¹ Physical Sciences Platform, Sunnybrook Research Institute, Toronto, Canada

² Department of Medical Biophysics, University of Toronto, Toronto, Canada

Introduction

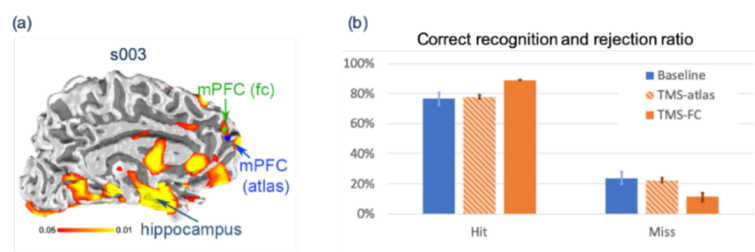
Memory integrity is crucial for species survival. However, our memory capacity diminishes as we age. In Alzheimer's disease (AD) patients, the hippocampus, a critical neural substrate supporting episodic memory formation, demonstrates degenerative changes. To date, there is no medication available to prevent such degeneration. In animals and humans suffering from neurodegenerative diseases, direct electrical stimulation of the hippocampal region can help maintain neuronal function. However, this technique is invasive and limits its use in clinical practice. Transcranial magnetic stimulation (TMS) is a non-invasive brain circuitry modulatory method for treating brain disorders, such as major depression disorder (MDD), to induce network-based neuroplastic changes. TMS has shown improving clinical outcomes for MDD. In this study, we delivered TMS pulses to functionally connected cortical regions in healthy adults and examined whether the memory function can be altered.

Methods

One session of magnetic resonance imaging (MRI) and two sessions of TMS were performed for each participant. Informed consents were obtained from all participants after approval by the Research Ethical Committee of Sunnybrook Hospital. MRI data were acquired on a 3T MRI (Prisma, Siemens) with a 64-channel whole-head coil array. Anatomical MRI was collected with a magnetization-prepared rapid gradient echo (MPRAGE) pulse sequence with 1-mm isotropic resolution. Resting-state functional magnetic resonance imaging (fMRI) was acquired using T2*-weighted echo-planar imaging (TR/TE = 2000/36 ms, flip angle = 90°, 24 slices, 3-mm isotropic resolution). FreeSurfer was used to automatically label the hippocampus, including its subfields, from anatomical MRI. Resting-state fMRI was used to reveal the functional connectivity of the hippocampus by correlating the average fMRI time series within the anatomically defined hippocampus and the whole brain. The TMS target at the medial prefrontal cortex (mPFC) was either an individual's functional connectivity centroid to the hippocampus (*fc* condition) or a common anatomical landmark (*atlas* condition). The mPFC target was delivered with an intermittent theta-burst (iTBS; 50-Hz inter-pulse-interval; 3 pulses per train; 200 ms inter-train interval; 600 pulses in total) protocol by a figure-of-eight coil (MRi-B91, MagVenture, Denmark) connected to a TMS stimulator system (MagPro X100, MagVenture, Denmark). The TMS coil was placed and oriented under neuronavigation guidance (Rogue Research). A memory task consisting of two phases was used to test memory function. In the encoding phase, participants were instructed to distinguish between animal or non-animal images. After 20 minutes in retrieval phase, participants distinguished between old and novel images. A distractor task was performed between two phases. The memory performance was quantified by the percentage of correctly identified (hit; shown in encoding and recognized in retrieval) and missed (miss; shown in encoding but not recognized in retrieval) images.

Results

Fig. (a) shows the functional connectivity to the hippocampus during the resting-state fMRI in one representative participant. The brain dynamics at mPFC were significantly correlated with the hippocampus. However, the centroids of the mPFC functionally connected to the hippocampus (*mPFC (fc)*; green dots) deviated from the atlas coordinate by 5.0 mm. According



to our preliminary results (N=3), delivering the iTBS at the mPFC, the memory function was found improved by increasing the detection of old items (Hit↑ and Miss↓): Hit: 76% Baseline; 78% TMS-atlas; 89% TMS-FC; Miss: 24% Baseline; 22% TMS-atlas; 11% TMS-FC (**Fig. (b)**). This performance improvement was significantly larger for targeting the personalized mPFC region (*TMS-fc*) than the atlas coordinate (*TMS-atlas*).

Conclusions

We demonstrated that iTBS of the mPFC determined by the individual's resting-state fMRI leads to significant memory improvement, compared to TMS targeting at an atlas coordinate. The results suggest that individual brain mapping is a promising way to improve the neuromodulatory efficacy of TMS.

Investigating cortical GABA+ and Glx Levels in Individuals with Social Anxiety Disorder (SAD) Using Proton Magnetic Resonance Spectroscopy

Sonja Elsaid^{1,3}, Ruoyu Wang¹, Stefan Kloiber^{1,3,4}, Kimberly L. Desmond³, and Bernard Le Foll^{1,3}

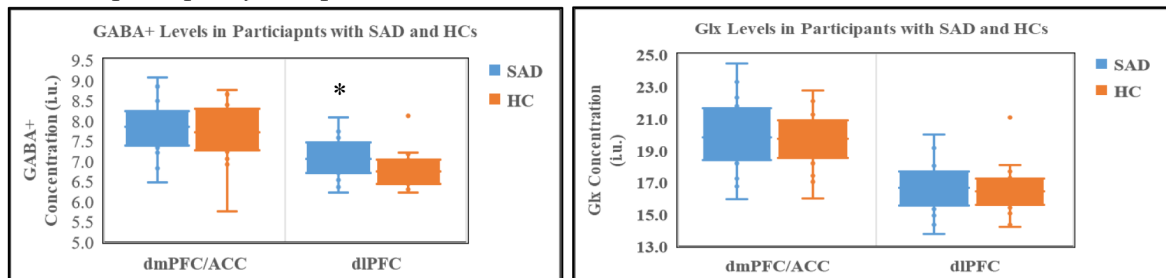
¹Institute of Medical Science, University of Toronto; Toronto, ON; ²Translational Addiction Research Laboratory, Centre for Addiction and Mental Health (CAMH), Toronto, ON; ³Brain Health Imaging Centre, CAMH, Toronto, ON; ⁴Campbell Family Mental Health Research Institute, CAMH, Toronto, ON

Introduction: Individuals with Social Anxiety Disorder (SAD) experience significant dysfunction in all aspects of life¹. The implicated pathophysiologies may be related to dysregulation in the ‘fear neurocircuitry’². In recent studies, downregulated γ -aminobutyric acid (GABA)+ was associated with social anxiety in the dorsomedial prefrontal cortex and anterior cingulate cortex (dmPFC and ACC). However, these imbalances still have not been fully investigated in other brain regions, such as the dorsolateral prefrontal cortex (dlPFC)². Thus, our objective was to investigate levels of GABA+ and Glx (glutamix: glutamate + glutamine) in dmPFC/ACC and dlPFC in individuals with SAD in comparison to their sex-age-matched healthy controls (HCs).

Methods: Twenty-six participants with a mean age: 25.3 ± 5.0 ; 61.5 % F; who on the Liebowitz Social Anxiety Scale (LSAS)³ scored 98.1 ± 13.6 for total scores, 50.7 ± 8.0 for LSAS Anxiety, and 47.4 ± 8.2 for LSAS Avoidance subscale) were compared to 26 HCs (mean age: 25.2 ± 4.4 61.5 % F; LSAS Total: 7.8 ± 6.3 ; LSAS Anxiety: 5.2 ± 4.4 ; LSAS Avoidance: 2.5 ± 3.7). Both groups were scanned with a GE MR750 3T scanner, which uses a 32-channel head coil (Nova Medical). GABA+ and Glx data were acquired with MEGA-PRESS⁴ (MEscher-GARwood Point RESolved Spectroscopy) sequence, using sequence parameters: TE/TR=68/1500ms, 384 averages, and acquisition time=10.4 min. GABA+ and Glx peaks were quantified with Gannet 3.1.5⁵. GABA+ and Glx were reported in institutional units (i.u.), whereby water signal was used as an internal water reference, with both water and metabolites corrected according to Gasparovic et al., 2006⁶. Following data processing, the spectral quality check was performed, and poor-quality data points were removed⁷.

Results:

* $p \leq 0.05$;
** $p \leq 0.01$



Correlation for SAD Participants (Pearson's r)	LSAS Anxiety	LSAS Avoidance	Total LSAS
GABA+ dmPFC/ACC (n = 25)	-0.70**	-0.25	-0.56**
Glx dmPFC/ACC (n = 24)	-0.57**	-0.15	-0.42*
GABA+ dlPFC (n = 22)	-0.15	0.29	0.08
Glx dlPFC (n = 22)	-0.13	0.26	0.07

Conclusion: GABA+ levels were higher in dlPFC in SAD participants than in HCs, possibly indicating the loss of GABA_A receptors and decreased degradation of GABA⁸. Although no between-group differences in GABA+ or Glx were shown in dmPFC/ACC, decreases in both GABA+ and Glx with the increasing severity of SAD may indicate neuronal and glial cell damage in dmPFC/ACC as SAD progresses². Given that dlPFC is involved in selecting sensory information to be brought to conscious awareness, dlPFC impairments may lead to ‘mistakenly’ interpreting some social cues as threatening. Disturbances in the dmPFC/ACC may contribute to improper inhibition of the limbic system and consequently the ‘misinterpretation’ of the sensory signal also as threatening. The implied aberrances in neurocircuitry may be manifested as symptoms of SAD. The demonstrated disturbances in dmPFC/ACC and dlPFC may serve as molecular targets for novel pharmacological treatments for SAD.

References: ¹Kessler et al. *Arch Gen Psych*, 2005; ²Elsaid et al., *In J of MedSci*, 2022; ³Liebowitz *Mod Prob of Pharmpsych*, 1987; ⁴Mescher et al., *NMR Biomed*, 1998; ⁵Edden et al., *J of MRI*, 2013; ⁶Gasparovic et al., *Magn Reason Med*, 2006; ⁷De Graaf, *In Vivo MRS Spect.*, 2009; ⁸Michaels et al., *Prelim Find of Psych Research*, 2014.

Microstructural MRI Evolution During Adult Mouse Brain MaturationNaila Rahman^{1,3}, Jake Hamilton^{1,3}, Kathy Xu^{2,3}, Arthur Brown^{2,3}, Corey A. Baron^{1,3}*Department of Medical Biophysics, Western University, London, ON, Canada¹ Department of Anatomy and Cell Biology, Western University, London, ON, Canada² Robarts Research Institute, London, ON, Canada³*

Introduction: Although rodent models are a predominant study model in neuroscience imaging research, there is limited research characterizing healthy rodent brain maturation. This motivates further study of normal brain maturation in rodents to exclude confounds of cerebral developmental changes from interpretations of disease and injury mechanisms and better understand the contrast mechanisms of microstructural MRI metrics. Here, we explore the evolution of tensor-valued diffusion MRI (dMRI) and magnetization transfer saturation (MTsat) MRI, which is specific to changes in myelin content¹, in mice *in vivo*. Beyond conventional dMRI, tensor-valued dMRI is useful to separate various sources of diffusion kurtosis² (total (K_{total}), isotropic (K_{iso}), and anisotropic (K_{aniso}) kurtosis), which quantifies the deviation of water diffusion away from Gaussian diffusion. Changes to K_{iso} and K_{aniso} reflect changes to cell size heterogeneity and changes to fiber microstructure, respectively.

Methods: 11 C57Bl/6 mice (5 females) were scanned longitudinally on a 9.4 T Bruker small animal scanner at 4 timepoints: 3, 4, 5, and 8 months of age. The tensor-valued dMRI protocol consisted of linear and spherical tensor encoded acquisitions with b-value shells of 1000 s/mm² (12 directions) and 2000 s/mm² (30 directions) with parameters: in-plane resolution 175 x 200 μ m, slice thickness 500 μ m, TE/TR = 26.8/10000 ms, 3 averages, total scan time of 45 minutes. The MTsat protocol included three FLASH-3D scans and one B1 map scan to correct for local variations in flip angle.

ROIs investigated included global white matter, deep gray matter and cortex (WM, DGM, CX, respectively). To first investigate if the MRI metrics changed significantly over time, repeated measures MANOVAs were performed for each metric, over all ROIs. Metrics with a significant MANOVA were followed up by separate ANOVAs within each ROI, and then by Tukey HSD test to determine differences across time. DAPI and Olig2 staining, to stain for nuclei and oligodendrocytes, respectively, were performed at 3 and 8 months of age to acquire a ground truth.

Results: K_{total} revealed significant increases over time in all ROIs, which was driven by increases in K_{iso} while K_{aniso} remained stable (Figure 1). Increases in K_{total} and K_{iso} with age were matched with increases in MTsat. Immunohistochemistry revealed increases in oligodendrocyte (myelin forming cells in the brain) content in the hippocampus (Figure 2) at 8 months of age compared to 3 months, comparable to other brain regions and mice.

Conclusion: The trends observed here are comparable to literature in mice³ and humans⁴, while the trajectories of the tensor-valued dMRI metrics provide novel insight. Our results suggest myelination during brain maturation is not a main contributor to K_{aniso} in axons, which has been hypothesized previously³. In contrast, we show increased K_{total} is driven by K_{iso} , which may reflect increased oligodendrocyte content, which is linked to myelin formation, supported by increased MTsat. This work shows that there are ongoing microstructural changes even after mice are considered “adults” and provides new interpretations of dMRI changes during brain maturation.

References: 1. Helms et al. MRM (2008). 2. Szczepankiewicz et al. Neuroimage (2014). 3. Han et al. Brain Behav. (2021). 4. Lebel et al. Neuroimage (2018).

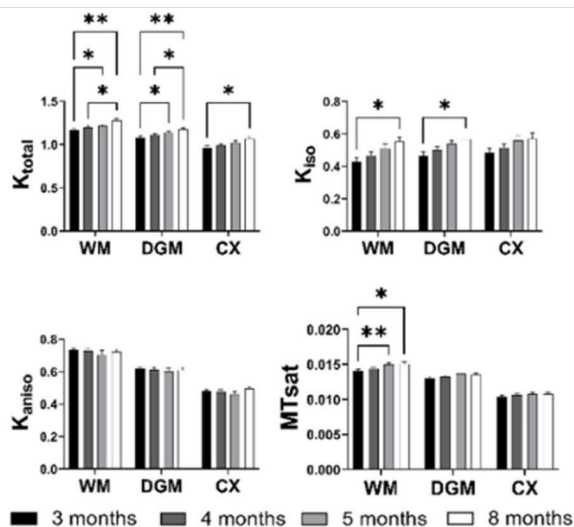


Figure 1. MRI parameter evolution in white matter (WM), deep gray matter (DGM), cortex (CX). Mean values with standard deviation (error bars) are shown. Asterisks represent significant results (* $p < 0.05$, ** $p < 0.01$, *** $p < 0.001$).

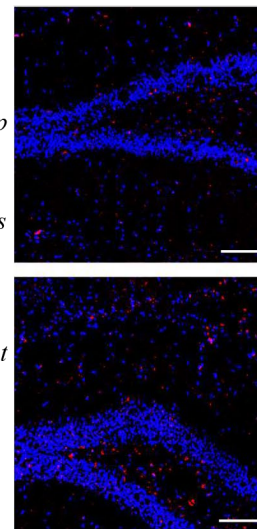


Figure 2. Olig2 (red) and DAPI (blue) staining showing oligodendrocytes and nuclei, respectively, in the dentate gyrus of the hippocampus. At 8 months (bottom panel), a marked increase is observed in oligodendrocyte content, compared to 3 months (top). Scale bar: 20 μ m.

Session 11 Talks: Cardiac and Lung

Abstracts

Novel 4D Flow MRI Technique Without Contrast Agents for Pediatric Congenital Heart Disease

Valérie Béland^{*1,2}, Datta Singh Goolaub^{*1}, Sharon Portnoy¹, Shi-Joon Yoo³, Christopher Z. Lam³, and Christopher K. Macgowan^{1,2}

¹Translational Medicine, The Hospital for Sick Children, Toronto, ON, Canada, ²Medical Biophysics, University of Toronto, Toronto, ON, Canada, ³Diagnostic Imaging, The Hospital for Sick Children, Toronto, ON, Canada

Introduction: Magnetic resonance imaging (MRI) is important for cardiovascular assessment, planning and giving appropriate treatment to patients with congenital heart disease (CHD). Most specifically, 4D flow is a valuable MRI technique as it provides a three-dimensional view of the heart, major vessels, and volumetric blood flow measurements. 4D flow often relies on injections of a contrast agent like gadolinium to make the blood flow appear brighter in the acquired images. However, contrast agents are contraindicated in patients with poor kidney function. Moreover, the systemic deposition of contrast agents and their long-term side effects are still under study, and in rare cases, can cause the development of nephrogenic systemic fibrosis.¹ To mitigate the need for a contrast agent, we have developed a novel 4D flow MRI reconstruction technique, hereafter referred to as slice-to-volume reconstruction (SVR) 4D Flow MRI. This approach acquires multiple slices with 2D phase contrast (PC) MRI. Each individual slice has freshly magnetized blood, providing a high blood signal. Slices are then reconstructed into a dynamic flow-sensitive volume with high resolution and blood signal. This study aims to validate the application of SVR 4D Flow MRI in pediatric patients with CHD.

Methods: 7 pediatric patients (9-18 years) with CHD were scanned on a clinical 1.5T MRI (Avanto^{FIT}, Siemens Healthineers) with informed consent. 2D PCMRI data were acquired using a spiral trajectory and continuous spatial shift (0.005mm/TR; TR = 7.5ms) in the slice direction. This constant spatial shift allows dense sampling in the slice direction and facilitates reconstruction. The spiral 2D PCMRI data were then combined into a volume using SVR 4D Flow MRI. For comparison, conventional cartesian 2D PCMRI data was acquired and used as a reference. Great vessels were segmented to analyze mean blood flow and track complex flows during a cardiac cycle.

Results: Across all vessels, SVR 4D Flow MRI agreed with cartesian 2D PCMRI ($F_{SVR\ 4D} = 1.02F_{2D\ PCMRI} - 4.8$, $r^2 = 0.95$, depicted in Figure 1). Bland-Altman analysis had a bias of 3.6 mL/sec with limits of agreement [-8.1, 15.4] mL/sec. Additionally, SVR 4D Flow MRI, provided dynamic volumetric magnitude images (Figure 2A), dynamic angiograms (Figure 2B), and particle traces (Figure 3) tracking blood through the heart of pediatric patients with CHD.

Conclusion: SVR 4D Flow MRI has a high slice in-flow effect, providing accurate flow quantification in the great vessels of the heart and high-quality anatomical and angiographic images without contrast agent injection.

Abbreviations

AAO: ascending aorta, DAO: descending aorta, IVC: inferior vena cava, LA: left atrium, LPA: left pulmonary artery, LV: left ventricle, MPA: main pulmonary artery, RA: right atrium, RPA: right pulmonary artery, RV: right ventricle, SVC: superior vena cava

References

[1] Rao, S., Madueme, P., Podberesky, D., & Cartoski, M. J. (2020). Cardiac magnetic resonance imaging and computed tomography for the pediatric cardiologist. *Progress in Pediatric Cardiology*, 58, 101273. <https://doi.org/10.1016/j.ppedcard.2020.101273>

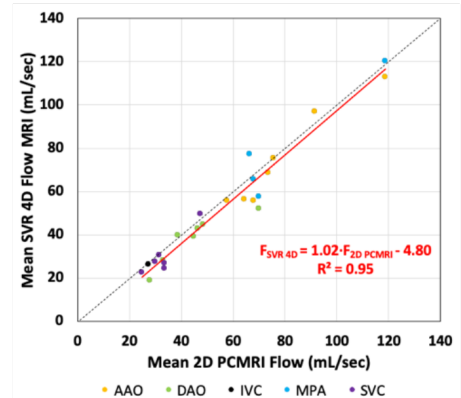


Figure 1. Linear regression comparing mean flow measurements from SVR 4D Flow MRI and Cartesian 2D PCMRI in the great vessels of pediatric patients with CHD

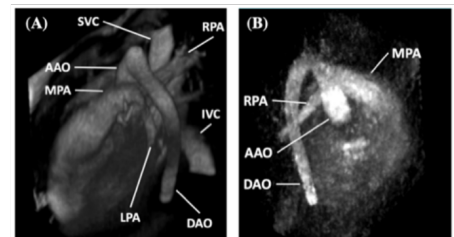


Figure 2. SVR 4D Flow MRI of patient with Ebstein anomaly (A) volumetric magnitude image depicts the cardiovascular anatomy, (B) angiogram image depicts the freshly magnetized blood in great vessels.

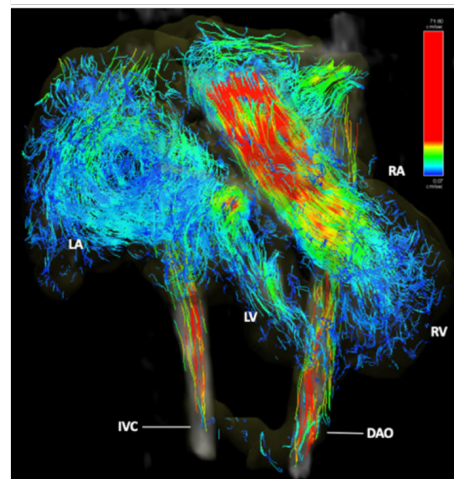


Figure 3. Particle traces of blood flow over a cardiac cycle in a pediatric patient with supervalvular aortic stenosis and Williams syndrome using SVR 4D Flow MRI.

Automated Diaphragm Dome Segmentation and Height Analysis for Chest CT Images in COPD

Daniel Genkin BEng¹, Sarah Beydoun BSc², Olivia Iorio BSc², Wan Tan MD³, Jean Bourbeau MD²,
Bryan Ross MD², and Miranda Kirby PhD⁴

¹Department of Electrical, Computer, and Biomedical Engineering, Toronto Metropolitan University, Toronto, Canada; ²Respiratory Epidemiology and Clinical Research Unit, Research Institute of McGill University Health Centre, Montreal, Canada; ³Center for Heart, Lung Innovation, University of British Columbia, Vancouver, Canada; ⁴Department of Physics, Toronto Metropolitan University, Toronto, Canada.

Introduction: Chronic obstructive pulmonary disease (COPD) is a progressive lung disease characterized by spirometry-defined airflow limitation and airway remodeling. However, skeletal muscle remodeling is a known extra-pulmonary manifestation of the disease^{1,2}. The diaphragm, which is the primary respiratory muscle, is known to lose its dome-like shape in COPD^{3,4}. To quantify diaphragm morphology on chest computed tomography (CT) imaging, existing approaches estimate the bottom surface of the lungs⁶ or rely on complex mathematical modeling⁷, but do not segment the structure itself. The objective of this study was to develop an automated diaphragm dome segmentation methodology. We hypothesize that a morphological biomarker extracted from diaphragm dome segmentations, known as diaphragm dome height, will have high agreement with manual measurements, discriminate healthy participants from those with COPD, and correlate with lung function.

Methods: Participants with and without COPD defined by spirometry from the Canadian Cohort Obstructive Lung Disease (CanCOLD)⁸ were included in this retrospective cross-sectional study. From the CT images, the left and right diaphragm dome heights were manually measured by two independent observers. A deep learning model was implemented to automatically delineate the abdominal and thoracic organs⁹. The overlap between a dilation (sphere, $r=5\text{mm}$) of the liver, spleen, stomach, intestinal tract, and the lower lung lobes was deemed the region-of-interest (ROI). Rays were then cast downwards in the ROI to identify the bottom-most points of each lung. Any voxel belonging to the cardiovascular structures, spine, spinal cord, intercostal space, and lungs restricted any leakage. The largest volume for each hemisphere after a 3D convex hull operation on the bottom-most points was isolated, and the diaphragm was segmented by removing any non-diaphragmic tissue in the space. The maximum perpendicular height between each dome base to the bottom surface of the lung for all slices was defined as the diaphragm dome height. Automated and manual dome height measurement agreement, differences between healthy participants and those with COPD, and associations with forced expiratory volume in 1 second (FEV_1) were quantified using the intraclass correlation coefficient (ICC), Mann Whitney U-test, and Spearman correlations, respectively.

Results: 87 participants were included: $n=45$ healthy (47% females; age= 66.7 ± 10.0 yrs; $\text{FEV}_{1\% \text{pred}}=102.3\pm 18.1\%$, $\text{FEV}_1/\text{Forced Vital Capacity (FVC)}=0.77\pm 0.05$) and $n=42$ with COPD (45% females; age= 67.2 ± 9.9 years; $\text{FEV}_{1\% \text{pred}}=83.0\pm 19.7\%$, $\text{FEV}_1/\text{FVC}=0.61\pm 0.08$). The automated diaphragm dome height measurement was successfully extracted from all participants and there was excellent agreement with manual measurements (Observer 1: Left (L) ICC=0.85 [0.77,0.90]; Right (R) ICC=0.92 [0.88,0.95]; Mean (M) ICC=0.91 [0.85,0.94]; Observer 2: L-ICC=0.82 [0.71,0.89]; R-ICC=0.78 [0.62,0.86]; M-ICC=0.81 [0.62,0.89]; Average: L-ICC=0.90 [0.85,0.93]; R-ICC=0.90 [0.85,0.93]; M-ICC=0.91 [0.87,0.94]). Furthermore, the automated diaphragm dome height (average between both hemispheres) was different between healthy participants and COPD (healthy: $34.7\pm 4.3\text{mm}$; COPD: $32.8\pm 5.8\text{mm}$; $p<0.05$), and correlated with FEV_1 measurements ($\rho=0.32$; $p<0.05$).

Conclusions: A novel, fully automated methodology to extract the diaphragm dome was successfully developed which demonstrated excellent agreement with manual measurements and was capable of quantifying greater flattening in COPD compared to healthy participants. Future studies will apply the automated methodology on a larger cohort, investigate measurement reproducibility, and investigate biomarkers characterizing diaphragmic remodeling in COPD, such as diaphragm shape-based measures and density-based metrics that reflect muscle quality.

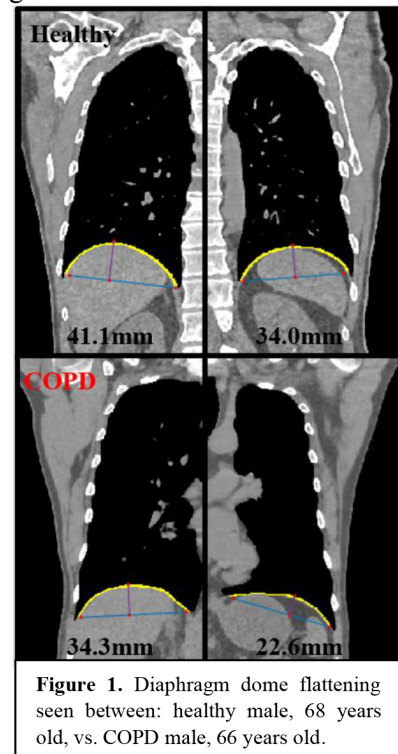


Figure 1. Diaphragm dome flattening seen between: healthy male, 68 years old, vs. COPD male, 66 years old.

References

¹Tanimura K, Am Thorac Soc. 2016; ²McDonald ML, Ann Am Thorac Soc. 2014; ³Salito C, Med Biol Soc. 2015; ⁴Ottenheim CA, J Respir Crit Care Med. 2005; ⁵Donovan AA, Ann Am Thorac Soc. 2021; ⁶Chang Y, Med Phys. 2016; ⁷Karami E, J Med Imaging. 2016; ⁸Bourbeau J, COPD. 2014; ⁹Wasserthal J, Radiol AI. 2023.

Physical replication and validation of mathematical mitral valve models

Patrick Carnahan^{a,b}, Charles C. X. Yuan^a, John Moore^a, Gianluigi Bisleri^c, Daniel Bainbridge^d, Terry M. Peters^{a,b}, and Elvis C. S. Chen^{a,b,e}

^a.Imaging, Robarts Research Institute, London, CA, ^c.Cardiac Surgery Department, St. Michael's Hospital, University of Toronto, Toronto, CA

^b.School of Biomedical Engineering, ^d.Department of Anesthesiology, London Health Sciences Centre, ^e.Electrical and Computer Engineering, Western University, London, CA

INTRODUCTION: Mitral valve (MV) disease affects 2% of the Canadian population and 10% of those over the age of 75, with approximately 20% of this group requiring surgical intervention.¹ Evidence indicates the volume of MV repair cases that a surgeon performs is a determinant not only of successful mitral repair rates, but also freedom from reoperation and patient survival.² Heart simulator technologies have been developed which rely on patient-specific data to create valve replicas for surgical training and planning. Alternatively, mathematical models of the mitral valve have been developed for computational applications, however, these models have not been replicated as dynamic, physical valve models and validated in a heart simulator system. We propose a new parametric representation of the mitral valve based on a combination of valve models from prior literature, combining both accurate leaflet shape, and annular geometry. Additionally, we utilize existing heart-simulator technology to validate our parametric MV model, replicated as a dynamic silicone physical valve.

METHODS: To create a valve that captures both leaflet and annulus geometry, we adapted existing mathematical mitral valve models from Shen *et al.* and Park *et al.*^{3,4} The work of Shen *et al.*³ describes a parametric model of the mitral leaflets based on a set of piece-wise elliptic cylinder equations, with a flat, elongated annulus. We adapt their equations to adjust the annulus shape in the $x - y$ plane by replacing the x and y components with a bean-shaped geometry given by $(ax + x^2 + y^2)^2 = a^2y$, where $a=1.2$. We have selected the parameter a for these equations to match the anterior-posterior (AP) diameter, and commissure-commissure diameter of a healthy valve. We then use the hyperbolic paraboloid model of the annulus from Park *et al.*⁴ to modify the annulus from a flat structure to the anatomically correct 3-dimensional saddle shape with the resulting geometry shown in Figure 1. The systolic valve model is then manufactured into a physical MV replica (Archetype Biomedical Inc.) and integrated into a pulse-duplicator system⁵. We adjust chordae tendineae lengths for six chordae integrated into the valve leaflets (2 anterior, one on each of P1 and P3, and two on the P2 leaflet) to best mimic healthy conditions. We simulate a prolapsed P2 leaflet by loosening the chordae tension to mimic a ruptured chord. We use a transesophageal echocardiography (TEE) probe to capture b-mode and colour Doppler ultrasound to evaluate valve function in terms of regurgitation and captured atrial and ventricular pressures.

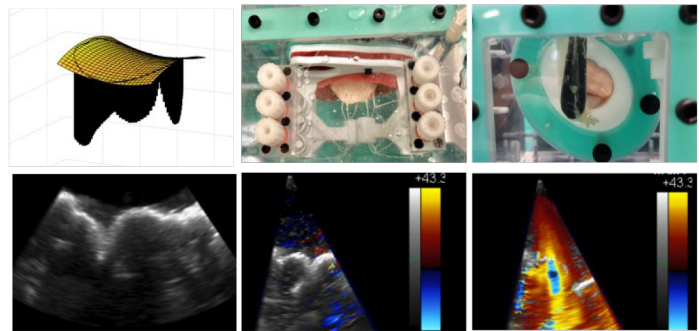


Figure 1: Generated valve geometry (top-left). Silicone valve replica in pulse duplicator (top-middle and top-right). TEE image of valve (bottom-left), with Doppler images showing valve in healthy configuration (bottom-middle) and significant regurgitation in tethered configuration (bottom-right).

RESULTS: The replicated dynamic valve model shows no regurgitation at systolic LV pressures of 130.0mmHg, and atrial pressure 8.5mmHg. The valve shows expected systolic and diastolic behavior, with a visually realistic appearance as determined by an expert cardiac imaging clinician. This valve is constructed with healthy valve geometry, however under conditions replicating a ruptured chord the valve behaviour changes from healthy to regurgitant, as shown by color Doppler and a maximum drop in systolic LV pressure to 100.0mmHg.

CONCLUSIONS: To our knowledge, we are the first to demonstrate a physical replica of an *a priori* mathematical MV geometric model. We demonstrate that a physical valve replica simulated in a pulse-duplicator shows healthy valve behaviour. Furthermore, we can induce regurgitation in this valve by loosening chordae tension. Future work will include further development of pathological valve models through modification of parameters controlling annular diameter, individual leaflet length and leaflet shape, with evaluation against this healthy baseline valve.

REFERENCES: 1.Asgar, A. W., *Canadian Journal of Cardiology* 33(9), 1197–1200 (2017). 2. Chikwe, J., *JACC* 69(19), 2397–2406 (2017). 3.Shen, X., *PLOS ONE* 12, e0183362 (aug 2017). 4. Park, J., *Semin. Thorac. Cardiovasc. Surg* 31(3), 399–411 (2019). 5.Ginty, O. K., *Innovations (Phila)* 13, 11–22 (jan 2018).

Multi-slice Hyperpolarized ^{129}Xe Fractional Ventilation Mapping in Pediatric Cystic FibrosisFaiyza Alam^{1,2}, Brandon Zanette², Sharon Braganza², Daniel Li², Felix Ratjen^{2,3} and Giles Santyr^{1,2}.¹Department of Medical Biophysics, University of Toronto, Toronto, ON, Canada, ²Translational Medicine Program, SickKids, Toronto ON, Canada, ³Division of Respiriology, SickKids, Toronto, ON, Canada

Introduction: Conventional pulmonary function tests (PFTs) are insensitive to early changes in pediatric cystic fibrosis (CF)¹ lung disease and limited in monitoring the effects of novel CFTR modulator therapies due to their inability to resolve regional changes. Novel imaging techniques can assess this directly by providing an image of the inhaled gas distribution. Performing MRI during multiple breath washout following a single inhalation of hyperpolarized (HP) ^{129}Xe gas (MBW Xe-MRI) results in regional maps of fractional ventilation (FV), measuring gas clearance/breath^{1,2}. Previously, we used a single non-selective coronal slice centred on the chest cavity which resulted in significant anterior/posterior (A/P) partial volume effects². Multiple slices add spatial resolution in the slice direction that improve detection of regional changes and allow for calculation of a gravitational gradient (a potential biomarker). Previously, we tested feasibility of multi-slice FV in healthy adults³. Here, we test feasibility in pediatric CF, compare single- and multi-slice FV maps, and compute FV gravitational dependence in disease.

Methods: This ongoing work was performed with institutional approval. 4 CF participants to date (mean age 15 ± 2 years) underwent single and multi-slice MBW Xe-MRI. ^{129}Xe gas was polarized ($\sim 20\%$) using a commercial polarizer (Polarean 9820, Durham, NC). MRI was performed at 3T (Prisma, Siemens, Erlangen, Germany) with a rigid elliptical birdcage transmitter and flexible 8-channel receive array (Rapid Biomedical, Rimpark, Germany). Following an inhalation of HP ^{129}Xe (dosed to 10% of total lung capacity (TLC), diluted with N_2 to 1/6 TLC), participants were coached through tidal breathing of room air with interleaved breath-holds (~ 5 s apart) at peak inhalations where MR images were acquired. Details of the single-slice² and multi-slice³ acquisitions are described previously. Data analysis was performed using a variable T_1 method⁴. FV values are reported as whole-map means. For gravitational dependence, mean FV for each slice was plotted against the distance from the posterior lung.

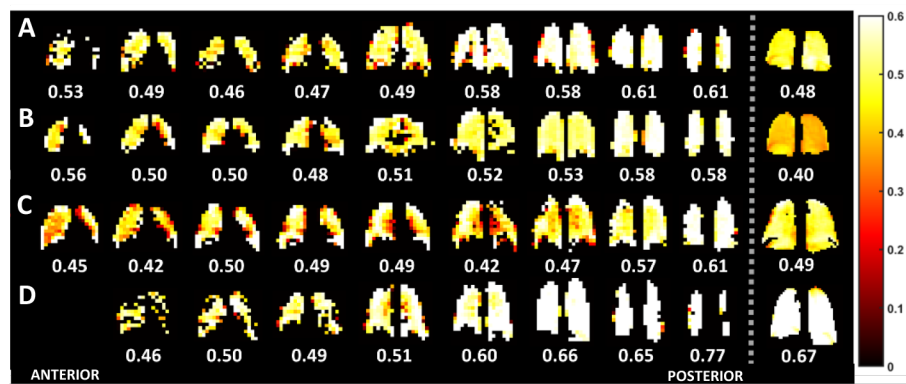


Figure 1: Multiple-slice (left) and single-slice (right) FV maps for all pediatric participants.

Results: Multi-slice MBW Xe-MRI was feasible in all participants. Figure 1 shows FV maps for all participants/slices and the corresponding single-slice FV map. Median [IQR] multi-slice FV for participants A-D are 0.53 [0.49 0.59], 0.52 [0.50 0.56], 0.49 [0.44 0.52], and 0.55 [0.50 0.65] respectively. Figure 2 displays the FV gravitational gradients for all participants; where mean gradient was $-0.0154 \pm 0.0064 \text{ cm}^{-1}$.

Conclusion: Multi-slice MBW Xe-MRI was feasible in pediatric CF. While the in-plane resolution for the multi-slice maps was lower than the single-slice maps, voxel volumes are significantly improved (4050 mm^3 vs $11,250 \text{ mm}^3$). Multi-slice maps were able to resolve regions of disease that were obscured in the single-slice projections, most prominent in participant C, who also had the lowest lung function of all four patients as reported by clinic PFTs. Median FV was consistent between techniques, but tended to be slightly higher in multi-slice, likely due to increased FV in posterior slices. Mean gradient in CF was similar to literature in healthy participants^{3,5}, likely due to more mild disease in kids. Interestingly, participant C had a lower gradient than in health, consistent with the observed phenomenon of attenuated gradients in disease⁶. Presently, we are accruing data in controls to see if multi-slice methods better differentiate between CF/health than single-slice. Multi-slice MBW Xe-MRI may provide an improvement over single-slice for following regional changes in CF due to increased spatial resolution in the slice direction and the gradient as a potential biomarker. In future, improved in-plane resolutions will improve its ability to resolve regional changes.

REFERENCES: [1] Couch et al., MRM. (2019) 84(1), 304-311. [2] Alam et al., JMRI. (2023) 58(3), 936-948. [3] Alam et al., ISMRM. (2023) #4572. [4] Morgado et al., MRM. (2018) 80(6):2670-2680. [5] Horn et al., J. Appl. Physiol. (2014) 116(2), 129-139. [6] Pennati et al., Radiology. (2014) 273(2):580-90.

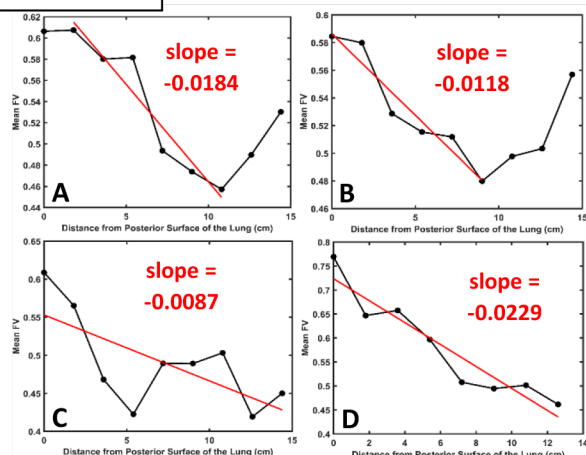


Figure 2: FV gravitational dependence for all participants.

Session 12 Talks: Neuroimaging 2

Abstracts

Investigating Brain GABA and Glutamate+Glutamine Levels in Chronic Pain Patients with and without Opioid Use Disorder: A Magnetic Resonance Spectroscopy Study

Claire Shyu¹⁻⁵, Sheldon Bereznick^{1,5}, Kevin Butler^{2,8}, Sonja Elsaid^{1-4,7}, Andrew Smith^{3,4}, Isabelle Boileau²⁻⁷ and Bernard Le Foll¹⁻⁷

¹Translational Addiction Research Laboratory, ²Brain Health Imaging Centre, ³Campbell Family Mental Health Research Institute and ⁴Addictions Division, Centre for Addiction and Mental Health, Toronto ON ⁵Department of Pharmacology and Toxicology, ⁶Department of Psychiatry, ⁷Institute of Medical Science, University of Toronto, Toronto ON; ⁸School of Psychology, College of Health and Science, University of Lincoln, UK.

Introduction: In Canada, opioids cause the most prescription drug-related overdose deaths, and that rate is still rising¹. Chronic pain patients taking prescribed opioids long term are at increased risk of opioid addiction, where more than 10% of patients develop opioid use disorder (OUD) compared to just 0.2% in the general population². However, it is unclear what neurochemical factors put certain individuals at risk³. Alterations in GABA (γ -aminobutyric acid) and Glx (glutamate + glutamine) levels have been implicated in several substance use disorders^{3,4}. However, little is known about GABA and Glx status in OUD. Using Proton Magnetic Resonance Spectroscopy (MRS), the present study aims to determine whether brain regional levels of GABA and Glx are altered in chronic pain patients with OUD (OUD+) compared to chronic pain patients taking prescription opioids with no OUD history (OUD-) and healthy controls (HC).

Methods: 18 participants (OUD+ n=10; OUD- n=8) were scanned on a GE MR750 3T scanner with 32-channel head coil (Nova Medical). Using MEGA-PRESS (MEscher-GARwood Point RESolved Spectroscopy) sequence, the right insula (6:46min, TE/TR=68/1500ms, 192 averages) and left dorsal lateral prefrontal cortex (DLPFC, 5:12min, TE/TR=68/1500ms, 256 averages) data were acquired with editing RF pulse width of 14.4ms. GABA+ (GABA+ macromolecules) peak was quantified using Gannet 3.1⁵. Glx values were processed with FID-A⁶ and analyzed using LCModel⁷. Gannet and SPM12 were used for voxel-to-T1-weighted image registration. GABA and Glx are reported in institutional units with unsuppressed water signal as internal water reference and values are corrected for partial volumes of CSF/GM/WM using tissue segmentation with FSL (FMRIB Software Library). A one-way ANOVA and post-hoc comparison test was conducted to compare results between the three groups.

Results: In the insula, but not the DLPFC, GABA levels were higher in OUD+ compared to HCs by 8.9% but were not significantly different from OUD-. Glx levels in the insula and DLPFC were not significantly different in OUD+ compared to HCs. However, Glx was 31.0% higher in the DLPFC in OUD+ compared to OUD-.

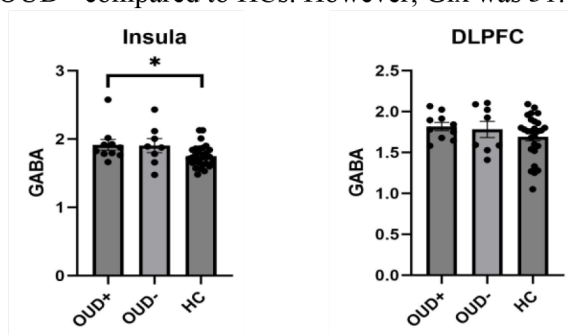


Fig 1. Mean GABA in OUD+, OUD-, and HCs in the Rt-Insula (HC n=30; $F=3.380$; $\eta^2=0.131$) and Lt-DLPFC (HC n=27; $F=1.057$; $\eta^2=0.048$) (* $p < 0.05$).

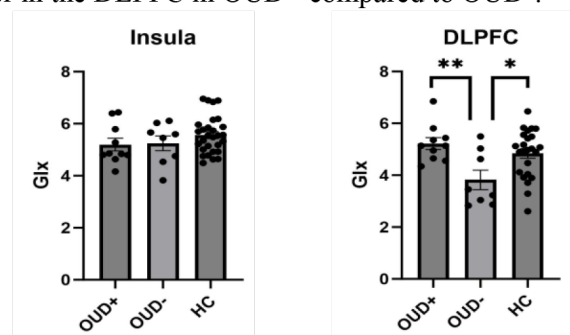


Fig 2. Mean Glx in OUD+, OUD-, and HCs in the Rt-Insula (HC n=29; $F=1.227$; $\eta^2=0.053$) and Lt-DLPFC (HC n=24; $F=5.669$; $\eta^2=0.225$). (* $p < 0.05$; ** $p < 0.01$).

Conclusion We found that Glx levels in the DLPFC, but not GABA were different between chronic pain patients taking opioids with and without OUD. Insula GABA levels in OUD+ individuals were also significantly higher compared to HCs. The clinical significance of these variabilities may relate to pain pathophysiology, medication use, and mood and anxiety symptoms, which remains to be explored in our ongoing study.

References: 1) Public Health Agency of Canada. 2023.; 2) Dalhamer et al. *National Health Statistics Report*. 2021.; 3) Shyu et al. *Brain Sci*. 2022.; 4) Chen et al. *Psychiatry Res. Neuroimaging*. 2021.; 5) Edden et al. *JMRI*. 2014.; 6) Simpson et al. *MR in Med*. 2017.; 7) Provencher, S.W. *NMR Biomed*. 2001.

Towards brain blood metabolite measurement using MRS with pseudo-continuous arterial spin labeling

Peter Truong¹, Thomas W Okell², and Jamie Near^{1,3}

¹Physical Sciences Research Platform, Hurvitz Brain Sciences Program, Sunnybrook Research Institute, Toronto, ON, Canada, ²Wellcome Centre for Integrative Neuroimaging, FMRIB Division, Nuffield Department of clinical Neurosciences, University of Oxford, Oxford, United Kingdom, ³Department of Medical Biophysics, University of Toronto, Toronto, ON, Canada

Introduction Standard single-voxel magnetic resonance spectroscopy (MRS) measures the signatures of metabolites within a user-selected volume of interest (VoI). This signal arises from metabolites within all tissues in this VoI¹. However, there is another volume that might also influence the resulting metabolite signal: blood. The brain is heavily vascularized, having a blood volume of approximately 5.4ml per 100g of grey matter tissue and 2.6ml per 100g of white matter tissue². In the imaging realm, Arterial Spin Labeling³ (ASL) is an increasingly popular MRI-based method used for visualizing and quantifying cerebral blood flow or perfusion without the use of contrast-agents. Pseudo-Continuous ASL⁴ (pCASL) is a widely used labeling scheme where a train of short inversion pulses are utilized for tagging and control, offering high SNR while staying within SAR limits. While ASL is commonly used to assess blood water perfusion in the brain, it has yet to be used, to our knowledge, to assess blood metabolite signals in the brain. We have developed a pulse sequence for single voxel spectroscopy with a pseudo-continuous arterial spin labeling preparation (SVS-pCASL), which combines the RF tagging pulse train from pCASL⁵ with a standard PRESS MRS localization sequence.

Methods The pulse sequence is shown in **Figure 1**. Background suppression⁶ (BGS) and pCASL RF pulse trains are performed prior to excitation. As a proof of concept, we wanted to first see if we can achieve an ASL effect on the PRESS water signal. One healthy volunteer (27 F) was scanned using a 3T Siemens Prisma-XR (Erlangen, Germany) using a 20-channel head and neck coil. A 50 (RL) x 37 (AP) x 27 (SI) mm³ voxel was placed in the parietal region (**Figure 2**). The axial pCASL labelling slab was placed below the cerebellum and the axial background suppression slab was placed at the level of the VoI. We acquired spectra with post labeling delay (PLD) times ranging from 100ms to 1800ms. The following parameters were used for the pCASL pulse train: gaussian rf pulse; rf duration = 500 us; total tag duration = 1000ms; number of pulses = 666; flip angle = 20 degrees; mean tag gradient = 0.8 mT/m, tag gradient amplitude = 6 mT/m. MRS scanning parameters were: TR = 4s, TE = 30ms, number of points = 2048, spectral width = 2000 Hz, number of averages = 8.

All processing was performed using the FID-A processing toolbox ([Github.com/CIC-methods/FID-A](https://github.com/CIC-methods/FID-A)). Data were coil combined, frequency and phased corrected using spectral registration⁷, then averaged. A difference spectrum was made from subtracting the averaged control spectrum from the averaged tagged spectrum.

Results The plots of the difference spectra at different PLDs are shown in **Figure 3**. We observe that the subtracted water peak at ~4.6ppm is negatively increasing, maxing out at 1000ms PLD, then starting to decrease again. A closer look of the tagged, control and difference spectra with PLD=1000ms are shown in **Figure 4**.

Conclusions In our proof-of-concept preliminary SVS-pCASL scans, we were able to observe an ASL effect with a maximum signal difference using a PLD of 1000ms. With only 8 averages, we observed some peaks between 3-3.7 ppm, however, more in-vivo scans are needed to determine if these are metabolite resonances. With further optimization, we hope that SVS-pCASL will allow measurement of brain blood metabolites.

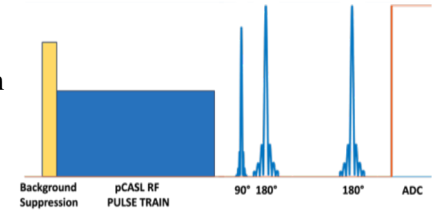


Figure 1: Pulse sequence diagram of SVS-pCASL

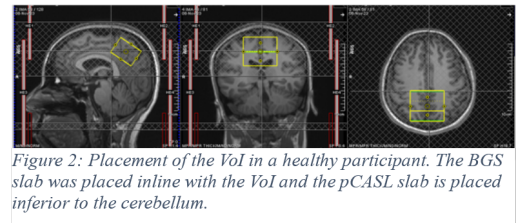


Figure 2: Placement of the VoI in a healthy participant. The BGS slab was placed inline with the VoI and the pCASL slab is placed inferior to the cerebellum.

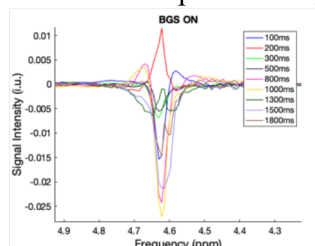


Figure 3: Overlay plots of the difference spectrum with varying PLD time.

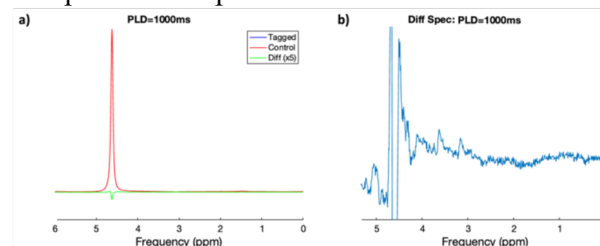


Figure 4: a) Overlay plot of the tagged, control, and difference spectrum (scaled up 5x) with PLD=1000ms. b) Zoom in of the difference spectrum

References 1. Gasparovic et al. NMR in biomedicine 2018. 2. Li et al. MRM 2021. 3. Detre et al. MRM 1992. 4. Dai et al. MRM 2008. 5. Okell et al. ISBFM 2013. 6. Gunther et al. MRM 2005. 7. Near et al. MRM 2015.

Regional brain abnormalities in resting state functional MRI persist past symptom resolution: preliminary findings

Ethan Danielli^{1,2}, Nicholas Simard^{2,3}, Dinesh Kumbhare^{1,4}, Michael D Noseworthy^{2,3,5}

1. KITE Research Institute, UHN, Toronto; 2. Imaging Research Centre, St. Joseph's Healthcare Hamilton, Hamilton; 3. Department of Electrical and Computer Engineering, McMaster University, Hamilton; 4. Faculty of Medicine, University of Toronto, Toronto; 5. Department of Radiology, McMaster University, Hamilton.

Introduction: Routine clinical magnetic resonance imaging (MRI) scans fail to detect concussion-related brain injuries, and symptom self-reporting is highly subjective [1]. Subtle brain damage can be detected using advanced MRI analyses [2,3]. However, is the brain healed once concussion symptoms are resolved? The objective of this ongoing study is to track recovery post-concussion using personalized MRI methodology in comparison to post-concussion symptoms, and it is hypothesized that objectively measured brain abnormalities identified using resting state functional MRI (rsfMRI) and diffusion tensor imaging (DTI) will align with symptoms acutely but persist beyond symptom resolution.

Methods: Three acutely concussed (<2 weeks post-injury) adults (2 male 1 female, aged 26.7 ± 0.6) who were all right-handed athletes with no clinical diagnosis of psychiatric or neurological conditions. Participants 1 and 3 had no previous concussion history or diagnosis, and participant 2 had sustained three previous concussions. Participants completed the PCSS, DASS42, and an MRI session (3D T1, rsfMRI, and DTI) acutely and 3-months post-concussion. The MRI data was analyzed to measure rsfMRI temporal complexity (Hurst exponent= H) and DTI fractional anisotropy (FA) within each brain voxel [4]. Region-of-interest (ROI) masks were applied across 29 cerebral gray matter (GM) and 18 cerebellar ROIs to evaluate voxel-wise H values (rsfMRI) and FA values (DTI). These calculations were also made on 243 age and sex-matched healthy controls to establish a healthy baseline. A personalized ROI-based Z-score analysis was implemented where lower FA and reduced H (i.e., Z-scores ≤ -2.5) was hypothesized to indicate abnormality and compared against clinical tests. Recovery was measured using paired t-tests for PCSS score, DASS42 score, and number of cerebral H abnormalities using RStudio to identify differences between the acute and three-month follow-up values based on confidence intervals; Shapiro-Wilks normality testing was done for each metric prior to performing t-tests.

Results: The mean PCSS and DASS42 scores decreased significantly ($p=0.015$) after 3-months for all three participants (i.e., PCSS went from 24 to 6 and DASS42 went from 15 to 7). There were numerous brain GM functional abnormalities present acutely (Abnormal ROIs: Participant 1=9 (**Figure 1A**), Participant 2=20, Participant 3=24) and at 3-months post-concussion (Abnormal ROIs: Participant 1=10 (**Figure 1B**), Participant 2=9, Participant 3=18). There were only 3 brain WM abnormalities noted. As hypothesized, the number of GM abnormalities did not statistically decrease by 3-months post-concussion (95% C.I. -9.6 20.3, $p=0.27$). The same abnormal ROIs remained abnormal after 3-months.

Conclusions: These initial findings suggest that many brain abnormalities did not return to within a normal range after 3-months despite symptoms decreasing or resolving. Since two of the three participants had not previously sustained a concussion, the GM abnormalities detected with our MRI analysis can be more confidently attributed to their recent concussion. It was unexpected to detect so few white matter abnormalities [5,6]. These results should be corroborated with more participants and additional assessments at 6-months post-concussion when symptoms should be completely resolved.

References: [1] Chamard E, et al. *Brain Injury*. 2018;32(7):816–831. [2] Cassoudealle H, et al. *J Neurosci Res*. 2021;99(2), 446–454. [3] Dona O, et al. *PLOS ONE* 12(1):e0169647. [4] www.tbifinder.com [5] Asken BM, et al. *Brain Imag Behav*. 2018;12(2):585–612. [6] Mustafi SM, et al. *J Neurotrauma*. 2017;35(22):2653–64.

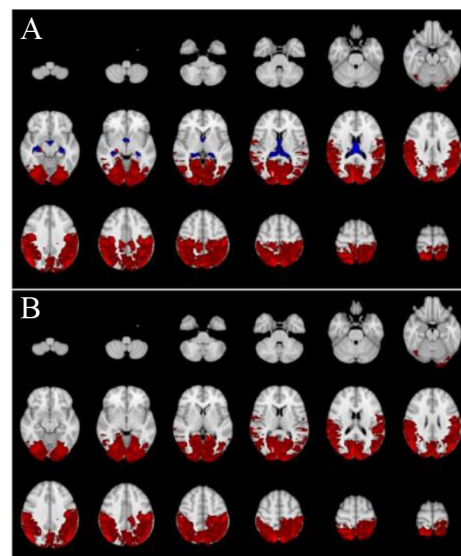


Figure 1. Visualization of the abnormal gray matter brain regions for participant one (A) acutely (9 abnormal ROIs) and (B) after 3-months (10 abnormal ROIs). Abnormal gray matter ROIs are coloured red and abnormal white matter ROIs are coloured blue.

Title: Hippocampal subfield-specific volume and diffusion changes in treatment resistant depression

Authors: Mahdiah Varvani Farahani^{1,2,3}, Nardeen Yalda^{1,2}, Georgia Gopinath¹, Darren Liang⁴, Lena Palaniyappan^{5,2,3}, Amer M. Burhan^{6,7}, Stefan Köhler^{1,2,*}, Ali R. Khan^{1,2,3,*} (* co-senior authors)

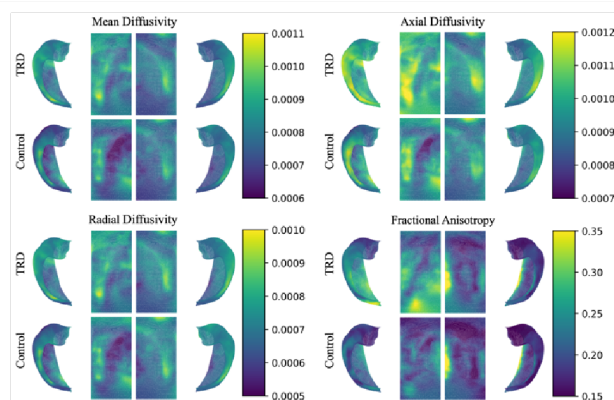
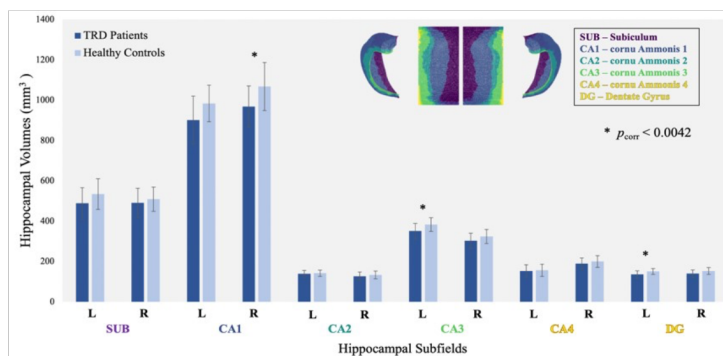
Affiliations: ¹Western University, Canada, ²Western Institute for Neuroscience, Canada, ³Robarts Research Institute, Canada, ⁴Centre for Addiction and Mental Health, Canada, ⁵Douglas Mental Health University Institute, Canada, ⁶Ontario Shores Centre for Mental Health Sciences, Canada, ⁷Temerty Faculty of Medicine, Canada

Introduction: Depression is a debilitating yet common mental disorder characterized by a persistent feeling of sadness and reduced interest in previously enjoyable activities (APA, 2013). In addition to its clinical symptoms, depression has also been associated with cognitive deficits, including impaired declarative memory functioning (Dillion & Pizzagalli, 2018). Relatedly, neuroimaging studies have consistently found significantly lower hippocampal volumes in depressed patients than in healthy controls (Gray et al., 2020). Here, we examined hippocampal subfield-specific volumes and grey matter (GM) diffusion in a clinical sample of individuals with treatment resistant depression (TRD).

Methods: We studied 22 patients with TRD (9 males, $M_{age} = 39.5$, $SD_{age} = 13.3$), recruited from the Therapeutic Brain Stimulation Clinic at Parkwood Institute, and 21 age and sex-matched healthy controls (9 males, $M_{age} = 38.7$, $SD_{age} = 14.0$), recruited from the OurBrainsCAN registry. We collected high resolution (0.8 mm isotropic) T1w MPRAGE whole brain images as well as diffusion-weighted images of the hippocampus (1 mm isotropic; b-value = 500; as per Treit et al., 2018) with a 3T Siemens Prisma 32-head coil MRI scanner. We ran HippUnfold v1.2.0 on our T1w images to obtain hippocampal subfield segmentations. Expecting to observe reductions in hippocampal subfield volumes of TRD patients compared to controls, we tested our hypothesis using Bonferroni adjusted alpha levels of .0042 per each one-tailed test (.05/12). Furthermore, we pre-processed the diffusion data before running HippUnfold for subfield segmentations of diffusion tensor imaging (DTI) metrics; mean diffusivity (MD), axial diffusivity (AD), radial diffusivity (RD), and fractional anisotropy (FA).

Results: As compared to healthy controls, TRD patients presented with significantly reduced volumes in their left dentate gyrus (DG; $t(41) = -2.95$, $p = .0026$), left cornu Ammonis 3 (CA3; $t(41) = -2.90$, $p = .003$), and right CA1 ($t(41) = -2.95$, $p = .0026$; Figure 1). Patients also presented with increased MD, AD, and RD relative to controls, but this finding was not significant (Figure 2).

Conclusions: Expected subfield-specific hippocampal volume reductions were observed in TRD patients vs



controls. Additionally, the literature suggests increased GM diffusivity, as observed in our patients, can reflect microstructural alterations or the breakdown of microstructural barriers to diffusion (Henf et al., 2017; Weston et al., 2015). These results warrant further investigation into the structural abnormalities observed in the hippocampi of individuals with depression. Future research from our group will also be exploring the relationship between these structural abnormalities and behavioural measures of hippocampal-dependent memory functioning.

Figure 1. Left and right hippocampal subfield volumes in TRD patients and healthy controls.

SUB, subiculum; CA, cornu Ammonis; DG, dentate gyrus.

Figure 2. Mean diffusivity, axial diffusivity, radial diffusivity, and fractional anisotropy measures of TRD patients and healthy controls mapped onto the canonical and unfolded hippocampal surface.

Session 13 Pitches: Cardiac, Lung, Image Processing

Abstracts

Comparing Visual Search Strategies: Pathologists' Adaptability to Non-Medical Contexts

Alana Lopes¹, Sean Rasmussen³, Ryan Au¹, Tricia Chinnery¹, Jaryd Christie¹, Robert Policelli¹, Anurag Sharma³, Christopher Tran³, Joanna Walsh³, Bret Wehrli³, Aaron D. Ward^{1,2}, and Matthew Cecchini³

¹Departments of Medical Biophysics, Oncology², Western University, London ON

³Department of Pathology and Laboratory Medicine, London Health Sciences Centre, London ON

Introduction: The role of a pathologist involves routinely completing numerous image search and classification tasks. The identification of tumour in lymph nodes is an example of a repetitive rare element search task that requires pathologists to identify and classify small foci of tumour, which can subsequently change the course of a patient's care by adding additional therapies to their treatment plan. In general, pathologists rely on their image search and classification skills to determine their final diagnostic assessment. For this reason, pathology is a field that requires years of training for visual search and classification of cellular features. This raises the question of whether this training gives pathologists an advantage in image search tasks outside of pathology. The objective of this study was to use eye tracking technology to determine if the training a pathologist receives translates to a non-domain specific search task, and whether pathologists perform this search task differently from a lay audience.

Methods: Six board certified pathologists were recruited as observers. Similarly, six graduate students with no professional experience in digital image search were recruited as lay observers. For the non-domain specific search task, each observer was presented with five fixed digital "Where's Waldo?" puzzles and asked to search for the "Waldo" character, which was only present in three of the five images. Similarly, a domain-specific search task was subsequently given to each pathologist, presenting them with five fixed images of a breast digital pathology slide at 15x magnification. The task was to search for a single mitotic figure, which was only present in three of the five images (Fig. 1). The observers' eye gaze data (saccade angle, amplitude and velocity, fixation duration, and gaze transition entropy) were collected using the Tobii Pro Fusion eye tracker. Linear discriminant analysis (LDA) was performed to find the one-dimensional representation that best separated the observer groups. The false negative rate (FNR), at which the observer incorrectly classified the target when their foveated vision landed on the figure, was also recorded.

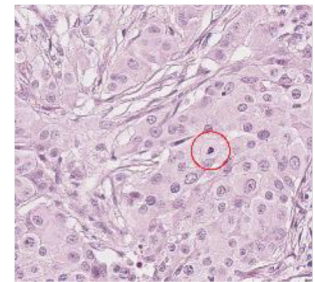


Fig. 1: Digital breast pathology image; mitotic figure circled in red.

Results: For the "Where's Waldo?" search task, pathologists had a significantly shorter median fixation duration (244 ms) than lay people (300 ms, $p < 0.0001$). Additionally, the median peak saccade velocity of pathologists was $82.1^\circ/\text{second}$ compared to $77.8^\circ/\text{second}$ for lay people ($p = 0.02$). Pathologists' median fixation rate was 3.17/second, compared to 2.61/second for the lay audience ($p < 0.0001$), while the saccade rate was 2.77/second for pathologists versus 2.47/second for lay people ($p < 0.0001$). There was no significant difference between the two cohorts for FNR, implying that pathologists' increased speed is not at the expense of accuracy. Further, the median gaze transition entropy was equivalent amongst the two groups at a value of 0.12, signifying a low complexity and high predictability in scan path for this task. As shown in Fig. 2a, pathologists' scan paths differ from those of lay people, with an LDA misclassification rate of 10.2%. Similarly, a significant difference was found between pathologists' scan path for "Waldo" vs. mitotic figures, with an LDA misclassification rate of 0% (Fig. 2b).

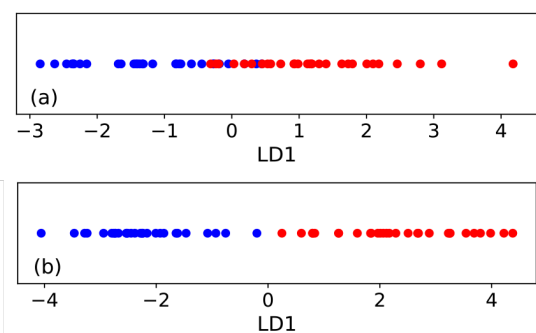


Fig. 2: One-dimensional unscaled LDA depiction (LD1) of scan path for (a) pathologists (blue) and graduate students (red) for the "Where's Waldo?" search task and (b) the "Where's Waldo?" (blue) and mitotic figure (red) search tasks.

Conclusions: Pathologists' professional training does not provide improved accuracy in non-domain search tasks but does improve the speed of their search and classification, without loss of performance. This implies that pathologists gain an enhanced decisional capacity throughout their training and experience, allowing them to rapidly classify the objects of their fixations without compromising accuracy, both within and outside pathology.

CNR degradation in dual-energy thoracic imaging with photon-counting detectors

Jeffrey Dhari and Jesse Tanguay

Department of Physics, Toronto Metropolitan University, Toronto, Canada, M5B 2K3

Introduction: Lung cancer is the leading cause of cancer death with the survival rates being low in its advanced stages, thus the key to survival is detection at earlier stages. However, smaller nodules may be obscured and not detected due to overlaying bone structures. Photon-counting detectors (PCD) enables single exposure dual-energy (DE) x-ray imaging of lung nodules allowing for the removal of bone structures and potentially providing higher image quality. The physical mechanisms of detection in PCDs may degrade the contrast-to-noise ratio (CNR) of lung nodules in DE images. The purpose of this study is to develop models of the CNR in a DE x-ray image of a lung nodule to identify and quantify the detection mechanisms that degrade the CNR. In addition, the model CNR has been validated against experimental data.

Methods: The DE CNR has been modelled for five theoretical PCDs, with each model incorporating one extra element of realism from the previous model with the first model being an ideal detector which detects every incident photon in the correct energy bin and the final model being a realistic PCD which includes the effects of charge sharing, electronic noise and detects scattered x-rays. The CNR was computed as a function of high energy threshold separating the low and high energy bins for tube voltages of 90 kV to 130 kV, where the threshold varied from 30 keV to $\sim 10\%$ of the maximum energy of the beam. Model predictions were compared to a cadmium telluride PCD with $100 \times 100\text{-}\mu\text{m}^2$ detector elements, a $750\text{-}\mu\text{m}$ thick x-ray converter and two energy bins. The experimental study was done with a phantom built to simulate attenuation, scatter, and contrast for lung cancer imaging. Analog charge summing was used to reduce the effects of charge sharing in both the model and experiment. A noise rejection threshold was set to 17 keV, which was empirically found to suppress electronic noise. This noise threshold was applied to models in which the electronic noise was incorporated.

Results: There was generally good agreement between the model and experimental CNR, with the model CNR being within 5% to 15% of the experimental CNR. The model was also able to predict the trends seen in the experimental data. The addition of realistic multiplicity, which includes k-fluorescence and charge sharing degrades the CNR the most with a degradation of $\sim 26\%$. The factor that degrades the CNR the least is electronic noise with a degradation of $\sim 0.5\%$. The total degradation of CNR from a PCD was $\sim 44\%$.

Conclusions: For DE thoracic imaging in a PCD, the effects of charge sharing, and k-fluorescence have the most detrimental effects on the CNR, therefore the mitigation of these effects should be implemented to achieve the greatest CNR in a PCD.

System specifications for success of a novel synthetic mask energy subtraction technique

Lisa M. Garland and Ian A. Cunningham

Robarts Research Institute, Department of Medical Biophysics, Western University

Introduction: Among the various treatments for cardiovascular disease, percutaneous coronary intervention (PCI) is a technique whereby a permanent wire stent is placed on the blockage, effectively addressing the plaque buildup restricting blood flow in the vasculature. Clear visualization is critical to ensure the stent has not collapsed or fractured, which could lead to restenosis or more severe complications. Overlapping anatomic structures, including the lungs and ribs, make vessels and metal stents difficult to visualize under x-ray fluoroscopy during PCI as well as during follow-up examination. Methods such as digital subtraction angiography (DSA) can effectively suppress background structures, however, this is primarily successful under the condition that all structures are stationary and that a mask (pre-injection) image can be obtained. In instances where structures may not be stationary, energy subtraction angiography (ESA) has been explored to selectively suppress a structure based on the attenuation coefficient variation at low and high x-ray energies. While ESA images can be obtained in milliseconds, making them more practical for cardiac imaging, they are unable to suppress both bone and tissues simultaneously. Work by Yamamoto et al. used the maximum pixel value across a set of consecutive x-ray images of a coronary artery to generate a synthetic mask, but found the soft tissue motion was too severe, resulting in an unsuccessful method. We aim to use ESA to eliminate soft tissue in conjunction with processing techniques similar to Yamamoto et al. to enhance visualization of vessels and wire stents. This advanced technique requires the imaging system to meet various thresholds such as quantum noise limit, scatter-to-primary ratio (SPR) modulation transfer function (MTF), kV switching speed, and more.

Methods: A MATLAB simulation was developed in-house to calculate both iodine and nickel signal-to-noise ratio (SNR) for a wide range of x-ray parameters to determine the optimal settings for the ESA component of this technique. This simulation was also integral to determining the required thresholds for various parameters, including the maximum SPR and quantum noise limit. A proof-of-concept experiment was performed using an anthropomorphic chest phantom with a nitinol stent and iodine-filled tube, using optimal x-ray settings determined from our simulation. The phantom was stationary while the stent and tube were manually shifted to simulate cardiac motion (approx. 3-5mm shifts), and a set of ESA images were acquired to generate the synthetic mask. The demanding qualities of this technique require a kV switching generator and an ultra-low noise detector such as the prototype CMOS system used for concept validation. Quantification of this equipment was performed using an in-house software to generate the MTF, detector quantum efficiency (DQE), and the waveforms of the kV switching speed.

Results: Simulation results revealed the optimal x-ray settings for 11 different parameters to yield the greatest iodine/nickel SNR per unit dose. By optimizing these components of the imaging protocol, an SNR similar to that of DSA was achieved even using a stationary attenuation filter for both the low and high energy images, which is approximately 50% the SNR of conventional imaging. Using the weighted ESA images, soft tissue was suppressed from the image set such that only bone and the material of interest (iodine or nickel) remained, and the pixel intensities were evaluated across the ESA image to determine which pixels contained nickel or iodine. Waveform measurements indicated that step kV switching could be achieved within a millisecond when using a higher mA setting due to the electrical properties of the tube. We achieved a quantum noise limit 50x lower than a conventional top-tier amorphous silicon detector. Consecutive ESA images were acquired at 30 frames per second using the prototype kV switching generator, and our code was used to evaluate pixels not containing the stent/iodine to construct the synthetic mask image.

Conclusions: Our efforts indicate that ESA imaging in conjunction with a novel pixel evaluation method may allow for successful creation of a mask image, thereby suppressing all background structures and enhancing visualization of the stent/iodine during PCI procedures. By using the ESA images for this technique, artifacts from soft tissue motion will be mitigated and digitally subtracted images of the iodine/stent alone are obtainable. With the use of advanced prototype equipment, this technique may improve confidence in the diagnosis of collapsed and fractured stents in real time both during PCI and post-procedure non-invasively.

SegFormer for Precise Quantification of Lung Ventilation Defects in Hyperpolarized Gas Lung MRI

Ramtin Babaeipour¹, Ryan Zhu², Harsh Patel², Matthew S Fox^{2,3} and Alexei Ouriadov^{1,2,3}

¹School of Biomedical Engineering, Faculty of Engineering; ²Department of Physics and Astronomy; ³Lawson Health Research Institute, London, Canada, The University of Western Ontario, London, ON, Canada

Introduction: Ventilation defects in the lungs, often due to airway obstructions or tissue damage (1), can be assessed using hyperpolarized ¹²⁹Xe/³He lung MRI (2). Current semi-automated methods for quantifying these defects (3), although effective, are time-intensive. Deep Learning, particularly in image segmentation, is revolutionizing medical imaging. Convolutional Neural Networks (CNNs) like UNet (4) are standard, but Vision Transformers (ViTs) (5) have emerged as a promising alternative. ViTs, such as SegFormer (6), excel in capturing long-range dependencies with less bias, addressing CNNs' limitations like low-resolution outputs. This study explores SegFormer's efficacy in automatically segmenting and quantifying ventilation defects in hyperpolarized gas MRI.

Methods: Our study involved 56 participants, including 9 healthy individuals, 28 with COPD, 9 with asthma, and 10 with COVID-19, yielding 1456 2D slices segmented via MATLAB R2021b using hierarchical K-means clustering. Data was evenly distributed across training (80%), validation (10%), and testing (10%) sets. We employed PyTorch on dual NVIDIA GA102, GeForce RTX 3090 GPUs, and used landmark-based image affine registration for aligning proton and hyperpolarized slices. SegFormer architecture, featuring hierarchical decoding, overlapping patches for boundary recognition, MLP-head for segmentation, and a Bottleneck Transformer for efficiency, was utilized.

Results:

This study evaluated SegFormer's performance using different Mix Transformer encoders (MiT), with MiT-B0 for fast inference and MiT-B2 for optimal performance. SegFormer, especially with ImageNet pretraining, showed superior results compared to CNN-based models, achieving high Dice Similarity Coefficient (DSC) values, while requiring fewer computational resources and less training time. Detailed DSC results are presented in Table 1, with specific case studies for hyperpolarized MRI in Figure 1.

Discussion and Conclusion: Our study demonstrates SegFormer's superior performance in hyperpolarized gas MRI, excelling in accuracy and efficiency over UNet and Unet++. Its novel approach to spatial context in medical imaging, without traditional positional encodings, shows significant promise. While focused on a specific cohort, SegFormer's potential for broader clinical application in MRI is evident.

We acknowledge the support of the Natural Sciences and Engineering Research Council of Canada, R5942A04, and a Western University Research Catalyst Grant.

References:

- Harris et al. PLOS ONE, vol. 7, no. 12
- Perron et al., J. Magn. Reson., vol. 348, p. 107387
- Kirby et al., Acad. Radiol., vol. 19, no. 2, pp. 141–52
- Ronneberger et al., 2015, MICCAI 2015, vol 9351
- Dosovitskiy et al., ICLR 2021, <https://openreview.net/forum?id=YicbFdNTTy>
- Xie et al., arXiv:2105.15203, arXiv, 28 Oct. 2021.

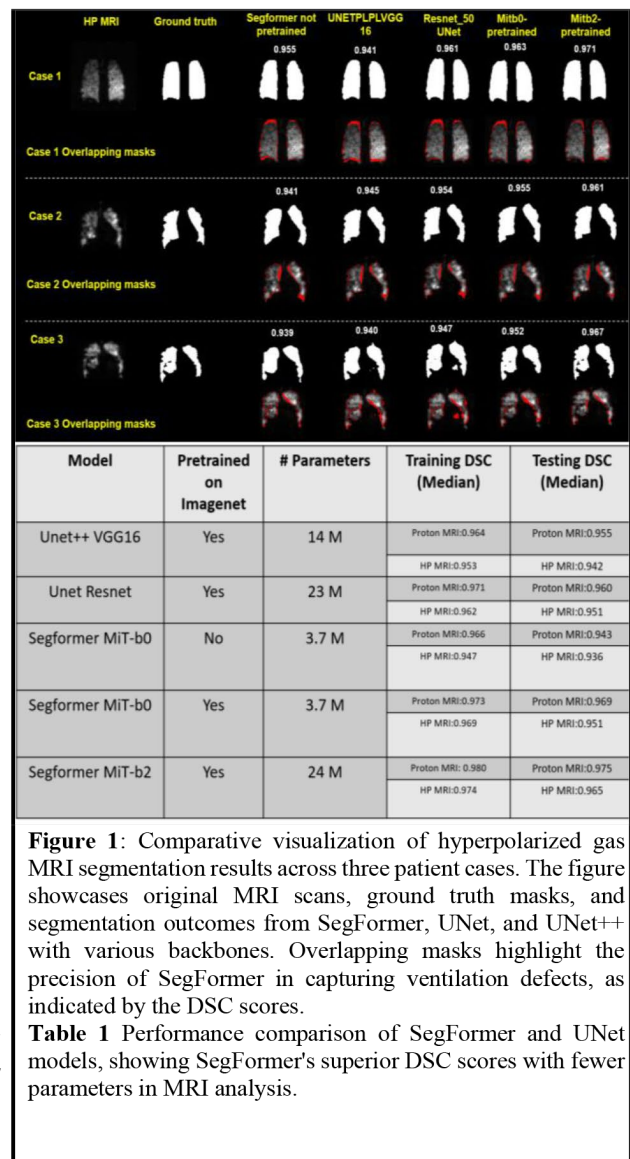


Figure 1: Comparative visualization of hyperpolarized gas MRI segmentation results across three patient cases. The figure showcases original MRI scans, ground truth masks, and segmentation outcomes from SegFormer, UNet, and UNet++ with various backbones. Overlapping masks highlight the precision of SegFormer in capturing ventilation defects, as indicated by the DSC scores.

Table 1 Performance comparison of SegFormer and UNet models, showing SegFormer's superior DSC scores with fewer parameters in MRI analysis.

Fractional Ventilation Mapping using Multiple Breath Washout MRI in the Rat Lung: Comparison of Hyperpolarized ^{129}Xe and Perfluoropropane Gases

Shaelyn Horvath^{1,2}, Daniel Li², Brandon Zanette², Faiyza Alam^{1,2}, and Giles Santyr^{1,2}. ¹Department of Medical Biophysics, University of Toronto, Toronto, ON, Canada, ²Translational Medicine Program, The Hospital for Sick Children, Toronto ON, Canada.

Introduction: A recent and sensitive research-based tool for monitoring pulmonary function is the nitrogen (N_2) multiple breath washout (MBW) test, measuring ventilation heterogeneity. However, this method is only indicative of global washout and cannot detect regional changes in lung disease. More recently, MBW hyperpolarized ^{129}Xe MRI (HP Xe-MRI) has been used to acquire images as a function of gas washout breath allowing for the mapping of fractional ventilation (FV), reflecting regional gas replacement per breath¹. Unlike HP Xe-MRI^{2,3}, fluorinated gases such as perfluoropropane (PFP) are thermally polarized with recoverable MRI signal, allowing for normoxic breath-holds and a more affordable, accessible technique for young patients. MBW PFP-MRI is feasible in adults⁴, however, comparison of PFP to HP ^{129}Xe for FV mapping has yet to be studied. Animal models allow for less variability between subjects and control over ventilation parameters not possible in humans. Bleomycin is a widely reproduced animal model of lung injury which results in inflammation, indicative of restrictive lung disease⁶. In this work FV maps derived from MBW Xe-MRI and MBW PFP-MRI in two cohorts of mechanically ventilated rats (healthy and bleomycin instilled) are compared using similar washout paradigms.

Methods: All methods followed animal use protocols approved by The Hospital for Sick Children's Laboratory Animal Services. Two cohorts of rats were used; cohort A consisted of 7 healthy Sprague-Dawley rats and cohort B consisted of 6 Sprague-Dawley rats which were previously anesthetized and instilled with a solution of bleomycin in saline (2.5 mg/kg) in the left pulmonary main bronchus. 14 ± 4 days later, they were prepared to be imaged as previously described⁵. Cohort A also followed this imaging protocol: Briefly, each rat was anesthetized, intubated, and connected to a custom MR-compatible mechanical ventilator (Spinance, Philadelphia PA). MBW MRI was conducted using a 2D GRE sequence at 3T, 6 pre-breaths of gas and 6 air washout breaths, with breath-hold images acquired at peak inspiration of each air washout breath. Breath-holds were 2s and 10s for HP ^{129}Xe (Polarean Inc., Durham, NC) and PFP (Airgas, Radnor, PA), respectively. Due to the short relaxation time of fluorinated gases, 10 averages were acquired for each PFP-MRI washout image in and MBW was repeated 20 times for further signal averaging. Following imaging, lung tissue was removed, fixed, and stained for histological analysis. Data analysis was performed using MATLAB as previously reported^{2,3}. FV maps calculated from PFP-MRI and Xe-MRI were then compared based on image-wide mean \pm standard deviation of FV values.

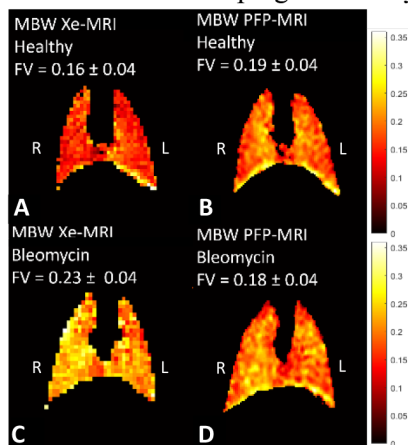


Figure 1: A: FV map from MBW Xe-MRI in cohort A. B: FV map from MBW PFP-MRI in cohort A. C: FV map from MBW Xe-MRI in cohort B. D: FV map from MBW PFP-MRI in cohort B.

Results: Ventilation and imaging procedures were well tolerated by the rats, including the switching of gases. Figure 1 shows representative FV maps from Cohort A using MBW Xe-MRI (A) and MBW PFP-MRI (B), and cohort B using MBW Xe-MRI (C) and PFP-MRI (D). The overall mean FVs were 0.20 ± 0.15 and 0.23 ± 0.10 for Xe and PFP respectively for cohort A, and 0.26 ± 0.23 and 0.21 ± 0.08 for cohort B. Figure 2 shows FV values from both gases and each cohort vs a line of identity. The Pearson correlation was 0.83 ($P=0.02$) for Cohort A and 0.69 ($P=0.13$) for Cohort B. T-tests calculated p-values between methods were 0.04 for Cohort A and 0.22 for Cohort B. Between cohort p-values were 0.17 and 0.39 for Xe-MRI and PFP-MRI, respectively.

Conclusions: This study demonstrates the feasibility of MBW PFP-MRI in both healthy rats and rats instilled with bleomycin. The p-value in cohort A is significant, indicating that MBW Xe-MRI and MBW PFP-MRI are statistically different in health, however the fairly strong positive relationship between the methods is valuable. Mean FV_{PFP} values are less distinguishable between cohorts than mean FV_{Xe} values. FV_{Xe} values were increased in cohort B, which is consistent with previous studies in humans^{1,7}. These increased values may be due to overcompensation of the right lung for the damaged lung¹. FV_{PFP} values, however, were similar between cohorts A and B. This may be due to the less viscous properties of PFP than Xe, meaning that the restrictive nature of bleomycin may have had a lower effect on this gas type. Future work includes regional image analysis between left and right lungs in cohort B and comparison to histology to assist interpretation of imaging results. Further studies with larger cohorts are required to investigate the repeatability of these measures. Overall, MBW PFP-MRI may provide a more regional, physiological description of ventilation dynamics compared to more common static measures, specifically in restrictive cases.

References: [1] Alam et al. JMRI. 2023;58(3):936-948. [2] Morgado et al. MRM. 2018;80(6). [3] Couch et al. MRM. 2012; 68(5). [4] Goralski et al. JCI Insight. 2020; 5(2). [5] Santyr et al. MRM. 2008;59(6):1304-1310. [6] Moeller et al. IJBCB. 2008;40(3):362-82. [7] Couch et al. MRM. 2020; 84(1).

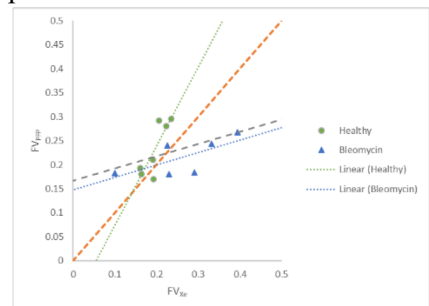


Figure 2: Identity plot comparing image wide mean FVs calculated from MBW PFP-MRI and MBW Xe-MRI. Orange line is the line of identity. Grey line is the line of best fit for both cohorts. Cohort A is depicted by green circles with a green line of best fit, and cohort B is depicted by blue triangles with a blue line of best fit.

Automatic Fetal MRI Segmentation with Volume and Weight EstimationsAdam Lim^{1,2}, Justin Lo^{1,2}, Matthias W. Wagner³, Birgit Ertl-Wagner^{3,4}, Dafna Sussman^{1,2,5}

¹Department of Electrical, Computer and Biomedical Engineering, Faculty of Engineering and Architectural Sciences, Toronto Metropolitan University, Toronto, ON M5B 2K3, Canada, ²Institute for Biomedical Engineering, Science and Technology (iBEST), Toronto Metropolitan University and St. Michael's Hospital, Toronto, ON M5B 1T8, Canada, ³Division of Neuroradiology, The Hospital for Sick Children, Toronto, ON M5G 1X8 Canada, ⁴Department of Medical Imaging, Faculty of Medicine, University of Toronto, Toronto, ON M5T 1W7, Canada, ⁵Department of Obstetrics and Gynecology, Faculty of Medicine, University of Toronto, Toronto, ON M5G 1X8, Canada

Introduction: Fetal magnetic resonance imaging (MRI) is crucial for monitoring fetal development. However, the existing workflow demands radiologists to manually delineate each scan to localize fetal anatomy, a task requiring expertise and proving to be both cumbersome and time consuming. Despite the challenges, this segmentation process is essential for identifying and monitoring structural/growth abnormalities, as well as conducting biometric measurements [1]. Although there are existing semi/fully automatic approaches, they face constraints like limited clinical applicability, restricted gestational age range, computational expense, and a lack of biometric measurements [2, 3, 4]. Therefore, we aim to overcome these limitations by developing a fully automatic, fast deep learning algorithm for whole body fetal segmentation, and precise calculations of fetal volume and weight.

Methods: We curated a dataset of 4663 2-dimensional (2D) whole body fetal MRIs from 72 scans (20-37 weeks gestational age), split into training, validation, and testing sets using an 80:10:10 split. A combination of manual labeling and active learning was used to generate the ground truth labels. The segmentation network extends the U-Net architecture, incorporating enhancements including spatial and channel attention mechanisms, along with multi-level feature extraction techniques via dilated convolution. A post processing smoothing filter was also implemented to further improve the quality of the output segmentations. The fetal volume and weight estimations were computed based on the network predicted masks, yielding percentile outputs.

Results: The segmentation network achieved an average of 96% in Dice Similarity Coefficient (DSC) and Intersection over Union (IoU). A sample segmentation is illustrated in the figure. These results surpassed other state-of-the-art segmentation networks shown in the table.

Model	Precision	Recall	IoU	DSC
U-Net	0.9273	0.9376	0.9200	0.9158
Attention U-Net	0.9597	0.9382	0.9332	0.9319
U-Net++	0.9471	0.9221	0.9194	0.9144
DeepLabV3	0.9589	0.8727	0.9043	0.8954
Proposed	0.9863	0.9725	0.9632	0.9645



Conclusion: The ensuing algorithm would greatly benefit radiologists in the fetal segmentation task by effectively diminishing both cognitive and physical workloads, and thereby enhancing the overall efficiency of the current fetal MRI process. Future work includes expanding the network's capacity to accommodate further sub-segmentations of additional fetal anatomy such as various organs.

References: [1] C. Kadji, M. F. Camus, E. Bevilacqua, M. M. Cannie, T. C. Sanchez, and J. C. Jani, "Repeatability of estimated fetal weight: Comparison between MR imaging versus 2D ultrasound in at- and near-term patients," *European Journal of Radiology*, vol. 91, pp. 35–40, Jun. 2017, doi: [10.1016/j.ejrad.2017.03.005](https://doi.org/10.1016/j.ejrad.2017.03.005). [2] J. Anquez, L. Bibin, E. D. Angelini, and I. Bloch, "Segmentation of the fetal envelope on ante-natal MRI," in *2010 IEEE International Symposium on Biomedical Imaging: From Nano to Macro*, Apr. 2010, pp. 896–899. doi: [10.1109/ISBI.2010.5490131](https://doi.org/10.1109/ISBI.2010.5490131). [3] D. Ryd, A. Nilsson, E. Heiberg, and E. Hedström, "Automatic Segmentation of the Fetus in 3D Magnetic Resonance Images Using Deep Learning: Accurate and Fast Fetal Volume Quantification for Clinical Use," *Pediatr Cardiol*, vol. 44, no. 6, pp. 1311–1318, Aug. 2023, doi: [10.1007/s00246-022-03038-0](https://doi.org/10.1007/s00246-022-03038-0). [4] J. Lo *et al.*, "Cross Attention Squeeze Excitation Network (CASE-Net) for Whole Body Fetal MRI Segmentation," *Sensors*, vol. 21, no. 13, Art. no. 13, Jan. 2021, doi: [10.3390/s21134490](https://doi.org/10.3390/s21134490).

Survival Prediction of Lung Cancer Using Real and GAN Synthesized Low-Dose CT Images

Jenita Manokaran^a, Richa Mittal^b, Eranga Ukwatta^a,

^aUniversity of Guelph, School of Engineering; ^bGuelph General Hospital.

^a50 Stone Rd E, Guelph, ON, Canada N1G 2W1. ^b115 Delhi Street Guelph ON, Canada N1E 4J4.

Introduction: Lung cancer is the second most common and leading cause of cancer death globally. The 5-year survival rate is 64% when detected at the early stages and at the advanced stages of the disease, the survival rate is less than 3%¹. Early diagnosis and prior treatment play a vital role in improving the lung cancer patient's survival rate². Low-dose computed tomography (LDCT), a recommended screening tool for lung cancer aids in early diagnosis thereby lowering the mortality rate and radiation exposure to the patients³. So, in this work, we propose a 3D deep learning model for the accurate prediction of 5-year survival of lung cancer patients for better prognosis stratification and to optimize the treatment options in the affected patients.

Dataset: The dataset was taken from the National Lung Screening Trial (NLST), the largest screening program held in the United States in 2002 targeting high-risk populations that involve both current and former smokers. After data cleaning, a total of 79 biopsy-confirmed lung cancer patients (stage I to III) who were present in all follow-ups were chosen for this study. The 5-year survival rate of the patients was calculated by using the follow-up days and death status provided in the NLST dataset. The window width and level of -700 and 1700 were chosen for the Hounsfield Unit (HU) range. The range was linearly normalized between 0 and 255. Based on the LDCT chosen from NLST data, GAN synthesized data is also considered to increase the training data.

Method: The proposed deep learning model is developed based on a 3D ResNet backbone with 10 layers. After the ResNet backbone, an adaptive average pooling layer and a fully connected layer with 512 neurons complete the model. The proposed model was trained for over 200 epochs using an ADAM optimizer with a learning rate of 0.01. To handle the imbalanced data between survival and death, focal loss function with class weights was used during model training. A deep convolutional generative adversarial network (DCGAN) was trained to produce synthesized LDCT data. Fake images were generated per patient case and later combined with the real LDCT only for training data. The GAN model was trained for 400 epochs using an ADAM optimizer with a learning rate of $1e^{-5}$. Evaluation metrics such as area under the curve (AUC), precision, recall, and F1-score were considered. A train/valid/test split of 70/10/20 was used.

Preliminary results: All the LDCTs were interpolated to 128X128X5 volume before being fed into the proposed model. A comparative study on the number of slices selected per scan based on nodule location showed that the lower the number of slices, the higher the model AUC. Hence, for this study, we chose 5 slices (two above and two below the slice containing the nodule). Registration on the follow-up scans per patient case was performed using ITK snap as a preprocessing step. The proposed model when evaluated using the test set comprising of 60 patient cases, resulted in an AUC of 0.72, overall accuracy of 0.71, precision of 0.83, recall of 0.69, and F1-score of 0.75 for survival analysis. By training the proposed model on a combined training dataset (GAN and real LDCT), an AUC of 0.71 and an overall accuracy was 0.72 were achieved. Improvement in the model's performance was observed in both classes.

Conclusions: To the best of our knowledge, this is one of the first few studies that proposed a 3D deep learning model for a 5-year survival prediction of lung cancer patients by combining real and synthesized 3D LDCT scans. The proposed model on LDCTs will aid in the accurate prediction of 5-year survival in lung cancer patients and lower radiation exposure. Using GAN-generated synthesized data minimizes the need for a large, annotated dataset during model training. Also, a segmentation-free survival analysis proposed in this study aids clinicians in identifying high-risk patients, commencing personalized treatment options, and improves the health care efficiency in reducing mortality risk in Lung cancer patients.

Table 1: Results obtained using real and combined datasets

Dataset	Classes	Precision	Recall	F1-score
Real LDCT	Survived	0.83	0.69	0.75
	Died	0.57	0.75	0.65
	Average	0.71	0.7	0.72
Real and GAN LDCT	Survived	0.73	0.75	0.74
	Died	0.7	0.68	0.69
	Average	0.72	0.72	0.72

[1] H. Sung *et al.*, "Global Cancer Statistics 2020: GLOBOCAN Estimates of Incidence and Mortality Worldwide for 36 Cancers in 185 Countries," *CA Cancer J Clin*, vol. 71, no. 3, pp. 209–249, May 2021, doi: 10.3322/caac.21660.

[2] H. J. de Koning *et al.*, "Reduced Lung-Cancer Mortality with Volume CT Screening in a Randomized Trial," *New England Journal of Medicine*, vol. 382, no. 6, pp. 503–513, Feb. 2020, doi: 10.1056/NEJMoa1911793.

[3] C.-Y. Yang *et al.*, "Stage Shift Improves Lung Cancer Survival: Real-World Evidence," *Journal of Thoracic Oncology*, vol. 18, no. 1, pp. 47–56, Jan. 2023, doi: 10.1016/j.jtho.2022.09.005.

Characterizing the tumor microcirculatory system using Optical Coherence Tomography

Héctor Alejandro Contreras-Sánchez, William Jeffrey Zabel, Edward Taylor and Alex Vitkin

Introduction. Blood vessels have the main function to transport blood and deliver essential molecules to cells. In cancer, the microvascular system of solid tumors exhibit remarkable differences from healthy tissue in both morphology and functionality. Imaging of the tumor microcirculatory system is thus needed to understand the vascular role in certain biological mechanisms including tumor growth and response to cancer therapy. Here, we implemented a non-invasive approach using two Optical Coherence Tomography (OCT) extensions: speckle variance (svOCT) and Doppler OCT (DOCT) for imaging microvascular architecture and blood flow velocity simultaneously in a xenograft model of pancreatic cancer. This methodology will further allow longitudinal studies of tumor vascular and blood flow response to various cancer treatments. Particularly, Stereotactic Body Radiation Therapy (SBRT), towards studying the effects of SBRT in the tumor microcirculatory system in a pre-clinical setting.

Methods. A custom-made Swept-Source OCT (20 KHz A-scan rate) was used in this study. A phantom experiment consisting of a 305- μm inner diameter tube surrounded by static tissue-like gelatin was performed first (Fig. 1(a)-(c)), and a 1% intralipid solution was injected using an electronic syringe pump at different flow rates (0-30 $\mu\text{l}/\text{min}$) to determine the range of detectable velocities in the OCT system (Fig. 1(d)). Then, the morphological (svOCT) + blood velocity (DOCT) microvascular maps in healthy mouse skin and the pancreatic tumor model (Bx-PC3 cancer cell line) were acquired (6x6 mm^2 field-of-view) using the dorsal skin window chamber model. Two OCT-derived metrics: 1) velocity histogram and 2) vessel diameter vs blood velocity were used to quantitatively compare healthy skin and tumor microcirculatory systems (Fig. 1(e)-(f)).

Results. svOCT allows differentiation between static and moving elements in the phantom using the speckle variance effect (Fig. 1(b)), whereas DOCT enables velocity estimations of the moving fluid by measuring the Doppler phase shift of the backscattered signal (Fig. 1(c)). Blood velocity in small vessels such as capillaries are within the order of 1000 $\mu\text{m}/\text{sec}$, and minimum detectable velocity for this OCT system was found to be ≈ 200 $\mu\text{m}/\text{sec}$ (Fig. 1(d)). The velocity histograms in healthy and tumor microcirculation appeared positively skewed (not normally distributed), with a slightly greater mean velocity for the tumor (1.26 ± 0.02 mm/sec) compared with healthy skin (0.468 ± 0.006 mm/sec). Further, the diameter-velocity plot for healthy skin (Fig. 1(e)) shows a weak positive linear correlation ($r=0.478$) whereas a larger deviation from this trend was observed for the tumor (Fig. 1(f), $r=0.225$). The Pearson correlation coefficient can then be used as a goodness-of-fit parameter to discriminate between groups.

Conclusions. Preliminary results show that OCT is a good candidate to simultaneously study vascular architecture and blood velocity in a preclinical tumor model. This non-invasive platform will provide a better understanding of tumor microcirculatory system and its physiological role in radiobiology. Longitudinal experiments using different SBRT treatments regimes are currently being pursued using the proposed methodology.

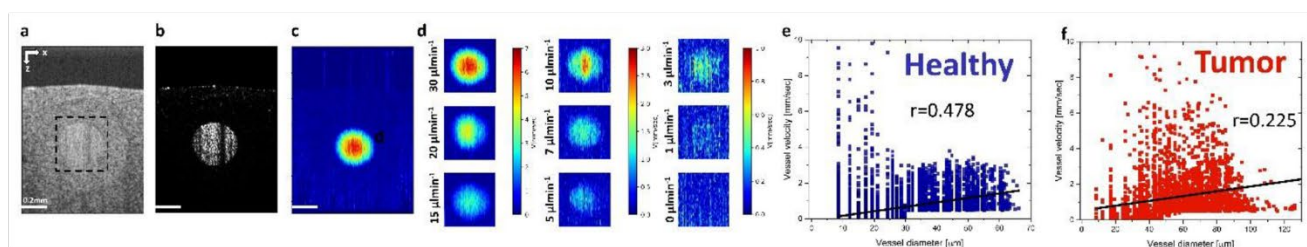


Figure 1: Preliminary results of the proposed OCT methodology. **a)** cross-sectional image of the phantom. **b)** and **c)** svOCT and DOCT images of the phantom respectively. **d)** velocity measurement at different flow rates. **e)** and **f)** diameter-velocity plots for healthy skin and tumor respectively. Scale bar is 0.2 mm.

Session 14 Pitches: Neuroimaging

Abstracts

Assessing the Sensitivity of Cerebral Blood Flow and Oxygenation to High-Intracranial Pressure Using Combined Optical Spectroscopy Techniques

S. Karagulleoglu-Kunduraci*, M. Diop

Department of Medical Biophysics, Western University, Canada

Introduction: Premature birth, occurring before 37 weeks of gestation, impacts 8% of Canadian infants and is linked to the underdevelopment of the cerebral vascular system. This underdevelopment, coupled with hemodynamic instabilities, heightens the risk of cerebral injuries in these infants, particularly intraventricular hemorrhage (IVH) in very low birth weight infants. IVH leads to hydrocephalus, the most common neuropathology in pediatric neurosurgery, characterized by increased intracranial pressure (ICP) and impaired cerebral autoregulation. Current monitoring methods such as ultrasonography can only detect injuries that have already occurred, highlighting the need for prognostic tools. Optical techniques such as near-infrared spectroscopy (NIRS) and diffuse correlation spectroscopy (DCS) enable the assessment of cerebral hemodynamics, oxygenation, and metabolic events, potentially identifying precursors to brain injury.¹⁻² We hypothesize that concomitant measures of cerebral blood flow (CBF), blood oxygenation, and oxygen metabolism will have the ability to detect high ICP. The study aimed to test this hypothesis with the combination of NIRS and DCS.

Methods: In this study, a hybrid NIRS/DCS system was utilized for simultaneous monitoring of CBF, oxygen saturation, and metabolism in neonatal piglets (n=9, 4 females, average age 3.17 days). Following anesthesia, a tracheotomy and catheter insertion were performed for respiratory control and vital signs monitoring. Intraventricular catheters were used for continuous ICP monitoring and saline infusion to manipulate ICP. NIRS and DCS probes were then secured to the piglets' heads using a 3D-printed holder. For the control group (n=2), baseline data were gathered at normal ICP levels (9±3mmHg). In the experimental group, ICP was incrementally raised to 30-40 mmHg, followed by a return to baseline. Measurements of blood oxygenation and CBF were continuously acquired with the NIRS and DCS systems, respectively. Measurements were used to quantify tissue chromophore concentrations (Hb, HbO₂)³, compute changes in cytochrome c oxidase (CCO)⁴, tissue saturation (StO₂) and CBF⁵ by applying approaches described in our previous reports. Baseline measurements were computed by averaging the time course of changes in Hb, HbO₂, CCO, and CBF in the control group. The study assessed cerebral perfusion pressure (CPP) by calculating the difference between mean arterial pressure and ICP. Pearson correlation and linear regression were employed to analyze the relationships between CPP, CBF, Hb, HbO₂, and StO₂, with Independent-Samples t-tests and ANOVA used to evaluate differences during ICP alterations.

Results: As anticipated, there were no significant changes in Hb, HbO₂, CCO, and CBF in the control group during the baseline measurements (i.e., at the baseline ICP=9±3 mmHg). Increasing ICP was accompanied by corresponding increases in Hb and decreases in HbO₂ ($p < 0.001$). In contrast, changes in ICP did not significantly impact CCO levels, which remained relatively stable throughout the experiment. Changes in all three parameters (Δ CPP, Δ CBF, and StO₂) displayed quick changes during the ICP alteration (Figure 1A). An increase in ICP led to a decrease in CPP, Δ CBF, and StO₂ ($p < 0.001$). Figure 1B illustrates that the regression analysis showed a strong correlation between changes in CBF and CPP ($r > 0.95$, $p < 0.05$, $R^2 > 0.89$).

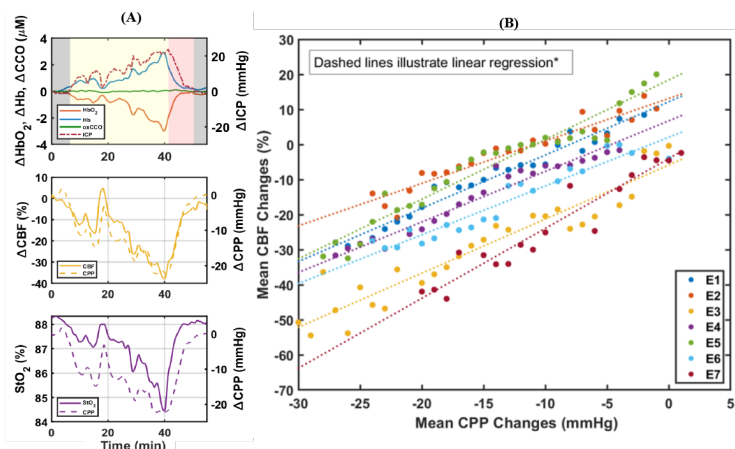


Figure 1:(A) Time dependent changes in Δ Hb, Δ HbO₂ and Δ CCO with Δ ICP, Δ CBF and StO₂ with Δ CPP from one piglet in the experimental group (E1). (B) Correlation between changes in mean CBF and CPP during ICP alterations for all piglets in the experimental group (E1, E2, E3, E4, E5, E6, E7).

Conclusion: This study demonstrates the potential utility of the hybrid optical technique in monitoring high ICP induced alterations in physiological parameters such as CBF and cerebral oxygenation. The findings show that changes in ICP are associated with alterations in the cerebral hemodynamic parameters, as evidenced by the changes in Hb, HbO₂, StO₂, and CBF. The findings of the present study suggest that CBF and cerebral oxygenation can detect elevated ICP and could be used as early indicators of elevated ICP that may result in brain injury.

¹ Rajaram A, et al., *Scientific Reports* 2022 12:1. 2022;12(1):1-10., ² Rajaram A, et al., *Biomed Opt Express*. 2018;9(6):2588.,

³ Diop M, et al., *J Biomed Opt.* 2014;19(5):057007., ⁴ Bale G, et al., *J Biomed Opt.* 2016;21(9):091307., ⁵ Diop M, et al., *Biomed Opt Express*. 2011;2(7):2068.

Exploring the Effects of Phospholipase A2 Inhibition on Brain Metabolism and Pathology in a Rat Model of Alzheimer's Disease

Emily Hiles^{1,2}, Ved Hatolkar², Colleen Bailey², Wendy Oakden², Tina Beckett², Mary Hill², JoAnne McLaurin^{2,3}, Jamie Near^{1,2}

¹Department of Medical Biophysics, University of Toronto, Toronto, Canada; ²Sunnybrook Research Institute, Toronto, Canada; ³Department of Laboratory Medicine and Pathobiology, University of Toronto, Toronto, Canada

Introduction: Alzheimer's disease (AD) currently has no effective treatments making it necessary to explore different therapeutic pathways¹. Magnetic resonance spectroscopy (MRS) offers a non-invasive modality to explore disease pathogenesis and treatment efficacy. Previous MRS studies in both animal models^{2,3} and humans⁴⁻⁷ have shown an increase in choline in AD which is thought to be due to the breakdown of cell membranes by the enzyme phospholipase A2 (PLA2)⁸. Our current working model of PLA2 in AD is illustrated in figure 1. This study aims to gain a deeper understanding of the role of PLA2 in AD through its inhibition in an animal model of AD. It is hypothesized that PLA2 inhibition will reduce choline levels and reduce memory impairment.

Methods: This study used the TgF344-AD rat model at 13 months of age which expresses mutant amyloid precursor protein and presenilin 1 genes⁹. Mepacrine was used to inhibit PLA2 via daily intraperitoneal injections. Total choline (TCh) levels were explored using MRS in both transgenic (Tg, n=8) and non-transgenic (NTg, n=6) animals before and after one week of treatment with either saline (n=7) or mepacrine (n=7). Localized proton MRS data were acquired on a 7 Tesla MRI system (Bruker, Billerica MA, USA) in the right dorsal hippocampus using a PRESS sequence (TR/TE = 2500/8.8 ms, 256 averages, acquisition time = 10.67 min). After the follow-up MRS scan, animals completed the Barnes maze including acquisition training, a probe trial, and reversal training.

Results: TCh levels were observed to decrease in the hippocampus following one week of treatment with mepacrine (1.25 ± 0.05 mM to 1.12 ± 0.10 mM averaged across both genotypes). TCh levels were more level after one week in the saline controls (1.20 ± 0.04 mM to 1.17 ± 0.05 mM averaged across both genotypes). Contrary to our expectations, TCh levels at baseline did not appear to differ between Tg (1.23 ± 0.06 mM, COV = 0.05) and NTg (1.21 ± 0.03 mM, COV = 0.02) genotypes. In the probe trial of the Barnes maze, the primary latency of Tg animals treated with mepacrine (7.33 ± 4.62 s) was observed to be faster than Tg animals treated with saline (40.75 ± 35.71 s) and similar to NTg animals treated with saline (9.00 ± 3.46 s).

Conclusions: Baseline TCh concentrations did not differ between NTg and Tg animals, contrary to a previous study at 7T². This study also showed notable overlap in TCh, therefore, we expect to see elevated TCh in Tg animals as the present study continues. Decreased TCh in mepacrine treated animals demonstrates that PLA2 was likely inhibited in the hippocampus. The preliminary Barnes maze results show promise that PLA2 inhibition improves long-term spatial memory formation which agrees with a previous study showing improved memory formation in PLA2 knockout AD mice¹⁰. Thus far, we have shown that PLA2 activity may contribute to memory impairment in AD which could make it a valuable therapeutic target. Future work will aim to explore pathological and neuroinflammatory changes in AD following PLA2 inhibition.

References:

1. Yiannopoulou KG et al. J Cent Nerv Syst Dis. 2020;12:1179573520907397.
2. Fowler CF et al. Brain Comm 2022;4(2):1-16.
3. Choi JK et al. Brain Res. 2014;1590:85-96.
4. Marhanska M et al. J Alzheimers Dis. 2019;68(2):559-569.
5. Joe E et al. Brain Imaging Behav. 2019;13(4):925-932.
6. Kantarci K et al. Neurology. 2004;63(8):1393-1398.
7. Meyerhoff DJ et al. Ann Neurol. 1994;36(1):40-47.
8. Klein J. J Neural Transm 2000;107:1027-1063.
9. Cohen et al. J Neurosci 2013;33(15):6245-6256.
10. Sanchez-Mejia RO et al. Nat Neurosci 2008;11:1311-1318.

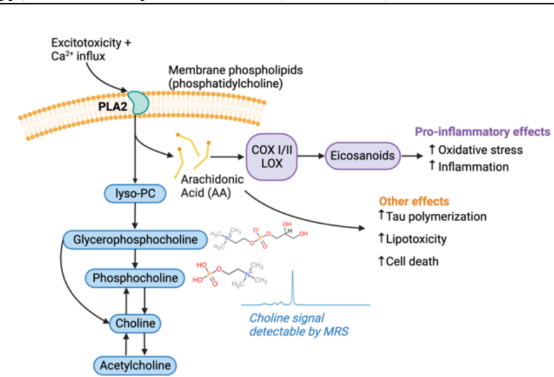


Figure 1. Working model of the role of PLA2 in AD. The pathways shown demonstrate the breakdown of phosphatidylcholine leading to measurable cholines and a pro-inflammatory pathway that may contribute to AD pathogenesis.

Cerebral blood flow during selective brain cooling in cerebral ischemia

Olivia L.H. Tong^{1,2,3}, Kevin J. Chung^{1,2,3}, Jennifer Hadway¹, Laura Morrison¹, Lise Desjardins¹, Susan Tyler¹, Marcus Flamminio¹, Lynn Keenlside¹, Ting-Yim Lee^{1,2,3}

¹Imaging Program, Lawson Health Research Institute, London, ON, Canada; ²Robarts Research Institute, London, ON, Canada; ³Department of Medical Biophysics, The University of Western Ontario, London, ON, Canada

INTRODUCTION: Despite the success of reperfusion therapy by mechanical thrombectomy for large vessel occlusion stroke, not all treated patients fully recovered their function. Selective brain cooling could be adjuvant therapy to maximize the beneficial effect of reperfusion and mitigate the adverse effects of whole-body cooling. However, clinical application is limited by the lack of optimal delivery methods and unknown treatment parameters. To improve delivery, we have designed a prototype called VINCI (the Vortex tube IntraNasal Cooling Instrument). While survival after large vessel occlusion stroke is critically dependent on cerebral blood flow (CBF), cerebral metabolic rate decreases 6-7% with each 1°C decrease in brain temperature.^{1,2} Hence, monitoring cerebral blood flow (CBF) may guide the optimal depth and duration of brain cooling. We hypothesize that VINCI can improve cerebral ischemia outcomes, and we aim to determine the relationship between CBF and brain cooling.

METHODS: 36 pigs (35.1 ± 10.0 kg) were used for this study. The animals were divided into ischemia and normal groups. Within the ischemia group, 23 pigs (33.5 ± 9.9 kg) were injected with a vasoconstrictor (ET-1) to induce ischemia. The animals were then assigned to untreated ischemia (i.e., no cooling; n = 7) and treated ischemia (i.e., brain cooling; n = 16) groups. In the treated normal (n = 13; 36.6 ± 10.1 kg) and treated ischemia groups, brain cooling was maintained for 18h before rewarming at a rate of 0.5°C. Throughout the study, realtime physiological variables and brain hemodynamics by CT perfusion (CTP) at pre-specified intervals were collected. The CTP was acquired at 1.0-second image intervals for 40 seconds, and then once every 15 seconds for a total of 150 seconds. Physiological variables, CTP parameters, and histology at sacrifice were compared. Statistical significance was demonstrated using non-parametric Kruskal Wallis tests followed by post hoc analysis. Dichotomous variables between groups were compared using the Fisher exact test.

RESULTS: Within the ischemia group, 5 out of 7 untreated animals succumbed to brain dead at 11.5 ± 2.0 h. 4 out of 16 VINCI-treated animals were brain dead at 17.3 ± 2.1h before rewarming. Intracranial pressures (ICP) by the last hour were 40.1 ± 18.8 mmHg, 25.9 ± 12.6 mmHg, and 16.1 ± 4.6 mmHg for the untreated ischemic, treated ischemic and treated normal animals, respectively. Brain cooling by VINCI improved survival (p = 0.05) and outcome (i.e., ICP, p < 0.01). All untreated and 8 out of 16 treated ischemic animals developed severe global hyperperfusion (high CBF) before rewarming (p = 0.03). This global hyperperfusion preceded significant changes in ICP from baseline. Within the treated ischemia group, the ICPs by the last hour were 33.3 ± 14.5 mmHg and 18.4 ± 1.9 mmHg for the animals with global hyperperfusion and without global hyperperfusion, respectively (p = 0.01). This finding was further corroborated by (1) the predicted lesion volume by CTP at the target temperature matched the true infarct by histology and (2) a smaller true infarct volume compared to that with global hyperperfusion (p < 0.05).

CONCLUSIONS: The global increase in CBF following reperfusion appears to be associated with disturbances in cerebrovascular hemodynamics. The absence of global hyperperfusion during brain cooling is associated with normal or slightly elevated ICP. Hypoperfusion during cooling seems to be critical for successful cooling. Hence, global hyperperfusion during cooling could be an early marker of ineffective neuroprotection in severe ischemic stroke. In future, the integrity of the blood-brain barrier during ischemia will be investigated. This work showed that CBF imaging could guide VINCI-enabled brain cooling as a neuroprotective therapy for ischemic stroke.

¹Yenari et al. (2012) *Nat. Neurosci.* ²Lyden et al. (2021) *Stroke*.

Longitudinal Changes in White Matter Diffusivity in First Episode Psychosis Patients

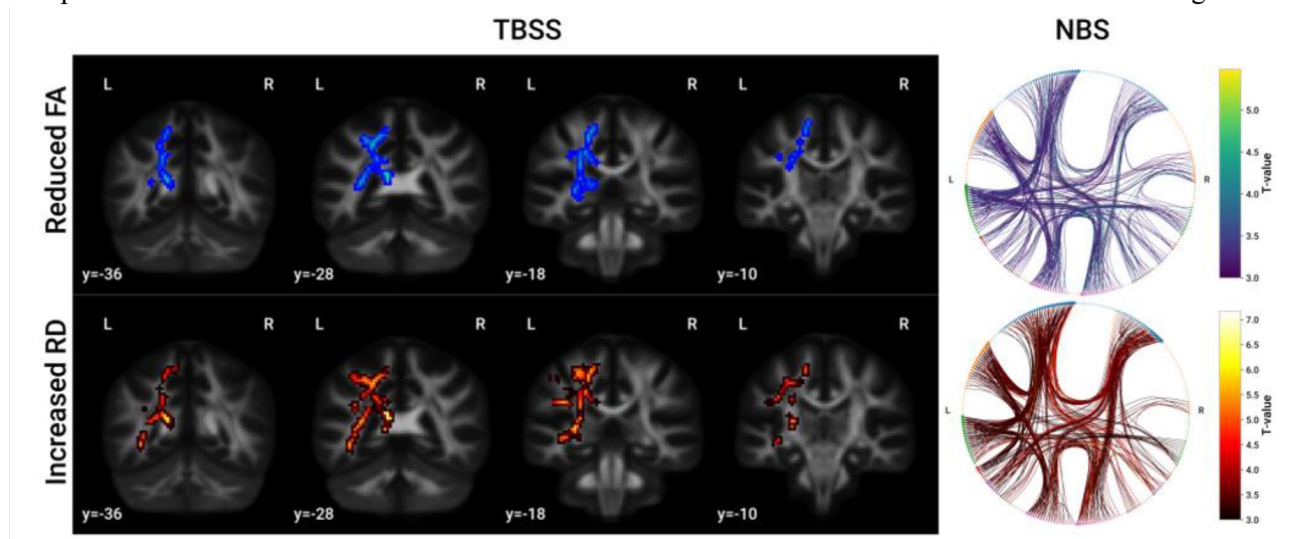
Peter Van Dyken¹, Ali R. Khan¹, Lena Palaniyappan²

¹Robarts Research Institute, Western University, London

²Douglas Mental Health University Institute, McGill University, Montreal

Introduction: Patients with chronic schizophrenia have marked disruption of white matter connectivity as shown by diffusion MRI¹. However, this disruption appears to be limited or absent in first episode psychosis (FEP) patients (Van Dyken, 2023, in review). Thus far, nearly all studies of FEP have been cross-sectional, preventing the disambiguation of schizophrenia as a white matter-altering disease and pre-existing white matter damage as a risk factor for intractable schizophrenia. Here, we explore a longitudinal cohort of FEP patients and healthy controls to investigate the first possibility: whether schizophrenia associates with changes in white matter diffusivity over time.

Methods: N=21 FEP patients and N=13 healthy controls were scanned twice with follow-up 6-12 months after baseline. Data was acquired with 7T MRI using diffusion-weighted ($b=0,1000$; 64 directions; 2mm res) and T1-weighted (MP2RAGE; 0.75mm res) protocols. Diffusion data was preprocessed with FSL and tractography was generated using MRTrix. Tract-based spatial statistics (TBSS) was used to measure voxel-wise differences between sessions³. After defining structural connectivity matrices using the Brainnetome atlas⁴, the Network Based Statistic (NBS) was used to identify connections with significant changes in FA and RD⁵. For all analyses, data were fit to a mixed linear model, with subjects as random effects and time by group as the fixed effect. Significance was based on a null distribution of 10,000 permutations with random group assignment. Multiple comparisons were corrected with threshold-free cluster enhancement² for TBSS and network clustering for NBS.



Results: In FEP patients, a region with significantly lower FA and higher RD in the second scan was found in the left hemisphere. Connections with decreased FA and increased RD were found predominantly in the left hemisphere. Changes in HCs were not significantly different from 0, however, the effects in FEP patients were also not significantly different from HCs.

Conclusions: A change in diffusivity toward the patterns observed in chronic patients can be seen in the left hemisphere of FEP patients, however, it is unclear if this change is mediated by schizophrenia or is merely an effect of time. Future analysis with large sample sizes should help to clarify this question.

References: 1. Kelly, S. (2018) [Widespread white matter microstructural differences in schizophrenia across 4322 individuals: Results from the ENIGMA Schizophrenia DTI Working Group](#). *Molecular Psychiatry* 23, 1261–1269. 2. Smith, S. M. (2009) Threshold-free cluster enhancement: addressing problems of smoothing, threshold dependence and localisation in cluster inference. *NeuroImage* 44, 83–98. 3. Smith, S. M. (2006) Tract-based spatial statistics: voxelwise analysis of multi-subject diffusion data. *NeuroImage* 31, 1487–1505. 4. Fan, L. (2016) [The Human Brainnetome Atlas: A New Brain Atlas Based on Connectional Architecture](#). *Cerebral Cortex* 26, 3508–3526. 5. Zalesky, A. (2010). Network-based statistic: identifying differences in brain networks. *NeuroImage* 53, 1197–1207.

Title: Neural biomarkers of Schizophrenia and Autism Spectrum Disorders during the empathic accuracy task

Ju-Chi Yu¹, Colin Hawco^{1,2}, Lindsay D. Oliver¹, Maria T. Secara^{1,2}, Iska Moxon-Emre¹, Fariah A. Sandhu³, Zara Z. Khan⁴, Peter Szatmari^{1,2}, Meng-Chuan Lai^{1,2}, Miklos Argyelan⁵, James M. Gold⁶, Sunny X. Tang⁵, George Fousias^{1,2}, Robert W. Buchanan⁶, Anil K. Malhotra⁵, Aristotle N. Voineskos^{1,2}, Stephanie H. Ameis^{1,2*}, Erin W. Dickie^{1,2*}

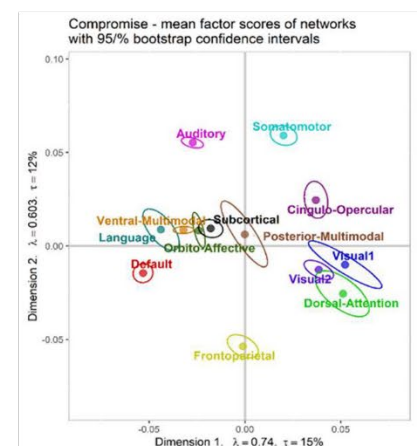
1. Centre for Addiction and Mental Health, Toronto, Canada
2. Department of Psychiatry, Temerty Faculty of Medicine, University of Toronto, Toronto, Canada
3. Department of Psychology, York University, Toronto, Canada
4. Department of Electrical and Computer Engineering, McMaster University, Hamilton, Canada
5. Zucker Hillside Hospital, Glen Oaks, NY, USA
6. Maryland Psychiatric Research Center, Department of Psychiatry, University of Maryland School of Medicine, Baltimore, MD, USA

Background: Schizophrenia (SSD) and Autism Spectrum Disorders (autism) are both characterized by social cognitive deficits, which vary substantially within, but overlap across, diagnoses. In this study, we aimed to identify group-specific and shared brain functional network configurations present during a social processing functional magnetic resonance imaging (fMRI) task.

Methods: Multimodal MRI scans were obtained using 5 3T scanners across 3 sites, where task MRI scans were collected using an EPI sequence with TR = 3s and in plane resolution = 3 mm². All scans were quality checked after being preprocessed using standard pipelines with fmriprep (including Synthetic distortion correction) and ciftify (with ribbon constrained surface projection). Background functional connectivity (i.e., with task and nuisance signals regressed out) during the empathic accuracy (EA) task from 411 participants (autism: N=67; SSD: N=174; Controls (HC): N=170) was first processed by ComBat to control for site effects, parcellated based on Glasser cortical and Tian subcortical atlases, and analyzed by DiSTATIS, a multivariate method that jointly analyzes multiple similarity matrices. DiSTATIS first combined the similarity matrices to create a *compromise* space, from which DiSTATIS then extracts latent dimensions (or called principal components) that characterize the dominant network configurations across participants and enabling comparison between groups in the same space. Bootstrap tests were used to examine network configuration and group differences.

Results: Two orthogonal dimensions were identified from DiSTATIS. The first dimension's configuration (explaining 14.98% of the signal) was characterized by differentiation between language (LAN) and default mode versus visual (VIS) and dorsal attention networks (DAN). The second dimension's configuration (explaining 11.97% of the signal) was characterized by differentiation between auditory, somatomotor versus frontoparietal networks. On group-wise comparison, HC showed specific differentiation between VIS and DAN ($p < .05$); autism showed specific differentiation between LAN and ventral-multimodal network ($p < .05$); and SSD showed specific non-differentiation between primary and secondary VIS ($p > .05$).

Conclusions: The prominent latent dimensions of the overall EA-related network configuration were similar across groups, with specific configurations of autism in LAN and of SSD in VIS. By comparing these results with similar analysis on resting-state scans, we could identify specific network configuration associated with emotion recognition. Future examination of their relationships with cognition and clinical outcomes can reveal potential biomarkers, which may inform future intervention studies or treatments, for social cognitive deficits in autism and SSD.



Probing Microstructural Orientations of Hippocampal Gray Matter in Alzheimer's Disease

Bradley G. Karat¹, Ali R. Khan^{1,2}

¹Centre for Functional and Metabolic Mapping, Robarts Research Institute, Western University, London, Canada, ²Department of Medical Biophysics, Western University, London, Canada

Introduction: The hippocampus plays key roles in memory and spatial navigation. The glial cells, neurites, and fiber pathways that make up the microstructure of the hippocampus are essential in producing these functions. Hippocampal microstructure tends to be oriented relative to three canonical hippocampal axes along its anterior-posterior (AP), proximal-distal (PD), and inner-outer (IO) directions (Figure 1D). Importantly, hippocampal microstructure is known to be affected by Alzheimer's disease

(AD). Examining the direction of diffusion relative to the hippocampal axes may provide a way to indirectly probe the orientationally-distinct hippocampal pathways that are affected in AD. It is hypothesized that diffusion orientations relative to the hippocampal axes will be altered in MCI and AD relative to controls. **Methods:** We used the Alzheimer's Disease Neuroimaging Initiative dataset (adni.loni.usc.edu), including diffusion (7 $b=0s/mm^2$ and 48 $b=1000s/mm^2$) and T1w structural MRI from 413 controls (CN), 153 mild cognitive impairment (MCI), and 44 AD participants. *HippUnfold*, a tool for surface-based subfield segmentation and hippocampal unfolding, was used to generate vectors along the AP, PD, and IO axes of the

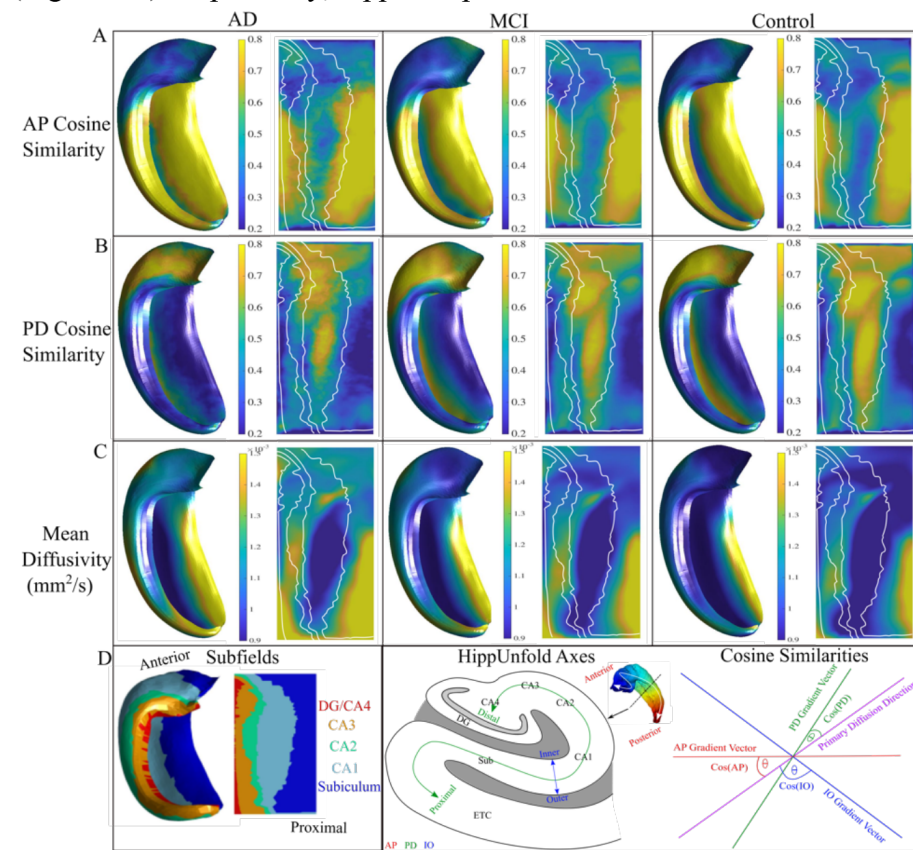


Figure 1. Group-averaged cosine similarities and mean diffusivity on the midthickness surface. (A-C) AP and PD cosine similarities and MD across groups of AD, MCI, and controls. (D) Subfields, HippUnfold axes, and cosine similarity calculation example.

hippocampus (Figure 1D). Diffusion tensor imaging (DTI) was used to generate metrics of mean diffusivity and the primary direction of diffusion. Cosine similarities were calculated as the dot product between hippocampal axis vectors and the primary DTI eigenvector (Figure 1D right). Cosine similarities were then sampled along the midthickness surface. Subfield averages of all metrics were then taken within each participant. Welch's ANOVA was performed to test whether the subfield distributions of each metric were significantly different across the groups. **Results:** AP diffusion (Figure 1A) within CA1 was significantly increased in AD relative to MCI and controls ($p<0.05$, $p<0.0005$, respectively), and within MCI compared to controls ($p<0.0005$). Figure 1B shows significant changes in the amount of PD diffusion across the groups. Within CA1, all groups were found to be significantly different from each other ($p<0.0005$), with controls having greater amounts of PD diffusion. Large differences in subfield MD can also be discerned across the groups (Figure 1C). **Conclusion:** In this work we show significant differences in the primary orientation of diffusion relative to three hippocampal axes between AD, MCI, and control participants within and across the subfields. Presumably these changes relate to hippocampal microstructural alterations that have been well documented in AD. An example of this could be known perforant path deterioration in CA1 manifesting as lower PD oriented diffusion.

Neural Circuitry and Therapeutic Targeting of Depressive Symptoms in Schizophrenia Spectrum Disorders

Julia Gallucci^{1,2}, Ju-Chi Yu¹, Lindsay D. Oliver¹, Hajer Nakua^{1,2}, Peter Zhukovsky¹, Erin W. Dickie^{1,2}, Zafiris J Daskalakis³, George Foussias^{1,2}, Daniel M. Blumberger^{1,2}, Colin Hawco^{1,2*}, Aristotle N. Voineskos^{1,2*}

1. Centre for Addiction and Mental Health, Toronto, ON, Canada
2. University of Toronto, Toronto, ON, Canada
3. University of California San Diego School of Medicine, La Jolla, CA, United States of America

Introduction: Depressive symptoms are common in Schizophrenia Spectrum Disorders (SSDs), with up to 80% of patients experiencing a depressive episode at some point in their illness. Both negative (e.g., anhedonia, alogia, amotivation) and depressive symptoms in SSDs lead to adverse effects on suicidality, prognosis, and quality of life. Conceptual similarities between depressive and negative symptoms complicate biomarker and intervention development. This study employed a data-driven approach to delineate the neural circuitry underlying depressive and negative symptoms in SSDs.

Methods: Data from three studies: two neuroimaging (fMRI/MRI) studies and a randomized repetitive transcranial magnetic stimulation (rTMS) trial were analyzed (n=157 SSDs) to assess brain-behavior relationships. Partial Least Squares Correlation (PLSC) investigated associations between resting-state functional connectivity and depressive and negative symptoms. Symptoms were assessed using the Calgary Depression Scale for Schizophrenia and Scale for the Assessment of Negative Symptoms. Functional connectivity of 392 regions of interest was derived as correlations between their mean time series obtained from a 7-minute resting-state fMRI scan. Secondary analysis of rTMS trial data (active n=37, sham n=33) were used to assess relationships between PLSC-derived symptom profiles and treatment outcomes.

Results: PLSC identified three latent variables (LVs) (all $p < 0.0001$) relating functional brain circuitry with symptom profiles (Figure 1). LV1 related a general depressive symptom factor with positive associations between and within Default Mode Network (DMN), Frontoparietal Network (FPN), and Cingulo-Opercular Network (CON). LV2 related negative symptoms (no depressive symptoms) via negative associations, especially between FPN and CON, but also between DMN with FPN and CON. LV3 related a guilt and early wakening depression factor via negative rather than positive associations to the DMN, FPN, and CON. The secondary visual network had a positive association with general depressive symptoms and negative associations with guilt and negative symptoms. Active (but not sham) rTMS to the bilateral dorsolateral prefrontal cortex (DLPFC) reduced general depressive but not guilt-related or negative symptoms.

Conclusions: Our findings clearly differentiate the neural circuitry underlying depressive and negative symptoms, and even segregated across the two-factor structure of depression in SSDs. These findings support divergent neurobiological pathways of depressive symptoms and negative symptoms in people with SSDs. As treatment options are currently limited, rTMS to the bilateral DLPFC is worth exploring further for general depressive symptoms in people with SSDs.

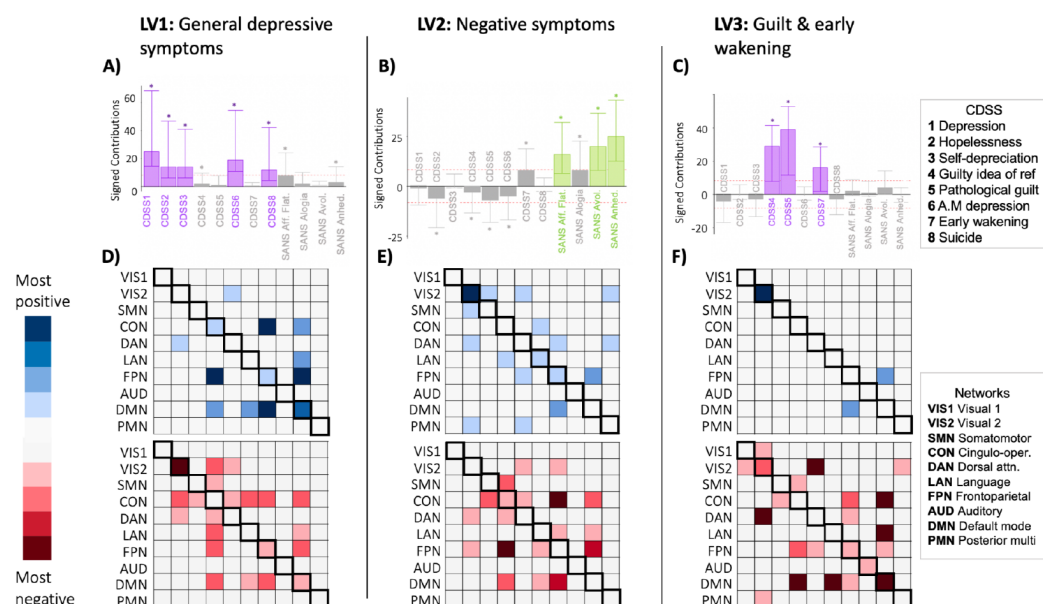


Figure 1: PLSC reveals multivariate patterns of negative and depressive symptoms with functional connectivity. A-C) Clinical symptoms contributing to LV1-LV3. D-F) Within- and between-network connectivity patterns contributing to LV1-LV3.

Brain Perfusion in Social Anxiety Disorder and the Relationship with Symptom Severity: An Arterial Spin Labeling Investigation

Christina F. Pereira^{1,5}, Mashal Ahmed^{1,7}, Shahtaj S. Dheda¹, Bernard Le Foll¹⁻⁶, Dafna S. Rubin-Kahana^{2,4}, Isabelle Boileau^{1,3,4,5}, Stefan Kloiber^{1,3,4,5,6}

¹Research Imaging Centre, ²Translational Addiction Research Laboratory, ³Campbell Family Mental Health Research Institute, Centre for Addiction and Mental Health, Toronto, Ontario, Canada

⁴Department of Psychiatry, ⁵Institute of Medical Science, ⁶Department of Pharmacology and Toxicology University of Toronto, Toronto, Ontario, Canada

⁷Schulich School of Medicine and Dentistry, University of Western Ontario, London, Canada

Background: Social Anxiety Disorder (SAD) is a prevalent condition impacting millions of Canadians. Arterial Spin Labeling (ASL) is a magnetic resonance imaging (MRI) technique that measures brain perfusion noninvasively. Studies of brain perfusion in SAD using single photon emission tomography (SPECT) have found regional elevations and reductions compared to healthy controls (HCs) and mixed correlations with symptom severity depending on brain region.¹ Limited research has investigated brain perfusion in SAD using ASL, however ASL on other psychiatric conditions characterized by social deficits has found regional and whole brain hypoperfusion compared HCs.^{2,3} With interest in exploring neural response in social anxiety, this study aimed to investigate cerebral blood perfusion and its relationship to SAD symptom severity using ASL in individuals with SAD compared to HCs.

Methods: Twenty-one individuals with SAD (males/females: 6/15; age:27.3(± 5.5)) completed an MRI scan measuring resting state ASL. Relationship between age and sex on brain perfusion was evaluated, demonstrating a significant effect of age only ($p = 0.01$). To compare brain perfusion across 9 regions of interest (ROI) to 50 HCs (males/females: 26/24; age: 25.5(±7.3)), a repeated measures ANCOVA controlling for age was used. Partial correlations were used to investigate the relationship between SAD symptom severity and brain perfusion.

Results: Whole brain perfusion was reduced by 4.8% in individuals with SAD compared to HCs, however this failed to reach significance ($F(1, 68) = 1.423$; $p = 0.237$). A significant ROIxGroup interaction was observed ($F(3.63, 247.17) = 3.121$; $p = 0.019$) with significant regional differences observed in the insula (- 8.3%, $p = 0.034$; other ROIs $p > 0.05$; Figure 1). SAD symptom severity was not correlated with whole brain ($r = - 0.242$, $p = 0.303$) or ROI perfusion ($- 0.301 < r < -0.150$; $p > 0.05$).

Significance: In this preliminary analysis, brain perfusion measured by ASL was not significantly associated with SAD or symptom severity, however significant differences were observed between groups in the insula. The insula has been implicated in SAD given its role in processing of emotion and introspective awareness and has been reported to have reduced volume in individuals with SAD.⁴ This finding requires further analysis and confirmation in larger samples to better understand brain perfusion in SAD.

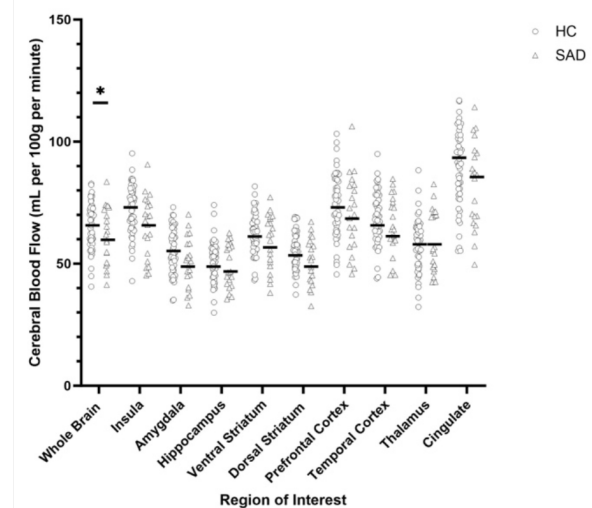


Figure 1: Mean brain perfusion rate across 9 ROIs in individuals with social anxiety disorder (represented by triangles) and healthy controls (represented by circles)

Citations

- Warwick JM, Carey P, Jordaan GP, Dupont P, Stein DJ. Resting brain perfusion in social anxiety disorder: A voxel-wise whole brain comparison with healthy control subjects. *Progress in Neuro-Psychopharmacology and Biological Psychiatry*. 2008;32(5):1251-1256. doi:10.1016/j.pnpb.2008.03.017
- Ye F, Du L, Liu B, et al. Application of pseudocontinuous arterial spin labeling perfusion imaging in children with autism spectrum disorders. *Frontiers in Neuroscience*. 2022;16. Accessed November 28, 2023. <https://www.frontiersin.org/articles/10.3389/fnins.2022.1045585>
- Oliveira IAF, Guimarães TM, Souza RM, et al. Brain functional and perfusional alterations in schizophrenia: an arterial spin labeling study. *Psychiatry Research: Neuroimaging*. 2018;272:71-78. doi:10.1016/j.pscychres.2017.12.001
- Kawaguchi A, Nemoto K, Nakaaki S, et al. Insular volume reduction in patients with social anxiety disorder. *Frontiers in Psychiatry*. 2016;7. doi:10.3389/fpsy.2016.00003

Heterogeneity in Functional Connectivity: Dimensional Predictors of Individual Variability during Rest and Task fMRI in Psychosis

Maria T. Secara^{1,2}, Lindsay D. Oliver¹, Julia Gallucci^{1,2}, Erin W. Dickie^{1,3}, George Foussias^{1,3}, James Gold⁵, Anil K. Malhotra⁴, Robert W. Buchanan⁵, Aristotle N. Voineskos^{1,3}, Colin Hawco^{1,3}

1. Campbell Family Mental Health Research Institute, Centre for Addiction and Mental Health, Toronto, ON, Canada
2. Institute of Medical Science, University of Toronto, Toronto, ON, Canada
3. Department of Psychiatry, University of Toronto, Toronto, ON, Canada
4. Department of Psychiatry, Division of Research, The Zucker Hillside Hospital Division of Northwell Health, Glen Oaks, NY, USA
5. Maryland Psychiatric Research Center, Department of Psychiatry, University of Maryland School of Medicine, Baltimore, MD, USA

Background

Individuals with schizophrenia spectrum disorders (SSD) often demonstrate cognitive impairments, associated with poor functional outcomes. While neurobiological heterogeneity has posed challenges when examining social cognition in SSD, it provides a unique opportunity to explore brain-behavior relationships. We examined the relationship between behavioral data and individual variability of functional connectivity at rest and during an emotional-processing task. We hypothesised that individuals with SSD would display greater heterogeneity in functional connectivity than controls, and that worse cognitive performance would be associated with greater individual variability.

Methods

Neuroimaging and behavioral data were analyzed for 193 individuals with SSD and 155 controls (total $n = 348$). The average time series was extracted from MNI-space fMRI data using the 360 cortical region surface-based Multimodal Parcellation 1.0 atlas. The Melbourne Subcortex Atlas (Scale II) was used to extract 32 subcortical regions. A mean time series was extracted for each of the 392 regions for both resting state and task residual data. Individual variability was quantified through mean correlational distance (MCD) of functional connectivity between participants; MCD was defined as a global 'variability score'. Hierarchical regressions were performed on variability scores derived from resting state and Empathic Accuracy (EA) task functional connectivity data to determine potential predictors (e.g., age, sex, neurocognitive and social cognitive scores) of individual variability.

Results

MCD of EA functional connectivity across SSD was found to be significantly higher than controls ($t = 2.92$, $p = 0.022$, Cohen's $d = 0.24$). This was replicated for the resting state data, with MCD of functional connectivity across SSD being significantly higher than controls ($t = 3.87$, $p < 0.001$, Cohen's $d = 0.41$). Mean correlational distance was also significantly lower in EA than in rest (paired-samples t -test; $t = 54.65$, $p = < 2.2e-16$), demonstrating participants entered a more similar connectivity pattern while performing the EA task. In the hierarchical regression, diagnosis remained significant when social cognition was included during rest ($p = 0.008$), but not during the EA task ($p = 0.50$); social cognition was significant during both rest and task (both $p = 0.01$).

Conclusions

Diagnostic differences were more prevalent during unconstrained resting scans, whereas the task pushed participants into a more common pattern which better emphasized transdiagnostic differences in cognitive abilities. Several hypotheses have suggested dysconnectivity in SSD due to abnormal functional integration. The dysconnectivity hypothesis may extend to the internally directed cognitive processes and self-referential nature of resting state, directly translating to the disorganized and increased variability observed in the SSD sample. Future work should consider both resting state and task-state connectivity when examining variability. Further validation of the variability underlying brain-behavior relationships could guide targeted treatment development for those exhibiting cognitive deficits, and future studies should consider individualized patterns of variability during task and rest to optimize individualized treatment.

Higher general intelligence is linked to stable, efficient, and typical brain connectivity patterns

Justin Ng^{1,2}, Ju-Chi Yu¹, Jamie D. Feusner^{1,2,3,4}, Colin Hawco^{1,3}

1. Campbell Family Mental Health Research Institute, Centre for Addiction and Mental Health, Toronto, ON, Canada
2. Institute of Medical Science, University of Toronto, Toronto, ON, Canada
3. Department of Psychiatry, University of Toronto, Toronto, ON, Canada
4. Department of Women's and Children's Health, Karolinska Institutet, Stockholm, Sweden

Introduction: General intelligence, the ability to excel across diverse situations, can be quantified by the positive correlations observed between nearly all cognitive tests. General intelligence can be measured by the g-factor (*g*), derived by extracting common variance underlying cognitive test scores. *g* is strongly linked to academic and professional achievement. Shared performance giving rise to *g* may be driven by shared mechanisms. A recent hypothesis suggests that *g* emerges from the capacity to dynamically and adaptively reorganize brain connectivity. Network reconfiguration can be assessed using dynamic functional connectivity (dFC), which captures the propensity of whole-brain connectivity to transition between recurring states. Conventional metrics focus on categorical switching frequencies which do not fully capture individual variation in continuous connectivity reconfiguration. Here, we supplement “frequency” measures by quantifying similarity between connectivity patterns as distances, where lower distances indicate greater similarity. We investigated “transition distance” during transitions between connectivity patterns in different states, and individual “idiosyncrasy”, measuring the distance of individual connectivity patterns to group-average state connectivity. We hypothesize that *g* exhibits associations with frequency, transition distance, and idiosyncrasy.

Methods: We utilized Human Connectome Project (HCP; $n=950$; male=448; age=28.65±3.70) cognitive and 3T resting-state fMRI data (TR=720 ms, TE=33 ms, flip angle=52°, voxel size=2 mm isotropic, 72 slices at multiband acceleration factor=8, 104x90 matrix) preprocessed using standard HCP pipelines including ICA-FIX with motion regression to remove spurious noise, and applied Partial Least Squares Correlation (PLSC). PLSC identifies sequential pairs of latent variables from linear combinations of two matrices (cognitive tests and reconfiguration metrics) which maximally capture the total covariance. Weighting of original variables quantifies the contribution. We investigated whether *g* (high weights for most tests) or domains (high weights for a subset) emerge as a property of reconfiguration (high weights for dFC metrics driving the relationship).

Results: The first pair (capturing most covariance) contained a cognitive latent variable with positive weights for most tests (Fig. 1), suggesting a strong data-driven relationship between *g* and reconfiguration. Corresponding reconfiguration latent variable weights characterize a positive association between *g* and stable maintenance (e.g., high dwell time) of states characterized by connectivity between networks involved in higher-order cognition, efficient reconfiguration (low transition distance between similar states, high distance between dissimilar states), and ability to sustain connectivity close to the group-average (low idiosyncrasy).

Conclusions: Our results hint at interesting principles of brain-behavior organization, suggesting that *g* is supported by efficient reconfiguration between stable and population-typical connectivity patterns.

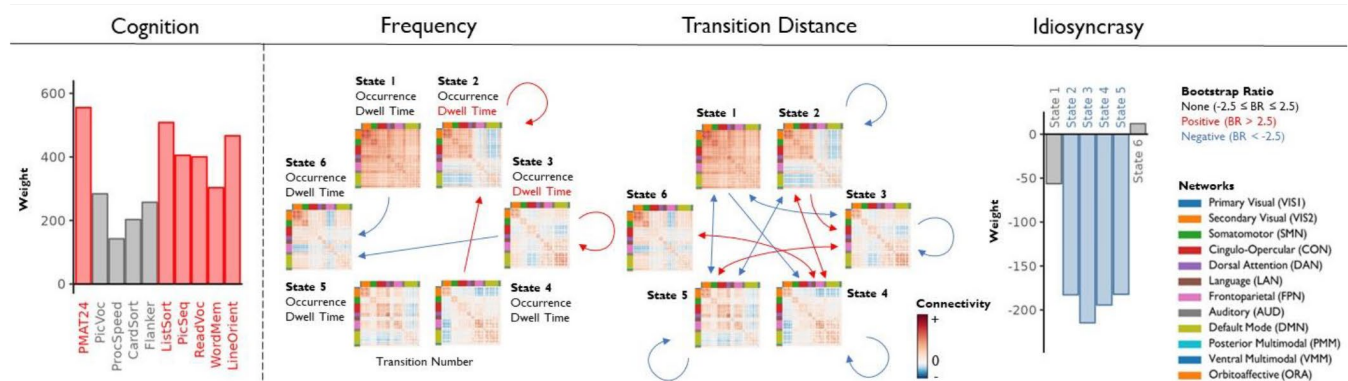


Figure 1. Results. States are characterized by positive (red) and negative (blue) connectivity between regions. Based on permutation testing, the covariance between cognition and reconfiguration latent variables was significant ($p < 0.05$). Based on bootstrapping, stable ($|BR| > 2.5$) positive (red) and negative (blue) weights for cognition (left of line) and reconfiguration (right) latent variables are illustrated. For frequency, occurrence refers to the probability of the state, dwell time refers to the average length of time the state exists, transition number refers to number of transitions, and arrows refer to specific transition probabilities. For transition distance, arrows refer to transition distance. For cognition and idiosyncrasy, loadings are shown.

Session 15 Talks: Deep/Machine Learning 2

Abstracts

Deep Learning-Enabled Quantitative Fluorescence Imaging for Surgery: Application to Post-Resection Residual Cancer

Jerry Wan,¹ Natalie Won,¹ Anjolaoluwa Adewale,¹ Christina Negus,¹
Alon Pener-Tessler,² Brian C. Wilson,¹ Jonathan C. Irish^{1,2} and Michael J. Daly¹

¹Princess Margaret Cancer Centre, University Health Network, Toronto ON, Canada

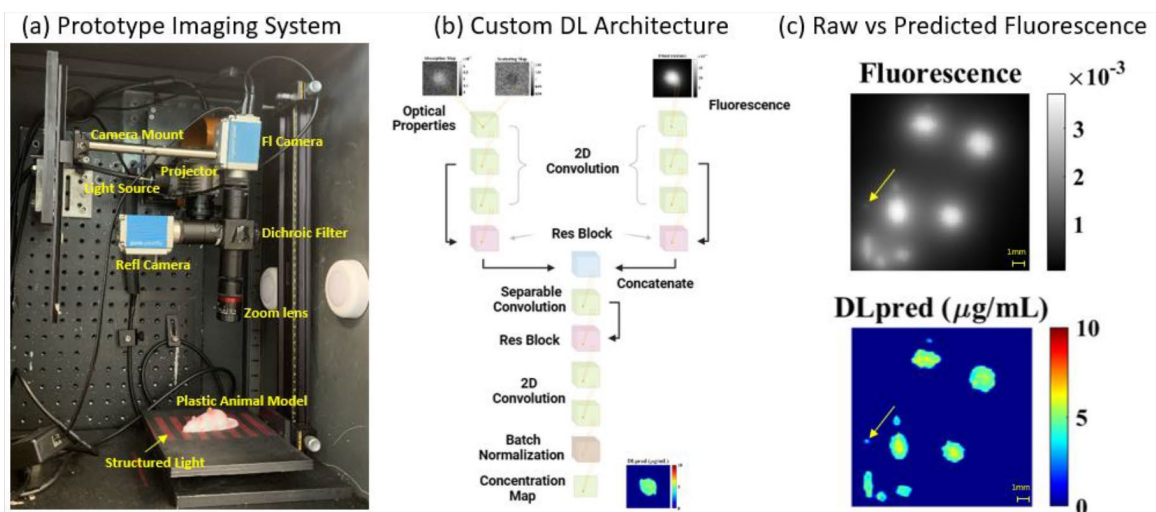
²Department of Otolaryngology – Head & Neck Surgery, University of Toronto, Toronto ON, Canada

Introduction: There is an unmet need to better identify residual tumor after resection during cancer surgery.¹ Fluorescence-guided surgery is an intraoperative imaging technique to help identify cancerous tumors, but traditional clinical imaging devices face challenges with delineating tumor margins due to image blurring caused by optical scattering. Our lab is developing a deep learning (DL)-enabled optical device (spatial frequency domain imaging) for fluorescence quantification to help overcome these challenges (Fig a). This study evaluates the effectiveness of this system to generate deblurred fluorescence images in multi-inclusion residual tumor models.

Methods: A numerical diffusion theory-based light propagation model was used to create reflectance and fluorescence images (161x161 @ 0.1mm) of 10,000 synthetic tumor shapes, represented by composite spherical harmonics of randomly generated order, degree, and radius. Tumor shapes have varying width and height (0.25–3 mm), absorption ($\mu_a=0.0015-0.015$), scattering ($\mu_s'=0.75-2 \text{ mm}^{-1}$), and fluorescence concentration (1–10 $\mu\text{g/mL}$). A Siamese convolutional neural network with ~ 1.9 million parameters was used to output fluorescence concentration maps from two types of input images: optical properties (absorption and scattering) and fluorescence (Fig b). A model was trained with 10,000 single tumors and tested with 350 multi-inclusion tumor images to mimic multiple deposits of residual cancer after resection.

Results: Model training online in Amazon Web Server took ~ 10 hrs (93 epochs) with the Adam optimizer. Model testing achieved a mean squared error (MSE) of 0.30 $\mu\text{g/mL}$ in fluorescence concentration over the 350 test cases. As shown in (Fig c), while the raw fluorescence images (top) display notable blurring due to light scattering, the deblurred DL predictions (bottom) produce sharper tumor borders and provide clearer visualization of small inclusions (arrows).

Conclusion: This deep learning-enabled optical device aims to provide improved residual tumor margin delineation over traditional clinical imaging devices, which are prone to blurring. This simulation study offers preliminary evidence of the DL algorithm's potential in accurately estimating fluorescence concentrations in multi-inclusion tumor images. Future work will test its clinical applicability through patient-derived phantoms and animal models with more realistic tumor shape and optical property heterogeneity.



References:

1. Orosoco et. al., Sci Reports 2018. Positive surgical margins in the 10 most common solid cancers.
2. Vahrmeijer et. al., Nat Rev Clin Oncol 20113. Image-guided cancer surgery using near-infrared fluorescence.

Evaluating the utility of deep learning for automatic tumor contouring in breast cancer surgery

Chris Yeung¹, T. Ungi¹, A. Jamzad¹, M. Kaufmann¹, R. Walker¹, S. Merchant¹, C.J. Engel¹,
D. Jabs¹, J. Rudan¹, P. Mousavi¹, G. Fichtinger¹
¹Queen's University, Kingston, Canada

INTRODUCTION: Breast-conserving surgery (BCS) is a procedure commonly performed to remove the tumor in patients with breast cancer. Positive margins occur when the excised tumor is not completely surrounded by healthy tissue, indicating that cancer tissue was potentially left behind. The NaviKnife is an electromagnetic (EM) tracking system designed to prevent positive margins by offering real-time visualization of the tumor and tools during surgery [1]. However, its adoption is hindered by a manual tumor contouring process which is subject to observer variability and increased personnel costs. While deep learning has the potential to eliminate these limitations via automatic contouring of the tumor from tracked ultrasound images, their viability in clinical practice is still unclear. Our objective is to evaluate the clinical utility of a deep learning model within the NaviKnife system. By analyzing the recorded cautery trajectories from previous BCS cases with respect to automatic contours, we demonstrate that high quantitative model performance does not necessarily translate into clinical effectiveness.

METHODS: 7318 B-mode ultrasound images collected from intraoperative scans of 33 patients enrolled in the NaviKnife study are used to train and test a U-Net using the nnU-Net framework [2]. Five additional intraoperative ultrasound scans are collected to evaluate model performance in previous BCS cases. EM tracking data is obtained using an NDI 3D Guidance system and recorded in 3D Slicer via the PLUS toolkit [3]. The tracked ultrasound images from the five cases are used as input for the nnU-Net model to reconstruct the tumor contour in 3D. For each frame in the recorded tracking data, the distance and anatomical position of the surgical cautery relative to the automatic contour is calculated (Fig. 1). Based on this, the overall margin status (positive or negative) for all six anatomical positions (anterior, posterior, superior, inferior, left, right) is predicted for the five cases. These predictions are compared with the ground truth margin status reported by pathology reports using the accuracy, sensitivity, and specificity metrics.

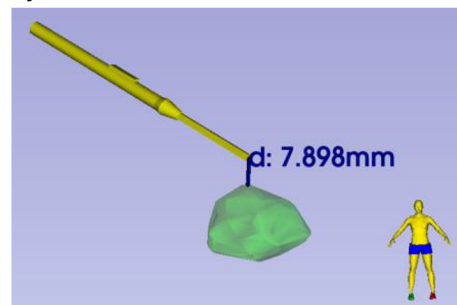


Fig. 1 The distance and position of the cautery (yellow) is determined relative to the automatic contour (green).

RESULTS: The nnU-Net model achieved a mean Dice, IoU, sensitivity, and precision of 0.96, 0.93, 0.96, and 0.97, respectively when evaluated on the test dataset. Two examples are shown in Fig. 2. Comparing the margin status based on recorded cautery trajectories with those reported by pathology yielded an accuracy, sensitivity, and specificity of 0.50, 0.75, and 0.43, respectively.

CONCLUSIONS: Despite the low accuracy, the predictive power of our model is likely greater due to the larger number of negative margins in our test cases. In fact, the low specificity indicates an overestimation of the true tumor boundary, which is more acceptable than a low sensitivity but provides little actionable information to the surgeon. Our findings highlight the need to focus more on application-specific evaluation methods rather than on quantitative performance when developing deep learning solutions for clinical practice.

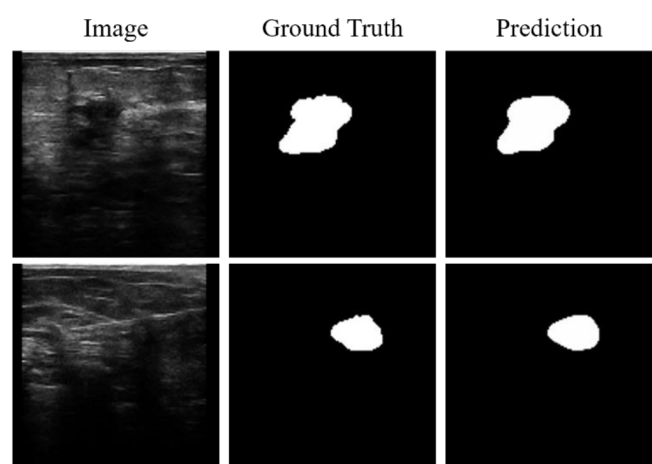


Fig. 2 Ultrasound image (left), ground truth tumor segmentation (middle), and nnU-Net prediction (right).

REFERENCES:

[1] T. Ungi *et al.*, *IEEE Trans Biomed Eng.*, vol. 63, no. 3, pp. 600–606, Mar. 2016. [2] F. Isensee *et al.*, *Nat Methods*, vol. 18, no. 2, pp. 203–211, 2021. [3] T. Ungi *et al.*, *Med Image Anal.*, vol. 33, pp. 181–186, 2016.

Development and evaluation of SlicerGPT: GPT tailored for enhancing interaction with 3D Slicer software

Pavel-Dumitru Cernelev, Colton Barr, Maha Kesibi, Andras Lasso, Tamas Ungi, Gabor Fichtinger
Laboratory for Percutaneous Surgery, Queen's University, Kingston, Canada

INTRODUCTION: 3D Slicer is a free, open-source software which provides a powerful development environment for creating image-guided therapy (IGT) application prototypes (slicer.org). The combination of its unique data types alongside a range of software and libraries, makes 3D Slicer a challenging tool to learn and use effectively. Language models such as OpenAI's ChatGPT and Meta's Llama have gained significant popularity for their role in making programming and writing tasks more accessible to those with varying skill levels. Recently, OpenAI introduced a new application called GPTs (Generative Pre-trained Transformer), allowing individuals to create and customize versions of the ChatGPT model to be tailored for specific tasks. Therefore, we have been developing SlicerGPT, a customized model for 3D Slicer development that aims to reduce the barrier of entry associated with IGT development with natural language to promote accessibility. In this work, we present the current progress and preliminary performance of SlicerGPT.

METHODS: We developed a specialized SlicerGPT using OpenAI's GPT feature (<https://openai.com/blog/introducing-gpts>). We evaluated various prompt engineering methods such as role assigning, instruction prompting, and priming prompting to provide refined instructions to the GPT model, ensuring relevant outputs related to 3D Slicer and medical imaging analysis. We integrated open-source knowledge around 3D Slicer such as the VTK user guide, Slicer documentation, Slicer extension data, and the Slicer discourse repository to provide additional knowledge to pull from. After the initial development of SlicerGPT, we conducted a series of tests to evaluate its performance versus GPT-4 and GPT-3.5. This involved creating a set of diverse programming questions which would require the understanding of the 3D Slicer libraries. Such as, "How do I change the background of the scene to red using the python interpreter?". The questions were designed to be easy to test with the python interpreter within 3D Slicer, to reduce bias. The user would provide the number of prompts it took to find the correct answer, stopping after 5 prompts, as well as feedback on a 1-5 scale on the accuracy, efficiency, learnability, and satisfaction of SlicerGPT.

RESULTS: We performed preliminary tests on this software with 3 users who had experience with creating and programming 3D Slicer modules. We found that SlicerGPT outperformed GPT-3.5, however this was outperformed by GPT-4. Moreover, our testers found that SlicerGPT took significantly longer to generate results. These results are preliminary, and the investigation is ongoing.

Model	Accuracy	Efficiency	Learnability	Satisfaction
SlicerGPT	60%	50%	70%	60%
GPT-4	90%	80%	80%	100%
GPT-3.5	40%	40%	40%	40%

CONCLUSION: The preliminary results demonstrated that 3D Slicer development can be done using natural language, yet these models are limited by the prompts provided and are susceptible to providing incorrect information. With the additional knowledge in SlicerGPT, the model decreased in accuracy, and it took significantly longer to generate results. Further research will include working towards implementing local language models or fine-tuning existing models to reduce incorrect answers and allow for open-source development. Additionally, before we can confidently recommend SlicerGPT to users' we must work on implementing methods of providing references such as weblinks to relevant resources and optimize the users prompts to help reduce extraneous results. By leveraging advancements in language models for the open-source development of IGT applications, 3D Slicer can become more inclusive and adaptable to user needs.

Exploring Osteosarcopenia Progression in Prostate Cancer Patients using AI-Enabled Musculoskeletal Imaging Biomarkers

Saleh Tabatabaei^{1,2}, Tayler D. Ross^{1,3,4}, Geoff Klein^{1,5}, Joel Finkelstein^{1,4}, Cari M. Whyne^{1,4}, Urban Emmenegger^{1,3}, Michael Hardisty^{1,4}
¹Sunnybrook Research Institute, ²Institute of Biomedical Engineering, University of Toronto, ³Institute of Medical Science, University of Toronto, ⁴Department of Surgery, University of Toronto, ⁵Department of Medical Biophysics, University of Toronto, Toronto, ON, Canada

INTRODUCTION: Osteosarcopenia is a progressive musculoskeletal (MSK) condition that is a combination of osteopenia/osteoporosis (decreased bone mineral density - BMD) and sarcopenia (low muscle mass and strength). In advanced prostate cancer, 73% of patients with 70 years or older have been classified with either osteopenia (55%) or osteoporosis (18%). Furthermore, over 50% of patients with prostate cancer have sarcopenia, placing prostate cancer among the highest for sarcopenia incidence. Although advanced therapeutics prolong survival in cancer patients, the period of active disease and treatment detrimentally impact MSK health. Osteosarcopenia can lead to increased falls, fractures, and poor patient outcomes. Osteoporosis and sarcopenia have primarily been studied separately, at single timepoints with Dual-Energy X-ray Absorptiometry (DEXA) and on 2D Computed Tomography (CT) scan slices, neglecting 3D analyses, temporal progression and possible interactions between bone and muscle health. This work aims to quantify osteosarcopenia progression in advanced prostate cancer patients with 3D CT-based imaging biomarkers. It is hypothesized that sarcopenia will progress over time, but that osteopenia may be masked by increased presence of sclerotic lesions in men with advanced prostate cancer.

METHODS: MSK biomarkers were calculated for advanced prostate cancer patients treated with systemic therapy at the Sunnybrook Odette Cancer Centre (2009-2021) using opportunistic prostate cancer surveillance images (REB#1862). Lumbar Spine 3D CT scans were reconstructed to 1mm isotropic voxel size from diagnostic axial, sagittal, and coronal reconstructions using a custom iterative approach. Using a combination of convolutional neural network architectures, the lumbar vertebral bodies (L1-L5) and psoas muscles were segmented. The superior and inferior region boundary of the psoas muscle was set at L2/L3 and L4/L5 disc mid-points. BMD of the lumbar vertebral bodies and the psoas volume and density were calculated.

RESULTS: 142 male patients (mean age=71 years [44-90 years]) with 475 CT scans with average follow up of 1034 days (45-3284 days) were analyzed. Throughout this period, BMD increased (17.1%), psoas volume decreased (6.5%), and psoas density decreased (17.1%). BMD was stable or decreased for 51.8% of subjects, while 25.9% of subjects had a >30% BMD increase. Psoas density and volume were decreased in 2/3 subjects. Moderate to weak correlations were found for the temporal rate of change of the MSK biomarkers (psoas volume vs. BMD $R^2 = -0.29$, psoas density vs. BMD $R^2 = -0.10$, psoas volume vs. psoas density $R^2 = -0.46$, all $p < 0.0001$).

CONCLUSIONS: This study quantifies marked longitudinal changes in osteosarcopenia biomarkers in advanced prostate cancer patients. The majority of patients experienced sarcopenia progression while undergoing prostate cancer treatments, highlighting the potential impacts of advanced therapeutics and disease progression. BMD increases were measured secondary to sclerotic metastatic lesions, a factor that must be considered in automated osteopenia evaluation. This study showed larger magnitude changes than previous reports, likely due to longer follow-up and use of quantitative 3D imaging biomarkers. 3D biomarkers might be more sensitive to changes than 2D biomarkers for longitudinal assessment. This investigation has tracked osteosarcopenia progression secondary to metastatic involvement; the methods can be applied to other MSK health-impacting conditions.

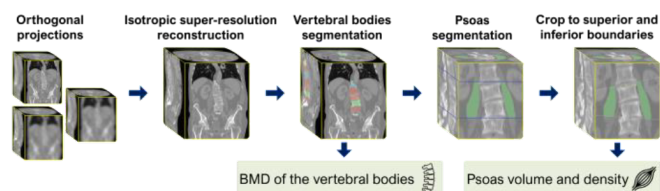


Figure 1. Biomarker extraction pipeline implemented in Python 3 using 3D Slicer.

Table 1: Statistical summary of change of calculated MSK biomarkers for the study cohort

Biomarker	Mean (Std Dev)	Median	Range (Min-Max)	Rate of Change
Bone Density (L2-L5)	17.3% (48%)	-1.1%	-61% — 260%	23.5% per year
Psoas Muscle Volume	-6.5% (34%)	-9.7%	-85% — 191%	-3.8% per year
Psoas Muscle Density	-17.1% (46%)	-15%	-195% — 208%	-6.9% per year

REFERENCES: [1] Kirk, B. et al. J Cachexia Sarcopenia Muscle 11: 609–618, 2020. [2] Yoo, J.I. et al. J Korean Med Sci 33(4), 2018. [3] Nandakumar, B. et al. Cancer 129(3):385–392, 2023. [4] Kovač, M.B. et al. J Geriatr Oncol (2023): 101594. [5] Ahern, D.P. et al. Spine J 21.10 (2021): 1738-1749. [6] Nowak, S. et al. Eur Radiol (2021): 1-10. [7] Rozynek, M. et al. Nutrition 89 (2021): 111227. [8] Surov, A. et al. J Parenter Enteral Nutr 46.8 (2022): 1761-1768. [9] Malkowicz, S.B. et al. J Clin Oncol 25.18_suppl (2007): 5116-5116

Session 16 Talks: MRI 2

Abstracts

Single Frequency Birdcage Coils for Improved ^{19}F Molecular MRI in MiceSean McRae ¹, Olivia Sehl ¹, Paco Martinez ¹, Paula Foster ^{1,2}, John Ronald ^{1,2,3}, and Timothy Scholl ^{1,2,4,5}¹ Department of Medical Biophysics, University of Western Ontario, London, ON² Imaging Laboratories, Robarts Research Institute, University of Western Ontario, London, ON³ Lawson Health Research Institute, London, ON, N6A 3K7, Canada⁴ Department of Physics and Astronomy, ON, N6A 3K7, Canada⁵ Ontario Institute for Cancer Research, Toronto, ON, M5G 0A3, Canada**Introduction:**

Fluorine-19 (^{19}F) magnetic resonance imaging (MRI) serves as a dynamic technique for *in vivo* detection of cellular and molecular events, offering quantifiable, background-free signals from ^{19}F spins. To maximize ^{19}F detectability and signal quantification, several important considerations must be made. For instance, it is necessary to have full coverage of the imaging subject to facilitate ^{19}F detection without prior knowledge of the signal location. Additionally, since cellular events occur at depth within tissue, it is important to maintain accurate signal quantification within a range of imaging depths. The choice of radiofrequency (RF) coil for an imaging experiment can have a significant impact on these factors. For example, birdcage coils provide full animal coverage with uniform B_1 field generation. In this work, we examined a new suite of small-bore birdcage coils for their improved animal coverage and homogenous B_1 field generation, and compared their ability to detect ^{19}F in deep tissue to a commercially available dual-tuned $^1\text{H}/^{19}\text{F}$ surface coil.

Methods:

We constructed three whole-mouse birdcage coils (^1H single-frequency, ^{19}F single-frequency, and $^1\text{H}/^{19}\text{F}$ switch tuned) with inner diameters of 31 mm and lengths of 85 mm. For practical use of single frequency birdcage coils, we also constructed a 3D-printed animal bed that could be fixed to the scanner bed to help prevent animal re-positioning during coil switching (<60 second coil switching times). To assess coil homogeneity, we constructed a phantom using gadolinium-doped water, with an internal concentric tube of the perfluorocarbon tracer *CelSense* (CelSense Inc.) to mimic the presence of ^{19}F in deep tissue. We acquired T_1 -weighted spoiled gradient echo images for ^1H and 3D balanced steady state free precession for ^{19}F imaging. To assess coil homogeneity, we calculated SNR as a function of depth for each of the slices within our phantom for both frequencies. Finally, to evaluate the detectability of ^{19}F in deep tissue *in vivo*, we injected 50 μL of the perfluorocarbon *V-Sense* (CelSense Inc.) bilaterally into the foot pads of female athymic nude mice (n=3) to promote uptake into lymph nodes and the liver. We imaged at one, two, eight, and 24 days post injection with both our surface and birdcage coils to compare the detectability of *V-Sense* within ^{19}F -containing organs.

Results:

SNR-depth profiles revealed that for proton imaging, the surface coil provided the highest SNR at close depth, with the single frequency and switch tuned birdcage coils only capable of achieving 78% and 58% of the surface coil at their maximum, respectively. For fluorine imaging, the single frequency birdcage coil achieved the maximum SNR, with the surface coil only able to achieve 58% of the birdcage coil's maximum SNR, and the switch tuned birdcage coil only achieving 44% of the single frequency coil's maximum. *In vivo* imaging revealed a significant increase in contrast-to-noise ratios ($p < 0.0001$) for the anatomical proton images using the single frequency ^1H birdcage coil compared to the surface coil. Figure 1 shows the increased SNR of fluorine in the renal lymph nodes through a $^1\text{H}/^{19}\text{F}$ overlay of a representative mouse 24 hours post injection (note the placement of the surface coil as shown in the axial image, green line showing depth of coronal slice shown).

Conclusions:

We have combined single frequency coils with a customized 3D animal bed to allow for the collection of whole mouse ^1H and ^{19}F images. Our single frequency coils demonstrated increased sensitivity for ^{19}F in deep tissue, as well as improved homogeneity. These improvements in homogeneity should translate to improved quantification of cellular/molecular events, which is the focus of our current work.

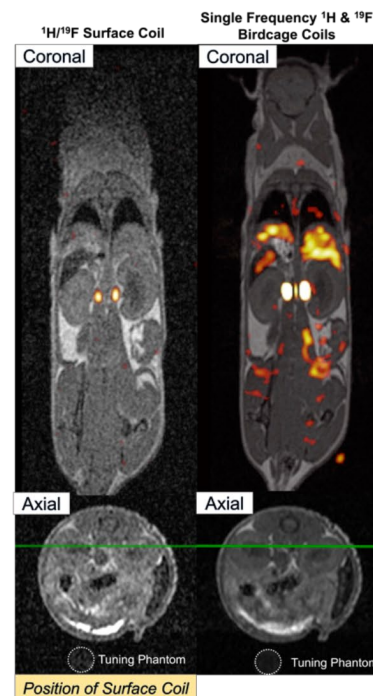


Fig 1: Representative mouse 24-hours post PFC injection.

Correction of motion and resulting field offsets for quantitative MRI using navigators

Miriam Hewlett,¹ Omer Oran,² Junmin Liu,³ and Maria Drangova^{1,3}

¹Medical Biophysics, Western University, London ON

²Siemens Healthcare Limited, Oakville ON

³Robarts Research Institute, London ON

Introduction: Magnetic resonance imaging (MRI) enables many quantitative brain imaging techniques with applications ranging from R2* and quantitative susceptibility mapping (QSM) for the study of neurological disorders [1] to fat fraction (FF) assisted attenuation correction for PET-MRI [2]. However, long scan times make it prone to motion artifacts [3]. Real-time motion estimates obtained using spherical navigators (SNAVs) enable prospective motion correction (PMC) with no additional hardware; however, residual artifacts may remain due to motion-induced magnetic field inhomogeneity. Such effects are even more prevalent at long echo times used for R2* and QSM. This work combines SNAVs with an additional free induction decay (FID) readout for zeroth order field measurement and correction of a multiparametric mapping protocol.

Methods: The combined FID-SNAVs (total readout < 10 ms) were interleaved in a 3D multi-echo gradient echo (GRE) sequence and tested on a 3T scanner (Siemens Prisma) using the product 32-channel head coil.

Acquisition parameters (FOV 25.6x25.6x19.2 cm, resolution 1.14x1.14x2.00 mm, TR 51 ms, TEs 3.28/4.72/6.22/7.72/9.49/16.75/23.90/31.10/ 38.16/45.40 ms, FA 15°, BW 1015 Hz/Pixel, GRAPPA R = 2, scan time 10:07) and processing pipeline for FF, R2*, and susceptibility mapping were based on a previously developed protocol [4]. Navigators were acquired with a frequency of 1.96 Hz (scan time increase 2:32); an additional baseline scan (0:17) was also acquired to accelerate motion estimation (covering rotations up to 6°).

One volunteer was scanned with and without PMC; the former processed with and without retrospective correction of field offsets using FID measurements. Motion was guided by moving crosshair projected into the scanner (trajectory based on a real unintentional motion case).

Results: Shown in Figure 1 are sample images and the corresponding quantitative maps for all scans. Similar motion trajectories, field offsets, were observed for motion scans with and without correction. PMC alone resulted in a noticeable improvement in image quality compared to the uncorrected result (reduction in NRMSE from 0.0524 to 0.0457); additional retrospective correction of field offsets reduced residual artifacts (NRMSE 0.0446). Quality of the corresponding quantitative maps also appears improved. Latency between FID-SNAV acquisition and FOV update was under 50 ms.

Conclusions: FID-SNAVs show promise for combined motion and field correction for quantitative MRI applications. Residual artifacts may improve with prospective correction of higher order field offsets. Future work will also investigate FID-based triggering of navigator acquisition to limit the increase in scan time.

References: [1] Martin, et al. *Neurology* 2008;**70**:1411-1417. [2] Catana *Phys Med Biol* 2020;**65**:23TR02. [3] Andre, et al. *J Am Coll Radiol* 2015;**12**:689-695. [4] Liu, et al. *NeuroImage* 2018;**172**:703-717.

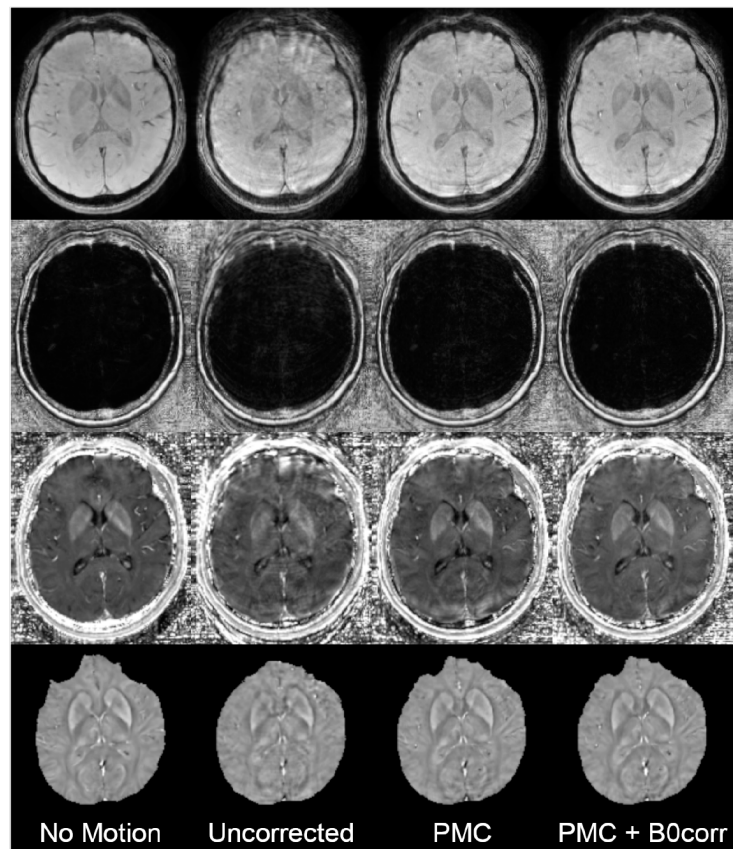


Figure 1. (Top) Sample slices from the magnitude images (TE 16.75 ms) acquired with no motion, motion but no correction, and motion with PMC, with and without additional field correction (B0corr). Below each are the corresponding maps of FF, R2*, and susceptibility.

Laterally Oscillating Trajectory for Undersampling Slices (LOTUS)

Mayuri Sothynathan^{1,2}, Corey Baron^{1,2}

¹Department of Medical Biophysics, Western University, London, Canada, ²Centre for Functional and Metabolic Mapping, Western University, London, Canada

Introduction: MR scan efficiency is significantly limited giving rise to motion artefacts and reduced image quality.¹ To mitigate this, various non-cartesian k-space trajectories have been used in conjunction with compressed sensing (CS) and simultaneous multislice (SMS).² CS exploits MR transform sparsity and resulting incoherent image artefacts to reconstruct images from undersampled data. Reconstruction is characterized by the relation $\hat{x} = \operatorname{argmin}_x \frac{1}{2} \|Ax - y\|_2^2 + \lambda \|\psi\|_1$. The data consistency term $\frac{1}{2} \|Ax - y\|_2^2$ measures the difference between reconstructed and acquired data, while the regularization term $\lambda \|\psi\|_1$ ensures sparsity; adjusting λ enables error minimization. While pure random sampling is impractical due to hardware and physiological constraints, trajectories mimicking interference properties of random sampling, increases CS efficacy.³ This study proposes a k-space trajectory for SMS imaging that behaves like a spiral in the x-y plane while oscillating sinusoidally in the z-direction — hence the name LOTUS (Fig. 1). The objective of this study is to investigate the properties of LOTUS to determine its ability to efficiently collect MR imaging data and reduce motion artifacts.

Methods: SMS MR signal acquisition using LOTUS was compared to standard single-shot spiral acquisition using simulation via MatMRI, an in-house MATLAB toolbox for MRI image reconstruction.^{4,5} Trajectory performance was evaluated by varying the λ to minimize MSE for the following standard deviation of noise values: 0, 2.5×10^{-5} , 5.5×10^{-5} . The following parameters were kept constant: FOV = $200 \times 200 \text{ mm}^2$, in-plane resolution = $1.5 \times 1.5 \text{ mm}^2$, slices = 2, and in-plane undersampling rate = 3. Although the equations of the sinusoid are not included here, the gradient amplitude and slew rate are deterministic from setting the k-space span and zero-crossings. Resulting mean square error (MSE) values for spiral and LOTUS acquisition were compared, reconstructed images were

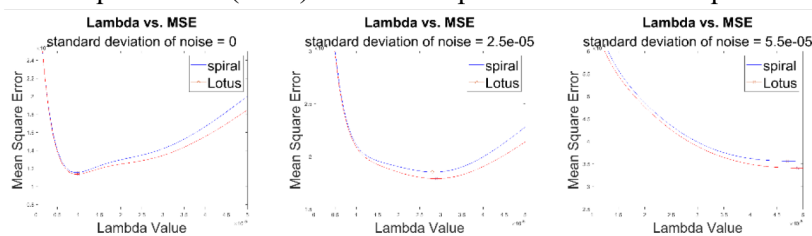


Fig. 2 Lambda value vs. MSE for standard deviation of noise values 0, $2.5e-5$, and $5.5e-05$

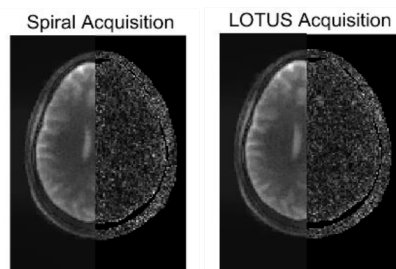


Fig. 3 Reconstructed and difference images for spiral and LOTUS SMS acquisition where the standard deviation of noise is $2.5e-05$ and lambda is selected such that MSE is minimized

reconstructed using the two trajectories (Fig. 3). However, the reduction in MSE suggests that LOTUS more effectively mimics random sampling to further disrupt coherence of aliasing artefacts and increase the efficacy of CS; thus, posing benefits to quantitative imaging. Future work will investigate g-factor and structural similarity index. A pulse sequence designed to follow the LOTUS trajectory using an ultra-high-field 7 Tesla Siemens head-only MRI scanner will be used to conduct phantom and human brain scans to evaluate LOTUS through comparison to other existing trajectories.

Conclusions: A novel k-space trajectory for MRI data acquisition, LOTUS, was determined, resulting in increased CS efficacy and the reduction of motion artefacts.

References: ¹Zaitsev et al. JMRI (2015), ²Turley et al. MRM (2013), ³Lustig et al. MRM (2007), ⁴Varella-Mattatal et al. MRM (2023), ⁵Baron (2023)

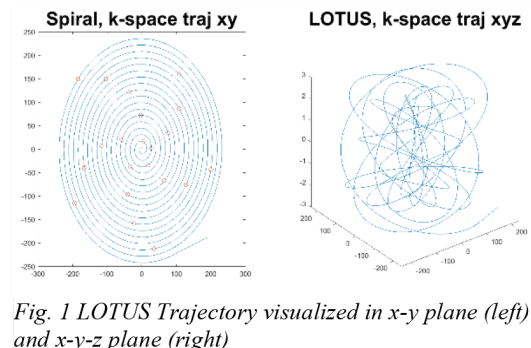


Fig. 1 LOTUS Trajectory visualized in x-y plane (left) and x-y-z plane (right)

evaluated visually for blurring and/or ghosting, and subtraction images were examined for discrepancies from the ground truth.

Results: LOTUS consistently exhibited lower MSE than spiral acquisition for all simulated values of λ (Fig. 2). Note, only one slice is shown. It is currently difficult to discern differences between images

Real-time radiation beam imaging on a 1.5T MR linear accelerator using quantitative T_1 mapping**Authors:** Brandon T.T. Tran^{1,2}, Liam S.P. Lawrence^{1,2}, Shawn Binda³, Brige P. Chugh³, and Angus Lau^{1,2}

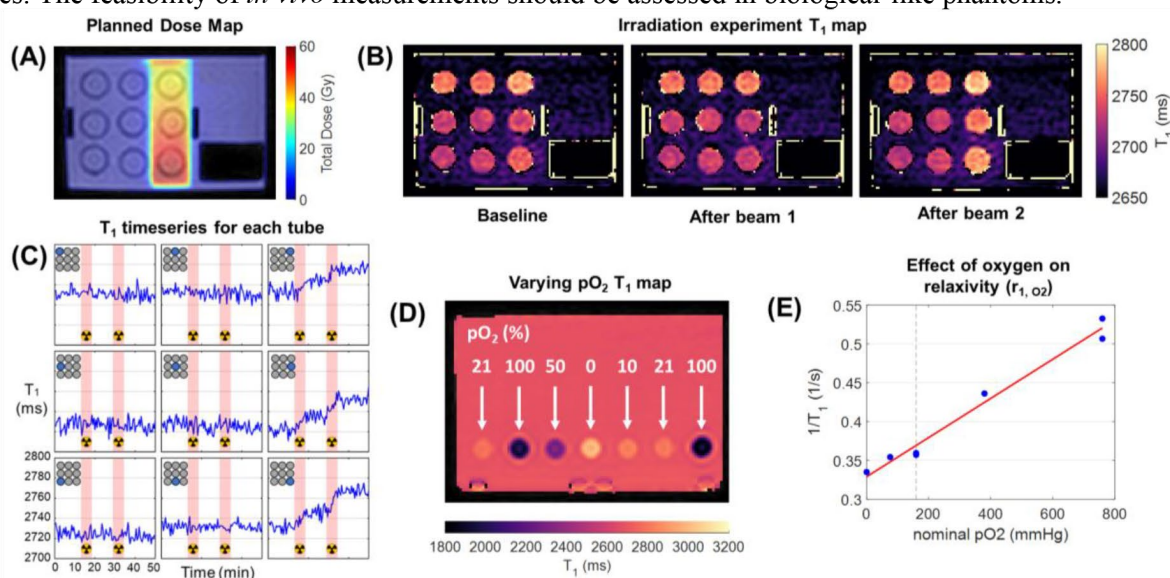
(1) Physical Sciences Platform, Sunnybrook Research Institute, Toronto, (2) Medical Biophysics, University of Toronto, Toronto, (3) Radiation Oncology, Sunnybrook Health Sciences Centre, Toronto

Introduction: MR-linear accelerators (MR-Linacs) enable concurrent irradiation and imaging. Direct imaging of radiation beam effects could enable more accurate dosimetry and *in vivo* dose verification, minimizing treatment margins. A previous study found that free radical scavenger solutions increased in T_1 -weighted intensity after irradiation¹. It was hypothesized that the dissolved oxygen, which is a known paramagnetic T_1 shortening agent, was decreased during water radiolysis leading to increased T_1 . In this study, we investigate the feasibility of using quantitative T_1 mapping and a 1.5T MR-Linac to detect real-time T_1 changes during irradiation.

Methods: Two experiments were performed to characterize (1) radiation-induced T_1 changes and (2) the effect of oxygen on ^1H relaxation rate (r_{1,O_2}). In the first experiment, nine 50 mL tubes were filled with ultrapure MilliQ water at atmospheric pressure, sealed using rubber septa to prevent gas exchange, and arranged in a 3x3 grid surrounded with tap water near room temperature. Imaging and irradiation were performed on a 1.5T Elekta Unity MR-Linac (Elekta AB, Stockholm, Sweden). Dynamic T_1/B_0 maps were acquired every 30 s using dual gradient-echo Look-Locker inversion recovery ($4 \times 4 \times 8 \text{ mm}^3$ resolution, $\text{TR}/\text{TE}_1/\text{TE}_2 = 7.0/1.9/4.8 \text{ ms}$, $\text{FA } 7^\circ$, maximum TI 15846 ms, 40 TIs, 8-channel anterior/posterior array) before, during and after irradiation. Look-Locker 3-parameter fitting was used to obtain T_1 maps². A radiation plan from a single gantry angle (180° , from underneath the bed; **Panel A**) was designed using Monaco treatment planning system (Elekta AB, Stockholm, Sweden) to irradiate the rightmost column with a total target dose of $\sim 50 \text{ Gy}$ delivered in two irradiations lasting 6 minutes each. In the second experiment, r_{1,O_2} was determined using samples of varying dissolved O_2 concentrations ($\text{pO}_2/\text{pN}_2 = 0\%/100\%$, $10\%/90\%$, $50\%/50\%$, $100\%/0\%$, $21\%/79\%$ [room air]).

Results: T_1 increased in irradiated tubes, with minimal changes to T_1 in non-irradiated tubes and surrounding tap water (**Panel B**). The baseline T_1 varied between different samples; this variation was likely due to non-uniform temperature within the phantom and slight differences in baseline O_2 concentrations. The T_1 increased linearly in irradiated tubes during beam-on periods (**Panel C**; shaded red regions indicate when beam is on). Mean T_1 changes were used to estimate $\Delta T_1/\text{Dose} = 0.71 \text{ ms/Gy}$. The effect of oxygen on ^1H relaxation was estimated to be $r_{1,\text{O}_2} = 0.25 \times 10^{-3} \text{ s}^{-1}/\text{mmHg}$ (**Panels D,E**) which agrees with existing empirical models³. Using r_{1,O_2} , the dissolved pO_2/dose was estimated to be -0.38 mmHg/Gy . This is much larger than estimates from radiation chemistry simulations¹ ($0.14 \mu\text{M/Gy} = -0.08 \text{ mmHg/Gy}$, assuming a conversion factor of $0.58 \text{ mmHg}/\mu\text{M}$). The results suggest there may be discrepancies between our 6 MV photon setup and literature, and that dissolved oxygen depletion during irradiation may not fully explain the observed real-time T_1 changes.

Conclusions: The irradiation of ultrapure water using a 1.5T MR-Linac resulted in measurable real-time T_1 changes. The feasibility of *in vivo* measurements should be assessed in biological-like phantoms.



References: 1. Wancura et al., *Med. Phys.*, 2023 2. Diechmann, *Magn. Reson. Med.*, 2005 3. Bluemke et al., *NMR Biomed.*, 2022.

Session 17 Talks: Cellular and Molecular Abstracts

Title: Comparing the Cellular Detection Limits of Magnetic Particle Imaging and Bioluminescence Imaging

Authors: Sophia D. Trozzo, John Kelly, & Paula J. Foster, Department of Medical Biophysics, Western University

Introduction: *In vivo* cell tracking can be performed using several different imaging modalities. We have previously shown that tumour cells stably transfected with luciferase and labelled with SPIO can be dually tracked *in vivo* using bioluminescence (BLI) and magnetic particle imaging (MPI) (1,2). Both techniques have certain advantages for cell tracking. For MPI, the signal is generated directly from SPIO, and this allows for high specificity and quantification of iron mass and cell number. BLI has high sensitivity and specifically detects live cells. Both techniques also have limitations. For MPI, the dynamic range is limited if several sources of signal with different concentrations of iron are present (3). The BLI signal experiences tissue attenuation which limits the depth of imaging to about 1-2 cm (2). In this study, we compared the *in vitro* cellular detection limits of BLI and MPI to determine the ideal conditions in which MPI and BLI should be used to advance cell tracking.

Methods: 4T1 murine breast cancer cells were transfected with firefly luciferase and labelled with SPIO (ProMag, Bangs Laboratories) at a concentration of 25 $\mu\text{g}/\text{mL}$. Following a 24-hour incubation, magnetic column separation was performed to remove unlabelled cells. To assess *in vitro* detection limits, labelled cells were serially diluted at a 1:2 ratio in 10 steps, from 51,200 cells down to 100 cells. The same samples were imaged with both BLI and MPI to directly compare detection limits. BLI images of five cell samples at a time were acquired every 60 seconds until the maximum average radiance was reached (20 min scan). MPI images of individual cell samples were then acquired using a 2D projection scan with high sensitivity (5.7 T/m gradient strength, 20 mT drive field amplitude, 2 min scan). For samples that could not be detected with 2D MPI, 3D images were acquired (30 min scan).

Results: BLI and MPI signal both demonstrated a linear relationship to cell number (Figure B, E & G). 2D MPI imaging revealed a cell detection limit of 6400 cells (A). 3D MPI improved this to 1600 cells (C). Two of three 800 cell samples had MPI signal that was quantifiable above five times the standard deviation of background noise. BLI was able to detect down to 100 cells (Figures D, E, F & G).

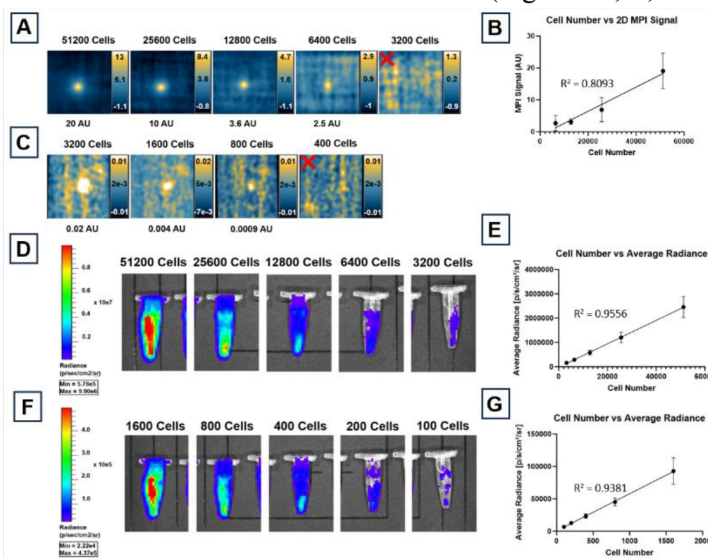


Figure 1. Cell detection limits for MPI and BLI. (A) 2D MPI images acquired for 51200 to 3200 cells, with a cellular detection limit of 6400 cells. A red “X” placed on the image of the undetectable 3200 cell sample. Quantified MPI signal values are shown below each image. (B) 2D MPI signal was quantified for each detectable cell sample ($p < 0.0001$). (C) 3D MPI images acquired for 3200, 1600, 800 and 400 cells, with quantified MPI signal depicted below each image. A red “X” is placed on the image of the undetectable 400 cell sample. (D) Representative BLI images for 51200 cells to 3200 cells. (F) Representative BLI images for 1600 cells to 100 cells. (E) Measured average radiance ($\text{p/s}/\text{cm}^2/\text{sr}$) values for triplicates of 51200 to 3200 cells ($p < 0.0001$), and (G) 1600 to 100 cells ($p < 0.0001$).

Conclusions: This is the first study to directly compare the *in vitro* cellular detection limits of MPI and BLI. BLI had a superior *in vitro* cellular detection limit. Several factors may contribute to the observed MPI cellular detection limit. A lower gradient strength is one way to improve MPI cellular sensitivity (4). Additionally, the development of MPI-tailored SPIO is expected to significantly improve sensitivity. Both modalities are considered to have low spatial resolution and this feature was not compared in this study as the focus was sensitivity and cellular detection limits. Preclinically, BLI and MPI can be used together to provide complementary information about tumour cell viability, proliferation, and metastasis. Tissue attenuation is a known limitation of BLI which can be mitigated by dual MPI tracking. Even with superficial melanoma tumours, BLI signal was scattered on mice with hair compared to shaved mice (5). To further characterize the conditions in which BLI and MPI can be used together for cell tracking, our next steps will assess *in vivo* detection limits of MPI and BLI, and the effects of different tissue depths on BLI cellular detection limits.

References: 1. Knier et al., *Journal of Biological Methods*, 2021. 2. Williams et al., *Tomography*, 2023. 3. Fink et al., *European Radiology Experimental*, 2023. 4. Harvell-Smith et al., *Nanoscale*, 2022. 5. Puaux et al., *International Journal of Molecular Imaging*, 2011

Spatial-Frequency Fluorescence Imaging for Surgical Guidance: Pre-Clinical Oral Cancer Experiments using Porphysome Nanoparticles

Christina Negus¹, Josephine La Macchia¹, Anjolaoluwa Adewale,¹ Elise Schwarz¹, Jason Townson,¹ Harley Chan,¹ Alon Pener-Tessler,² Esmat Najjar,² Brian C. Wilson,¹ Jonathan C. Irish^{1,2} and Michael J. Daly¹

¹Princess Margaret Cancer Centre, University Health Network, Toronto ON, Canada

²Department of Otolaryngology – Head & Neck Surgery, University of Toronto, Toronto ON, Canada

Introduction: Fluorescence imaging is an emerging technology for guiding cancer surgery, helping delineate tumors within tissue for more accurate resection.¹ Current fluorescence imaging techniques, however, are qualitative and do not account for tissue optical properties (absorption, scattering) and device settings, leading to limitations in their effectiveness. Our lab is developing a quantitative fluorescence device using spatial-frequency domain imaging (SFDI) for applications in oral cancer surgeries.² Here, we implement and validate quantitative SFDI fluorescence in pre-clinical animal models.

Methods: This ongoing study consists of two groups of mice utilizing an aggressive oral cancer cell line to create hind-flank tumors. A fluorescent nanoparticle (porphysomes) is injected 24 hours before surgery. In the first group (“unguided”), the tumors are resected without fluorescence imaging. In the second group (“fluorescence-guided”), the surgeon performs additional resection based on SFDI fluorescence images of the surgical bed after initial tumor removal. SFDI optical property maps are compared between two light propagation models using analytical diffusion theory and Monte Carlo methods for higher absorption.

Results: To date (n=10 in each group), 100% of the control group had tumor recurrence within 2 weeks post-resection, even though no visible residual tumor was evident in the surgical bed (Fig. a). In the fluorescence-guided group, tumor recurrence was reduced to 25%, based on additional resections guided by images that highlighted residual disease (Fig. b). Tumor recurrence can be attributed to undetected tumor cell clusters in this aggressive tumor model. To date, fluorescence images shown to the surgeon only correct for device settings (Fig. c), but retrospective correction for optical properties (Fig. d) shows that possible false positives (second arrow in c) may be corrected by accounting for local variations in blood absorption. Additional animal testing (n=10 in each group) is underway.

Conclusion: Using fluorescence imaging after tumor resection decreases the recurrence of disease within a mouse oral cancer model. This study provides baseline data on *in vivo* optical properties and nanoparticle concentration that will be used to optimize an adapted deep convolutional neural network to measure tumor depth and quantify fluorescence.

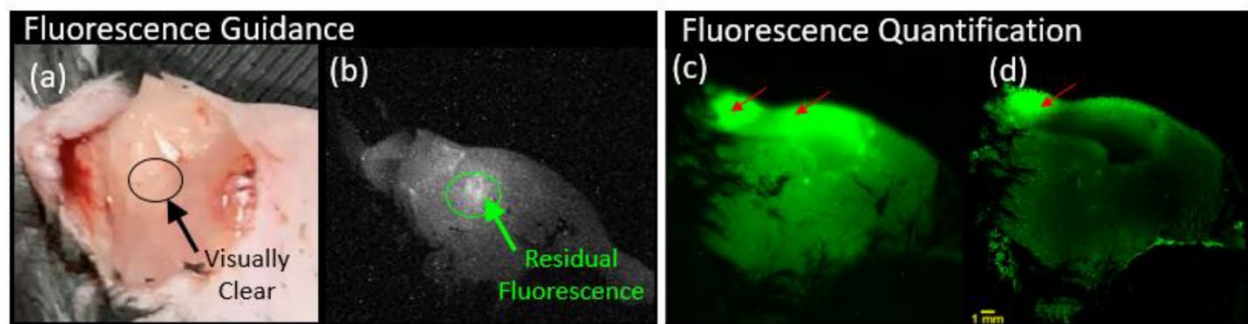


Figure. (a) Post-resection no visible tumor. (b) Fluorescent marked residual tumor. (c) Qualitative fluorescence with potential tumor locations marked. (d) Quantitative fluorescence after correction for optical absorption and scattering.

References:

1. Bou-Samra et. al., J Biomed Optics 2023. Intraoperative molecular imaging: 3rd biennial clinical trials update.
2. Daly et. al., SPIE BiOS 2021. Fluorescence depth estimation in pre-clinical oral cancer models using spatial frequency domain imaging.

Synaptic Density in Youth with a Substance Use Disorder and A Mental Health Challenge: Positron Emission Tomography Studies of [¹⁸F]SynVesT-1 In The Toronto Adolescent & Youth (TAY) Cohort Study

Maia Zilberman, Lujia (Ember) Yu, Jennifer Truong, Cassie Cote, Yuliya Nikolova, Erin Dickie, Stephanie Ameis, Kimberly Desmond, Carme Uribe, Dafna Kahana, Neil Vasdev, Daniel Felsky, Benjamin Goldstein, Kristin Cleverley, Darren Courtney, Lisa Hawke, Nicole Kozloff, Alexia Polillo, Martin Rotenberg, Lena Quilty, Wei Wang, George Foussias, Aristotle Voineskos, Omair Hussain & Isabelle Boileau

Introduction Adolescents and young adults with a mental health challenge have a high-rate of pathological drug use which increases their risk of developing substance use disorders (SUD) and other psychiatric illnesses. While the biological basis for this vulnerability is unknown, it has been proposed, based on converging preclinical and indirect neuroimaging data, that exposure to drugs of abuse during neurodevelopment may lead to impairments in synaptic density. Here we used positron emission tomography (PET) imaging of the synaptic vesicle glycoprotein 2A (SV2A) radiopharmaceutical [¹⁸F]SynVesT-1 to investigate whether synaptic density is lower in the brain of mental health service-seeking youth with a SUD relative to those without.

Method Participants enrolled in the TAY cohort study (<https://www.taycohort.ca/>) underwent clinical assessments and were invited to complete a PET scan with [¹⁸F]SynvesT-1 and arterial blood draws. All participants also completed a T1-weighted MRI scan for the purpose of region of interest (ROI) delineation. [¹⁸F]SynVesT-1 volume of distribution (V_T), a measure of SV2A binding, was computed for six brain ROIs using a 1-tissue compartment model (1-TCM). ROIs included the prefrontal, temporal and cingulate cortices, the hippocampus, amygdala and full striatum as these brain regions have been implicated in SUD. Image preprocessing and kinetic modeling were done using PMOD (4.2). An analysis of variance was conducted to test our hypothesis.

Results Participant scans (n = 29) were analyzed with arterial input function (11 M, 18 F; 20.4 years old). 17 (59%) participants had no history of SUD (7M, 10 F; 19.1 years old) and 12 (41%) met DSM-5 diagnostic criteria for a SUD (4 M, 8 F; 22.3 years old); of those, 7 met criteria for cannabis use disorder (CUD). Age was significantly different between the SUD and non-SUD groups (p = 0.001), such that the SUD group was slightly older. Since the majority of SUD's were CUD, this may be explained by the legal age of cannabis in Ontario, 19 years old. Unrestricted access to cannabis may have contributed to the development of SUD. The SUD group had a higher rate of trauma and stress related disorder (8/12 vs 5/17; p = 0.03) and a significantly lower rate of anxiety disorder (9/12 vs 17/17; p = 0.014). The ANCOVA with age found no significant differences in [¹⁸F]SynVesT-1 V_T in SUD vs non-SUD across the 6 ROIs (-4%; F(1, 28) = 0.58; p = 0.8). Differences in V_T values were the most marked in the prefrontal cortex: -3.7% lower (non-significantly) in SUD vs non-SUD. The co-efficient of variation was 16.6% across all ROIs.

Conclusion This study was the first to explore the relationship between SUD and synaptic density in youth with a mental health challenge. No differences were found at this stage. Further work is ongoing to increase the sample size and include youth without a mental health challenge in order to better understand the link between synaptic density and drug use.

Preliminary preclinical PET neuroimaging of [¹⁸F]ROCK202 for rho-associated protein kinase 2

Mark R. Bortolus,^{1,2} Junchao Tong,² Amanda J. Boyle,^{1,2} Andrea Narvaez,² Neil Vasdev,^{1,2} and Chao Zheng^{1,2*}

¹ Department of Psychiatry, Temerty Faculty of Medicine, University of Toronto, Toronto, ON

² Azrieli Centre for Neuro-Radiochemistry, Brain Health Imaging Centre, Centre for Addiction and Mental Health, Toronto, ON

Introduction: Activation of the Rho/Rho-associated protein kinase 2 (ROCK2) pathway is a therapeutic target for various neurological and neurodegenerative diseases including but not limited to Alzheimer's disease (AD), amyotrophic lateral sclerosis, and progressive supranuclear palsy.¹ Recently, the first brain-penetrant ROCK2 PET radiotracer labelled with carbon-11, [¹¹C]ROCK201, was evaluated in rodents, non-human primates, and a mouse model of AD.² To facilitate widespread use of ROCK2 PET imaging, we report the automated radiosynthesis and preliminary neuroimaging of a fluorine-18 labelled ROCK2 specific radioligand, [¹⁸F]ROCK202, in rodents.

Methods: ROCK202 is a selective inhibitor of ROCK2 with IC_{50} values of 14, 85, and 120 nM for ROCK2, ROCK1, and protein kinase A (PKA), respectively.³ The fluorine-18 labelled isotopologue (**Figure 1a**) was prepared on a commercial automated synthesis platform (GE Tracerlab FX2N) by nucleophilic substitution of its 2-nitropyridine precursor with [¹⁸F]KF/K₂₂₂/K₂CO₃ in DMSO solvent. LogD_{7.4} values were measured using the shake-flask method. PET imaging studies in Sprague-Dawley rats were conducted on Mediso PET-CT and PET-MR 3T scanners. The tracer was evaluated using 90-min dynamic PET imaging following tail-vein injection of the radiotracer into healthy control (HC) rats ($n = 4$, 2M/2F, ~8 mo). Regions of interest (ROIs) were determined following co-registration of individual CT or MR images to the Schwarz rat brain atlas.⁴ The regional time-activity curves (TACs) were extracted by applying ROI templates to the dynamic PET images.

Results: [¹⁸F]ROCK202 was prepared in $\geq 99\%$ radiochemical purity and molar activity of 176 ± 36 GBq/ μ mol ($n = 4$) at the end of synthesis with a radiochemical yield of $35 \pm 7\%$ ($n = 7$, decay-corrected relative to dry [¹⁸F]fluoride within 50 min synthesis time). The LogD_{7.4} was measured to be 3.36 ± 0.32 ($n = 8$). Imaging data obtained from PET-MR and PET-CT yielded comparable TACs. Rapid uptake of [¹⁸F]ROCK202 was observed in brains of HC male and female rats within 5 min (**Figure 1b**) with fast washout and a high peak whole-brain SUV of 3.92 ± 1.13 (**Figure 1c**). No skull uptake was observed, indicating a low likelihood of defluorination. Relatively higher tracer uptake was found in the putamen, medulla, thalamus, superior colliculus, bed nucleus of stria terminalis, cerebellum, and frontal cortex, with peak SUV ≥ 4.13 . This is consistent with the fact that ROCK2 is ubiquitously expressed in the rodent brain.⁵ Comparison of peak whole-brain SUVs for [¹⁸F]ROCK202 (3.92) and previously reported [¹¹C]ROCK201 (2.1)² show that both tracers have high brain uptake in HC rats, and their TACs indicate similar pharmacokinetic profiles (**Figure 1c** and **1d**).

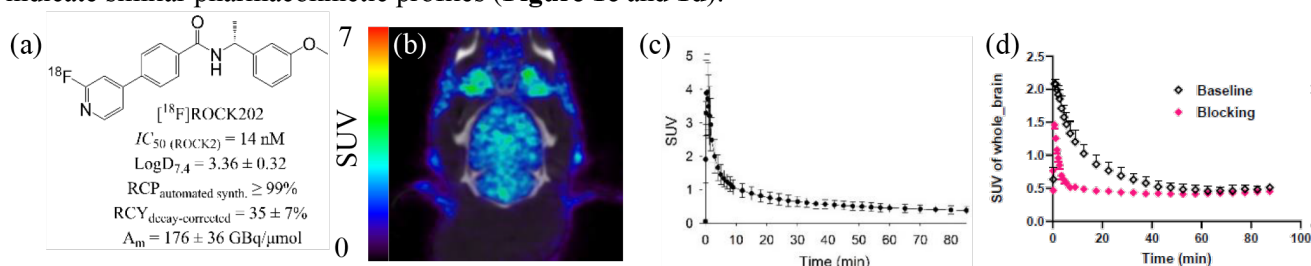


Figure 1. (a) Properties of [¹⁸F]ROCK202; (b) Representative PET image (0-5 min) of [¹⁸F]ROCK202 in HC rat; (c) Whole brain TAC in rats ($n = 2F/2M$). (d) Previously reported TACs of [¹¹C]ROCK201 in HC rats ($n = 2$).²

Conclusions: We developed and automated the radiosynthesis for the fluorine-18 labelled ROCK2-inhibitor, [¹⁸F]ROCK202. Preliminary PET imaging of [¹⁸F]ROCK202 showed high brain uptake and fast pharmacokinetics in rats. Further PET imaging studies including radiotracer uptake specificity (blocking) experiments using a ROCK2 inhibitor and evaluation in mouse models of neurodegenerative disease are underway.

References: (1) *Front. Cell. Neurosci.* **2021**; 15: 636017. (2) *J. Nucl. Med.* **2022**; 63(2): 2301. (3) *J. Med. Chem.* **2018**; 61: 11074–11100. (4) *Neuroimage.* **2006**; 32(2): 538–550. (5) *Cell Struct. Funct.*, **2012**, 37, 155.

Acknowledgements: M.R.B. is supported by an NSERC Postdoctoral Fellowship. N.V. is supported by the Azrieli Foundation, the Canada Research Chairs Program, Canada Foundation for Innovation, and the Ontario Research Fund. C.Z. is supported by the Alzheimer's Association (Grant No. AARF-22-919976).

Session 18 Talks: Ultrasound and Photoacoustic Abstracts

Three-Dimensional Ultrasound for Investigating Synovial Blood Flow Changes with Exercise in Thumb Osteoarthritis

Megan Hutter^{1,2}, Randa Mudathir^{1,2}, Carla du Toit², Assaf Kadar^{3,4}, Aaron Fenster^{1,2}, Emily Lalone^{3,5}

¹Faculty of Medical Biophysics, Western University, ²Robarts Research Institute, Western University, ³Roth | McFarlane Hand and Upper Limb Centre, St. Joseph's Health Care, ⁴Schulich School of Medicine and Dentistry, Western University, ⁵Department of Mechanical and Materials Engineering, Western University

Introduction: Inflammation of the joint lining, or synovium, is recognized as an important aspect of osteoarthritis (OA) and contributes to disease pathogenesis and symptoms.¹ Angiogenesis, a process of new blood vessel growth, is involved in inflammation and can disrupt the normal process of regulating joint blood flow.² The basal thumb joint is a common site of OA and an important joint involved in hand function. Thumb OA can limit function, and cause pain and disability. Physical therapy treatments, including exercise, are aimed to improve patient pain, stability, and function. However, the vascular changes and blood flow response to exercise are not fully understood in thumb OA. Ultrasound (US) imaging provides soft tissue and joint visualization. In addition, Doppler US technologies can detect and visualize blood flow. Active joint inflammation can be detected by the presence of Doppler signal, which is not present in healthy thumb joints. Previous synovial blood flow investigation has been limited to two-dimensional US visualization, lacking the comprehensive three-dimensional (3D) visualization of the detectable synovial vasculature. This work aims to assess and visualize detectable synovial blood flow changes with exercise in thumb OA patients using a 3DUS imaging system.

Methods: A 3DUS system was developed with Doppler imaging technologies to detect and visualize blood flow. The 3DUS device incorporated a motorized assembly that translated a semi-submerged US transducer across a linear region of interest. 3DUS images were acquired over a five-centimetre length using a 14L5 linear transducer with an operating frequency of 10 MHz, and a Canon Aplio i800 US machine with superb microvascular imaging (SMI) Doppler technology. Thirteen thumb OA patients were imaged with 3DUS SMI before and after completing two resistance thumb exercises, each for thirty seconds. The synovial volume was manually segmented for the pre- and post-exercise 3DUS SMI images. The coloured voxels within each segmentation were automatically counted with software. Synovial blood flow volumes and fractions were calculated and compared to thumb OA stage.

Results: 3DUS SMI images acquired pre- and post-exercise detected and visualized synovial blood flow in thumb OA patients (Fig. 1). The absolute mean change in US-detectable synovial blood flow volume with exercise was $1.31 \text{ mm}^3 \pm 2.59 \text{ mm}^3$ and $1.70 \text{ mm}^3 \pm 2.87 \text{ mm}^3$ for the thumb OA patients with detectable blood flow within the region of synovial inflammation. US-detectable synovial blood flow volume changes were from 0 to 9.53 mm^3 . Patients with higher OA stages had lower detectable synovial blood flow volumes.

Conclusion: This study demonstrated the ability of a novel 3DUS imaging device to investigate and measure the effect of exercise on US-detectable synovial blood flow in thumb OA. This work implemented a novel method of quantifying changes in blood flow to gain additional insight into the response of the synovial vasculature and its role in the disease process. This 3DUS device will be used to monitor thumb OA patients longitudinally and to further investigate the role of synovial blood flow on disease progression. This novel 3DUS device can provide a new method of measuring active joint inflammation and insight into the synovial blood flow and vasculature by monitoring changes and responses to treatment.

References: [1] Ashraf S, et al. (2008) *Curr Opin Rheumatol*. 20. [2] Haywood L, et al. (2001) *Histol Histopathology*. 16.

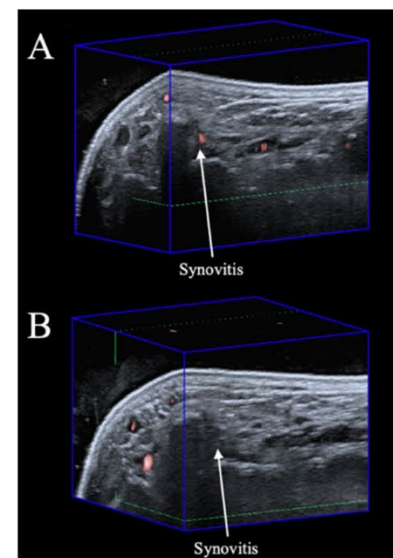


Figure 1. 3DUS SMI images (A) pre- and (B) post-exercise of a thumb OA patient.

Quantitative analysis of photoacoustic and ultrasound imaging of red blood cell aggregation in the human radial artery

Taehoon Bok¹, Michael Kolios^{1,2} and Eno Hysi^{1,3}

¹St. Michael's Hospital, ²Toronto Metropolitan University, ³University of Toronto

Introduction: The aggregation of red blood cells (RBCs) is a naturally occurring process induced by the cyclical changes in the vessel shear rate. The hyperaggregability of RBCs is observed in patients with diabetes and deep vein thrombosis¹. Measurement of RBC aggregation has been widely studied using *in vitro* techniques, and ultrasound imaging techniques have been developed for *in vivo* measurements¹. Our group has demonstrated that photoacoustic (PA) imaging can assess RBC aggregation alongside with US imaging². In this work, we investigate the use of quantitative PA and US imaging to characterize RBC aggregation in the human radial artery. These system-independent parameters, derived from quantitative US concepts, offer the potential of PA for mapping structural and functional changes during RBC aggregation.

Methods: Imaging was performed in the human radial artery of 12 healthy volunteers. Pulsed-wave Doppler was used to localize the radial artery by identifying its signature flow pattern and to measure the blood flow velocity synchronized with the co-registered PA/US images. PA images at 800 nm (an isosbestic point for oxy- and deoxyhemoglobin) were acquired simultaneously with US images using a VevoLAZR imaging system equipped with a 21 MHz probe (Fujifilm-VisualSonics). The PA-based spectral slope (SS) was calculated by normalizing the power spectrum of the PA signal obtained from the radial artery to that from a 6% RBC suspension (used as a reference phantom in US spectral analysis of RBC aggregation). For comparison with the US images, the effective scatterer size was calculated using the structure factor size estimation (SFSE) based on US spectral analysis.

Results: The representative PA amplitude (Fig. 1a) at the end-diastole (ED) was 2.5 dB greater than the one at the peak-systole (PS). RBC aggregation is enhanced during diastole due to the reduced shear rate, increasing the absorber size. This is reflected in the SS (Fig. 1b), with larger absorbers having greater negative values, i.e., -0.4 and -0.1 dB/MHz for the ED and PS, respectively. The US amplitude (Fig. 1c) at the ED was 3.4 dB greater than the one at the PS. Using the SFSE (Fig. 1d), the average number of cells forming the RBC aggregates was 3.1 at the ED, whereas the number of cells was 1.6 at the PS. The PA-based SS was implemented in the same manner as the US-based SS, although the impact of the optical fluence on the PA waves due to the skin above the radial artery was not considered.

Conclusions: This study elucidates the potential of quantitatively assessing RBC aggregation by PA/US imaging. Given that US imaging is co-registered with the functional PA datasets, it is also possible to estimate the size of RBC aggregates using the US-based SFSE. This study also demonstrates how PA/US imaging can be used to measure RBC aggregates in conditions where blood flow might be impaired due to hyper aggregation of RBCs.

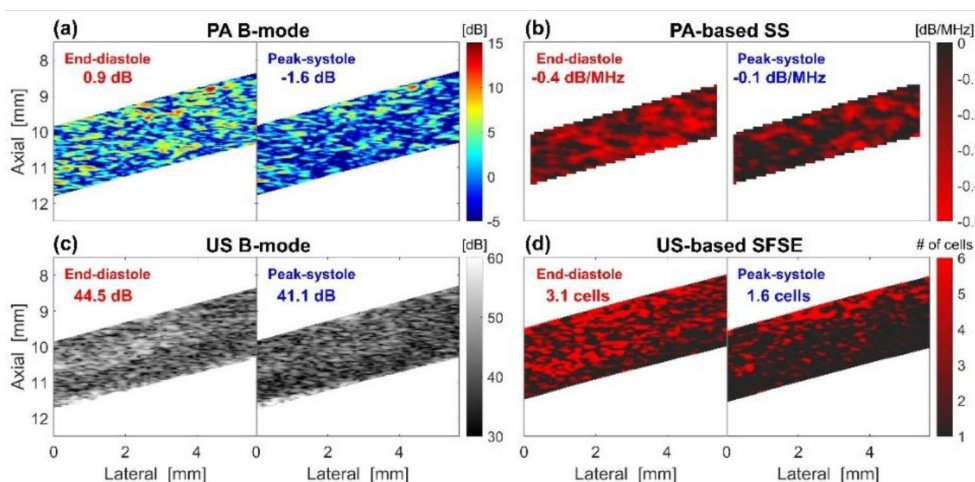


Figure 1. Representative photoacoustic (PA) and ultrasound (US) images of end-diastolic and peak-systolic blood flow in the radial artery: (a) PA B-mode, (b) spectral slope (SS) calculated from PA signal, (c) US B-mode, and (d) number of red blood cells forming aggregates calculated from US structure factor size estimation (SFSE).

References: 1. Baskurt, O. K., Neu, B. & Meiselman, H. J. *Red Blood Cell Aggregation*. (CRC Press, 2011).

2. Bok, T., Hysi, E. & Kolios, M. C. *In vivo* photoacoustic assessment of the oxygen saturation changes in the human radial artery: a preliminary study associated with age. *J Biomed Opt* **26**, 036006 (2021).

Ultrasound Transducers for Microvascular Imaging with Superharmonic Contrast Imaging: Resolution and Field of View Comparison

Elvira Catalina Vazquez Avila¹, Emmanuel Cherin², Jianhua Yin², Bojana Stefanovic^{1,2}, Christine Demore^{1,2}

¹ Department of Medical Biophysics, University of Toronto. ² Physical Sciences, Sunnybrook Research Institute.

Introduction:

Superharmonic contrast imaging (SpHI) is a new ultrasound imaging technique that takes advantage of the complex acoustics of microbubbles contrast agents (MBs) to visualise the microvasculature but requires a novel type of dual-frequency ultrasound transducer that operates at two separate frequency bands. For SpHI, ultrasound pulses transmitted at the lower frequency band are scattered non-linearly by MBs circulating in the bloodstream, generating broadband acoustic signals that are detected at the higher frequency band, typically 3 – 15x transmit pulse frequency, to detect the high-order harmonics. Since tissue does not have a strong harmonic response, the tissue signal is suppressed, and images of the microvasculature with high contrast-to-tissue ratio can be created. Conventional B-mode ultrasound images can also be acquired at the higher frequency band. One arrangement of these dual frequency ultrasound probes use a commercial array for the high frequency (HF) band and flanking transducers for the lower frequency (LF) band (Fig. 1A). We have made prototype dual-frequency probes with high frequency bands centered at 7 MHz, 21 MHz and 40 MHz. The 7 MHz device is designed for breast cancer imaging using a standard clinical probe for the high frequency component. The others are designed for the shallower imaging depths needed for pre-clinical imaging, and the 40 MHz device will be used for studying the neurovasculature changes in a rodent model of stroke. Here, we compare the resolution and imaging field of view for three dual-frequency probes with a wide range of frequency pairings.

Methods:

The frequency pairings for the probes are A: 0.9 MHz (transmit) and 7 MHz (receive and B-mode), B: 1.7 and 21 MHz, and C: 4 and 40 MHz. The center high frequency arrays were connected to either the Visualsonics F2 system (probe A) or the Visualsonics Vevo2100 (probes B, C). The low frequency elements were connected to a power wave generator and an amplifier and excited with 1 cycle of a sinusoidal pulse at the low frequency center frequency. The image field of view was determined by the number of samples that could be acquired by the ultrasound beamformer and centered near the fixed elevation focus of each high frequency array. Stock concentration of MBs were diluted in a beaker to yield a concentration of 500 MBs/mL and stirred continuously to distribute the scatterers. The peak signal from MBs was localised in the superharmonic contrast images. Resolution was determined by measuring the full-width half-max (FWHM) of the bubble signal in the lateral and axial direction. Bubbles were detected over the field of view of each probe.

Results:

The following mean values for the axial and lateral FWHMs (Fig. 1B) for each probe were obtained over their respective depths (Fig. 1C): [A] 14-28 mm depth, 284±9 µm (axial), 670±30 µm(lateral); [B] 16-22 mm depth, 33±1 µm(axial), 479±5 µm(lateral); and [C] 4-8 mm depth, 26±1 µm(axial) and 400±20 µm(lateral).

Conclusion:

We have presented the different imaging depths and resolutions achieved by the dual-frequency probes. An increase in transmit frequency resulted in better resolution, however, it also decreases the depth at which we can image and the size of image focus. The depth of field was determined the ultrasound scanner and its available acquisition mode; the receive-only operating mode of the Vevo2100 only captures half the image depth set for B-Mode. The F2 system does not have such constraints. Future probes will be designed for the F2 system to extend the field of view.

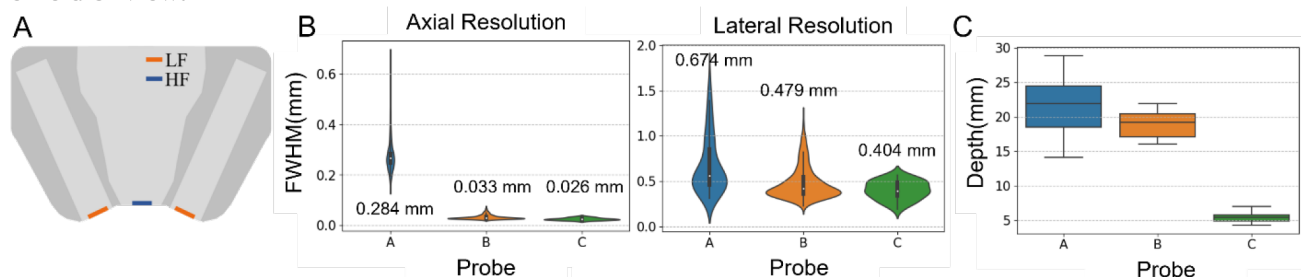


Figure 1. (A) Configuration of LF and HF elements for the dual frequency probe. Axial and lateral FWHMs distributions (B) and depth distributions (C) of the localized MBs for each probe.

Assessments of vascular damage during kidney transplantation using photoacoustic imaging

Sarah Dykstra¹, Alexander Koven², Michael Kolios³, Darren Yuen⁴, Eno Hysi⁵

¹University of Waterloo Department of Systems Design Engineering, ²St Michael's Hospital, Division of Urology, ³Toronto Metropolitan University, Department of Physics, ⁴St. Michael's Hospital, Division of Nephrology, ⁵University of Toronto, Department of Medical Biophysics

Introduction: Kidney transplantation is the most optimal treatment for end-stage renal disease, but wait times for deceased donor kidneys often exceed 5 years in Ontario, and outcomes are often unpredictable due to variable donor quality. Ischemic-reperfusion injury (IRI) worsens outcomes, as it is caused by transplant-related vascular damage leading to delayed graft function (DGF) and fibrosis [1]. IRI arises from blood flow stoppage and the reperfusion rush of inflammatory cytokines (Figure 1). Currently, the degree of IRI cannot be measured during transplant, making it challenging to predict its occurrence and severity. Photoacoustic (PA) imaging was selected for this study to quantify oxygen saturation (sO₂) and hemoglobin (HbT) non-invasively [2], potentially offering physicians a quantitative means of predicting short-term kidney transplantation complications and allowing for earlier interventions. I hypothesised that fibrovascular damage occurring during kidney transplantation can be accurately and noninvasively quantified using PA imaging.

Methods: In a 30-patient trial including 17 living donors (LD) and 13 deceased donors (DD), kidneys were imaged using PA imaging before and after reperfusion (Figure 1). PA scans were segmented to isolate the kidney region. Radiofrequency data from the scans was analyzed to quantify sO₂ and HbT in the cortex of each kidney using average PA signal amplitudes at 750 nm and 850 nm.

Results: PA scans performed before and after implantation indicate that PA imaging can quantify changes in oxygenation and hemoglobin levels (Figure 2a). Specifically, the HbT increased by 150% and the sO₂ increased by 84% post-reperfusion compared to pre-transplantation. The degree of increase differed for DD (Figure 2b), suggesting that the degree of vascular damage is significantly more pronounced in these grafts. This is likely related to the existing fibrovascular injury that is associated with DD grafts, and it is further exacerbated by the IRI that occurs during transplantation.

Conclusion: These trial results suggest that PA imaging has potential for clinical use in assessing kidney perfusion and IRI damage, and may be able to identify patients at greater risk for DGF. This trial has the potential to change the management of kidney transplants and improve clinical outcomes. Further work will investigate the relationship between kidney perfusion measurements and incidences and durations of DGF to evaluate the potential for PA as a screening tool in kidney transplantation.

References

- [1] Melih K V et al, *Transplant. Proc.*, 51(4): 1096-1100 (2019)
- [2] Steinberg I et al, *Photoacoustics*, 14:77-98 (2019)

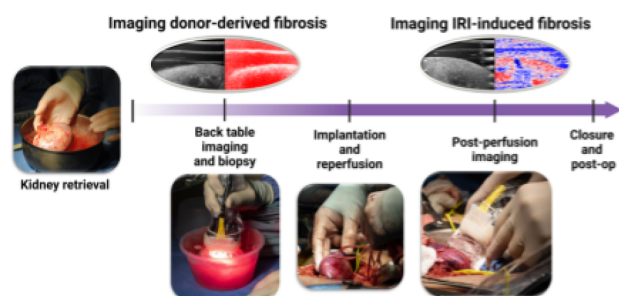


Figure 1. Schematic of clinical trial design

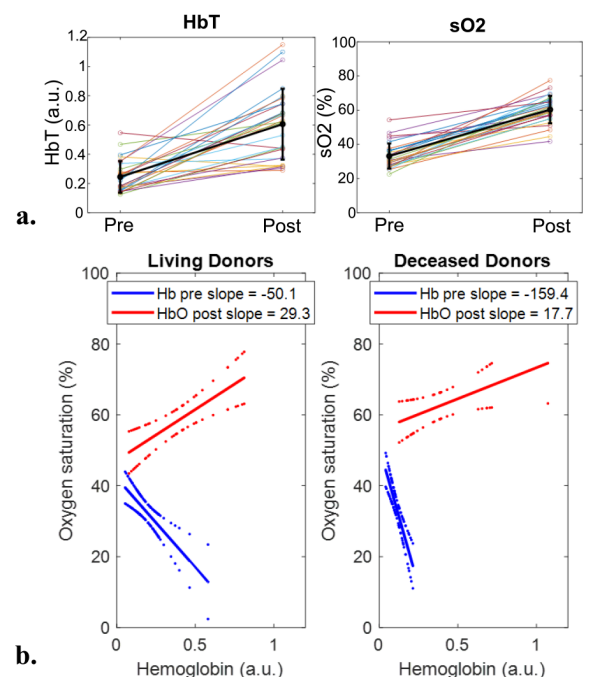


Figure 2. (a) Changes in the total hemoglobin content and sO₂ pre- and post-perfusion. (b) Relationship between oxygenation and hemoglobin for LD and DD

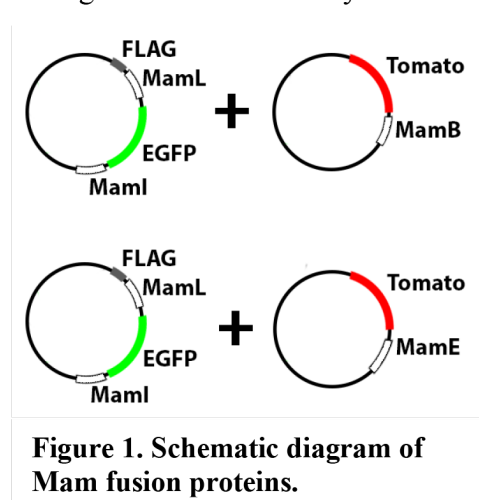
Session 19 Pitches: Cellular and Molecular Abstracts

Developing Magnetic Resonance Reporter Gene Imaging: Co-localization of Magnetotactic Bacteria Proteins.

Q. Sun¹, S. Hong¹, R.T. Thompson^{1,2}, F.S. Prato^{1,2,3}, D.E. Goldhawk^{1,2,3}

¹Imaging Program, Lawson Health Research Institute, ²Medical Biophysics & ³Collaborative Graduate Program in Molecular Imaging, Western University, London, Canada

Introduction: With its superb spatial and temporal resolution, magnetic resonance imaging (MRI) has great potential to track cellular activities that define early stages of disease [1]. To improve molecular imaging techniques, we are developing MRI reporter gene expression based on the magnetosome. In magnetotactic bacteria (MTB), magnetosome formation allows cells to concentrate and compartmentalize iron biominerals in membrane-enclosed vesicles [2]. Essential MTB genes *mamI*, *mamL*, and *mamB* have roles in designating the magnetosome vesicle and may also provide docking site(s) for additional proteins, such as MamE, that facilitate biomineralization [1-3]. This patent-protected technology [4,5] allows fine-tuning of iron contrast, enables MRI reporter gene expression of oncogenic transcription factor activity, and provides long-term molecular imaging and tracking throughout the cell's life cycle.



Hypothesis: In mammalian cells, MamI, MamL, and MamB or MamE co-localize on an intracellular membrane and interact to initiate formation of a rudimentary magnetosome-like nanoparticle.

Materials and Methods: MTB genes were cloned from *M. magneticum* sp. AMB-1 genomic DNA by PCR and inserted into vectors with fluorescent protein tags to create Mam fusion proteins (Fig. 1). MamL+I+B or MamL+I+E (Fig. 1) were expressed in human MDA-MB-435 melanoma cells—alone and in combination—using antibiotic selection. Expression of Mam fusion proteins was verified by Western blot. Subcellular location and co-localization of fusion proteins were examined with confocal microscopy (Nikon A1R Confocal Laser Microscope).

Results: While we have previously shown single- and co-expression of MTB proteins [6], this is the first report of triple MTB protein expression in mammalian cells. When MamB is expressed with MamI and MamL, all three proteins co-localize in a yellow, punctate pattern (Fig. 2A). Triple expression of MamI, MamL, and MamE also resulted in similar co-localization (Fig. 2B).

Discussion and Summary: To date, we have shown that MamI, MamL, and MamB individually affects cellular MR signal, and that MamE does not [6]. Therefore, we plan to evaluate the MRI signal and cellular iron content of cells [7] expressing MamL+I+B (to evaluate their potential synergistic effects) and of cells expressing MamL+I+E (to evaluate whether MamE affects MR signal while interacting with other magnetosome proteins).

References:

[1] Goldhawk *et al.* (2017) Design and Applications of Nanoparticles in Biomedical Imaging, pp 187-203 [2] Uebe & Schuler (2016) Nat Rev Microbiol 14:621 [3] Quinlan *et al.* (2011) Mol Microbiol 80:1075 [4] Goldhawk *et al.* (2014) Multi-Magnetics Inc [5] Prato *et al.* (2017) Multi-Magnetics Inc [6] Sun *et al.* (2023) Electronic Thesis and Dissertation Repository. 9281 [7] Sengupta *et al.* (2014) Front Microbiol 5:29

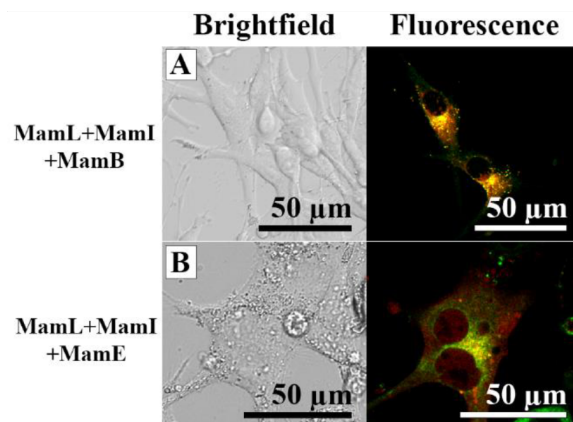


Figure 2. Confocal fluorescence images of MDA-MB-435 cells expressing MTB genes. Triple expression of MamL+I+B is shown in A, and of MamL+I+E is shown in B.

Visualizing Real-Time Mechanosensory Response of Endothelial Cells to Multi-Directional Wall Shear Stress

Kevin R.J. Moore¹, David W. Holdsworth^{1,2}, J. Geoffrey Pickering^{1,3,4}, Tamie L. Poepping^{1,3}

¹Medical Biophysics; ²Robarts Research Inst.; ³Biochemistry, ⁴Medicine, and ⁵Physics & Astronomy
The University of Western Ontario, London, Canada

Introduction: Endothelial cells (ECs) form the innermost lining of blood vessels and are able to sense and respond to local changes in blood flow including the induced wall shear stress (WSS) via mechanotransduction. Blood flow through a vessel can become disturbed when passing through bifurcations or plaque-burdened regions, which disrupts the direction and magnitude of WSS experienced by cells. ECs in these regions show activation of pro-inflammatory phenotypes, manifesting in the development and progression of atherosclerosis. The vascular changes seen in atheroprone regions is a result of EC dysfunction, which may be attributed to WSS with persistent variations in direction and magnitude, rendering the cell incapable of adapting to the flow stimuli. The earliest cell responses to these flow disturbances – particularly the mechanisms by which ECs sense and respond to different forms of WSS – are not well understood. Reactive oxygen species are naturally occurring by-products of various cellular activities and signalling cascades. Excessive increases in ROS generation within endothelial cells are an early indicator of a disruption of homeostasis and are thought to accelerate the progression of vascular diseases such as atherosclerosis and diabetes. It is hypothesized that within minutes of being exposed to WSS disturbances, ECs will exhibit forms of oxidative stress and damage. This study aims to measure the differences in ROS production in ECs due to different flow conditions to characterize atheroprone flow environments.

Methods: A novel microfluidic device has been fabricated from polydimethylsiloxane (Sylgard-184). The device consists of a small channel for fluid to pass over cultured ECs. Two opposing jets create varying levels of bi-directional and multi-directional flow fluctuations, recapitulating the various forms of WSS observed in regions of disturbed flow within the vasculature. Micro-particle image velocimetry (micro-PIV) has been used to measure the fluctuations in fluid velocity and derive WSS maps that quantify the variation in scrubbing effects experienced by each cell throughout the device (Fig. 1a).

Prior to imaging, cells are loaded with a fluorescent dye (5 μ M CM-H2DCFDA) in phenol-red-free, serum-free cell media for 30 minutes. The dye is retained in the cytoplasm of the ECs, where it does not fluoresce until hydrolyzed by superoxide radicals, causing it to emit green fluorescence. The device is imaged with a confocal inverted microscope (Nikon Ti2-E) while applying disturbed flow WSS. Images are captured every five minutes, and the fluorescence intensity of each cell is quantified using ImageJ.

Results: Within 30 minutes of being exposed to disturbed flow, up to a 7% increase in ROS generation is seen within the ECs. More notably, a differential response is seen for different types of WSS scrubbing, where regions with higher magnitude mean stress and more multidirectional WSS patterns correlate with larger increases in ROS generation (Fig. 1b). Dependence on the type of WSS is reinforced by the closely mirrored response from the left and right zones of the symmetric device.

Conclusion: We have successfully designed and manufactured a device that enables imaging live endothelial cells while being subjected to variations in wall shear stress direction and magnitude. The results of this experiment will contribute to the understanding of the differential response of endothelial cells to differential forms of WSS. The characterization of endothelial cell responses to varying flow patterns is essential in strengthening the link between endothelial cell response to flow and atherosclerotic development.

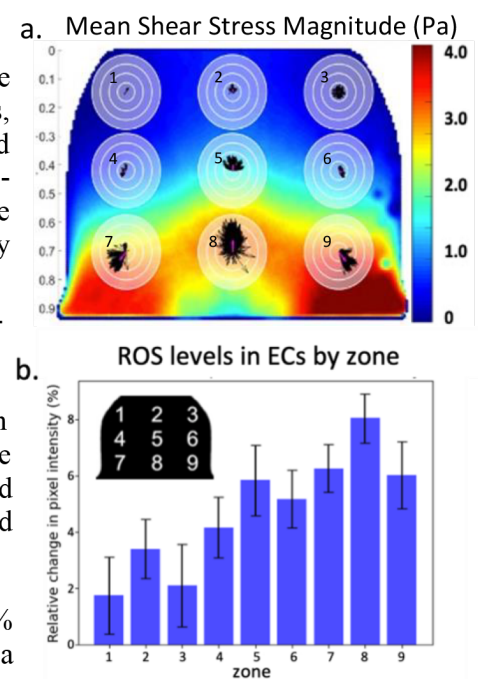


Fig. 1 a) Heatmap representing mean shear stress magnitude, derived from micro-PIV, throughout the microfluidic device. Quiver plots represent instantaneous shear stress vectors in 9 regions, labelled 1-9 **b)** bar chart displaying the increase in fluorescence from ROS dye in endothelial cells in each of the 9 zones after 30 minutes of disturbed flow. Error bars indicate standard error, n=742 cells.

Bridging Micro-to-Clinical Dosimetry for Alpha Particle Targeted Radionuclide Therapy

S. Ghaseminejad^{1,2}, T.T. Duong², C. Opara², D. De Sarno², A. Bertolet³, T.-Y. Lee^{1,2}

¹Medical Biophysics, Western University; ²Lawson Health Research Institute and Robarts Research Institute, London, Ontario; ³Radiation Oncology, Harvard Medical School, Boston, Massachusetts, USA

Background/Motivation: Targeted radionuclide therapy (TRT) has demonstrated notable success in treating neuroendocrine and prostate cancer. The current choice of radioisotope, ¹⁷⁷Lu, primarily emits beta particles. Alpha emitters like ²²⁵Ac are expected to be more effective due to their higher linear energy transfer (LET) and extremely short range (~80 μm), allowing for more precise targeting of cancer cells while minimizing damage to surrounding healthy tissue. This study aims to investigate how microscale ²²⁵Ac dosimetry can inform clinical dosimetry based on SPECT imaging spanning millimeters to centimeters.

Method: We constructed three 3D microscale cell models at 2 μm voxel resolution, each composed of a regular array of 20 μm cubic cells. These cells include an 8 μm cubic nucleus surrounded by a 4 μm wide cytoplasm, followed by a 2 μm wide layer of cell membrane. The cell models have a volume of 2.19 - 2.70 × 10⁻⁵ mL and had 343, 729, and 1,331 cells placed at distances of 40, 30, and 26 μm apart center to center corresponding to cell fractions of 0.10, 0.27 and 0.43, respectively. The activity was uniformly distributed in the cytoplasm, simulating radiopharmaceuticals that have been internalized into the cell. The dimensions of the cell models ensure that the central cluster of 3 × 3 × 3 cells experiences a full cross-fire effect from surrounding activities, considering the 80 μm range of ²²⁵Ac alpha particles. The time-integrated activity (TIA) distribution in the cell model was convolved with the whole decay chain dose point kernel (DPK) of ²²⁵Ac to determine the microscale absorbed dose distribution in the cell model at 2 μm resolution¹. The required ²²⁵Ac DPK was generated by the Monte Carlo code TOPAS² which is a wrapper around GEANT4 code. The heterogeneous microscale TIA in the cell model was blurred into a uniform distribution with the same total TIA and convolved with the ²²⁵Ac DPK to simulate the calculated absorbed dose distribution from SPECT measured TIA according to the MIRD-S value formalism¹.

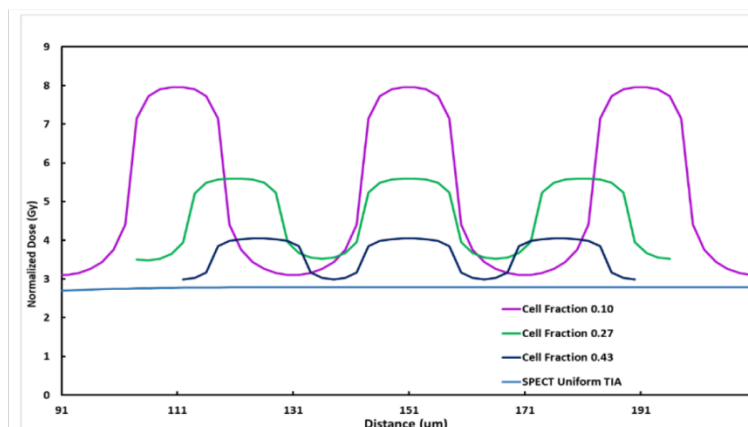


Figure 1. Comparison of the dose profiles through the center cluster of three cells for different cell fractions and uniform dose to the cells.

Results: Figure 1 shows the absorbed dose profiles normalized to the same total TIA through the center of the cell models where the full cross-fire effect from activities within the 80 μm range of ²²⁵Ac alpha particles is realized. The normalized total TIA corresponded to administering 100 kBq/kg of ²²⁵Ac at a Standardized Uptake Value (SUV) of 5.0 g/mL. As expected the microscale dose distributions were highly heterogeneous, peak to trough ratio decreased from 2.58 to 1.33 and the peak dose to the nucleus from 8.0 to 4.0 Gy as the cell fraction increased from 0.10 to 0.43. In contrast, SPECT-measured TIA was uniform and the same because of normalization, the absorbed dose distribution was the same for all cell models. As shown in the Figure, the ratio of the microscale to the SPECT scale nuclear dose decreased from 3.47 to 1.70 with increasing cell fraction.

Results: Figure 1 shows the absorbed dose profiles normalized to the same total TIA through the center of the cell models where the full cross-fire effect from activities within the 80 μm range of ²²⁵Ac alpha particles is realized. The normalized total TIA corresponded to administering 100 kBq/kg of ²²⁵Ac at a Standardized Uptake Value (SUV) of 5.0 g/mL. As expected the microscale dose distributions were highly heterogeneous, peak to trough ratio decreased from 2.58 to 1.33 and the peak dose to the nucleus from 8.0 to 4.0 Gy as the cell fraction increased from 0.10 to 0.43. In contrast, SPECT-measured TIA was uniform and the same because of normalization, the absorbed dose distribution was the same for all cell models. As shown in the Figure, the ratio of the microscale to the SPECT scale nuclear dose decreased from 3.47 to 1.70 with increasing cell fraction.

Discussion: Microscale cell models reveal that clinical dosimetry, reliant on TIA distribution measured through SPECT, may significantly underestimate cellular doses by several folds. The extent of this underestimation is tied to a crucial factor—the cellular fraction. This finding is of relevance to TRT because as cycles of treatment progress, the cellular fraction would decrease if the treatment is effective.

References: ¹Bloch et al. J Nucl Med. 1999;40:11S-36S. ²Perl et al. Med Phys. 2012; 39:6818-37

Title: Magnetic particle imaging serves as a biomarker for measuring tumour associated macrophage density in vivo

Authors: Nitara E. Fernando and Paula J. Foster

Imaging Research Laboratories, Robarts Research Institute, Canada

Department of Medical Biophysics, University of Western Ontario, Canada

Introduction: Tumour associated macrophages (TAMs) constitute up to 50% of the breast cancer microenvironment and are linked to adverse patient outcomes.¹ Conventionally, TAM density is assessed through immunohistochemistry (IHC); however, this relies on invasive biopsies and is not representative of the entire tumour.² Thus, there is a need for non-invasive, quantitative imaging for in vivo TAM assessment. Superparamagnetic iron oxide (SPIO) particles have been injected intravenously (IV) to label macrophages in situ for TAM imaging with MRI³; however, quantifying TAM density is challenging. Magnetic Particle Imaging (MPI) is emerging as an in vivo cellular imaging method and can provide measurements of iron mass which allow us to estimate cell number from images. MPI has previously been evaluated for TAM cell tracking, however, quantification was only possible for fixed tumour tissues imaged ex vivo due to known dynamic range limitations⁴. When iron samples with large differences in concentrations are present in the same field of view (FOV) there is signal oversaturation from the higher signal due to the requirement for regularization for stable reconstruction. The high uptake of SPIO in liver macrophages after IV injection prevented isolation of the lower TAM signal. This represents a major roadblock for in vivo MPI in applications where two or more sources of signal exist. In this study, we address this challenge by employing an advanced reconstruction algorithm, allowing for a small FOV to be focused on the tumour⁵. First, we demonstrate the utility of small FOV MPI as a fully quantitative approach for in vivo TAM imaging, and second, we compare TAM density in mammary tumours induced by two different breast cancer cell lines.

Methods: 4T1 and E0771 mouse breast cancer cell lines (100,000 cells) were administered subcutaneously to the fourth mammary fat pad of C57BL/6 mice (E0771, n=8) and BALB/c mice (4T1, n=8). Twenty days after the cell injection, 30mg/kg of a SPIO called Synomag-D-PEG (Micromod GmbH) was administered IV to mice and 24 hours later imaging was performed using the MomentumTM MPI scanner (Magnetic Insight, Inc.). Images were acquired with a 5.7 T/m selection field gradient, drive field strength of -23mT (z). To image TAM's with MPI, first an image was acquired using the native reconstruction with a 12 (z) x 6 (x) cm FOV, then the advanced reconstruction with a 3 (z) x 6 (x) cm FOV was

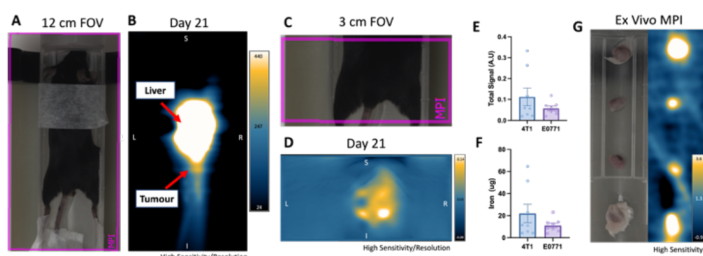


Figure 1. In vivo imaging of tumours using MPI following IV injection of SPIO. A 12 cm FOV is shown in A. The corresponding 2D MPI image is shown (B), where high liver signal oversaturates the tumour signal. With the advanced reconstruction, a 3 cm FOV can be applied over the tumour region (C), allowing for isolation of tumour signal (D). The signal obtained with small FOV imaging can be quantified as total signal (E) or iron content (F). Ex vivo imaging confirms iron presence in tumours (G).

reconstruction with a 3 (z) x 6 (x) cm FOV was focused on the tumour region. Total MPI signal and average iron per tumour were measured using Horos v4.0.0 RC5. Mice were euthanized and tumours were removed for ex vivo imaging.

Results: For imaging TAMs with the full FOV (Fig. 1A) we observed signal oversaturation from the liver region of the mouse and were unable to isolate and quantify signal from the tumour (Fig. 1B). This was solved using a FOV focused on the tumour region and the advanced reconstruction (Fig. 1C,D), which allowed MPI signal to be quantified for all tumours. There was no significant difference in MPI signal and average iron content

between the two tumours types (Fig. 1E, F). Additionally, no relationship was seen between tumour mass and iron content. Ex vivo imaging of tumours using MPI shows presence of signal in all tumours, confirming that signal observed in in vivo images is from tumours (Fig. 1G).

Conclusions: This work presents the first demonstration of in vivo imaging and quantification of TAMs using MPI. Ongoing histology will be used to validate the presence of iron-positive TAMs. This work also demonstrates the potential of MPI for other in vivo applications where dynamic range can cause limitations.

References: ¹Kelly et al. Br J Cancer. 1988, ²Zhou et al. Front Oncol. 2020, ³Daldrup-Link et al. Clin Cancer Res. 2011, ⁴Makela et al. Mol Imaging Biol. 2020. ⁵Konkle et al. PLOS ONE. 2015.

Monte Carlo Dosimetry Calculations of cellular S-values for ^{177}Lu and ^{225}Ac

T.T. Duong¹, C. Opera¹, S. Ghaseminejed^{1,2}, D. De Sarno¹, T.-Y. Lee^{1,2}

¹Lawson Health Research Institute and Robarts Research Institute, London, Ontario; ²Medical Biophysics, Western University.

Background: Targeted radionuclide therapy (TRT) utilizing beta or alpha-emitting radionuclides can treat metastatic cancer cells disseminated throughout the body, which are impossible to eradicate with surgery or external beam radiation therapy (EBRT). Although both ^{177}Lu and ^{225}Ac have been used for treating metastatic castration-resistant prostate cancer, clinical dosimetry is at best in the millimeter scale and may not capture the potentially heterogeneous dose distributions that microdosimetry could show; resulting in varying therapeutic results. The MIRDCell S-values¹ are traditionally used to calculate dose to different cell components including nucleus, cytoplasm, cell surface and whole cell resulting from activity deposited in any of the above listed components. Recently, the Monte Carlo code TOPAS (TOOl for PArTicle Simulation)-nBio² has been developed as an alternative to calculate these cellular doses. It has the advantage being more flexible in generating cell models. Moreover, it possesses the capability to simulate 3D tissue models, wherein cells and activities are distributed randomly throughout a specified tissue volume. As a prelude to applying 3D tissue models of TOPAS-nBio to investigate the microdosimetry of ^{177}Lu and ^{225}Ac treatment, this study aims to validate the cellular S-values calculated by TOPAS-nBio against those of MIRDCell software.

Materials and Methods: The single cell models used in this study consist of the nucleus and surrounding cytoplasm, represented by two homogenous concentric spheres of liquid water (density = 1 g cm⁻³). The respective radii of the nuclei and cells were (4 & 5 μm), (4 & 6 μm), and (4 & 8 μm). The radioactivity source was randomly distributed either in the cell surface, whole cell, cytoplasm, or nucleus. The cellular S values were calculated by TOPAS for five configurations (N ← N (nucleus), N ← Cy (cytoplasm), N ← Cs (cell surface), and N ← C (whole cell)) for ^{177}Lu and ^{225}Ac

radionuclides. The results were compared with S-values obtained with the MIRDCell software.

Results: Cellular S values for ^{177}Lu and ^{225}Ac are summarized in Table 1. The disparities between these values and MIRDCell S-values ranged from 4.03% to 12.44% for ^{177}Lu and 0.95% to 42.26% for ^{225}Ac . The absorbed dose from each decay of ^{225}Ac were approximately 115 times higher than that of ^{177}Lu .

Table 1: ^{177}Lu and ^{225}Ac Nuclear S-self values from an individual cell (GyBq⁻¹s⁻¹)

RC (μm)	RN (μm)	('Target' ← 'Source')	Nuclide Lu-177			Nuclide Ac-225		
			This study	MIRDCell	Deviation	This study	MIRDCell	Deviation
5	4	N ← Cs	4.12E-04	3.86E-04	6.86%	5.16E-02	5.06E-02	1.89%
		N ← Cy	5.93E-04	5.70E-04	4.03%	6.75E-02	6.69E-02	0.95%
		N ← N	1.83E-03	1.71E-03	6.83%	2.07E-01	1.47E-01	40.97%
		C ← Cs	6.58E-04	6.28E-04	4.70%	4.75E-02	6.36E-02	25.26%
		C ← C	1.08E-03	1.02E-03	5.92%	1.28E-01	9.47E-02	35.55%
6	4	N ← Cs	2.56E-04	2.32E-04	10.36%	3.38E-02	3.33E-02	1.36%
		N ← Cy	4.47E-04	4.04E-04	10.69%	5.45E-02	5.11E-02	6.70%
		N ← N	1.82E-03	1.71E-03	6.50%	2.07E-01	1.47E-01	40.98%
		C ← Cs	4.40E-04	4.15E-04	5.96%	3.39E-02	4.44E-02	23.58%
		C ← C	7.30E-04	6.71E-04	8.81%	7.99E-02	6.61E-02	20.86%
8	4	N ← Cs	1.34E-04	1.19E-04	12.44%	1.80E-02	1.83E-02	1.82%
		N ← Cy	2.57E-04	2.43E-04	5.69%	3.20E-02	3.31E-02	3.47%
		N ← N	1.79E-03	1.71E-03	4.83%	2.09E-01	1.47E-01	42.26%
		C ← Cs	2.33E-04	2.17E-04	7.36%	2.93E-02	2.53E-02	15.89%
		C ← C	3.82E-04	3.49E-04	9.57%	4.60E-02	3.76E-02	22.37%

Discussion: Monte Carlo calculations with TOPAS-nBio provide similar cellular S-values as MIRDCell for ^{177}Lu and ^{225}Ac . The differences between MC and MIRDCell may generally be attributed to discrepancies in the used nuclear databases. Furthermore, we have shown large disparities in the S values for ^{225}Ac N←N, which have been reportedly due to inherent limitations of using stopping power in MIRDCell's analytical calculations³. Further investigations into the underlying physics of ^{225}Ac decay and its interaction with cellular structures will be pursued in future research. Subsequent research endeavors will employ TOPAS-nBio in the analysis of multi-cell tissue models, aiming to quantify cellular absorbed dose, especially within the nucleus, to estimate the occurrence of double-strand breaks in DNA.

References: 1. Katugampola et al. *J Nucl Med.* 2022;63(9):1441-1449; 2. Schuemann et al. *Radiat Res.* 2019;191(2):125-138; 3. Goddu SM et al. *s. Society of Nuclear Medicine;* 2003.

MRI of bacteria: in vitro characterization of *Lactobacillus crispatus* ATCC33820 at 3T

Gabriel Varela-Mattatall^{1,2}, Sarah Donnelly¹,
Frank Prato^{1,2,3,4,5}, Gerald Moran⁶, Donna Goldhawk^{1,2,3}, Neil Gelman^{1,2,4}

¹ Imaging, Lawson Health Research Institute, London; ² Medical Biophysics, Western University, London; ³ Collaborative Graduate Program in Molecular Imaging, Western University, London; ⁴ Medical Imaging, Western University, London; ⁵ Physics & Astronomy, Western University, London; ⁶ Siemens Healthcare Limited, Oakville.

Introduction: Although the microbiome serves an important role in human health, there are few tools to reliably replicate the microbiome ex vivo due to its high complexity.¹ The ability to image bacteria with magnetic resonance imaging (MRI) has been previously explored in phosphate buffered saline (PBS) dilutions and indicates the potential for select bacteria to produce very high relaxation rates.² In this work, we characterize the bacteria *Lactobacillus crispatus* ATCC33820 (LC) diluted in stool samples to better simulate the intestinal tract, and we hypothesize that LC can influence relaxation rates from these samples at very low fractions of bacteria.

Methods: LC were cultured under standard conditions and washed with PBS, and then mixed with stool to generate 6 samples with fractions of [0, 6.25, 12.5, 25, 50, 100] % (volume/volume LC in stool). To examine relaxation rates as a function of LC/stool fractions samples were mounted in a 4% gelatin cell phantom³, and acquisitions were performed on a 3T MRI (Siemens Biograph mMR) with a 15-channel knee coil. The imaging protocol was: 1) variable-flip-angle (TE 1.63 ms, 8 flip angles (FAs) [5,10,...,40] °, TR 5 ms) to characterize R_1 ($1/T_1$); 2) multi-echo gradient-echo (9 TEs [1.92, 3.94, 6,...,25] ms, FA 10 °, TR 40 ms) to characterize R_2^* ($1/T_2^*$); and 3) single spin-echo (3 TEs [6.2, 12, 18] ms, TR 2 s) to characterize R_2 ($1/T_2$) for each sample. Parameters common for all sequences were: 0.5-0.6 mm in-plane, slice thickness 2 mm, and 3-4 averages. The model fitting was done with their corresponding non-linear models⁴, and in post-processing, we computed mean and standard error in regions-of-interest (approximately 100 voxels) for each sample and performed a t-test to evaluate significant differences.

Results: The t-tests showed a significant difference between stool alone and 6.25% LC/stool for R_1 , R_2 and R_2^* ($p < 0.001$ for all), indicating a very strong influence on relaxation rates even at low fractions. Figure 1 shows how these relaxation rates increased with LC fraction, but for R_1 and R_2^* this trend did not go beyond a fraction of 50%. The decreasing behavior on both R_1 and R_2^* curves was unexpected. Moreover, R_2' ($R_2^* - R_2$) shows its maximum at 50% LC/stool, which suggests an optimal fraction between bacteria and background media in terms of susceptibility-induced inhomogeneity.

Conclusion: LC are bacteria that exhibit a significant influence on relaxation rates when diluted in stool. Given the high relaxation rates from LC, we expect that the presence of these bacteria (or other lactobacilli high in manganese⁵) in the colon could potentially be detected within the background of colon contents, as these contents have lower relaxation rates than our current stool samples (e.g., R_1 of colon contents < 2 Hz vs ~ 10 Hz)⁶. Future work will expand the dilutions of LC in PBS and stool components to better simulate the contents of gastrointestinal tract for both standardization and sensitivity analysis. Our imaging protocol can be improved with shorter TEs for better characterization of relaxation rates at high fractions of LC/stool, and susceptibility quantification could explain changes in R_2^* and R_2' with LC fraction. In the future, in vivo imaging of the microbiome, through select bacteria, could improve our understanding of gut diseases.

References: [1] McDonald J. et al, J Microbiol Methods, 2013; [2] Donnelly S. et al, bioRxiv, 2022; [3] Sengupta A. et al, Front Microbiol, 2014. [4] Bidhult, S. et al, BMC Med Imaging, 2016; [5] Huynh, U. et al, ASM, 2021; [6] Wilkinson-Smith, V. et al, JPEN, 2018.

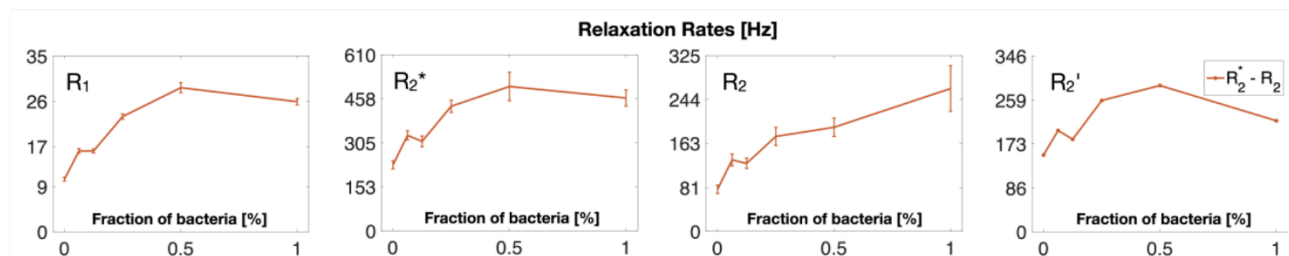


Figure 1- Relaxation rates of LC in fecal samples. Mean and standard error of relaxation rates, and field inhomogeneities (R_2') as a function of the fraction of bacteria. We attribute the slight shift at the 12.5% sample as human error during sample preparation.

PET imaging neuroinflammation with COX-1 targeted [¹¹C]PS13 in mouse models of multiple sclerosis.Amanda J. Boyle^{1,2}, Emily Murrell¹, Andrea Narvaez¹, Junchao Tong^{1,2}, and Neil Vasdev^{1,2}.¹Azieli Centre for Neuro-Radiochemistry, Brain Health Imaging Centre, Centre for Addiction and Mental Health (CAMH), Toronto, ON²Department of Psychiatry, University of Toronto, ON

Introduction: Multiple sclerosis (MS) is an autoimmune disorder of the central nervous system (CNS) caused by chronic neuroinflammation which leads to demyelination and neurodegeneration. MS can only be diagnosed following the onset of severe clinical symptom attacks when extensive demyelination and degeneration are present. Neuroinflammation in MS precedes the onset of clinical symptoms, therefore, molecular imaging of neuroinflammation has the potential for early diagnosis of MS. Cyclooxygenase-1 (COX-1) overexpression in microglial cells (resident macrophages of the brain) has been linked to disease progression in mouse models of MS. [1] [¹¹C]PS13 is a brain penetrating, highly potent and selective COX-1 PET radiotracer. [2] We hypothesize that [¹¹C]PS13 will detect changes in COX-1 density in mouse models of MS.

Methods: Automated radiosynthesis of [¹¹C]PS13 was performed as previously described [3]. PET/MR imaging of COX-1 was performed in a standard mouse model of MS, experimental encephalomyelitis autoimmune (EAE) mice (n=2), and wildtype (WT) mice (n=2); 8-12 weeks old females. Clinical symptoms were assessed by standard EAE scoring, and mice with clinical scores greater than 3 underwent PET/MR imaging.

Results & Discussion: The uptake of radioactivity following injection with [¹¹C]PS13 was higher in EAE mice compared to WT in all regions of the brain (Fig 1A), indicated by time-activity curves extracted from whole brain (Fig 1B). The brain regions where the highest accumulation of radiotracer was observed was the hippocampus with a slight trend in increased tracer accumulation in EAE compared to WT mice (Fig 1B). The greatest difference in uptake between EAE and WT mice was observed in the sacral spinal cord (SC) region (Fig 1C) and the cerebellum (Fig 1D). An increase in uptake in the cerebellum was observed in EAE mice compared to WT (0.38 ± 0.01 vs. 0.51 ± 0.04 SUV at 50 min; n=2, $p = 0.0492$). This preliminary data shows that [¹¹C]PS13 uptake is increased in EAE mice compared to WT mice and justifies further studies with this radioligand. Experiments underway include PET imaging with male EAE and male WT mice, as well as immunostaining to confirm that increased uptake of tracer correlates with increased COX-1 density, and autoradiography to validate the specific binding of [¹¹C]PS13 to COX-1 in EAE mice. Longitudinal PET/MR studies are planned to assess the potential of [¹¹C]PS13 to detect changes in COX-1 density in EAE mice prior to the onset of clinical symptoms.

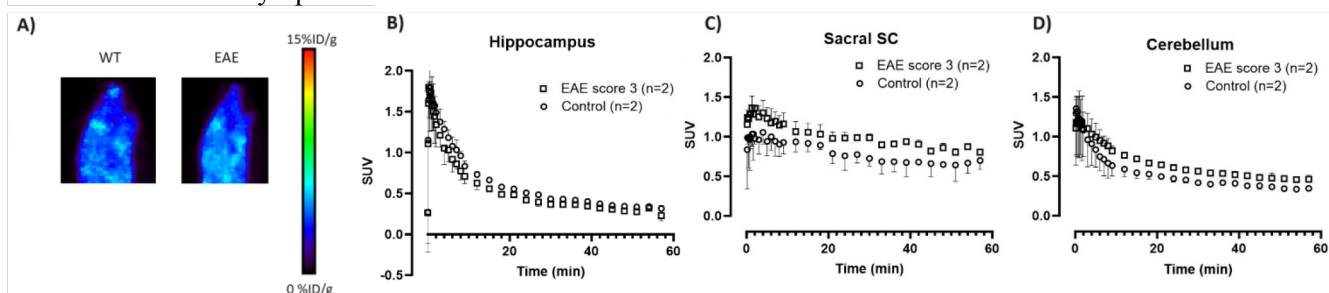


Fig. 1. A) PET images of the COX-1 PET radioligand, [¹¹C]PS13, in WT and EAE mice (score = 3) and associated time-activity curves extracted from B) hippocampus, C) sacral SC, and D) cerebellum regions of interest.

Conclusions: [¹¹C]PS13 is a promising tool for PET imaging neuroinflammation in MS, and despite overall low brain uptake in rodents compared to non-human primates we hope to demonstrate the potential of [¹¹C]PS13 in detecting changes in COX-1 density. We plan to translate [¹¹C]PS13 for clinical studies at CAMH.

References: [1] Deininger MH and Schluesener HJ. Cyclooxygenases-1 and -2 are differentially localized to microglia and endothelium in rat EAE and glioma. *J Neuroimmunol.* **1999**;95(1):202-208. [2] Kim et al. Evaluation of two potent and selective PET radioligands to imaging COX-1 and COX-2 in rhesus monkeys. *J Nucl Med.* **2018**;59:1907-1912. [3] Boyle AJ, et al. Repurposing [¹¹C]PS13 for PET imaging of cyclooxygenase-1 in ovarian cancer xenograft mouse models. *J Nucl Med.* **2021**;62(5):665-668.

Novel Hyperpolarized ^{129}Xe R3-Noria-methanesulfonate Supramolecular Cage at 3.0 T MRI

Viktoriia Bataarchuk^{1,2}, Yurii Shepelytskyi^{1,2}, Vira Grynko^{2,3}, Carson Hasselbrink⁴, Antal Halen Kovacs⁵, Aaron Hodgson⁶, Karla Rodriguez¹, Ruba Aldossary², Tanu Talwar¹, Brenton DeBoef⁷, Mitchell S. Albert^{1,2,8}

¹Chemistry Department, Lakehead University, Thunder Bay, Canada, ²Thunder Bay Regional Health Research Institute, Thunder Bay, Canada, ³Chemistry and Materials Science Program, Lakehead University, Thunder Bay, Canada, ⁴California Polytechnic State University, San Luis Obispo, USA, ⁵Applied Life Science Program, Lakehead University, Thunder Bay, Canada, ⁶Physics Program, Lakehead University, Thunder Bay, Canada, ⁷University of Rhode Island, Kingston, USA, ⁸Northern Ontario School of Medicine, Thunder Bay, Canada

Introduction: In the setting of molecular magnetic resonance imaging (MRI), the development of a contrast agent that overcomes the drawbacks of conventional MRI and provides high sensitivity holds significant promise for clinical applications. Hyperpolarized (HP) ^{129}Xe MRI is highly effective for functional lung and brain studies¹⁻³ and is emerging as a promising modality for molecular imaging⁴. In the present work, we introduce a novel first-in-kind water-soluble supramolecular cage – resorcinarene trimer methanesulfonate (R3-Noria-MeSO₃H) macrocycle – that has demonstrated two superior contrast mechanisms for HP ^{129}Xe MRI, resulting from an increase in the effective spin-spin relaxation and hyperpolarized chemical exchange saturation transfer (HyperCEST).

Methods: The study was conducted using a clinical Philips Achieva 3.0T MRI and a custom-built dual-tuned $^{129}\text{Xe}/^1\text{H}$ quadrature coil. R3-Noria-MeSO₃H was synthesized following established procedures⁵. Various samples of R3-Noria-MeSO₃H (0 mM, 1 μM , 5 μM , 0.01 mM, 0.05 mM, 0.1 mM, 1 mM, 2.5 mM, and 5 mM) in deionized water (DI H₂O), phosphate buffer saline (PBS), and saline were prepared. 1L of ^{129}Xe , polarized up to 56% using a commercial XeBox-10E (Xemed LLC) polarizer, was placed in a chamber and connected to a glass-fritted cell with 3 mL of the solution, allowing continuous flow. The MR spectroscopy (MRS) and HP ^{129}Xe MR GRE imaging (FOV= 125x125x20 mm³; TR/TE = 7.1 ms/2.15 ms; FA = 20^o, BW = 150 Hz/pixel) were performed on all samples. HP ^{129}Xe spectra were fitted with a 2-Lorentzian peak model, the chemical shift (CS), full-width-half-maximum (FWHM), and T₂^{*} were calculated. The image SNR was calculated as the mean signal value in a ROI within the frit phantom divided by the standard deviation of noise in a similar ROI in the background. To explore the HyperCEST effect, we conducted HyperCEST MRS and depletion spectra⁶, followed by HyperCEST imaging. Thus, a pair of HP ^{129}Xe images was obtained, utilizing depolarization pulses (16x30ms 3-lobe-sinc of 1200^o FA) applied at -100ppm for off-resonance and at +87ppm for on-resonance images. Pixel-wise recalculations were performed to generate SNR maps, which were thresholded and recalculated into HyperCEST depletion maps.

Results: The ^{129}Xe intensities were normalized to the pure solvent, and below 0.1 mM for DI H₂O and PBS no significant changes have been observed. However, a pronounced decline occurred at higher concentrations. Unlike the ^{129}Xe signal in PBS and DI H₂O, the signal in saline steadily decreased across all concentrations. Moreover, the dissolved-phase HP ^{129}Xe resonance in all solvents shifted linearly downfield as concentrations increased. The strongest downfield shift was observed in DI H₂O with a CS change rate of 2.76 \pm 0.24 ppm/mM. The dissolved-phase HP ^{129}Xe resonance demonstrated a weaker shift in PBS and saline with 2.26 \pm 0.08 ppm/mM and 1.93 \pm 0.03 ppm/mM, respectively. The HP ^{129}Xe peak FWHM increased non-linearly for concentrations above 0.1 mM. This indicates a significant ^{129}Xe T₂^{*} relaxation time shortening by a factor of 5.7, 6.8, and 5.9 for DI H₂O, PBS, and saline respectively. A HyperCEST effect was detected in all samples and showed an initial linear increase with concentration, plateaued, and started decreasing at the highest concentration. In DI H₂O, R3-Noria-MeSO₃H it was demonstrated at concentrations starting from 1 mM (Fig 1B). A maximum depletion of 70% in DI H₂O was observed at +90 ppm in 5mM. For PBS and saline, it was detected from 0.05 mM at +87 ppm.

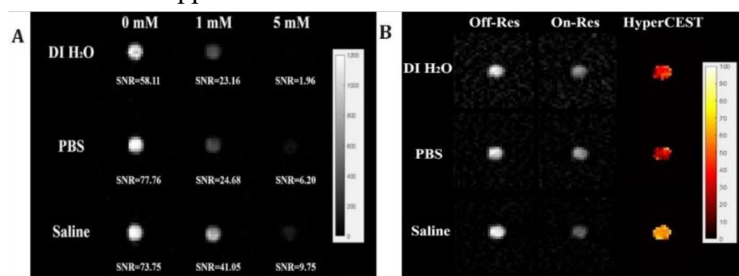


Figure 1. (A) HP ^{129}Xe in control, 1mM, 5mM and (B) HyperCEST images in 1mM of R3-Noria-MeSO₃H for DI H₂O, PBS, and saline solutions

Conclusions: The novel R3-Noria-MeSO₃H serves as a novel source of robust negative contrast for HP ^{129}Xe MRI and as a superior supramolecular cage for ^{129}Xe HyperCEST molecular imaging. The in vitro HyperCEST detectability limit, determined using a clinical 3.0T MRI, was found to be 50 μM , highlighting its potential for future clinical applications. However, conducting toxicity studies is essential to facilitate a successful transition to clinical studies, which will be a focus of future work.

Acknowledgments: This research was supported by a Natural Science Engineering Research Council Discovery grant (RGPIN-2017-05359), an Ontario Research Fund grant (ORF RE 09 029), and a MITACS Accelerate Grant (IT31144).

References: ¹Albert *et al.* "Biological magnetic resonance imaging using laser-polarized ^{129}Xe ." *Nature* 370.6486 (1994); ²Matheson *et al.* "Persistent ^{129}Xe MRI pulmonary and CT vascular abnormalities in symptomatic individuals with post-acute COVID-19 syndrome." *Radiology* 305.2 (2022); ³Shepelytskyi Y. Medical applications of ^{19}F and hyperpolarized ^{129}Xe magnetic resonance imaging. Diss. 2020; ⁴Schröder L. "Xenon Biosensor HyperCEST MRI." *Hyperpolarized and Inert Gas MRI*. Academic Press, 2017; ⁵Hasselbrink *et al.* "Development and Application of a Supramolecular Brønsted Acid Catalyst Based on the Noria Macrocycle." *The Journal of Organic Chemistry* 87.23 (2022); ⁶Grynko *et al.* "Cucurbit[6]uril Hyperpolarized Chemical Exchange Saturation Transfer Pulse Sequence Parameter Optimization and Detectability Limit Assessment at 3.0 T." *ChemPhysChem* 24.23 (2023).

Session 20 Pitches: Ultrasound and Optical Abstracts

Multi-Objective Multiple Instance Learning for Improving Prostate Cancer Detection in Ultrasounds

Mohamed Harmanani¹, Paul F. R. Wilson¹, Fahimeh Fooladgar², Amoon Jamzad¹,
Mahdi Gilany¹, Minh Nguyen Nhat To², Brian Wodlinger³, Purang Abolmaesumi², Parvin Mousavi¹

¹Queen’s University, Kingston, ON, Canada ²University of British Columbia, Vancouver, BC, Canada

³Exact Imaging, Markham, ON, Canada

INTRODUCTION:

Deep learning is typically used to detect prostate cancer (PCa) in small regions of interest (ROI) extracted from a needle trace region of the ultrasound image of a biopsy core. This approach suffers from weak labeling: ground-truth

histopathology labels

describe tissue properties of the entire biopsy core, and ROI labels are only an approximation of the true distribution of cancer. Multiple instance learning (MIL) approaches to PCa detection from ultrasound have recently been proposed as a solution [1] by leveraging

contextual information in multiple patches. In this work, we improve the performance of MIL models by introducing a novel learning objective that takes advantage of both Core-scale and ROI-scale predictions.

METHODS: We use 6607 biopsy cores collected from 693 patients who underwent prostate biopsy in five centers under the guidance of Trans-rectal ultrasound (TRUS). To mitigate label imbalance, we undersample the benign cores during training in order to ensure the dataset has an equal amount of benign and cancerous cores. We compare 2 models for ROI feature extraction: the ResNet18 [2] and the Compact Convolutional Transformer (CCT) [3]. We pre-train each model using self-supervised learning [4], then finetune them on the task of ROI-scale PCa detection. We then use the models as feature extractors and train a MIL feature aggregator on top of the extractor’s learned representations, using both cross-entropy (CE) loss and multi-objective (MO) loss. This workflow is shown in Figure 1. **RESULTS:** Our results are shown in Table 1. Among ROI-scale baselines with linear finetuning, the ResNet18 model achieves the highest Area Under the ROC Curve (AUROC). Both MIL models outperform the ROI-scale baselines, with the MO+MIL model obtaining the highest AUROC and Balanced Accuracy scores of 77.9 and 71.1 respectively.

CONCLUSION: Multi-objective learning combined with MIL has the potential to improve PCa detection in ultrasound data. **REFERENCES:** [1] Gilany et al., IJCARS 2023 [2] He et al., CVPR 2016 [3] Hassani et al., arXiv preprint [4] Bardes et al., ICLR 2022

Figure 1. A general pipeline for multi-objective MIL with a Transformer

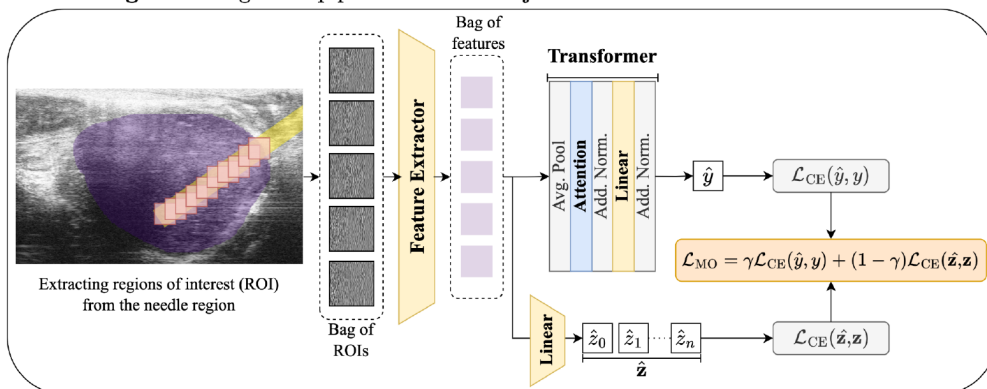


Table 1. Comparison of our method to various MIL and ROI-scale baselines

Extractor + Finetuner	Loss	AUROC	Bal. Accuracy	Sensitivity	Specificity
CCT + Linear	$\mathcal{L}_{CE}(\hat{z}_i, z_i)$	74 ± 4	69 ± 3	71 ± 7	66 ± 5
ResNet18 + Linear	$\mathcal{L}_{CE}(\hat{z}_i, z_i)$	76 ± 4	68 ± 3	65 ± 6	74 ± 4
CCT + MIL	$\mathcal{L}_{CE}(\hat{y}, y)$	71 ± 4	62 ± 3	62 ± 3	62 ± 3
ResNet18 + MIL	$\mathcal{L}_{CE}(\hat{y}, y)$	77 ± 2	64 ± 2	67 ± 27	57 ± 22
CCT + MO+MIL (ours)	\mathcal{L}_{MO}	72 ± 3	63 ± 3	53 ± 14	73 ± 9
ResNet18 + MO+MIL (ours)	\mathcal{L}_{MO}	78 ± 3	71 ± 6	76 ± 12	66 ± 20

A Four-Dimensional Ultrasound System for Assessing Ligament Laxity in Basal Thumb Osteoarthritis

Randa Mudathir^{a,b}, Megan Hutter^{a,b}, Carla du Toit^a, Assaf Kadar^{b,c}, Emily Lalone^{b,c}, Aaron Fenster^{a,b}

^aRobarts Research Institute, 100 Perth Drive, London, ON, Canada N6A 5K8

^bWestern University, 1151 Richmond Street, London, ON, Canada N6A 3K7

^cRoth McFarlane Hand & Upper Limb Centre, London, ON, Canada N6A 4V2

Introduction: Hypermobility, or joint laxity, has been hypothesized to be a risk factor for thumb osteoarthritis (OA) [1]. Previous studies assessing thumb biomechanics in thumb OA patients have utilized various imaging modalities including radiography, magnetic resonance imaging, computed tomography imaging, and ultrasound. However, these imaging techniques provide limited information on joint laxity during motion. However, four-dimensional ultrasound (4DUS) can detect joint laxity by visualizing the thumb's stabilizing ligaments during motion. Hence, this work utilizes a novel 4DUS imaging system to characterize the degree of joint laxity associated with varying stages of thumb OA progression.

Methods: A 4DUS system consisting of a motorized semi-submerged transducer assembly was developed. A high frequency transducer was automatically translated laterally back and forth along the location of the thumb joint. Five healthy volunteers and five thumb osteoarthritis patients were recruited to validate the system's capability to resolve the thumb's dorsoradial ligament during motion. 4D images of thumb abduction were collected from each participant. The images were reviewed by an MSK radiologist to confirm the anatomy of interest. 4DCT images of the same motion were acquired from each of the patients to be registered to the 4DUS images to validate the 4DUS system's capability to detect bony landmarks throughout motion. Each 4DUS image contained ten 3D volumes, and the distance between the bones of the thumb joint along with the length of the dorsoradial ligament in each volume were measured to characterize ligament laxity. These measurements were repeated multiple times over the course of two weeks to test for intra-rater and inter-rater reliability. Intra- and inter-class correlation coefficients were calculated to determine the reproducibility of the measurements.

Results: The lengths of the dorsoradial ligament from the 4DUS scans indicate a change in ligament length throughout thumb abduction in patients. The average maximum length of the dorsoradial ligament in the healthy cohort and patient cohort was 12.76 and 15.53 mm, respectively. Registration of the 4DCT images to the 4DUS images validated the 4DUS system's capability to detect bony landmarks, such as the base of the first metacarpal and the bony angulation of the trapezium, throughout motion. With intraclass and interclass correlation coefficients greater than 0.9, the ligament length measurements indicate excellent repeatability.

Conclusion: In this preliminary study, a novel 4DUS system for the assessment of ligament behavior during thumb motion was developed, and its reliability and reproducibility were tested. This system will be used in a larger cohort of thumb OA patients to evaluate a) the patterns of ligament laxity associated with various stages of disease progression and b) whether there are sex-differences in ligament laxity. This imaging system will provide a more robust explanation of the morphological changes to the thumb's stabilizing ligaments that influence the onset and progression of thumb OA. This will aid clinicians in detecting patients' predisposition to thumb OA and allow for the development of joint protection techniques to target patients with increased joint laxity.

References: [1] H.E. et al. (2015). In vivo recruitment patterns in the anterior oblique and dorsoradial ligaments of the first carpometacarpal joint. *Journal of Biomechanics* 48 (10); p. 1893-1898.

Realization of automated whole breast 3D Doppler ultrasound for characterization of breast lesions

A. Aziz^{1,5}, R. Abdul Rahman², C. K. S. Park³, T. Trumpour^{4,5}, J. Bax⁵, L. Gardi⁵, D. Tessier⁵, K. Barker⁵, T. Poepping², A. Fenster^{2,4,5}

¹Department of Biomedical Engineering, ²Department of Physics & Astronomy, Western University, ³Division of Medical Physics and Biophysics, Department of Radiation Oncology, Brigham and Women's Hospital and Dana-Farber Cancer Institute, Harvard Medical School, Boston MA, United States, ⁴Department of Medical Biophysics, ⁵Robarts Research Institute, Western University, London ON, Canada

Introduction: Breast cancer is the most common cancer in women worldwide, causing 685,000 deaths annually. Timely diagnosis is crucial for reducing mortality. While mammography is the gold standard in breast cancer screening, it has reduced sensitivity in women with dense breasts, often requiring supplemental imaging which may be inaccessible in underserved communities. Hence, a need exists for accessible, cost-effective, point-of-care technologies for the early diagnosis of breast cancer, especially for underserved populations and women with dense breasts. Conventional ultrasound (US) is widely accessible but has limitations in breast cancer screening, especially for grading tumour severity. Doppler US, specifically Power Doppler (PD) and superb microvascular imaging (SMI), may provide superior information on tumour aggressiveness and histological grade. Thus, our group developed a 3D automated breast ultrasound (ABUS) device with built-in Doppler visualization capabilities to facilitate definitive diagnosis of breast cancer in limited resource settings. [1] The objective of this work was to characterize the Doppler capabilities of the system.

Methods: The 3D ABUS device is compatible with any commercially available US system and is comprised of a custom-designed 3D-printed dam conforming to patient anatomy, an adjustable compression assembly to stabilize the breast, and a mechanically-driven scanning mechanism. To test the system, a Canon Aplio i700 US system (Canon Medical Systems, Tochigi, Japan) and a high-resolution 14L5 (10 MHz) linear transducer were used. A workstation capable of real-time image acquisition, 3D US reconstruction, and multiplanar visualization was also developed. [2] The software was modified to identify coloured pixels in order to accommodate for Doppler acquisitions. Hardware and software capabilities for 3D Doppler were developed and tested with a custom-designed non-anatomical flow phantom. The 3D-printed vessel was embedded in a colloidal agar-based background material, enriched with glycerol and cellulose to simulate acoustic properties and backscattering of breast tissue. Blood-mimicking fluid (Shelley Medical Imaging Technologies, London, Ontario, Canada) was pumped through the phantom, and collected 2D images were reconstructed into a 3D Doppler image in real-time for evaluation.

Results: Figure 1 shows the first-ever proof-of-concept flow phantom 3D ABUS images, demonstrating the feasibility of 3D Doppler imaging. Importantly, this demonstrates the ability of the 3D ABUS system to reconstruct images in 3D using both PD and SMI Doppler US, which has not been demonstrated with commercially available systems. Figure 1 clearly demonstrates flow of fluid through the phantom as its volume is fully saturated with Doppler signal. The 3D Doppler image of the vessel mimic can also be dynamically viewed at any oblique and non-oblique view.

Conclusions: We successfully developed an automated, cost-effective, portable, and patient-dedicated 3D ABUS system capable of 3D PD and SMI imaging. These results demonstrate potential to improve the characterization of breast cancers, especially in limited-resource and increased-risk populations, including those with dense breasts. These capabilities would enable earlier detection, diagnosis, and increase the likelihood of survival in populations impacted with breast cancer. The code implemented in this study is available upon request; please contact A. Fenster at afenster@robarts.ca for access.

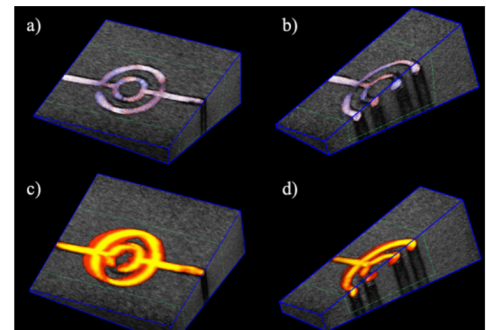


Fig. 1: 3D Doppler ABUS images of the flow phantom with a) transverse and b) coronal views of SMI signal, and c) transverse and d) coronal views of PD signal.

[1] Aaron Fenster, Jeffrey Bax, David Tessier, and Claire K S Park, US Provisional Patent 63/335,857, 2022. [2] Park, C. K. S. et al., Medical Imaging 2023: Ultrasonic Imaging and Tomography, 12470, 8–14, 2023.

Plane Wave Approaches with Dual-Frequency Arrays for Superharmonic Contrast Imaging

Jing Yang^{1,2}, Emmanuel Chérin², Jianhua Yin², Paul A. Dayton³, F. Stuart Foster^{1,2}, and Christine E.M. Démoré^{1,2}, ¹University of Toronto, Toronto, Canada, ²Sunnybrook Research Institute, Toronto, Canada, ³Joint Department of Biomedical Engineering, University of North Carolina and North Carolina State University, Chapel Hill, NC, USA

Introduction

Superharmonic imaging (SpHI) using dual-frequency (DF) transducers enables high-contrast microvasculature imaging. This technique takes advantage of the broadband nonlinear response of the microbubble (MB) contrast agent and utilizes the higher order harmonics for image reconstruction, thus suppressing tissue clutter. Previous SpHI demonstrations are limited to stationary or slow flow imaging due to the low acquisition rate with walking-aperture approaches. Plane wave imaging approaches are investigated to overcome the challenge. We previously introduced a DF probe with a low-frequency (LF; 2 MHz; 32 elements) array behind a high-frequency (HF; 21 MHz; 256 elements) array, and demonstrated HF plane wave (HFPW) imaging where improved frame rate and image contrast were observed compared to walking-aperture imaging. We also presented beam steering with the LF array. Here, we investigate 2D and 3D SpHI and evaluate image contrast *in vitro* and *in vivo*.

Methods

Two VevoF2 systems (VADA-mode; FUJIFILM Visualsonics, Toronto) were used to drive LF and HF arrays for SpHI; systems were synchronized by initiating LF transmit via triggers from HF system, and delaying the start of HF receive. Element-specific delays were programmed for LF aperture to steer beams at 9 angles ($\pm 10^\circ$, $\pm 7.5^\circ$, $\pm 5^\circ$, $\pm 2.5^\circ$ and 0°). Data were captured on 64 HF channels; 4 receive events were required for a full frame. *In vitro* SpHI was performed on a tissue-mimicking phantom (2 wt% agar; 1 wt% silica) with a 1.27 mm diameter channel. 2D images of the water- or contrast-filled channel and the matrix were acquired in SpHI and HFPW imaging. *In vivo* SpHI of a mouse breast cancer tumor xenograft was performed prior to and after contrast injection; 3D data sets were acquired. Image contrast *in vitro* was computed as $20\log_{10}(\overline{E}_c/\overline{E}_t)$ where \overline{E}_c and \overline{E}_t are the mean signal envelopes in the contrast-filled channel and the matrix.

Results

All *In vitro* SpHI frames (Figure 1A) showed almost complete suppression of backscattered signals from the tissue-mimicking matrix to the background noise level. Image contrasts of 23.5 and 26 dB were found for the MB-filled channel in the 0° and compounded SpHI frames, respectively; 6.5 dB was found for the HFPW image. For *in vivo* mouse tumor imaging (Figure 1B), SpHI images revealed vascular structures and tumor perfusion. SpHI acquisition frame rate reached 3.5 kHz at 0° and reduced to 396 Hz with 9 Tx angles, which was still ~ 40 times that of previously used walking-aperture approaches (~ 10 Hz). 3D acquisitions took < 30 seconds over the 12 mm motor range covering the tumor volume. These results demonstrated that plane wave imaging approaches can improve SpHI frame rate while maintaining a high image contrast.

Conclusion

We implemented plane wave imaging approaches for SpHI with improved acquisition frame rates while maintaining image contrasts for vascular visualization, enabling the potential of SpHI in fast flow imaging. The ultrafast acquisition is also important for advanced techniques such as super resolution imaging or ultrasound localization microscopy.

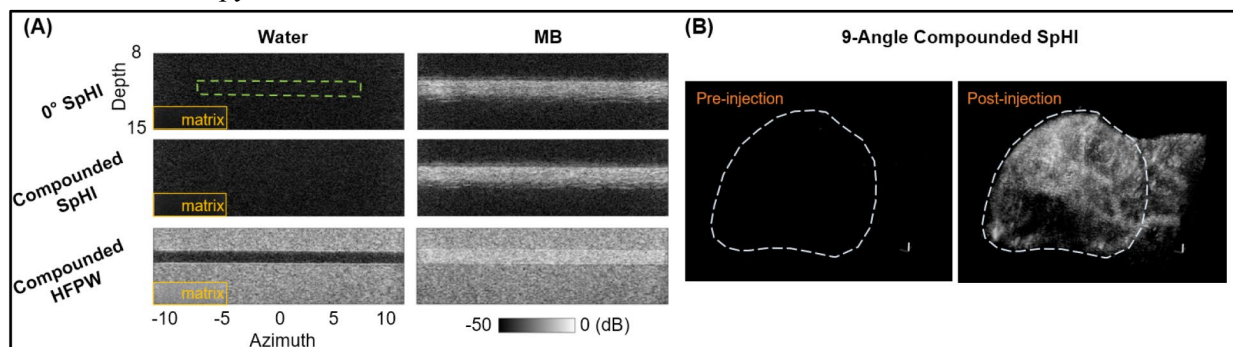


Figure 1: **A)** Images panel of water- and contrast-filled channel acquired by SpHI (0° and 9-angle compounded) and HFPW imaging (25-angle compounded; up to $\pm 11.76^\circ$, increment: 0.98°). Images of the tissue-mimicking matrix are shown as insets. A ROI for contrast computation is shown. Images are normalized to the peak contrast signal found in each imaging mode. Axes are shown in millimeters. **B)** Maximum-intensity-projections of volume-rendered 3D SpHI data sets of a subcutaneous breast cancer tumor xenograft prior to and after MB contrast injection. The tumor volume is delineated with a dashed line. Scale bars along the 3 orthogonal axes shown at the bottom right represent 1 mm.

Color Doppler Ultrasound for the Diagnosis of Placenta Accreta Spectrum Using Fused Texture Features from Multiple Domains

Dylan Young^{1,2}, Naimul Khan¹, Sebastian R Hobson^{1,3,4}, Dafna Sussman^{1,2,3*}

¹Department of Electrical, Computer and Biomedical Engineering, Toronto Metropolitan University, Toronto, Canada; Institute for Biomedical Engineering, Science and Technology (iBEST) at Toronto Metropolitan University
²St. Michael's Hospital, Toronto, Canada & Keenan Research Centre for Biomedical Science, St. Michael's Hospital. ³Department of Obstetrics and Gynaecology, Faculty of Medicine, University of Toronto, Toronto, Ontario, Canada. ⁴Department of Obstetrics and Gynaecology, Mount Sinai Hospital, Toronto, Ontario, Canada.

Introduction: Placenta accreta spectrum (PAS) disorders are a result of abnormal invasion of the placenta into the Nitabuch fibrinoid layer of the placental-endometrial interface and beyond [1]. Abnormal adherence to the uterine wall upon delivery can lead to massive haemorrhage or even maternal death [2]. Published mortality rates are 7%, and may reach up to 30% in cases without prenatal diagnosis [3]. Ultrasound is the primary imaging modality for PAS diagnosis, but the lack of universal experience and standardized descriptors for the disease poses considerable challenges in its diagnosis [2]. Recent studies reveal global disparities in diagnosing and managing PAS, as clinicians in underserved centers, especially in low- and middle-resource countries, may lack the expertise for routine diagnosis [4]. This study seeks to advance current research by integrating color Doppler (CD) ultrasound texture features for the automatic diagnosis of PAS, specifically by identifying texture features linked to the disease. This novel approach involves the development of a 'discriminative index' (DI) produced by a linear classifier to generate disease predictions, outperforming classical machine learning (ML) techniques.

Methods: We acquired 147 trans-abdominal CD ultrasound images from patients from a single center in Toronto, Canada, each displaying the midsagittal view of the placenta and its myometrial interface. These were split into 98 PAS and 49 non-PAS (placenta previa) cases. Among these, 49 images each were selected randomly as PAS and non-PAS controls. For each image, the placental tissue was identified by an expert maternal fetal medicine specialist, and a region of interest was acquired. 351 different texture features were extracted from each individual grayscale, RGB and HSV channel in an attempt to preserve any features that may be related to the disease (1760 features total). After preprocessing and outlier removal, the data were divided into 75% training/validation and 25% testing sets. The optimal subset of 15 features was determined through a two-step process: initial ranking and elimination based on Fisher's ratio, followed by additional subset refinement using extra trees regression.

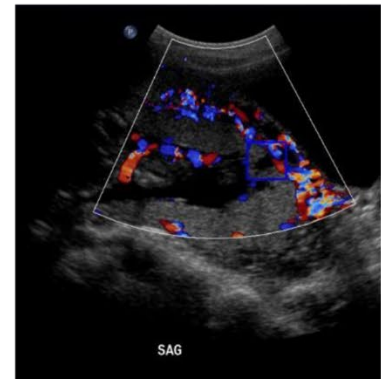


Fig. 1. Sample CD image for patient with PAS.

Results: The highest performing ML model (AdaBoost) developed using the 15 features subset yielded an 80% test accuracy and $80 \pm 14\%$ 5-fold cross validation (CV) accuracy. Conversely, the DI method achieved test and 5-fold CV accuracies of 88% and $85 \pm 9\%$, respectively. Notable features included in the feature subset were variance (HSV), Zernike's moments radius (RGB), and a number of gray-level co-occurrence matrix and discrete wavelet transform features. These signify the effectiveness of discriminant texture features for accurate disease detection without the need for artificial intelligence-based tools.

Conclusion: This study highlights the effectiveness of CD image-derived texture features in detecting PAS. Automated tools in clinical sonography could mitigate existing limitations, given the absence of published research on texture features for PAS diagnosis using ultrasound alone. Ongoing research aims to connect discriminant texture features with established clinical markers, reducing expert dependence and enabling standardized quantification of sonographic criteria for PAS identification. This has the potential to improve global diagnostic management, irrespective of resource availability.

References: [1] Fonseca A, Ayres de Campos D. Best Pract Res Clin Obstet Gynaecol. 2021 Apr;72:84–91. [2] Kaelin Agten A, Jones NW. Obstetrics, Gynaecology & Reproductive Medicine. 2019 Jul 1;29(7):189–94. [3] Nieto-Calvache AJ, et al. AJOG Glob Rep. 2021 Aug;1(3):100012. [4] Brown AD et al. International Journal of Gynecology & Obstetrics. 2022;158(1):129–36.

Multimodal scattering agent for the development of training phantoms: Finding a substitution for Talc.

Joeana Cambranis^{a,d}, Emma Zhang^b, Olivia Qi^b, Shuwei Xing^{a,d}, Terry M. Peters^{a,b,c,d}, and Elvis C. S. Chen^{a,b,c,d,e}

^aSchool of Biomedical Engineering, ^bSchulich School of Medicine & Dentistry, ^cRobarts Research Institute, ^dDepartment of Medical Biophysics, ^eDepartment of Electrical and Computer Engineering, Western University, London, Ontario, Canada

Introduction: The development of training phantoms for image-guided needle puncture procedures is an ongoing field. The need for a training phantom to present anthropomorphic features, both imaging and physical characteristics, is an important part of their development. Polyvinyl Alcohol cryogel (PVA-c) is a non-toxic, hyperbolic and synthetic polymer widely used as the base for phantom bodies, thanks to its longevity, low cost, structural stability and mechanical behaviour.¹ Talc is often used as a scattering agent since it provides speckle and backscatter² and is relatively easy to mix with PVA-c. In addition, Talc has compatibility with multiple imaging modalities (Ultrasound (US) and Computed Tomography (CT))³. Recently, it was discovered that Talc contains amphibole asbestos, making it a carcinogen.⁴ This discovery calls for finding a substitute for Talc in the development of PVA-c multimodal phantoms. In this work, we present a scattering agent of low-cost, easy-to-obtain, which shares multimodality similarities with Talc.

Methods: PVA-c-based sample phantoms were created using a 10% w/w ratio. All samples underwent five Freeze-Thaw Cycles (FTC) as described in Chazot, et al., (2022)³ to obtain the same stiffness and imaging results. Scattering agents were added to the samples using different concentrations during three experiments. For experiment one, baking soda and glass spheres were tested in concentrations of 5%, 1% and 0.5% w/w. Experiment two consisted of testing baby powder (principal ingredient: potato starch), Zinc oxide powder, Cinnamon powder and MICA powder using a concentration of 0.5% on each sample. The concentration was chosen after the qualitative results of experiment one. Finally, experiment three tested a larger range of percentages of baby powder (7.5%, 5%, 3%, 1%, 0.5% and 0.3%) to analyze the differences. For each experiment, US (Canon Medical Systems, Aplio i700, transducer i8CX1), and CT (Canon Medical Systems, Aquilion ONE) were acquired using an abdomen protocol. All sample scans were qualitatively compared against the scans of a Talc sample of 7.5%, as previously used in a liver phantom development.³

Results: Among all scattering agents, non-talc-baby and Zinc powders presented the best qualitative results under US imaging. The results were smooth and did not present shadowing or very bright edges as observed with other agents. Under CT, all scattering agents were visible, however, non-talc-baby powder and baking soda were the most similar to Talc scans. Figure 1 shows the scans of the Talc and non-talc-baby powder samples (7.5% each), both looking very similar in both modalities.

Conclusion: Non-talc-baby powder was the one agent that complied with the characteristics needed in all imaging modalities. This agent promises to be an excellent substitution for Talc to use as a scattering agent for PVA-c phantom constructions. Future work includes more testing of the non-talc-baby powder samples, specifically their lifespan, including needle puncture and shelf life. Magnetic resonance imaging (MRI) for all samples is already planned and expected to be performed soon. Similar results are expected from the MRI samples.

References: [1] Li, P., et al., (2018). Tissue mimicking materials in image-guided needle-based interventions: A review. *Materials Science and Engineering*. [2] Taghizadeh, S., et al., (2018). Development of a Tissue-Mimicking Phantom of the Brain for Ultrasonic Studies. *Ultrasound in Medicine and Biology*. [3] Chazot, N., et al., (2022). Development of a multi-modal liver phantom with flow for the validation and training of focal ablation procedures. *Medical Imaging 2022: Image-Guided Procedures, Robotic Interventions, and Modeling*. [4] Stoiber, T., et al., (2020). Asbestos Contamination in Talc-Based Cosmetics: An Invisible Cancer Risk. *Environmental Health Insights*, 14.

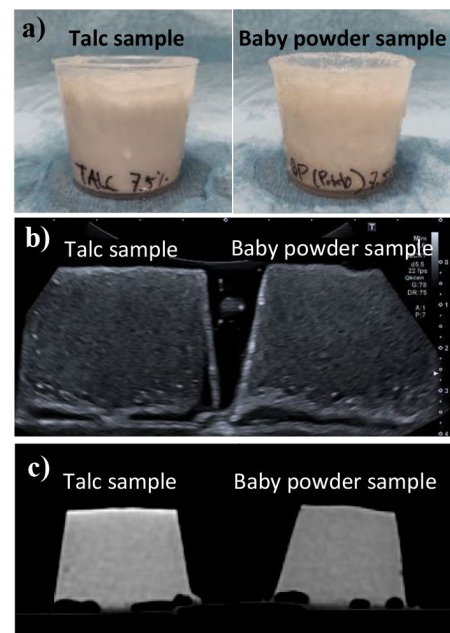


Fig. 1 Talc and Baby powder samples (7.5% each) comparison analysis. a) Body samples. b) US scans of both samples. c) CT scans of both samples.

Qualitative Validation of a Cost-Effective Contrast Agent for Use in Doppler Flow Test Phantom

Emma Zhang^a, John Moore^b, Joana Cambranis^{b,c}, Gian L. Bisleri^f, Terry M. Peters^{a,b,c,d}, and Elvis C. S. Chen^{a,b,c,d,e}

^aSchulich School of Medicine & Dentistry, ^bRobarts Research Institute, ^cSchool of Biomedical Engineering,

^dDepartment of Medical Biophysics, ^eDepartment of Electrical and Computer Engineering · Western University,

London, Ontario, Canada ^fSt. Michael's Hospital · University of Toronto, Toronto, Ontario, Canada

Introduction: Red Blood Cells (RBC) in the Circulatory system serve as natural Ultrasound Contrast Agents (UCA) in Doppler Ultrasound (US).¹ When studying the hemodynamics of cardio-vascular phantoms, particles in blood mimicking fluid (BMF) mimic the physical and acoustic properties of RBC, allowing a better image visualization and acquisition in Colour Doppler signal detection.² However, current commercial BMF might be costly and require extensive time for cleaning after experiments. Therefore, users might result in using distilled water as medium instead. Yet, water does not contain particles that mimic RBC and shows poor image visualization in Doppler US. In this work, we present an experimental UCA for use in Doppler flow tests in cardiovascular phantoms. The significance of our work is a cost-effective UCA that contains particles that mimic RBC and generate Doppler signal, is easy to manufacture and requires little preparation/clean-up when compared to the commercially available BMF.

Methods: Contrast agent formula consisted of 2L of water and 5% of Tide Free & Gentle Liquid Landry Detergent with 0.02% of Zinc Oxide Powder to mimic particles. All components were added to a 3-Liter Water Reservoir connected to an inner tube diameter of 8.52 mm. Experimental UCA was perturbed rigorously for 1 minute and suspended 40 cm above the experimental set up to ensure proper mimicking of blood flow velocity. The experimental UCA was held still for 5 minutes before the outflow from Water Reservoir. The experiment set up consisted of experimental UCA inside the Water Reservoir, a Phillips EPIQ 7C Ultrasound system, a 3D-printed holder for tube connected to the UCA and an US transducer (Phillips X7-2t, 2-7MHz) to ensure direct flow within a fixed distance as shown in Figure 1.a. Flow rate of experimental UCA was set to 379-757 mL/minute. A commercially available BMF (BMF-US) based on the formulation presented by Ramnarine et al.,² was previously validated for use in Doppler flow test objects, and thus is used as the ground truth in our study. For qualitative analysis, Doppler images were acquired from both BMF-US and experimental UCA.

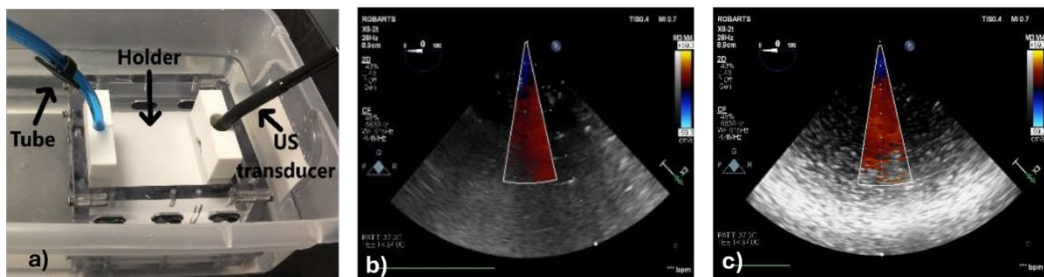


Figure 1. a) Experiment setup. **b)** Ground Truth: BMF. **c)** Experimental UCA.

Results: Total time used to fabricate and test the experimental UCA was 13 minutes. Experimental Doppler image (Figure 1.c) presents similar characteristics to the Ground Truth (Figure 1.b). Both start with negative doppler shift at top of the Doppler box, represent by dark blue. Majority of the bottom of Doppler box showed particles with positive doppler shift, represent by dark red. The similarity in colour of Doppler indicates similarity in velocity and direction of flow in experimental UCA and commercially available BMF.

Conclusions: Results show experimental UCA creates similar properties to commercial BMF. In addition to the advantage of inexpensive and effective Doppler UCA, time used to clean experimental UCA from set up was fast and only required rinsing the 3D printed holder. Future experiments include mimicking specific blood flow in veins (i.e., carotid artery, jugular vein) by changing tube diameters or height of Water Reservoir, addition of viscosity property of blood to UCA and increase in blood flow detection time.

References: [1] Samavat, H., et al., (2006) "An ideal blood mimicking fluid for Doppler ultrasound phantoms". *Journal of Medical Physics*. [2] Ramnarine, K. V., et al., (1998) "Validation of a new blood-mimicking fluid for use in Doppler flow test objects". *Ultrasound in Medicine & Biology*.

Polarimetric image guidance on resected breast tumors to optimize mass spectrometry analysis

Michael D. Singh^{1,*}, Lan Anna Ye¹, Michael Woolman¹, Arash Zarrine-Afsar^{1,2}, Alex Vitkin^{1,3}

¹Department of Medical Biophysics, University of Toronto, Toronto, ON, Canada

²Department of Surgery, University of Toronto, Toronto, ON, Canada

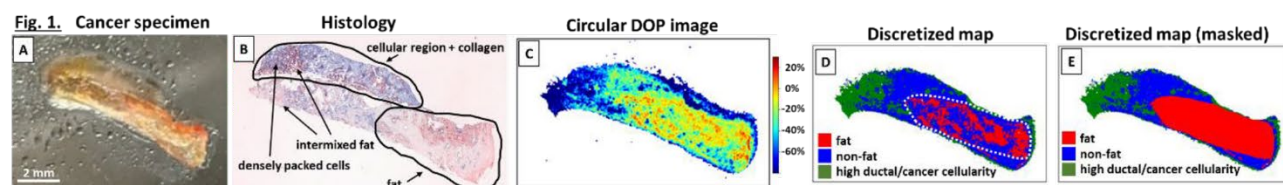
³Department of Radiation Oncology, University of Toronto, Toronto, ON, Canada

*michaeldhillon.singh@mail.utoronto.ca (presenting author)

Introduction: Mass spectrometry (MS) is a molecular composition analysis technique which enables comprehensive oncological characterization of tissues; however, its clinical utility remains limited due to lengthy analysis times [1]. Additionally, a promising variant of MS, known as picosecond infrared laser MS (PIRL-MS), faces challenges when probing adipose tissue (i.e., fat) due to melting and subsequent contamination of the rest of the specimen. Therefore, MS and its variants can benefit from a guidance tool which avoids non-informative and problematic regions of tissue to save time and prevent contamination. Polarized light imaging (i.e., *polarimetry*) is an excellent candidate for this task since it is sensitive to tissue microstructure while being fast, non-invasive, and label-free with minimal tissue preparation. This was demonstrated in our previous collaborative studies on simple, flat, and thin (4 μm) breast tumour slices [1-3]. To further advance this approach, we are performing polarimetric imaging of clinically realistic, thick (1-4 mm) and uneven breast resections to (1) delineate fat (for MS avoidance), and (2) identify ductal cell regions (MS typically acquires oncological information from cells). Our results show that polarimetric image guidance enables MS targeting of non-adipose tissue with potential to also identify cellular-rich regions (see **Fig. 1**). These results may enable intraoperative diagnostics and on-site breast biopsy adequacy assessment via MS to enable faster and more efficient breast cancer diagnoses.

Methods: Polarimetric images of resected human breast specimens (3 cancer, 2 healthy) were analyzed. Circular ‘degree of polarization’ (DOP) images were mainly studied. DOP quantifies how correlated the circular polarization waves remain after interacting with each tissue. Circular DOP is calculated by taking the difference between the intensity of right-handed and left-handed circular polarization then normalizing by the total circular polarization intensity (thus represented as a percentage). Details on this calculation and the schematic of the setup can be found in [5]. Automated data acquisition and analysis can be performed in less than 5 minutes.

Results and conclusion: Circular DOP images exhibit contrast between fat, non-fat tissue, and highly cellular regions, shown in **Fig. 1(A-C)**. Colour-coded discretized maps can then be generated by thresholding the circular DOP image to indicate each tissue type, as seen in **Fig. 1(D,E)**. This enables MS avoidance of problematic fatty tissue to prevent contamination, while targeting information-rich cell regions to save significant time. It is hypothesized that the contrast is achieved through circular DOP’s sensitivity to ‘scatterer size’, which has been demonstrated in our recent studies on tissue-like material [4,5]. Specifically, in breast tissue, polarized light mainly interacts with fat cells, ductal/cancer cell nuclei (and other sub-cellular components), and collagen. Fat cells are the largest components, whereas ductal/cancer cell constituents are the smallest components; thus, it may be likely that circularly DOP’s sensitivity to scatterer size enables differentiation between these tissue types. The next steps are to confirm the presence of this phenomenon and study its potential uses.



[1] Tata et al. Chem. Sci. 7.3 (2016): 2162-2169. [2] Woolman et al. Sci. Rep. 7.1 (2017). [3] Tata et al. Sci. Rep. 6.1 (2016). [4] Singh and Vitkin. BOE 12.11 (2021). [5] Singh and Vitkin. Sci. Rep. 13.1 (2023)

Polarization speckle pattern analysis for the investigation of optical properties in biological tissue

Carla Kulcsar¹, Daniel Louie², Michael Singh¹, Alex Vitkin^{2,3}

¹ Medical Biophysics, University of Toronto, Canada

² Princess Margaret Cancer Research Tower, University Health Network (UHN), Canada

³ Princess Margaret Cancer Centre, Department of Radiation Oncology, UHN, Canada

Introduction

When a coherent light source interacts with a sample, it generates a speckle pattern, resembling a salt-and-pepper-like texture. Speckles arise from the interference of light passing through a volume, introducing phase differences into the initially coherent wavefront. As a consequence, speckles exhibit high sensitivity to subwavelength optical properties of a sample. Speckle patterns not only occur in intensity, but also in the polarization state of light (shown in the figure). By examining *polarization speckle patterns*, we extend traditional intensity measurements to exploiting multiple light wave characteristics, such as the plane of wave oscillation (polarization) and phase properties (speckle). Making use of this multidimensional analysis, we aim to quantify the relationship between polarization speckle patterns and the turbidity of a volumetric sample. This may prove helpful in the investigation of biological tissue, specifically the diagnosis of cancer tissue during neoplasia in cancer progression, during which the scattering properties of tissue have been shown to change.

Methods

Our set up consists of a HeNe laser illuminating a volumetric sample. We conducted experiments on solid phantoms with varying scattering coefficients, utilizing titanium dioxide in resin to adjust the scattering properties of the volume. Images of the backscattered speckle patterns are acquired using a CCD camera. To fully capture the polarization state of each speckle in one polarization speckle pattern, we acquire six images filtered for different polarizations. Acquisitions are made for two different input polarization states (linear and circular).

Results

Initial results on samples with varying turbidity show that speckle size ($16\mu\text{m}$ to $28\mu\text{m}$) and contrast increase significantly with turbidity in the intensity domain. The power spectrum of lower turbidity samples further exhibits a lower cut-off frequency than high turbidity samples.

In comparison to intensity speckles, speckle patterns in stokes vector components and polarization ellipse features (tilt and ellipticity) are sensitive to the input state of light, exhibiting a constant offset in contrast, skewness and kurtosis between linear and circular input.

In addition to investigating volume-property-dependent changes in these metrics, we also observed a spatial correlation (calculated by a 2D cross-correlation between speckle images) of intensity speckle patterns and degree of polarization speckle patterns. This indicates a close relationship between intensity fluctuations and the degree of polarization in a speckle pattern.

Conclusions

In this study, we gained a more fundamental understanding of the generation of polarization speckle patterns and were able to show that characteristic polarization speckle pattern metrics depend on the scattering properties of a volumetric sample. This may prove helpful in detecting neoplasia during cancer progression, in which the scattering properties of the tissue are expected to change.

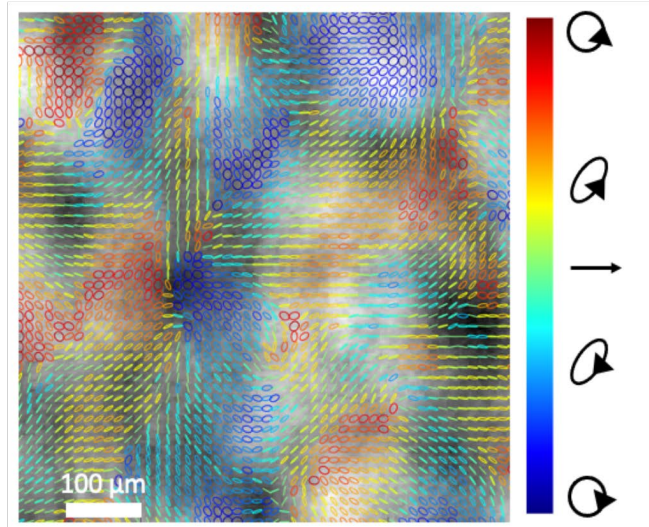


Figure: Intensity speckle pattern in black and white overlaid with polarization state speckle pattern. Color represents the polarization ellipse state of the light.

Author Index

Author Name	Presentation	Page
Abdollahi, Melika	P3-02	37
Abdul Rahman, Rayhan	P20-03	162
Abolmaesumi, Purang	P8-03	82
	P20-01	160
Adewale, Anjolaoluwa	O15-01	131
	O17-02	142
Ahmed, Mashal	P14-08	127
Alam, Faiyza S.	O11-04	104
	P13-05	115
Albert, Mitchell S.	P19-08	158
Aldossary, Ruba	P19-08	158
Alexander, Sandra	O2-01	31
Allam, Nader M.	P8-06	85
Ameis, Stephanie	P14-05	124
	O17-03	143
Appleby, Ryan	P4-07	54
Argyelan, Miklos	P14-05	124
Au, Ryan	P13-01	111
Aziz, Amal	P20-03	162
Babaeipour, Ramtin	P13-04	114
Bailey, Colleen	O2-02	32
	P14-02	121
Bainbridge, Daniel	O11-03	103
Bang, Jin-Young	O6-04	66
Banh, Jacqueline	P7-02	69
Barker, Kevin	P8-09	88
	P20-03	162
Baron, Corey	O2-04	34
	P4-03	50
	P4-04	51
	O10-04	99
	O16-03	138
Barr, Colton A.	P7-07	74
	O15-03	133
Barr, Keiran	P7-07	74
Bartling, Mandolin	P7-01	68
Batarchuk, Viktoriia	P19-08	158
Bax, Jeffrey	P8-04	83
	P20-03	162

Author Name	Presentation	Page
Beckett, Tina	P14-02	121
Beland, Valerie	O11-01	101
Bellyou, Miranda	O2-03	33
Berazher, Renee	O2-01	31
Bereznick, Sheldon D. H.	O12-01	106
Berman, David	P7-05	72
Bernards, Nicholas	O6-03	65
Bertolet Reina, Alejandro	P19-03	153
Beydoun, Sarah	O11-02	102
Bierbrier, Joshua	O1-01	26
	O9-03	93
Billings, Nicola B.	P4-07	54
Binda, Shawn	O16-04	139
Bisleri, Gianluigi	P7-03	70
	O11-03	103
	P20-07	166
Blumberger, Daniel	P14-07	126
Boccanfuso, Joe	P7-08	75
	P7-09	76
	P7-10	77
Boctor, Emad	O9-04	94
Boileau, Isabelle	O12-01	106
	P14-08	127
	O17-03	143
Bok, Taehoon	O18-02	147
Bortolus, Mark R.	O17-04	144
Bourbeau, Jean	P3-03	38
	O11-02	102
Boyle, Amanda	O17-04	144
	P19-07	157
Braganza, Sharon	O11-04	104
Brown, Arthur	P4-03	50
	O10-04	99
Buchanan, Robert	P14-05	124
	P14-09	128
Burhan, Amer	O12-04	109
Burki, Lubna	P4-05	52
Butler, Kevin	O12-01	106
Cambranis Romero, Joeana N.	P7-03	70
	P20-06	165
	P20-07	166

Author Name	Presentation	Page
Campos, Leonardo	P7-08	75
	P7-09	76
	P7-10	77
Cardarelli Leite, Leandro	O9-02	92
Carnahan, Patrick	O11-03	103
Caro Lopez, Nicholas	P7-02	69
Castilla, Alejandra	P4-08	55
Cecchini, Matthew	P13-01	111
Cernelev, Pavel-Dumitru	O15-03	133
Chan, Nyein	P7-04	71
Chen, Elvis C. S.	P3-10	45
	P7-03	70
	O11-03	103
	P20-06	165
	P20-07	166
Chen, Juan	O6-03	65
Cherin, Emmanuel	P8-02	81
	O18-03	148
	P20-04	163
Chinchalongporn, Vorapin	P4-08	55
Chinnery, Tricia	P13-01	111
Cho, Eunyoung	O5-02	59
Christie, Jaryd R	P13-01	111
Chu, Jonathan	P3-04	39
Chugh, Brige	O6-02	64
	O16-04	139
Chung, Kevin J.	P14-03	122
Cleverley, Kristin	O17-03	143
Connolly, Laura	P7-04	71
	O9-04	94
Contreras Sanchez, Hector Alejandro	P8-06	85
	P13-08	118
Cote, Cassie	O17-03	143
Courtney, Darren	O17-03	143
Cunningham, Ian	P7-06	73
	P13-03	113
Daly, Michael	P7-01	68
	O15-01	131
	O17-02	142
Danielli, Ethan	O12-03	108
Das, Sunit	O6-02	64
Daskalakis , Zafiris	P14-07	126

Author Name	Presentation	Page
Davision, Colleen	P7-04	71
Davoudi, Heidar	P3-02	37
Dayton, Paul	P20-04	163
de Kort, Jessica C.	P3-08	43
de Ribaupierre, Sandrine	O1-03	28
De Sarno, Danny	P19-03	153
	P19-05	155
DeBoef, Brenton	P19-08	158
Deguet, Anton	O9-04	94
DeMatteo, Carol	O10-01	96
Demore, Christine	P8-02	81
	O18-03	148
	P20-04	163
Desjardins, Lise	P14-03	122
Desmond, Kimberly	O10-03	98
	O17-03	143
Detsky, Jay	O6-02	64
Dhari, Jeffrey	P13-02	112
Dheda, Shahtaj	P14-08	127
Dickie, Erin	P14-05	124
	P14-07	126
	P14-09	128
	O17-03	143
Ding, Lili	O6-03	65
Diop, Mamadou	P14-01	120
Do, Richard	P8-08	87
Donnelly, Sarah C.	P19-06	156
Drangova, Maria	O9-02	92
	O16-02	137
du Toit, Carla	O18-01	146
	P20-02	161
Dubovan, Paul I.	O2-04	34
	P4-04	51
Dubroy-McArdle, Céline	P8-07	86
Duimering, Adrienne	O1-01	26
Dunn, Alexander	O5-02	59
Duong, Thanh-Tai	P19-03	153
	P19-05	155
Durocher, Emma	O6-01	63
Dykstra, Sarah	O18-04	149
Ebrahimi, Mehran	P3-02	37
Eed, Amr	O2-03	33

Author Name	Presentation	Page
Elkind, Emese	P7-07	74
Elsaid, Sonja	O10-03	98
	O12-01	106
El-Sayes, Abdullah	O6-03	65
Emmenegger, Urban	O15-04	134
Engel, Jay	O15-02	132
Erb, Jason	P3-11	46
Ertl-Wagner, Brigit	P13-06	116
Fan, Victoria	P3-10	45
Felsky, Daniel	O17-03	143
Fenster, Aaron	O1-03	28
	P8-04	83
	P8-09	88
	O18-01	146
	P20-02	161
	P20-03	162
Fernando, Nitara	P19-04	154
Feusner, Jamie	P14-10	129
Fichtinger, Gabor	O1-01	26
	O1-04	29
	P3-08	43
	P3-11	46
	O5-04	61
	P7-04	71
	P7-05	72
	P7-07	74
	O9-01	91
	O9-03	93
	O9-04	94
	O15-02	132
	O15-03	133
	Finkelstein, Joel	O15-04
Fisher, Carl	O6-03	65
Flammino, Marcus	P14-03	122
Fleming, Peter	P7-06	73
Flueraru, Costel	P8-06	85
Foltz, Warren	P8-06	85
Fooladgar, Fahimeh	P20-01	160
Foster, Paula	O16-01	136
	O17-01	141
	P19-04	154

Author Name	Presentation	Page
Foster, Stuart	P8-02	81
	P20-04	163
Foussias, George	P14-05	124
	P14-07	126
	P14-09	128
	O17-03	143
Fox, Matthew	P4-09	56
	P13-04	114
Gadde, Suresh	O6-01	63
Gaede, Stewart	P3-06	41
	O6-04	66
Gallucci, Julia	P14-07	126
	P14-09	128
Garamvolgyi, Tivadar	P7-07	74
Gardi, Lori	P8-04	83
	P20-03	162
Garland, Lisa	P13-03	113
Gelman, Daniel	O9-02	92
Gelman, Neil	P19-06	156
Genkin, Daniel	O11-02	102
Geremia, Nicole	P4-03	50
Ghaseminejad, Shahin	P19-03	153
	P19-05	155
Ghoshbiswas, Rajshree	P4-08	55
Gilany, Mahdi	P8-03	82
	P20-01	160
Gilbert, Kyle	O2-03	33
Gold, James	P14-05	124
	P14-09	128
Goldhawk, Donna E.	P19-01	151
	P19-06	156
Goldstein, Alyssa	O6-03	65
Goldstein, Benjamin	O17-03	143
Goolaub, Datta	O11-01	101
Gopinath, Georgia	O12-04	109
Graham, Simon J.	P4-01	48
Gregor, Alexander	O6-03	65
Grynko, Vira	P19-08	158
Guan, Yanran	P8-05	84
Guru Prasad, Venkat	P7-02	69

Author Name	Presentation	Page
Hafey, Chris	P7-08	75
	P7-09	76
	P7-10	77
Haidegger, Tamás	O5-04	61
	P7-07	74
	O9-01	91
Halim, Michael	O6-03	65
Hamghalam, Mohammad	P8-08	87
Hamilton, Jake	P4-03	50
	O10-04	99
Hanks, James	P7-08	75
	P7-09	76
	P7-10	77
Hardisty, Michael	P3-04	39
	O15-04	134
Harmanani, Mohamed	P8-03	82
	P20-01	160
Harris, Gordon	P7-08	75
	P7-09	76
	P7-10	77
Hasselbrink, Carson	P19-08	158
Hatolkar, Ved	P14-02	121
Hawco, Colin	P14-05	124
	P14-07	126
	P14-09	128
	P14-10	129
Hawke, Lisa	O17-03	143
Hewlett, Miriam	O16-02	137
Hiles, Emily	P14-02	121
Hill, Mary	P14-02	121
Hisey, Rebecca	O1-01	26
	O1-04	29
	P3-11	46
	O9-01	91
	O9-03	93
Hobson, Sebastian	P20-05	164
Hodgson, Aaron	P19-08	158
Holden, Matthew S.	O1-01	26
	P8-05	84
	O9-03	93

Author Name	Presentation	Page
Holdsworth, David W.	O1-02	27
	P3-07	42
	P3-09	44
	P7-06	73
	P7-11	78
	O9-02	92
	P19-02	152
Hong, Selinia	P19-01	151
Hoover, Douglas	P8-09	88
Horvath, Shaelyn E.	P13-05	115
Husain, Omair	O17-03	143
Hutter, Megan	O18-01	146
	P20-02	161
Hwang, Dae Kun	P3-05	40
Hysi, Eno	O18-02	147
Iorio, Olivia	O11-02	102
Irish, Jonathan	P7-01	68
	O15-01	131
	O17-02	142
Iseman, Rachael	P7-05	72
Jabs, Doris	O15-02	132
Jamaspishvili, Tamara	P7-05	72
James, James	P3-03	38
Jamzad, Amoon	P7-05	72
	P8-03	82
	O15-02	132
	P20-01	160
Jarnagin, William	P8-08	87
Jegatheeswaran, Sinthuran	P3-05	40
Kadar, Assaf	O18-01	146
	P20-02	161
Kahana, Dafna	P14-08	127
	O17-03	143
Karagulleoglu Kunduraci, Sule	P14-01	120
Karat, Bradley G.	P14-06	125
Kashif, Mohammad	P3-05	40
Kaufmann, Martin	P7-05	72
	O15-02	132
Keenlside, Lynn	P14-03	122
Kelly, John	O17-01	141
Kerr, Adam	O2-04	34
Kesibi, Maha	O15-03	133

Author Name	Presentation	Page
Khan, Ali R.	P4-04	51
	O12-04	109
	P14-04	123
	P14-06	125
Khan, Naimul	P20-05	164
Khan, Zara	P14-05	124
Kholer, Stefan	O12-04	109
Khorasani, Mohammadali	P8-10	89
Kim, Andrew	O9-01	91
Kirby, Miranda	P3-03	38
	O11-02	102
Kitner, Nicole	P3-08	43
Klein, Geoff	O15-04	134
Kloiber, Stefan	O10-03	98
	P14-08	127
Klosa, Elizabeth H.	O5-04	61
Kolios, Michael	O18-02	147
Komeili, Amin	P4-07	54
Korzeniowski, Martin	P3-08	43
Kosik, Ivan	P3-01	36
	O5-01	58
Kovacs, Antal Halen	P19-08	158
Kozloff, Nicole	O17-03	143
Kulcsar, Carla	P20-09	168
Kumbhare, Dinesh	O12-03	108
La Macchia, Josephine	O17-02	142
Lad, Jigar	P8-10	89
Lafleur, Dawson	P3-11	46
Lai, Meng-Chuan	P14-05	124
Lalone, Emily	O18-01	146
	P20-02	161
Lam, Christopher	O11-01	101
Lam, Wilfred	P8-07	86
Lasso, Andras	O15-03	133
Lau, Angus	O6-02	64
	O16-04	139
Law, Christine	O1-01	26
	O9-03	93
Lawrence, Liam S. P.	O6-02	64
	O16-04	139
Laxer, Sam	O2-03	33

Author Name	Presentation	Page
Le Foll, Bernard	O10-03	98
	O12-01	106
	P14-08	127
Lee, Hsin-Ju	O10-02	97
Lee, Mitchell	O5-02	59
Lee, Tim	P8-01	80
Lee, Ting-Yim	P3-06	41
	O6-04	66
	P14-03	122
	P19-03	153
	P19-05	155
Leonard, Simon	O9-04	94
Levendovics, Renáta	O5-04	61
Lewis, Rob	P7-08	75
	P7-09	76
	P7-10	77
Li, Celina	O6-03	65
Li, Daniel	O11-04	104
	P13-05	115
Liang, Darren	O12-04	109
Lim, Adam	P13-06	116
Lim-Fat, Mary Jane	O6-02	64
Lin, Fa-Hsuan	O10-02	97
Liu, Junmin	O16-02	137
Liu, Wei	P3-05	40
Lo, Justin	P13-06	116
Long, Bining	P8-05	84
Lopes, Alana	P13-01	111
Louie, Daniel	P8-01	80
	P20-09	168
Lugez, Elodie	P3-05	40
	P7-02	69
Lui, Harvey	P8-01	80
Ma, Jenny	O6-03	65
Macgowan, Chris	O11-01	101
Majumdar, Anamitra	P8-10	89
Makimoto, Kalysta M.	P3-03	38
Malhotra, Anil	P14-05	124
	P14-09	128
Manokaran, Jenita	P13-07	117
Maralani, Pejman	O6-02	64
Markevich, Stefanie	P7-01	68

Author Name	Presentation	Page
Martinez, Paco	O16-01	136
Matsuura, Naomi	O6-01	63
McGrath, Sean F	O6-01	63
McLachlin, Stewart	P3-04	39
McLaurin, JoAnne	P14-02	121
McRae, Sean	O16-01	136
Mendez, Lucas	P8-04	83
Menon, Ravi	O2-03	33
	O2-04	34
Merchant, Shaila	O15-02	132
Mesrkhani, Teo	P3-05	40
	P7-02	69
Milner, Jaques	P3-07	42
Mittal, Richa	P13-07	117
Moga, Kristof	P7-07	74
Mojtahedi, Ramtin	P8-08	87
Moore, John	P7-03	70
	O11-03	103
	P20-07	166
Moore, Kevin R. J.	P19-02	152
Moran, Gerald	P19-06	156
Morrison, Laura	P14-03	122
Morton, David	O9-01	91
Motz, Ben	P3-01	36
	O5-01	58
Mousavi, Parvin	P3-08	43
	P7-04	71
	P7-05	72
	P8-03	82
	O9-01	91
	O9-04	94
	O15-02	132
	P20-01	160
Moxon-Emre, Iska	P14-05	124
Mudathir, Randa	O18-01	146
	P20-02	161
Murrell, Emily	P19-07	157
Mushtaha, Farah N.	P4-04	51
Myrehaug, Sten	O6-02	64
Najjar, Esmat	P7-01	68
	O17-02	142
Nakua, Hajer	P14-07	126

Author Name	Presentation	Page
Narvaez, Andrea	O17-04	144
	P19-07	157
Nasser, Jamiel	P8-04	83
Near, Jamie	O2-02	32
	P4-01	48
	P4-05	52
	P4-08	55
	O12-02	107
	P14-02	121
Negus, Christina	P7-01	68
	O15-01	131
	O17-02	142
Ng, David K.-H.	O9-02	92
Ng, Justin	P14-10	129
Nikolov, Hristo	O9-02	92
Nikolova, Yuliya	O17-03	143
Noseworthy, Michael	P4-06	53
	O10-01	96
	O12-03	108
Nowikow, Cameron	P4-06	53
	O10-01	96
Nussey, Daniel	P8-07	86
Oakden, Wendy	P14-02	121
Okell, Thomas	O12-02	107
Olding, Tim	P3-08	43
Oliver, Lindsay	P14-05	124
	P14-07	126
	P14-09	128
Opara, Chidera	P19-03	153
	P19-05	155
Oran, Omer	O16-02	137
Ouriadov, Alexei V.	P4-09	56
	P13-04	114
Palaniyappan, Lena	O12-04	109
	P14-04	123
Park, Claire	P20-03	162
Patel, Harsh	P13-04	114
Pener-Tessler, Alon	P7-01	68
	O15-01	131
	O17-02	142
Peramakumar, Denesh	O1-04	29
Pereira, Christina	P14-08	127

Author Name	Presentation	Page
Perron, Samuel	P4-09	56
Peters, Terry M.	P3-10	45
	P7-03	70
	O11-03	103
	P20-06	165
	P20-07	166
Phillips, Jamie	P8-01	80
Pickering, Geoffrey	P19-02	152
Poepping, Tamie	P19-02	152
	P20-03	162
Policelli, Robert	P13-01	111
Polillo, Alexia	O17-03	143
Pollmann, Steven	P3-09	44
Portnoy, Sharon	O11-01	101
Prado, Marco	P4-03	50
Prado, Vania	P4-03	50
Prato, Frank	P19-01	151
	P19-06	156
Purkey, Eva	P7-04	71
Qi, Olivia R. Y.	P7-03	70
	P20-06	165
Quereshy, Fayez	P8-10	89
Quilty, Lena	O17-03	143
Radcliffe, Olivia	P7-04	71
Rahman, Naila M.	O10-04	99
Rasmussen, Sean	P13-01	111
Ratjen, Felix	O11-04	104
Rezvanjour, Sara	P3-03	38
Roa, Felipe	P8-02	81
Rock, Jason	P4-01	48
Rodgers, Jessica R.	P3-08	43
Rodriguez, Karla	P19-08	158
Ronald, John	O16-01	136
Ross, Bryan	O11-02	102
Ross, Tayler Declan	O15-04	134
Rotenberg, Martin	O17-03	143
Rudan, John	P7-05	72
	O15-02	132
Rukas, Daniel	P7-08	75
	P7-09	76
	P7-10	77
Ruschin, Mark	O6-02	64

Author Name	Presentation	Page
Sadanand, Siddharth	O2-01	31
	P4-02	49
	O5-02	59
Sahgal, Arjun	O6-02	64
Sandhu, Fariah	P14-05	124
Santyr, Giles	O11-04	104
	P13-05	115
Sare, Daniel	O5-02	59
Schimmer, Pamela	O6-03	65
Scholl, Timothy	O16-01	136
Schuurmans, Carol	P4-08	55
Schwarz, Elise	O17-02	142
Secara, Maria T.	P14-05	124
	P14-09	128
Sedghi, Alireza	P7-08	75
	P7-09	76
	P7-10	77
Sehl, Olivia C.	O16-01	136
Senthil, Sneha Vaishali	P4-05	52
Serra, Stefano	P8-10	89
Sharma, Anurag	P13-01	111
Sharma, Bhanu	O10-01	96
Shepelytskyi, Yurii	P19-08	158
Shyu, Claire	O12-01	106
Sikstrom, Lee	O1-02	27
	P7-06	73
Simard, Nicholas	O12-03	108
Simpson, Amber	P8-08	87
Simpson, Andre	P4-08	55
Singh, Michael D.	P20-08	167
	P20-09	168
Singh, Nidhi	P8-02	81
Smith, Andrew	O12-01	106
Soenjaya, Yohannes	P8-02	81
Soliman, Hany	O6-02	64
Song, Hyunwoo	O9-04	94
Sothynathan, Mayuri	O16-03	138
Stanisz, Greg	P4-02	49
	P8-07	86
Stefanovic, Bojana	O18-03	148
Stewart, James	O6-02	64
Stobbe, Rob	P4-02	49

Author Name	Presentation	Page
Sun, Qin	P19-01	151
Sunderland, Kyle	O9-01	91
Surry, Kathleen	P8-04	83
	P8-09	88
Sussman, Dafna	O2-01	31
	P4-02	49
	O5-02	59
	P8-07	86
	P13-06	116
	P20-05	164
Syeda, Ayesha	P7-05	72
Szabo, Robert	O9-01	91
Szatmari, Peter	P14-05	124
Szentimrey, Zachary	O1-03	28
Tabatabaei, Saleh	O15-04	134
Tahmasebi, Mahdi	O5-03	60
Tai, Elizabeth	O9-02	92
Takács, Kristóf	O5-04	61
Talwar, Tanu	P19-08	158
Tan, Wan-Cheng	P3-03	38
	O11-02	102
Tang, Sunny	P14-05	124
Tanguay, Jesse	P13-02	112
Tavallaei, Ali	O5-02	59
	O5-03	60
Taylor, Edward	P8-06	85
	P13-08	118
Taylor, Russ	O9-04	94
Tchvialeva, Lioudmila	P8-01	80
Tessier, David	P20-03	162
Therriault, Aimee	O6-02	64
Thompson, R. Terry	P19-01	151
Thornton, Kanchana	P7-04	71
Timmons, Brian	O10-01	96
To, Minh Nguyen Nhat	P8-03	82
	P20-01	160
Tong, Junchao	O17-04	144
	P19-07	157
Tong, Olivia	P14-03	122
Townson, Jason	O17-02	142
Tran, Brandon	O16-04	139
Tran, Christopher	P13-01	111

Author Name	Presentation	Page
Tran, Haphan	P7-02	69
Trozzo, Sophia D.	O17-01	141
Trumpour, Tiana	P8-04	83
	P8-09	88
	P20-03	162
Truong, Jennifer	O17-03	143
Truong, Peter	O12-02	107
Tseng, Chia-Lin	O6-02	64
Tumanova, Kseniia	P8-10	89
Tun, Aung Tin	P7-04	71
Tyler, Susan	P14-03	122
Ukwatta, Eranga	O1-03	28
	P4-07	54
	P13-07	117
Umoh, Joseph U.	P3-07	42
	P7-06	73
Ungi, Tamas	P3-08	43
	P3-11	46
	P7-04	71
	P7-07	74
	O9-01	91
	O15-02	132
	O15-03	133
Urban, Trinity	P7-08	75
	P7-09	76
	P7-10	77
Uribe, Carme	O17-03	143
Uthayakumar, Deeva	O2-02	32
Valic, Michael S.	O6-03	65
Van Dyken, Peter	P14-04	123
van Gaalen, Alissa J. L.	P8-09	88
Varela-Mattatall, Gabriel E. M.	O2-04	34
	P19-06	156
Varvani Farahani, Mahdiah	O12-04	109
Vasdev, Neil	O17-03	143
	O17-04	144
	P19-07	157
Vazquez Avila, Elvira Catalina	O18-03	148

Author Name	Presentation	Page
Vitkin, I. Alex	P8-06	85
	P8-10	89
	P13-08	118
	P20-08	167
	P20-09	168
Voineskos, Aristotle	P14-05	124
	P14-07	126
	P14-09	128
	O17-03	143
Wagner, Matt W.	P13-06	116
Walker, Ross	O15-02	132
Wallace, Bill	P7-08	75
	P7-09	76
	P7-10	77
Walsh, Joanna	P13-01	111
Wan, Jerry	P7-01	68
	O15-01	131
Wang, Chao	O2-02	32
Wang, Ruoyu (James)	O10-03	98
Wang, Wei	O17-03	143
Ward, Aaron	P13-01	111
Warren, Jade	P7-05	72
Weersink, Robert	P3-01	36
	O5-01	58
	O6-03	65
Wehrli, Bret	P13-01	111
Whyne, Cari	O15-04	134
William, Wasswa	P7-06	73
Wilson, Brian	P3-01	36
	O5-01	58
	O6-03	65
	P7-01	68
	P8-02	81
	O15-01	131
	O17-02	142
Wilson, Kyle	P3-09	44
Wilson, Paul F. R.	P8-03	82
	P20-01	160
Wilson, Sydney	P7-11	78
Wodlinger, Brian	P8-03	82
	P20-01	160

Author Name	Presentation	Page
Won, Natalie J.	P7-01	68
	O15-01	131
Wong, Alexander	P3-04	39
Woolman, Michael	P20-08	167
Xia, Wenyao	P3-10	45
Xing, Shuwei	P7-03	70
	P20-06	165
Xu, Kathy	P4-03	50
	O10-04	99
Xu, Keshuai	O9-04	94
Yalda, Nardeen	O12-04	109
Yang, Jianming	O1-01	26
	O9-03	93
Yang, Jing	P20-04	163
Yau, Timothy	P3-06	41
Ye, Anna	P20-08	167
Yeung, Chris	O9-01	91
	O15-02	132
Yin, Jianhua	O18-03	148
	P20-04	163
Yoo, Shi-Joon	O11-01	101
Young, Dylan	P20-05	164
Yu, Ju-Chi	P14-05	124
	P14-07	126
	P14-10	129
Yu, Lujia	O17-03	143
Yuan, Charles	O11-03	103
Zabel, William	P8-06	85
	P13-08	118
Zanette, Brandon	O11-04	104
	P13-05	115
Zarrine-Afsar, Arash	P20-08	167
Zeman, Peter	O2-03	33
Zeng, Haishan	P8-01	80
Zhang, Emma	P20-06	165
	P20-07	166
Zheng, Chao	O17-04	144
Zheng, Gang	O6-03	65
	P8-02	81

Author Name	Presentation	Page
Zheng, Mark	O6-03	65
Zhu, Ryan	P13-04	114
Zhukovsky, Peter	P14-07	126
Ziegler, Erik	P7-08	75
	P7-09	76
	P7-10	77
Zilberman, Maia	O17-03	143